$Na_{1/2}Bi_{1/2}TiO_3$-Based Piezoceramics for High-Power Applications

Fachbereich Material- und Geowissenschaften, Technische Universität Darmstadt

Dissertation zur Erlangung des akademischen Grades Doktor-Ingenieur (Dr.-Ing.)
von Daniel Bremecker

1. Gutachten: Prof. Dr. Jürgen Rödel
2. Gutachten: Prof. Dr. Andreas Klein

Darmstadt den 28.11.2023

TECHNISCHE
UNIVERSITÄT
DARMSTADT

Bremecker, Daniel : $Na_{1/2}Bi_{1/2}TiO_3$-Based Piezoceramics for High-Power Applications
Darmstadt, Technische Universität Darmstadt,
Jahr der Veröffentlichung der Dissertation auf TUprints: 2023
URN:
Tag der mündlichen Prüfung: 08.09.2023

Erklärungen laut Promotionsordnung

§ 8 Abs. 1 lit. c PromO

Ich versichere hiermit, dass die elektronische Version meiner Dissertation mit der schriftlichen Version übereinstimmt.

§ 8 Abs. 1 lit. d PromO

Ich versichere hiermit, dass zu einem vorherigen Zeitpunkt noch keine Promotion versucht wurde. In diesem Fall sind nähere Angaben über Zeitpunkt, Hochschule, Dissertationsthema und Ergebnis dieses Versuchs mitzuteilen.

§ 9 Abs. 1 PromO

Ich versichere hiermit, dass die vorliegende Dissertation selbstständig und nur unter Verwendung der angegebenen Quellen verfasst wurde.

§ 9 Abs. 2 PromO

Die Arbeit hat bisher noch nicht zu Prüfungszwecken gedient.

Darmstadt den 28.11.2023 _____

Daniel Bremecker

Content

Symbols and Abbreviations

NBT	$Na_{1/2}Bi_{1/2}TiO_3$
KBT	$K_{1/2}Bi_{1/2}TiO_3$
BT	$BaTiO_3$
NBT-xBT	$(1-x)Na_{1/2}Bi_{1/2}TiO_3–xBaTiO_3$
NBT-xKBT	$(1-x)Na_{1/2}Bi_{1/2}TiO_3–x(K_{1/2}Bi_{1/2})TiO_3$
NBT-xKBT-yLBT	$(1-x-y)Na_{1/2}Bi_{1/2}TiO_3–x(K_{1/2}Bi_{1/2})TiO_3-y(Bi_{1/2}Li_{1/2})TiO_3$
PZT	$Pb(Zr,Ti)O_3$
PT	$PbTiO_3$
KNN	$(K_{1-x}Na_x)NbO_3$
BCZT	$(Ba,Ca)(Ti,Zr)O_3$
BF	$BiFeO_3$
BLSF	bismuth layer-structured ferroelectrics
B_{49}	Bi deficiency
B_{51}	Bi excess
DW	domain walls
EPR	electron paramagnetic resonance spectroscopy
FE	ferroelectrics
MPB	morphotropic phase boundary
MRD	multiples of random distribution
PFD	pole figure density
PNR	polar nanoregions
RF	Relaxor ferroelectric
RoHS	Restriction of Hazardous Substances
SEM	scanning electron microscopy
TSDC	thermally stimulated depolarization current
XRD	X-ray diffraction
a	lattice constant short direction
AC	alternating electric field/alternating current
c	lattice constant long direction
C	capacity
e	decay coefficient
E_C	coercive field
E_d	depolarization field
E_j	electric field
E_{pol}	poling field
d_{ijk}	piezoelectric constant
d_{33}^*	large signal piezoelectric coefficient in 33 directions
D_i	dielectric displacement
DC	direct current

f	frequency
f_{AR}	anti-resonance frequency
f_R	resonance frequency
$\pm f$	changed frequency
g	Goldschmidt tolerance factor
I	current
In	intensity
k_{ij}	electromechanical coupling coefficient
L	inductance
N_1/N_2	number of cycles
P_i	macroscopic polarization
P_{max}	maximum polarization
P_{rem}	remanent polarization
P_s	spontaneous polarization
Q_{ij}	mechanical quality factor
$R_{A,B}$	ionic radius of a cation on A- or B-site
R_O	ionic radius of oxygen
s^E_{ijkl}	compliance
S_{ij}	mechanical strain
S_{neg}	negative strain
S_{offset}	offset strain
S_{pol}	poling strain
S_{rem}	remanent strain
t	time
$tan(\delta)$	dielectric loss
$tan(\varphi)$	piezoelectric loss
$tan(\gamma)$	elastic loss
T	temperature
T_B	Burns temperature
T_C	Curie temperature
T_d	depolarization temperature
T_f	Vogel-Fulcher temperature
T_{F-R}	transition temperature from ferroelectric to relaxor
T_m	temperature of local maximum in the permittivity
T_{R-F}	transition temperature from relaxor to ferroelectric
T_{VF}	Vogel-Fulcher temperature
T_0	Curie-Weiss temperature
R	resistance
RT	room temperature
U	applied voltage
U_m	mechanical energy density
v	vibration velocity
V	measured voltage
W	power input

W_{air}	weight in air
W_{fl}	weight in water
X	reactance
Z	impedance
$\propto_i/\propto_j$	low/high boundaries of respective angle range
δ_T	tetragonal distortion
δ_R	rhombohedral distortion
ε^*	permittivity
ε'	real part of the permittivity
ε''	imaginary part of the permittivity
ε_o	permittivity of the vacuum
ε_r	relative permittivity
λ	wavelength
ρ	density
ρ_{air}	density air
ρ_{fl}	density water
σ	conductivity
σ_{jk}	mechanical stress
Ψ	angle between poling and observed direction
χ_{ij}	susceptibility
ω	angular frequency

1 Introduction

The world's resources are shrinking rapidly, and the efficient use of resources is becoming increasingly important. As a result, there is a growing demand for efficient energy conversion from electrical to mechanical energy. Piezoelectric materials are one such solution to this problem, as they can convert electrical energy to mechanical energy and vice versa. Piezoelectric materials have become attractive for a wide range of applications, including sensors, actuators, transducers, and motors. Examples of such applications include fuel injectors, operators for optical lenses and mirrors in cameras, ultrasonic cleaning and welding, sonar sensors, and ink-jet printers.[1] Piezoelectric devices are often compared to electromagnetic technology, but they have a number of superior properties, such as precise controlling properties, fast response, miniaturization, high efficiency, and resistance to harsh environmental conditions. Therefore, piezoelectric materials have become an extremely rapidly growing segment. The most commonly used ferroelectric material for piezoelectric applications is the solid solution $Pb(Zr,Ti)O_3$ (PZT). This material is used in more than 95% of the entire piezoelectric market.[2] The material´s properties can be engineered in a very broad range by optimizing its chemistry, processing, and microstructure, making PZT a popular choice due to its versatility and efficiency in energy conversion.

In addition to the need for the efficient use of resources, the toxicity of lead for humans and the environment has led to a broad research field for lead-free ferroelectric materials and triggered the development of new concepts and technologies. The use of lead-based ceramics is regulated by the Restriction of Hazardous Substances (RoHS) in the European Union (EU).[3] PZT has an exception from the RoHS directive until a suitable replacement is found. Despite the efforts made in the past few decades, PZT remains the most widely used material system, and it seems there is no single material system that can completely replace it.[4] Individual solutions for specific applications continue to emerge, and some material systems even outperform PZT in certain applications.[5] Therefore, there is a need for further research to develop and optimize alternative lead-free materials with desirable piezoelectric properties while addressing the environmental and health concerns associated with the use of lead-based ceramics.

This work addresses the challenges associated with $(Na_{1/2}Bi_{1/2})TiO_3$-based (NBT) materials and establishes their potential as replacements for PZT in high-power applications (high-power refers to electrical excitation and operation in mechanical resonance at high vibration velocity). NBT-based materials, such as $(Na_{1/2}Bi_{1/2})TiO_3$-$xBaTiO_3$ (NBT-xBT) and $(Na_{1/2}Bi_{1/2})TiO_3$-

$x(K_{1/2}Bi_{1/2})TiO_3$ (NBT-xKBT), have been identified as promising candidates due to their stable mechanical losses with increasing output power, in contrast to PZT, which exhibits strongly increasing mechanical losses under the same conditions.[6] Despite these advantages, there remain several challenges associated with NBT-based materials, including a lack of mechanistic understanding and unknown issues regarding the transfer from laboratory to real-world applications. Therefore, the following questions are addressed:

- What properties are crucial for the use in high-power applications, and why?
- How do the material properties change when measured under application-like conditions?

Systematic chemical modifications of the NBT-xBT and NBT-xKBT systems are discussed regarding their electromechanical properties, such as the piezoelectric coefficient, coupling factor, and different losses, including dielectric and electromechanical losses. This discussion includes their evaluation regarding temperature stability. A general doping strategy is established for the NBT-xBT and NBT-xKBT systems, enabling for a mechanistic discussion and comparison with doping in systems such as PZT and $BaTiO_3$ (BT). In addition to the optimization and mechanistic discussion, the NBT-based materials are evaluated and classified for use in high-power applications. This process involves fatigue measurements and comparison with a current PZT standard material. Finally, a theory is developed and proposed to explain the underlying mechanism of why NBT-based materials have low and stable extrinsic contributions with increasing output power. Therefore, the following questions have not been adequately answered up to now and are a major part of this work:

- Is there a general guideline for designing the properties of NBT-based materials for high-power applications, and what are the underlying physical mechanisms it is based on?
- How do the long-term performances of NBT-based alternatives compare with currently used standard materials?
- What is the origin of the exceptional stable extrinsic contribution to the strain against the increasing vibration velocity of NBT-based materials?

2 Theoretical Background

This chapter provides the fundamental framework necessary to understand the descriptions and discussions made in this work. It has been organized as follows: The first subchapter reviews the material groups ranging from dielectrics to relaxor ferroelectrics (RF). The next subchapter discusses ferroelectric materials (FE) in the context of high-power applications; specifically, the conditions and the material properties required for such applications are elucidated. Ferroelectric hardening and approaches for ferroelectric hardening will be discussed in a separate subchapter. Subsequent subchapters elaborate on texturing and fatigue and in which contexts they are used in this work.

The last section summarizes the material systems of interest for this work, specifically the (1-x)$Na_{1/2}Bi_{1/2}TiO_3$–x$BaTiO_3$-based (NBT-xBT-based) materials and the (1-x)$Na_{1/2}Bi_{1/2}TiO_3$–x$(K_{1/2}Bi_{1/2})TiO_3$-based (NBT-xKBT-based) materials.

2.1 From Dielectrics to Pyroelectrics

The information given in this chapter is taken from the text-books and review-papers by Moulson et al. [7], Waser et al. [8], Jaffe et al. [9] and Damjanovic [10].

Dielectrics are insulators and can be polarized by an external electric field (E_j). The macroscopic polarization (P_i) is a sum of all dipole moments and is related to the external electric field. The polarization and the electric field are correlated by the susceptibility (χ_{ij})

$$P_i = \varepsilon_0 \chi_{ij} E_j \quad (1)$$

with the permittivity of the vacuum (ε_o). The susceptibility and the relative permittivity (ε_r) are related through the following equation:

$$\chi_{ij} = \varepsilon_r - 1 \quad (2)$$

By applying an electric field to a dielectric material, a surface charge is generated given by the dielectric displacement (D_i). The correlation of the dielectric displacement with the external electric field and the polarization is described as:

$$D_i = \varepsilon_0 E_i + P_i = \varepsilon_o \varepsilon_r E_i \quad (3)$$

The macroscopic polarization is the sum of the electronic, ionic, dipole and space charge contributions (Figure 1). Electronic polarization exists in all dielectrics. Negatively charged electrons are displaced relative to the positive nucleus with the application of an electric field. In ionic crystals, ionic contributions are caused by the displacement of positively charged cations and negatively charged anions. In materials with preexisting dipoles, the dipoles can be aligned in the direction of the external electric field and contribute to the macroscopic polarization. Mobile charges like electrons, holes or ions can be moved by the external electric field and accumulate at potential barriers, such as grain or phase boundaries. The accumulation of charge results in an inhomogeneous charge carrier distribution, known as a Maxwell-Wagner polarization, and occurs in ceramics, primarily at grain boundaries and electrode-ceramic interfaces.[11, 12]

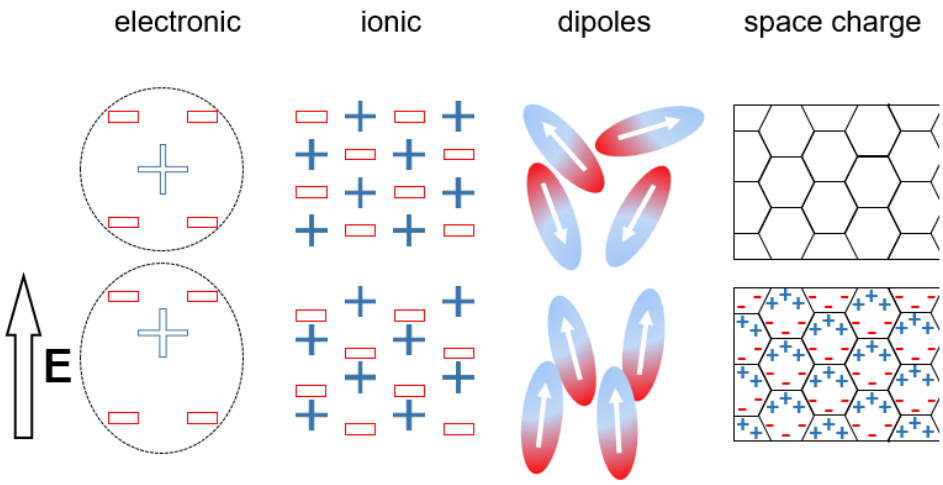

Figure 1: Microscopic polarization mechanisms with and without applied external electric field (redrawn after ref. [8]).

The microscopic polarization mechanisms behave differently in a constant (DC) or an alternating electric field (AC). The relaxation process of each polarization mechanism is time-dependent which leads to a phase shift of the sample response to an AC-field. Hence, the dielectric permittivity is described as a complex quantity:

$$\varepsilon^* = \varepsilon' + i\varepsilon'' \tag{4}$$

The dielectric loss is given by the ratio of the imaginary to the real part of the permittivity and is defined as:

$$tan(\delta) = \frac{\varepsilon''}{\varepsilon'} \tag{5}$$

The imaginary part of the permittivity increases with leakage current or dielectric adsorption. The frequency dependence of the permittivity is summarized in Figure 2. The different polarization mechanisms strongly influence the permittivity at characteristic frequencies.

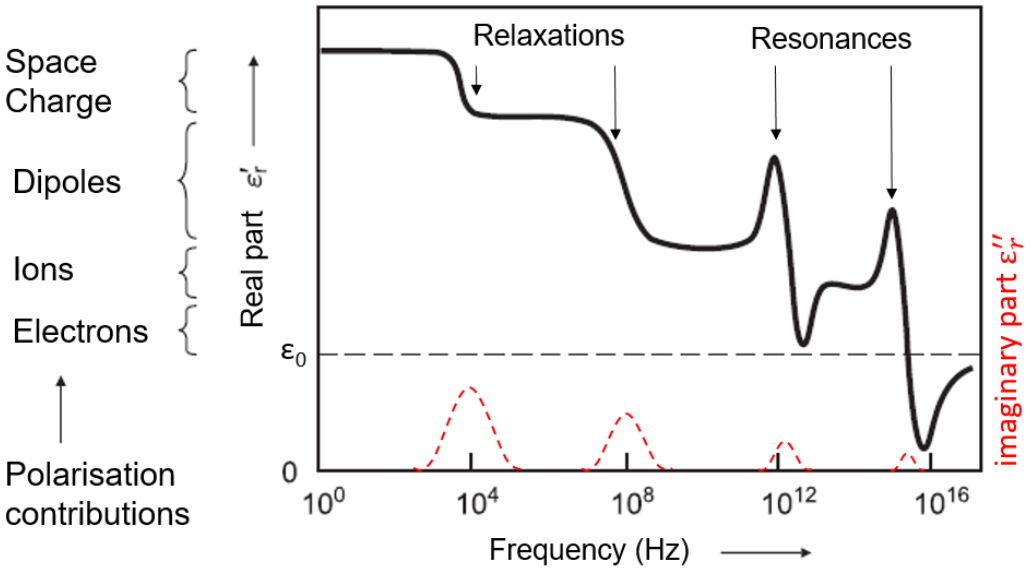

Figure 2: Frequency-dependent real (black) and imaginary (red) parts of the permittivity (redrawn after ref. [8]).

An external electric field induces charge displacement in dielectric materials. A material is “piezoelectric” if mechanical stress can also induce charge displacement in the material. Piezoelectrics are a subgroup of dielectrics. For a material to be piezoelectric it must have a non-centrosymmetric crystal structure or a structure lacking a center of inversion. 21 of 32 crystallographic point groups are non-centrosymmetric. All point groups are piezoelectric, with the exception of point group 432, which has four- and three-fold rotation axes, which eliminate all piezoelectric coefficients. The direct piezoelectric constant (d_{ijk}) describes the correlation between the induced electric displacement and the applied mechanical stress (σ_{jk}) as well as the dielectric contribution of the permittivity (ε^{T}_{ik}) and the electric field (E_k). The inverse piezoelectric effect describes the correlation of mechanical strain (S_{ij}) and applied electrical field. There is an elastic contribution described by Hooke´s law which includes the compliance (s^{E}_{ijkl}) and the stress (σ_{kl}).

$$D_i = d_{ijk}\sigma_{jk} + \varepsilon^{T}_{ik}E_k \quad (6)$$

$$S_{ij} = d_{ijk}E_k + s^{E}_{ijkl}\sigma_{kl} \quad (7)$$

Of the 20 piezoelectric crystal classes, 10 show spontaneous polarization (P_s) in the absence of an electric field. Hence, these materials are polar materials and contain a dipole moment. Spontaneous polarization occurs when the centers of the negative and positive charges in a unit cell do not coincide. A change of the spontaneous polarization can be induced by a change in temperature. The changed polarization can be measured by altered density of electric charges on the surface. These 10 crystal classes associated with spontaneous polarization are known as pyroelectric materials (Figure 3).

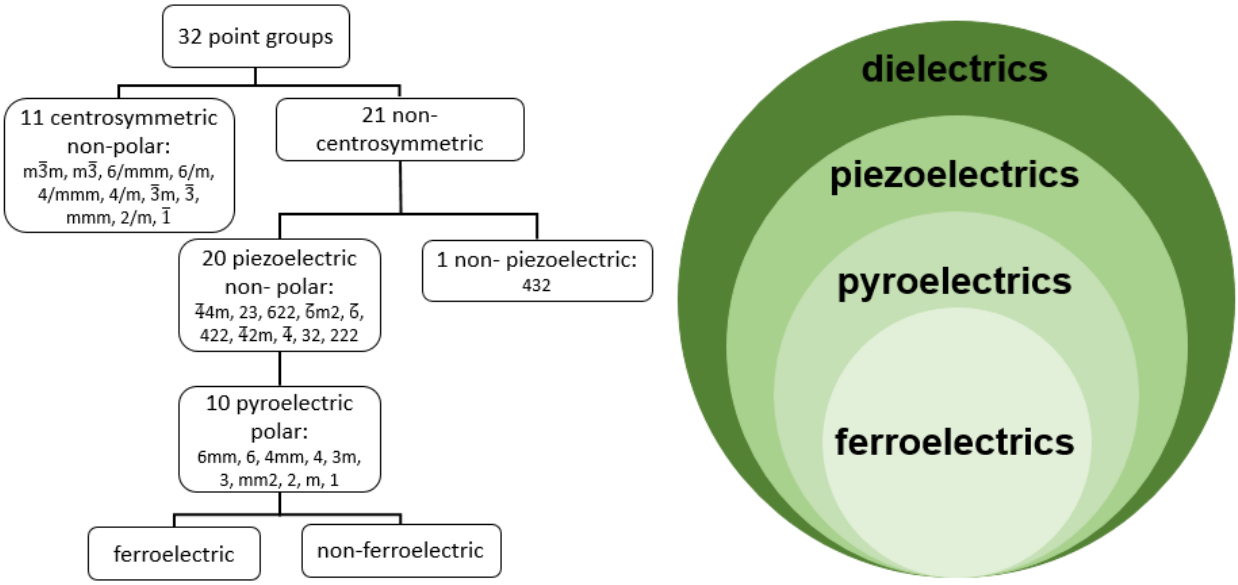

Figure 3: Left: Overview and classification of 32 point groups according to crystal point groups, symmetry and polarity. Right: Classification of di- , piezo- , pyro- and ferroelectrics.[1]

In some pyroelectric materials, spontaneous polarization can be reversed by an external field. These materials are known as ferroelectrics. Ferroelectricity is necessary for the practical use of the piezoelectric effect in polycrystalline materials.

2.2 Ferroelectrics

Unless otherwise noted, this chapter is based on articles by Hall [13] and Damjanovic [10] and books by Lines and Glass [14] and Waser et al. [8].

Ferroelectricity was first described in 1921 by Joseph Valasek, who discovered it in single-crystal Rochelle salt ($KNaC_4H_4O_6$-$4H_2O$).[15] A general definition of ferroelectricity was proposed by Jaffe [16] in 1956:

"The ability of certain crystals of electrically polar structure to switch the direction of polarity under the influence of a strong electric field between several crystallographically equivalent directions and to retain their new orientation after removal of the field."

To obtain piezoelectrically-active ferroelectrics, one must polarize them and induce a preferred orientation of polarization. Ferroelectricity in polycrystalline ceramics was first discovered in $BaTiO_3$ (BT) in 1946 by van Hippel which remains a prototype material for ferroelectricity.[17, 18] BT has a perovskite structure (ABX_3)[I], like most ferroelectric materials in use.[19] The perfect cubic perovskite structure can be expressed by the Goldschmidt tolerance factor [20]:

$$g = \frac{R_A + R_O}{\sqrt{2}(R_B + R_O)} = 1 \qquad (8)$$

The ions are assumed to be perfect spheres with radii R_A of the cation on the A-site (corner), R_B of the cation on the B-site (body center) and R_O of the oxygen ion (center of the faces, see Figure 4). Generally, a perovskite structure is stable between $0.9 < g < 1.1$. If g is closer to unity, the distortion is low, corresponding to a lower Curie temperature (T_C). If g is greater than one, a tetragonal distortion is favored, while with a g lower than one, a rhombohedral or orthorhombic distortion is typically observed. Ionic radii and temperature influence the crystal structure.[II] BT can be found in cubic, tetragonal and rhombohedral distortions, (Figure 4).

[I] In the context of ferroelectric ceramics usually given as ABO_3 since most ferroelectric ceramics are oxides.

[II] The ionic radius is influenced by the temperature as well.

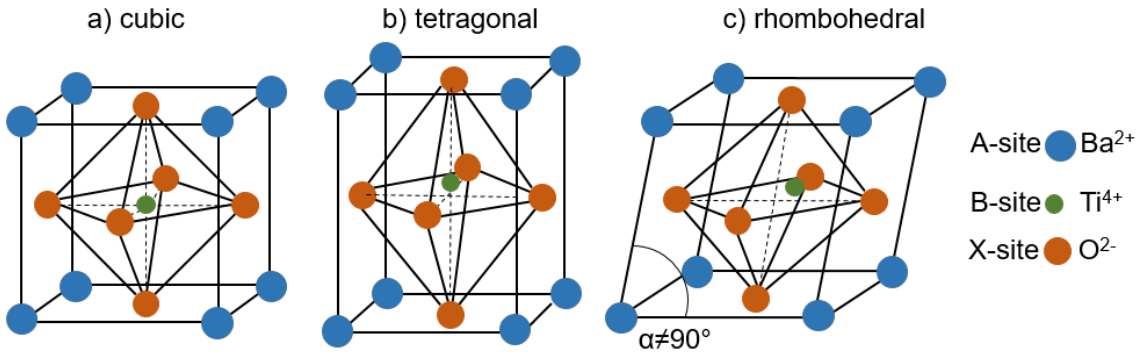

Figure 4: Perovskite unit cell of $BaTiO_3$. a) Cubic, $P_s = 0$. b) Tetragonal, $P_s \neq 0$. c) Rhombohedral, $P_s \neq 0$.

Exemplified by BT, the characteristic phase transitions and the response to an external electric field of a ferroelectric material will be explained here:

Upon cooling below 128°C, the crystal structure of BT changes from a paraelectric cubic structure to a ferroelectric tetragonal structure.[21, 22] As this phase transition is discontinuous, it is classified as a first-order phase transition and occurs between the Curie temperature (T_C) and the slightly lower Curie-Weiss temperature (T_0). The discontinuity occurs in P_s, which jumps from zero to a finite value at the transition temperature. In some ferroelectrics, the phase transition is a second-order phase transition where $T_C = T_0$.[23] The spontaneous polarization is caused by the displacement of the B-site cation away from the center. The two possible polarization directions, in the positive and negative direction, are energetically equal, since the free energy of the ferroelectric unit cell forms a double-well potential. Surface charge is generated due to the spontaneous polarization, resulting in a charge-compensating depolarization field (E_d). A large depolarization field is energetically unfavored. To reduce the electrostatic energy, areas with the same polarization direction, called ferroelectric domains, form.[24] Domain walls (DWs) form between domains with different orientations. The so-called “twinning process” develops in domains with opposite directions separated by DWs, referred to as the 180° domain configuration. A typical domain wall width is 1-10 nm. The reduction in electrostatic energy by creation of domains is counteracted by the energy required to create domain walls. The domain type also is determined by crystal structure, defects and mechanical stress. For example, in tetragonal crystals, 180° and 90° DWs form, whereas in rhombohedral crystals, 71°, 109° and 180° DWs form. Under mechanical stress, non-180° DWs form. DWs of 180° do not involve elastic deformation and therefore cannot compensate for mechanical stress. The initial random orientation of domains in polycrystals generates a net zero macroscopic polarization. The random orientation can be influenced by an external electric field. If the external electric field is sufficiently strong, a remanent polarization (P_{rem}) greater

than zero will remain. This process will be discussed in the context of polarization and strain as illustrated in Figure 5.

The process explained in the following paragraph is based on the switching behavior of domains and originates from domain nucleation and translation of DWs. Ferroelectric polarization loops and strain loops typical exhibit hysteresis behavior. In the virgin state (Figure 5 A), no macroscopic polarization (*P*) is present in the polycrystal. By increasing the electric field on a virgin sample, the polarization increases linearly. The strain (*S*) increases quadratically (Figure 5 A-B). By further increasing the electric field, irreversible domain wall motion occurs and results in a nonlinear increase of polarization and a non-quadratic increase in strain (Figure 5 B-C).

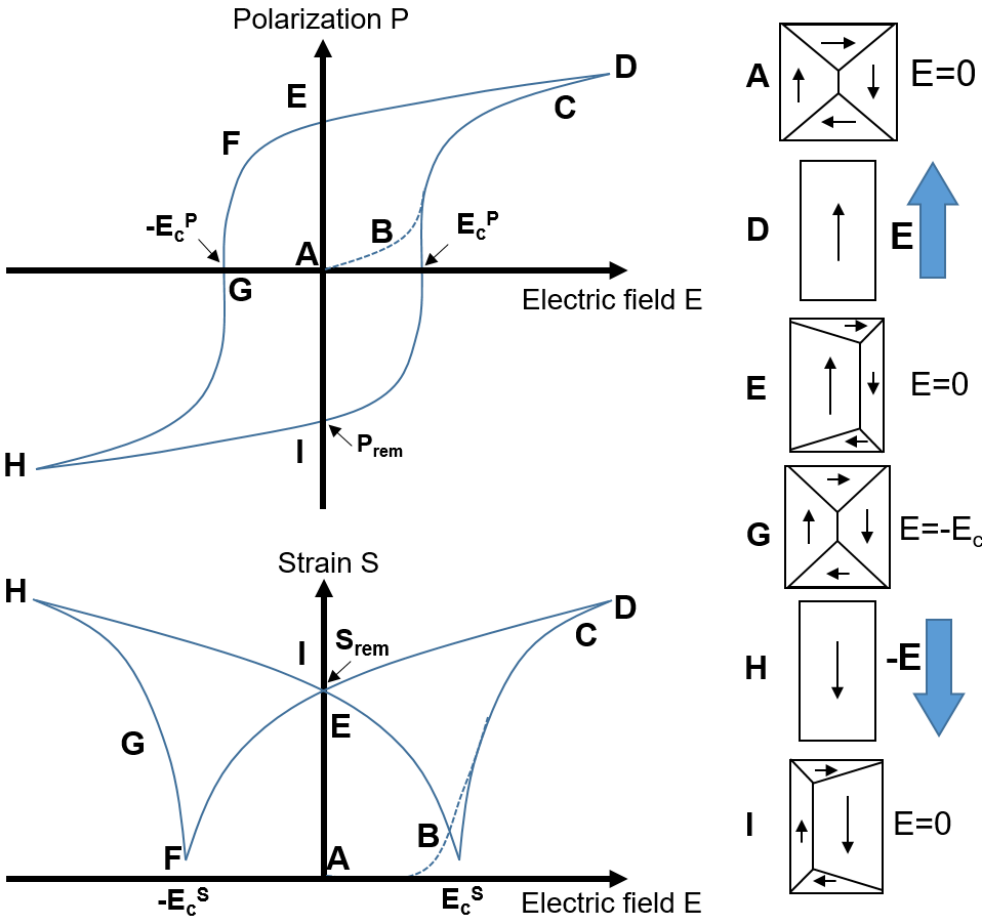

Figure 5: Representational ferroelectric hysteretic behavior of the polarization (*P*) and strain (*S*) throughout application of an external electric field. Schematic domain configurations of several moments during the poling process are depicted. Black arrows illustrate the polarization (redrawn after ref. [25])

Since all domains are oriented parallel to the field, further increase of the electric field leads to a linear response of the polarization and strain (Figure 5 C-D). When the field is reduced again,

backswitching of domains takes place due to internal mechanical and electrical fields. *P* and *S* deviate from a linear decrease (Figure 5 D-E). A remanent polarization remains at zero electric field (Figure 5 E). Similarly, the remaining strain at zero electric field is called remanent strain (S_{rem}; Figure 5 E). The remanence is caused by domains which stay in their new orientation. An electric field greater than the coercive field (E_C) is needed to return the polarization to zero or reverse it. The coercive field is not constant but depends on frequency, temperature and mechanical stress.[26-28] The coercive field can be defined by zero polarization (E_C^P; Figure 5 G) or the minimum of the strain (E_c^S; Figure 5 F). When defining the coercive field by the polarization, the coercive field is correlated with the electric field at which the domain wall movement is maximized. When defining the coercive field by the minimum strain, the coercive field is correlated with the point of switching initiation.[1] It should be noted that, although the polarization returns to zero, the strain often remains non-zero. A schematic domain configuration is depicted in Figure 5 G. By further decreasing the electric field (or increase of the negative electric field), switching and saturation similar to the positive field direction occur (Figure 5 G-H). After removing the external electric field, the ferroelectric sample contains a remanent polarization with negative sign and a positive strain (Figure 5 I). Ideally, the polarization loop is symmetrical. A shift of the loop along the electric field axis results in an internal bias electric field. A shift of the loop is related to aging and ferroelectric hardening which is discussed in a later section.[29]

Figure 6 describes the key parameters discussed in this work, obtained by polarization and strain measurements against the electric field.

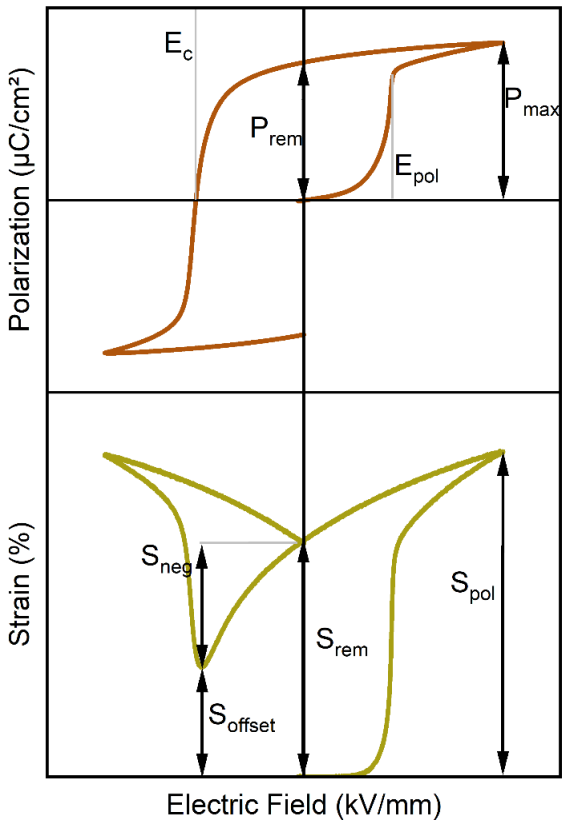

Figure 6: Characteristic parameters obtained from large-signal measurements: E_c = coercive field, E_{pol} = poling field, P_{max} = maximum polarization, P_{rem} = remanent polarization, S_{rem} = remanent strain, S_{pol} = poling strain, S_{neg} = negative strain, S_{offset} = offset strain.

2.3 Relaxor Ferroelectrics

This chapter is primarily based on works by Moulson[7], Priya et al.[30], Ye[31], Kleemann[32] and Bokov et al. [33].

Relaxor ferroelectrics (RF) are a subgroup of ferroelectrics (FE) and were first discussed in 1954 by Smolenskii et al. [34]. The term “relaxor” was first introduced in 1987 by Cross.[35] Relaxor ferroelectrics differ from stereotypical ferroelectric materials in their dielectric, piezoelectric and ferroelectric responses. Relaxor ferroelectrics often are perovskites with high piezoelectric activity. The microstructure is commonly described as polar regions within a non-polar matrix. The differences between FE and RF temperature dependence and response to

an external electric field will be described in this subchapter, followed by a brief outline of some common theoretical models.

Figure 7 illustrates the temperature dependent permittivity (ε´) of relaxor ferroelectrics. At high temperatures, all FEs and RFs are centrosymmetric and non-polar. Although the ions can deviate from the ideal perovskite structure, these polar nuclei are destabilized by the additional electric and elastic fields in these regions. Therefore, no spontaneous net polarization is present. The material is paraelectric and the temperature dependent permittivity (ε´) follows the Curie-Weiss law.

The temperature at which some nuclei become stable is called the Burns temperature (T_B). The permittivity will deviate from the Curie-Weiss law below this temperature.[36] Regions with a dipole moment are very small and can orient freely; these are called polar nanoregions (PNRs). No net macroscopic remanent polarization is apparent in this state. Despite the material´s lack of a macroscopic structural change, properties already change, and the material enters a new phase known as the “ergodic relaxor” phase. Further cooling leads to the growth of PNRs in both volume and number. The increase in polar volume causes an increase in permittivity. The dynamics of the PNRs depend on their size thus PNRs react more slowly as they increase in volume. The distribution of size leads to a distribution in relaxation time and a frequency dispersion in which the permittivity is lower at higher frequencies. The frequency dispersion is the highest at T_m, the local maximum in the permittivity.

Upon further cooling, two cases must be separated. In the first scenario, PNRs grow during the cooling process but become less dynamic and freeze in motion. The material is in a glass-like transition and may be described as non-ergodic, in which dipoles are correlated and interact with one another. This freezing temperature (T_f) is the Vogel–Fulcher temperature. The correlation length of PNRs increases with further cooling, whereas the number of PNRs decreases as they merge into larger PNRs.
Canonical relaxor ferroelectrics (RFs) do not experience a temperature induced phase transition into the ferroelectric state. In a canonical RF, a ferroelectric long-range order can be introduced by the application of an external electric field or mechanical stress.[37]

In a second scenario, the ergodic relaxor may adopt into a ferroelectric phase during cooling; this is known as non-canonical relaxor. The transition temperature from relaxor to ferroelectric is marked by $T_{R\text{-}F}$ in Figure 7b-d. The material transforms from a state with higher symmetry, such as a cubic structure to a state with lower symmetry, such as a tetragonal or rhombohedral

crystal structure. The behavior of a non-canonical relaxor adopted into a ferroelectric phase is similar to that of a conventional FE but the domain wall configuration is more diffuse, and some parts still reflect a cubic structure on the microscopic level.[38, 39]

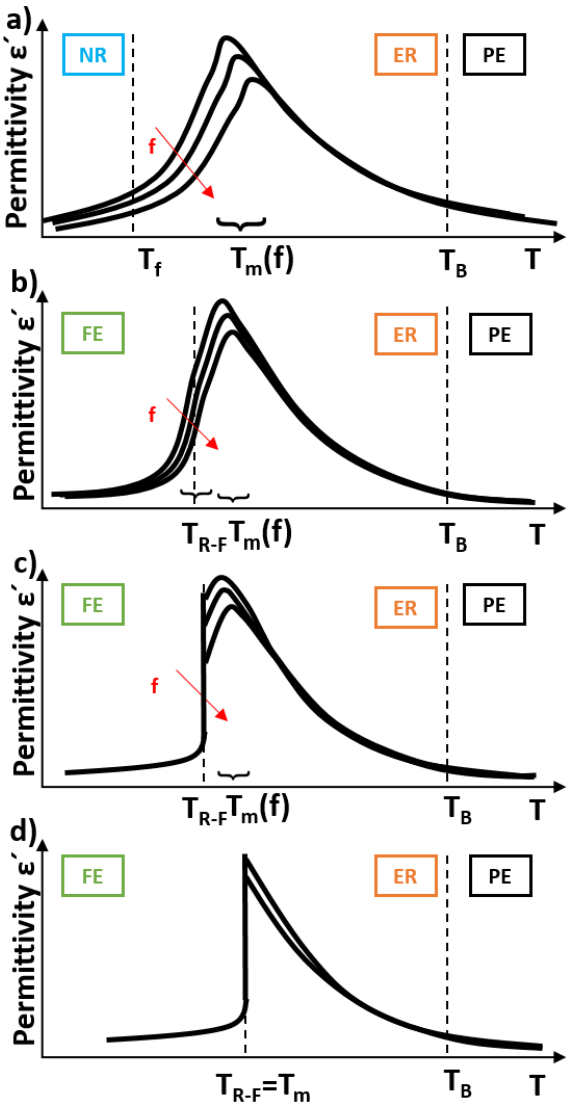

Figure 7: Permittivity vs. temperature of canonical (a) and non-canonical (b-d) relaxors. b) The RF-FE phase transition is diffuse between T_{R-F} and T_m. c) The RF-FE phase transition is sharp between T_{R-F} and T_m. d) The RF-FE phase transition is sharp at $T_{R-F} = T_m$ (redrawn after ref. [33]).

Apart from the permittivity, the polarization and strain responses to an electric field also differ in a RF compared to a normal FE. There are also dissimilarities between the ergodic relaxor (ER) and the non-ergodic relaxor (NR) (Figure 8). When applying an electric field to an ER, the PNRs will align in the field direction and a polarization can be measured. By removing the electric field, the PNRs randomly redistribute. Hence, the remanent polarization in an ER approaches zero (Figure 8a). The related strain can be high without any remanent or negative

strain (Figure 8c). The strain in an ER is caused by electrostriction, phase transformation and domain alignment. In the case of a non-ergodic relaxor, an irreversible ferroelectric long-range order can be introduced by application of a sufficiently high electric field (Figure 8b and d). A typical characteristic is the difference of the first and the second strain loop. A phase transition is present in the first loop, resulting in a large strain. After reaching the ferroelectric state, the strain loops show the typical butterfly-loop associated with a FE.

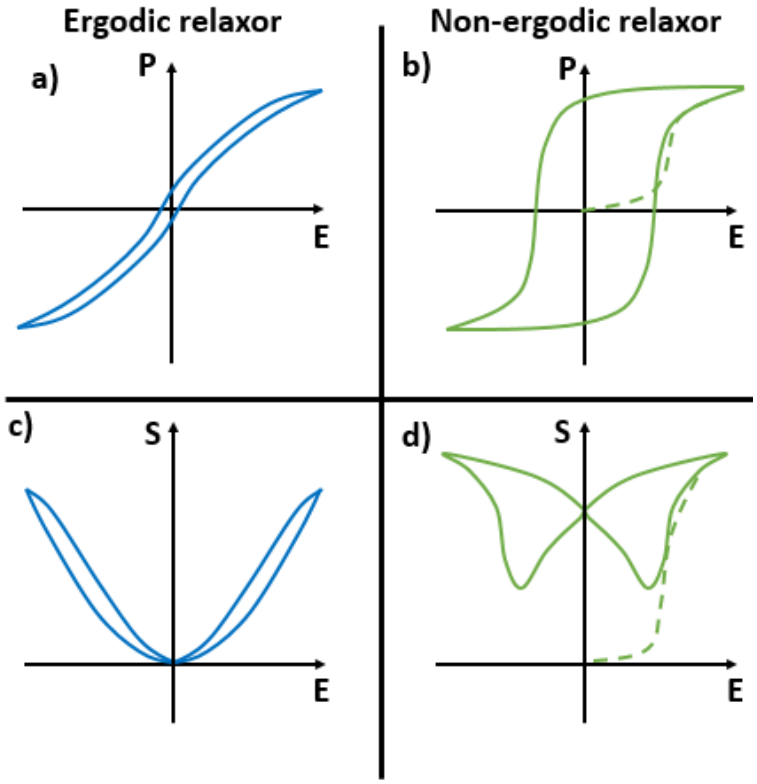

Figure 8: Polarization and strain responses with the application of an electric field on canonical ergodic and non-ergodic relaxors. a) and c) Polarization and strain of an ergodic relaxor. b) and d) Polarization and strain response of a non-ergodic relaxor with induced ferroelectric long-range order (redrawn after ref. [40]).

Multiple approaches exist to describe the observed behavior of ferroelectric relaxors. An early model established by Cross et al. [35], known as the superparaelectric model, was adapted by Viehland et al. [41, 42] into the dipolar glass model. Chemical inhomogeneity causes randomized dipoles. During cooling, PNRs form with increasing interactions. PNRs of different sizes vary in their depolarization temperature and broaden the transition temperature, resulting in a second-order phase transition. The breathing model proposes that PNR boundaries are vibrations similar to the behavior of domains in ferroelectric materials.[43, 44] Another common approach to explain the RF properties is the random field model. The disorder in the crystal

causes a random field distribution and prevents the formation of well-defined dipole moments at high temperature. However, with decreasing temperature, dipoles can form.[45, 46] Despite the development of these models, a common accepted theory has not been agreed upon in the community.

2.4 Ferroelectrics in High-power Applications

This chapter elaborates on the driving conditions of a ferroelectric material in high-power applications, which are necessary to understand the key material properties and the focus of this work. This subchapter first discusses an ultrasonic transducer to exemplify the boundary conditions. Next, the consequence for material properties is highlighted and ferroelectric hardening is explained in detail.

Ferroelectric ceramics can be used not only as actuators, sensors, and frequency or voltage generators, but also as ultrasonic high-power devices such as motors, cutters, cleaners and welders.[7, 47-49] A transducer is an energy converter. In the case of ultrasonic transducers, electrical energy is converted into mechanical energy. For ultrasonic devices, the piezoelectric effect of ceramics is often utilized.[50] For applications with a very high-power output in the range of kilowatts, the so-called Langevin transducers are most common. In a Langevin transducer, typically two ceramic rings (often Navy type 1 PZT) are clamped between two metal pieces (Figure 9).[51] The metal pieces have two main functions. Firstly, they amplify the signal. The transducer resonates as one system with the ceramic rings at the vibration node in the middle of the transducer. The longer displacements at the metal parts are more effective, since typically the mechanical loss in steel and aluminum is lower than in the ceramic parts. In addition, the shorter displacement of the ceramic prevents rapid fatigue. Secondly, metal parts are used for acoustic impedance matching to the device. Metals with different densities additionally increase the vibration amplitude.[50] The aluminum piece has a conical shape to enhance the output of the transducer. Mechanical coupling of the system is achieved by mechanically pre-stressing the transducer with a bolt. This influences the resonance frequency and ensures compressive stress at the ceramic, preventing it from fast mechanical failure.[50, 51]

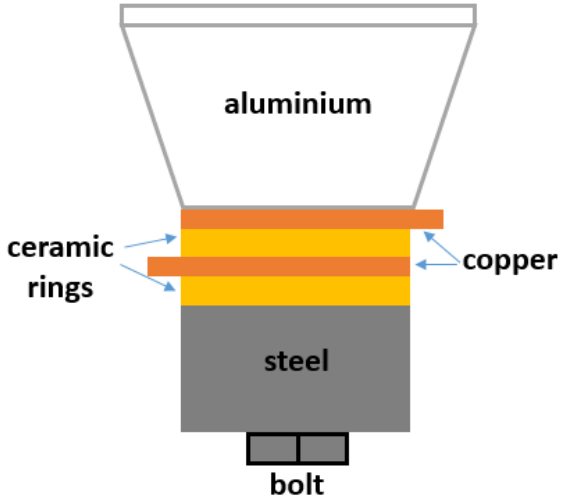

Figure 9: Langevin ultrasonic transducer with two ceramic rings, copper electrodes, steel at the base and aluminum at the top. The transducer is clamped by a bolt (redrawn after ref. [51]).

The conversion between electrical and mechanical energy is described by the following electromechanical coupling coefficient.[7]

$$k_{ij}^2 = \frac{\text{output mechanical energy}}{\text{input electrical energy}} = \frac{\text{output electrical energy}}{\text{input mechanical energy}} \tag{9}$$

The coupling coefficient is always between 0 and 1. However, it does not describe the conversion efficiency, since parts of the converted energy will return to the source during the completion of a vibration cycle.[52] The coupling coefficient is related to the electromechanical coefficients by the following equation:

$$k_{ij}^2 = \frac{d_{ij}^2}{s_{ij}^E \varepsilon_{ij}^T} \tag{10}$$

Ultrasonic devices are normally driven in resonance. A device may be driven in, or near, resonance because of the amplified mechanical response. Several material properties, such as the electromechanical coefficients and the losses, determine the resonance characteristics, such as frequency or amplification factor. The geometry of the driven ceramic also influences the resonance characteristics. Usually, the more complex the geometry, the more complex the waveform of the oscillation. A ring for ultrasonic transducers is mainly a mixture of the coupling coefficient of the thickness mode, k_t, and the planar mode, k_p. In addition to these two modes, the transverse length mode, k_{31}, and the longitudinal length mode, k_{33}, were also investigated. A detailed description of all resonance modes used to determine the electromechanical

coefficients can be found in the European Standards EN 50324.[53] Figure 10 provides an example of the transverse length mode. A standing wave develops with a node in the middle of the sample. The vibration velocity has the same waveform with the highest velocity at both ends of the sample but with opposite direction. The strain and stress are also a half-sine but are shifted in position. The maximum strain and stress are both in the middle of the sample. If the sample is driven at sufficiently high velocity or power, it will increase in temperature due to losses. The maximum temperature (*T*) is located at the position with the highest stress.

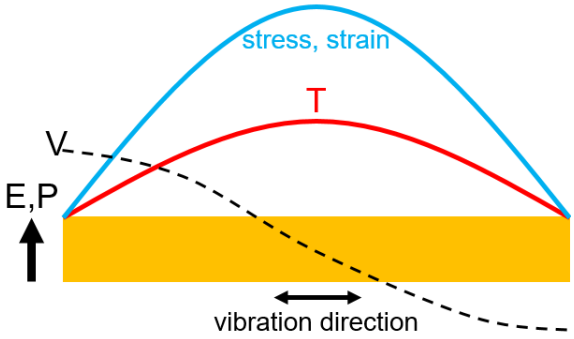

Figure 10: Piezoelectric sample driven in the 31-transverse length mode in the first harmonic resonance. Blue: strain and stress. Red: temperature. black dashed: vibration velocity distribution through the sample length.

One problem in real-world applications is the non-linearity of transducers. With increasing field and stress levels, resonance frequency shifts and a hysteresis effect occurs.[54, 55] This results from a shift of the energy of the first harmonic to overtones.[56] Electrical and mechanical coefficients, such as the elastic compliance, depend on the mechanical stress level or electric field strength and result in a non-linear amplitude response.[57, 58] It is important to note that, although a material may initially appear promising when measuring the small-signal parameters at room temperature, the same material may not be suitable for real applications in ultrasonic high-power devices. Small-signal parameters are usually determined in conditions which deviate from the conditions found in real applications.

A transducer transforms electrical energy into mechanical energy. Ideally, a transducer is as efficient as possible. Additionally, a large power output is needed for most applications. The mechanical energy density (U_m) of a transducer is proportional to the density (ρ) and the square of the vibration velocity (v).[59]

$$U_{\mathrm{m}} \approx \frac{1}{2}\rho v^2 \tag{11}$$

$$\text{with} \quad v_{\mathrm{i}} = \frac{4}{\pi}\sqrt{\frac{\varepsilon_{\mathrm{ij}}^{\mathrm{T}}}{\rho}}\, k_{\mathrm{ij}} E_{\mathrm{j}} Q_{\mathrm{ij}}^{\mathrm{R}} = \frac{4}{\pi}\frac{d_{\mathrm{ij}}}{\sqrt{s_{\mathrm{ij}}^{E}\rho}} E_{\mathrm{j}} Q_{\mathrm{ij}}^{\mathrm{R}} \tag{12}$$

The vibration velocity is the sample edge displacement per second. In other words, it is the angular frequency (ω) multiplied by the edge displacement. From Equations (11) and (12), it is apparent that the vibration velocity is proportional to the mechanical energy density. Hence, *v* is used to compare materials and to evaluate their suitability for high-power applications. The vibration velocity itself depends on elastic compliance (*s*) which can only be tuned to a small extent by chemical modification. The electric field strength is often limited due to the sample dimensions and the amplifier capabilities. Therefore, the piezoelectric coefficient, *d*, and the mechanical quality factor, Q_{ij}, should be maximized.

Losses and ferroelectric hardening

This segment will first introduce the quality factor, Q, and its correlation to losses. The link to ferroelectric hardening will be explained, and different approaches for ferroelectric hardening are summarized.

In general, the quality factor is the reciprocal of losses. In the context of vibration, it represents the ratio between stored energy and energy loss during one cycle.[60] In the ferroelectric community, *Q* is denoted as the mechanical quality factor, Q_{m}, although the expression “electromechanical quality factor” would be more accurate to account for the coupling of the mechanical and electrical loss in piezoceramics. Three types of losses are distinguished: the dielectric loss, *tan*(δ), the piezoelectric loss, *tan*(φ), and the elastic loss, *tan*(γ).[61, 62] Loss can be described by a delay of the response to an external driving field. Mathematically, loss is described by a complex number in which the imaginary part accounts for the phase delay. The angle can be determined as follows:

$$tan(\delta) = \frac{\varepsilon''}{\varepsilon'} \tag{13}$$

$$tan(\varphi) = \frac{d''}{d'} \tag{14}$$

$$tan(\gamma) = \frac{s''}{s'} \tag{15}$$

From a microscopic perspective, losses in piezoceramics can be separated into intrinsic and extrinsic contributions.[63, 64] The intrinsic loss contribution is associated with piezoelectric

lattice deformation. A larger angle between the external electric field and the polarization leads mostly to polarization rotation and a higher intrinsic response, and thus to a higher piezoelectric coefficient, but also to higher loss.[65] The extrinsic loss contribution is associated with domain wall motion, grain- and interphase boundaries and defect diffusion.[66, 67] Extrinsic contributions in piezoceramics are associated with domain wall motion only. Domains with a small angle to the external electric field will increase in size due to the domain wall motion. It has a time-lagging and a hysteresis effect, which both cause losses. A detailed description of the losses is given by Liu et al. [68]. Introducing defects such as donor dopants into the system can facilitate the domain wall motion and increase the electromechanical losses. On the other hand, a different type of defect, like acceptor dopants or precipitates, can decrease the domain wall motion via pinning. In ferroelectrics, extrinsic loss contributions primarily are tailored by ferroelectric hardening or softening[III].

Ferroelectric soft materials are defined by properties such as a low electrical and mechanical coercive field, large maximum and remanent polarization, a rectangular polarization loop and a broad hysteresis caused by substantial losses. They are favorably used as actuators due to their large electromechanical coefficients, like the piezoelectric and dielectric coefficients.[9] There is no significant time dependency of the properties after poling (no aging).

Ferroelectric hard materials are characterized by a large electrical and mechanical coercive field and a small hysteresis due to minor electromechanical losses. In contrast, the piezoelectric and polarization responses are lower compared to a soft ferroelectric material from the same fundamental composition. Hence, ferroelectric hard materials compromise lower losses with lower piezoelectric activity (Figure 12). The properties after poling are time-dependent (aging). An internal bias field can form and cause a polarization loop shift along the abscissa, leading to a larger coercive field along the poling direction.[69]

[III] The wording “soft and hard ferroelectric” materials was adapted in the past from ferromagnetism.

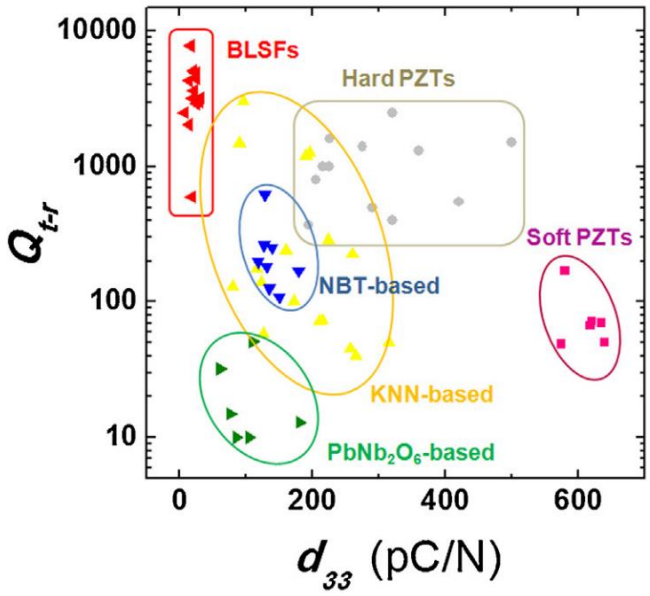

Figure 11: Relationship between mechanical quality factor and piezoelectric coefficient d_{33} for different material systems (Figure 50a) from Ref. [68], used with permission from Elsevier). "BLSFs" refer to as bismuth layer-structured ferroelectrics.

Different processing conditions can influence ferroelectric characteristics, such as microstructure [70], temperature, crystal structure [71] and chemical modification. Chemical modification by doping is the most effective and common method.[9, 72] Donor-doping is the substitution of an A-site or B-site ion in the perovskite structure with an ion with a greater positive valence. To maintain charge neutrality, A-site or B-site vacancies form during the processing steps, like sintering or calcination. Donor-doping softens the material by increasing domain wall mobility. The exact mechanism of donor-doping is still under debate.[64] Ferroelectric hardening by doping is accomplished by acceptor-doping. Acceptor-dopants normally occupy the B-site of the perovskite structure with lower positive charge. Oxygen vacancies form to maintain charge neutrality. Oxygen vacancies can diffuse towards the acceptor and form defect complexes (Figure 12a).[73, 74] Since, this is a diffusion process, it is temperature- and time-dependent and thus referred to as aging. The defect complexes can orient in the surrounding polarization direction to minimize the electrostatic and elastic energy.[75, 76] Maintaining their orientation leads to a stable polarization/domain configuration and thus to reduced domain wall motion and ferroelectric hardening. Defect complexes or single defects can accumulate inside the domains [75, 77], at the domain walls [78] or at the grain boundary [79] (Figure 12).

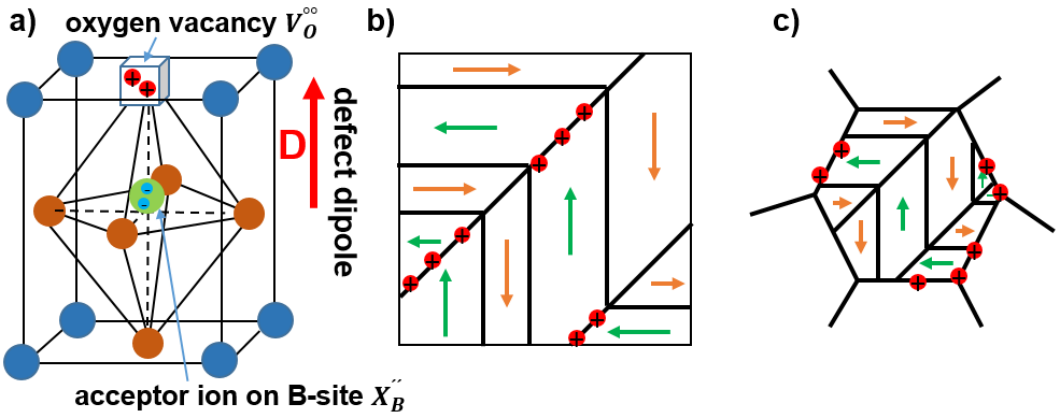

Figure 12: Different domain stabilization mechanisms, corresponding to their length scale. a) Volume effect. b) Domain wall effect. c) Grain boundary effect (redrawn after ref. [80]).

The composite approach is another method to ferroelectrically harden a material and was established in recent years. In this method, a non-ferroelectric inclusion is introduced into a ferroelectric matrix.[81, 82] This inclusion can be a secondary phase or precipitates.[83] Domain wall movement is hindered by inter- and intragranular stress caused by strain incompatibilities of the matrix and the inclusion. During poling of a polycrystalline sample, grains will deform differently according to their orientation, leading to strain incompatibilities.[84] This strain is intensified by elastically rigid inclusions such as ZnO. See Figure 13 for a schematic description: First, the inclusion is removed from the matrix (Figure 13a) to allow an unconstrained deformation during poling (Figure 13b). Refitting of the inclusion into the matrix (Figure 13c) reduces the matrix strain (Figure 13d). The effect is most pronounced near the inclusion and decreases with increasing distance. In the case of semiconductor inclusions, a different explanation exists, it involves trapped charges at the interface of the inclusion and matrix. The model of trapped charges is mainly discarded.[85] Other additional effects from the secondary phase, such as the interdiffusion from second phase ions into the matrix, cannot be ruled out.[86]

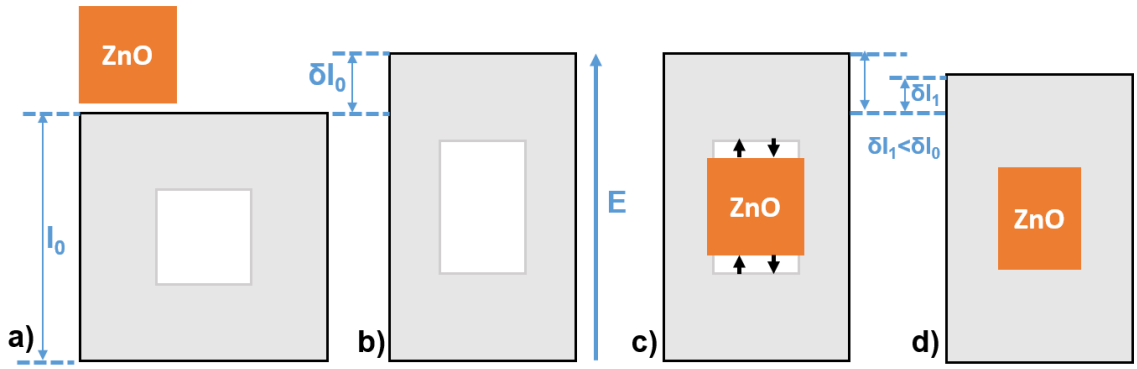

Figure 13: Schematic illustration of the strain incompatibilities between the ferroelectric matrix and ZnO inclusion (Eshelby approach). Stresses (black arrows) are shown along the electric field direction. a) Cut out of ZnO inclusion. b) Transformation of matrix during poling. c) Inclusion does not fit into the matrix and causes stress. d) Stress prevents elongation of matrix phase (redrawn after ref. [82]).

2.5 Poling-induced Texture

The term "texture" can be used in multiple contexts. Here, it will be introduced both in general sense and specifically in relation to this work.

In ordinary sintered piezoceramics, the orientation of grains is random, resulting in properties that are the average of all grains and thus usually isotropic. However, intentional alignment of grains can be achieved through various processing techniques such as hot working, magnetic alignment, templated grain growth, and less common methods like freeze casting.[87] Single crystals exhibit anisotropic electromechanical properties, with electromechanical coefficients reaching maximum values along specific directions.[88] By aligning the grains in a polycrystalline ceramic, anisotropy, known as grain texture, can be induced. With increasing degree of texture, the properties of the material approach those of a single crystal.[89] Polycrystalline ceramics that are not initially textured during processing can also be textured through poling, which is sometimes referred to as "domain texture" (grains are not oriented). It's important to distinguish poling-induced texture from texture discussed in literature, which is often related to processing. This work will focus solely on poling-induced domain texture. In an unpoled piezoceramic material, the polarization vectors are oriented randomly. By applying an external field, such as an electric field, the polarization vectors align with the field direction. When the external field is removed, the polarization switches back to the crystalline orientation. A remanent anisotropy remains within the material. The maximum possible degree of anisotropy or texture depends on the crystalline symmetry and is significantly lower than that

of processing-textured materials. Jones et al. [90] calculated the maximum possible degree of texture for different crystal symmetries and crystal directions. In principle, the maximum possible degree of texture can be calculated for each direction within every crystal symmetry. However, here only the direction of possible polarizations is discussed. In the tetragonal crystal symmetry, this direction is [001], while in the rhombohedral symmetry, it is [111]. If the material is initially untextured and no phase transformation occurs during the poling process, the maximum possible degree of texture induced by poling is three and four for tetragonal and rhombohedral symmetry, respectively. The values are given in multiples of random distribution. In other words, in a tetragonal material, the maximum achievable number of unit cells oriented in the same direction is three times higher than in the random case. Chapter 4.6.3 provides further details on the method for determining the texture degree of piezoceramics in directions different from the poling direction.

2.6 Electromechanical Fatigue

Fatigue of ferroelectrics is primarily discussed within the context of electrical or mechanical loading. However, in this study, fatigue is investigated under resonance conditions with specific vibration velocities. The main loading stress and underlying mechanisms of fatigue remain unknown. Therefore, this section aims to distinguish between the term "fatigue" as commonly used in the literature and its specific usage within this dissertation.

Fatigue and aging share closely related underlying mechanisms and are usually discussed in the context of defects and microcracks. Aging leads to the degradation of ferroelectric ceramics over time without external loading. Conversely, fatigue causes degradation through mechanical or electrical loading.[80] Electrical loading associated with fatigue is typically applied above the coercive field, resulting in domain switching and occasional phase transformation. Independent of the material, the observed degradation is mostly attributed to two main mechanisms. The first mechanism involves domain wall pinning due to diffusion and accumulation of defects, leading to domain fragmentation and a reduction in switchable volume. Degradation resulting from domain wall pinning is usually reversible through heat treatment or by loading with decreasing electrical field strength.[91-93] The second degradation mechanism is the formation of irreversible microcracks.[80, 94] The degradation process is material-specific and depends on factors such as loading time, number of cycles, temperature, frequency, and the type of signal. In terms of fatigue, mechanical loading has been less investigated compared to electrical

loading, as ferroelectrics are primarily used for their functional properties rather than their structural properties. The domain wall orientation affects the fracture toughness, which is a crucial quantity for mechanical fatigue performance.[95]

In this study, fatigue is examined under resonance conditions with high vibration velocity. It is not attributed solely to electrical or mechanical loading but rather a combination of both. Only a limited number of studies have investigated the behavior of piezoceramics under high vibration velocity and continuous workload. Hill et al. [96] examined the formation of microcracks in PZT during electrical loading in resonance but did not provide a specific vibration velocity. The density of microcracks was found to be higher in cycled samples compared to uncycled samples. Although higher operation temperatures reduced microcrack formation, they did not eliminate it. Furthermore, partial depolarization was observed in specimens cycled at 180 °C, which was not the case for specimens cycled at lower temperatures or annealed at 180 °C without electrical cycling. Other studies did not investigate fatigue under resonance at specific vibration velocities but instead measured the increase in temperature resulting from internal losses until reaching a steady state.[97, 98]

Therefore, this study establishes a new method for fatigue measurement by subjecting different materials to fatigue under resonance conditions at defined vibration velocities for the same number of cycles, using sample geometries chosen according to standards.

3 Materials and Status Quo

There will be a short introduction about the necessity of lead-free electroceramics and an introduction to the commercially used lead-based reference material. Next, this chapter introduces the current literature of the material systems predominantly investigated in this work. The properties of pure (1-x)$Na_{1/2}Bi_{1/2}TiO_3$-x$BaTiO_3$ (NBT-xBT) are elucidated, and subsequently its variants, such as doped compositions and composites, are discussed. The same aspects are addressed for the (1-x)$Na_{1/2}Bi_{1/2}TiO_3$-x$K_{1/2}Bi_{1/2}TiO_3$ (NBT-xKBT) system.

To understand the search for lead-free electroceramics, the current status of piezoelectric materials must first be introduced. The annual piezoelectric materials and device market is worth more than 20 billion USD and had a predicted annual growth of over 6% in the year 2020.[99] The largest share is taken by PZT. PZT-based materials are used in a very broad range of ferroelectric applications because of their superior electromechanical properties, adaptability, thermal stability and because they are cheap to mass-produce.[100-102] The total amount of PZT produced is estimated between 1250-4000 tons per year, which is equivalent to 800-2560 tons of lead.[102] This carries high risk for the environment and humans (especially for children), as lead is poisonous.[103] Lead accumulates in the human body over time and can cause reduced brain development and hence a lower IQ, reduced educational attainment and reduced social behavior. Lead poisoning is believed to be irreversible and may increase the risk of spontaneous abortion.[104, 105] The European Union introduced legislation to reduce the amount of hazardous substances like lead in 2002.[106] In the Restriction of Hazardous Substances (RoHS), the use of lead for piezoelectric materials is currently exempted, since there is currently no lead-free replacement (Exemption 7(c)-I, presumably extended in 2023). Besides the properties and toxicity of new materials, the costs and reproducibility must also be considered.[107] The most promising material systems are based on sodium potassium niobate ($(K_{1-x}Na_x)NbO_3$ (KNN); the alkaline bismuth titanates $Na_{1/2}Bi_{1/2}TiO_3$ (NBT) and $K_{1/2}Bi_{1/2}TiO_3$ (KBT); the barium titanates $BaTiO_3$ (BT) and $(Ba,Ca)(Ti,Zr)O_3$ (BCZT); and bismuth ferrite $BiFeO_3$ (BF).[5, 108] In comparison to PZT, the lead-free alternatives have either large electromechanical properties or good thermal stability but not both.[4] There is currently no material which can replace PZT for its broad variety, but rather there are distinct materials for different applications. One field of application is the high-power section. Two promising candidates for high-power applications are the NBT-xBT and NBT-xKBT systems, which will be introduced in detail in the next section.

Both material systems are contrasted to one of the current standard materials: the commercially available P4 (CeramTec, Plochingen, Germany). P4 is a solid solution between $PbZrO_3$ and $PbTiO_3$ and is located at the tetragonal side of the morphotropic phase boundary (MPB). It is classified as a Navy type 1 hard PZT ceramic. Its exact composition is unknown. Confirmed dopants are Sr^{2+}, Sn^{4+} and Cd^{2+}. It is assumed that either Fe^{3+}, K^+ or both are used as acceptor dopants, since they are regular dopants in Navy type 1 PZT. A comprehensive overview of doping effects in PZT is given by Jaffe et al.[9] and Berlincourt [109].

Sr and Sn are both isovalent dopants with Sr substituting on the A-site and Sn substituting on the B-site.[109, 110] The main effects of isovalent-doping are a lower Curie point and a higher permittivity. All other properties change negligibly. Fe and Cd are both acceptor dopants on the B-site, and K is an acceptor dopant on the A-site.[109, 111] Acceptor-doping decreases the permittivity, piezoelectric coupling, and compliance and increases the electrical and mechanical quality factors. Despite the high Q_m values, PZT (including P4) has a low stability of Q_m against vibration velocity.[55, 112] With increasing power output Q_m decreases (Figure 17) resulting in heat generation and limited power output density.[113] The decrease in Q_m derives from increasing extrinsic contributions and is independent of the PZT variant.[114] In addition to their toxicity, this represents a major drawback of lead-based ceramics.

3.1 $(1-x)Na_{1/2}Bi_{1/2}TiO_3$-$xBaTiO_3$

NBT-xBT is a solid solution of $Na_{1/2}Bi_{1/2}TiO_3$ (NBT) and $BaTiO_3$ (BT) with sodium, bismuth and barium on the A-site and titanium on the B-site.[115] This solution exhibits a morphotropic phase boundary (MPB) in the range of 6-7 mol% BT. Since it is sensitive to the processing conditions, the reported properties vary among publications. In the unpoled state, the crystal structure features weak distortions which led to the proposal of various models to describe the average structure.[116-119] On the NBT-side, the crystal structure is predominantly rhombohedral *R*3*c* with an anti-phase octahedral tilting ($a^-a^-a^-$ according to Glazer notation).[120] On the BT-side, it is tetragonal *P*4*mm*. In addition, tetragonal short-range areas or monoclinic areas within the rhombohedral phase have been proposed.[121, 122] At the MPB, the rhombohedral *R*3*c* and tetragonal *P*4*bm* structure coexist.[123] Compositions near the MPB are often described by a pseudocubic crystal structure, since the distortions are weak and difficult to detect with normal lab X-ray diffraction techniques.[124, 125] However, transmission electron microscopy (TEM) has confirmed the coexistence of the *R*3*c* and *P*4*bm* phases.[118, 126] The structure changes with temperature and electric field, making it subject to constant debate.[118, 127] Ma et al. [127]

published a phase diagram with electric field (Figure 14) based on *in situ* transmission electron microscopy. NBT-5.5BT (5.5 mol% BT) and NBT-6BT in the unpoled state consist of the *R*3*c* and *P*4*bm* phases. During the poling process, the *P*4*bm* phase transforms irreversibly into the *R*3*c* phase in the NBT-5.5BT. Hence, in the poled state, pure *R*3*c* phase is found. The symmetry of NBT-6BT (6 mol% BT) changes in two steps according to Ma et al.. The solid solution first transforms into *R*3*c* and *P*4*mm* at approximately 3.2 kV/mm. Above ~5 kV/mm, NBT-6BT transforms into pure *R*3*c* in a similar manner to NBT-5.5BT. The NBT-7BT (7 mol% BT) compositions transform first from pure *P*4*bm* into *P*4*bm* and *P*4*mm* and then into *R*3*c* and *P*4*mm*. The first change occurs at ~2.5 kV/mm and the second at around ~3.2 kV/mm. The green area of Figure 14 marks regions of coexisting crystal symmetries. The coexistence of crystal symmetry is attributed to a higher piezoelectric response. The energy profile is flattened anisotropically, allowing for easier polarization rotation.[128] Small-signal d_{33} values of 125-167 pC/N are reported.[115, 127]

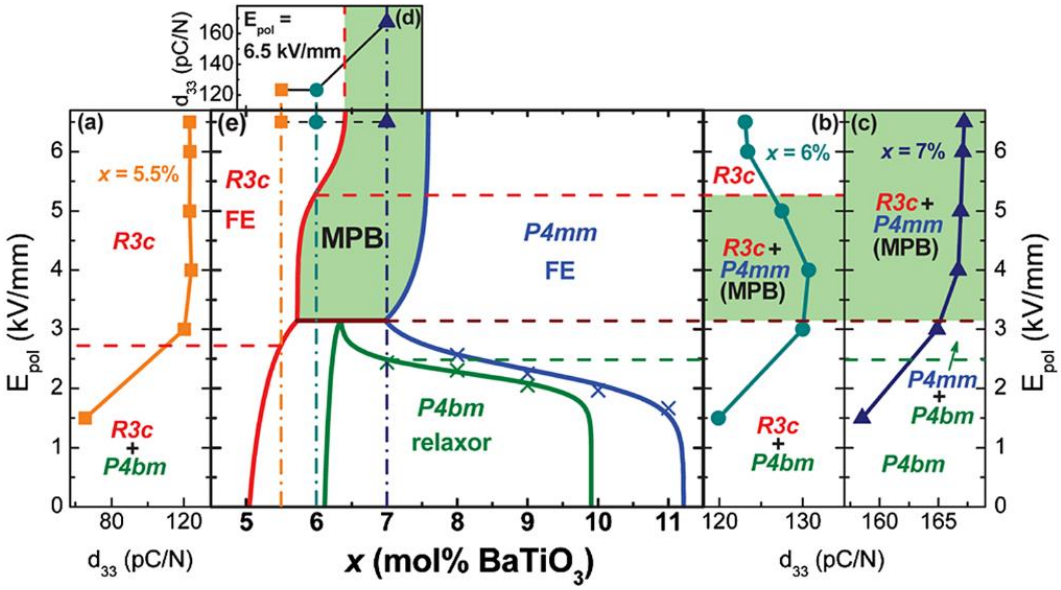

Figure 14: Field dependent phase diagram of NBT-xBT near the MPB (e). The piezoelectric coefficient d_{33} is given as a function of the poling field (E_{pol}) for NBT-5.5BT (a), NBT-6BT (b), and NBT-7BT (c). Piezoelectric constant (d_{33}) as a function of composition (d) with a poling field E_{pol} = 6.5 kV/mm (reused from ref. [127] with the permission of Physical Review Letters).

Adhikary et al. [129] previously published a temperature phase diagram for NBT-xBT in both the unpoled and poled states, utilizing temperature-dependent XRD and neutron powder diffraction. In the unpoled state, they observed a phase coexistence of *R*3*c* and *P*4*bm* up to approximately NBT-5.5BT. In contrast to Ma et al., Adhikary et al. did not find a region with a single *P*4*bm* phase from NBT-6BT to NBT-10BT. Instead, they observed a phase coexistence

of *P*4*bm* with the *R*3*c* phase from NBT-5.5BT to NBT-6.5BT, and a coexistence of *P*4*bm* with the *P*4*mm* phase above NBT-6.5BT up to NBT-18BT. In agreement with Ma et al., they found a single *R*3*c* phase in poled NBT-6.5BT and below, while compositions above NBT-6.5BT exhibited a tetragonal structure (*P*4*bm* and *P*4*mm*).

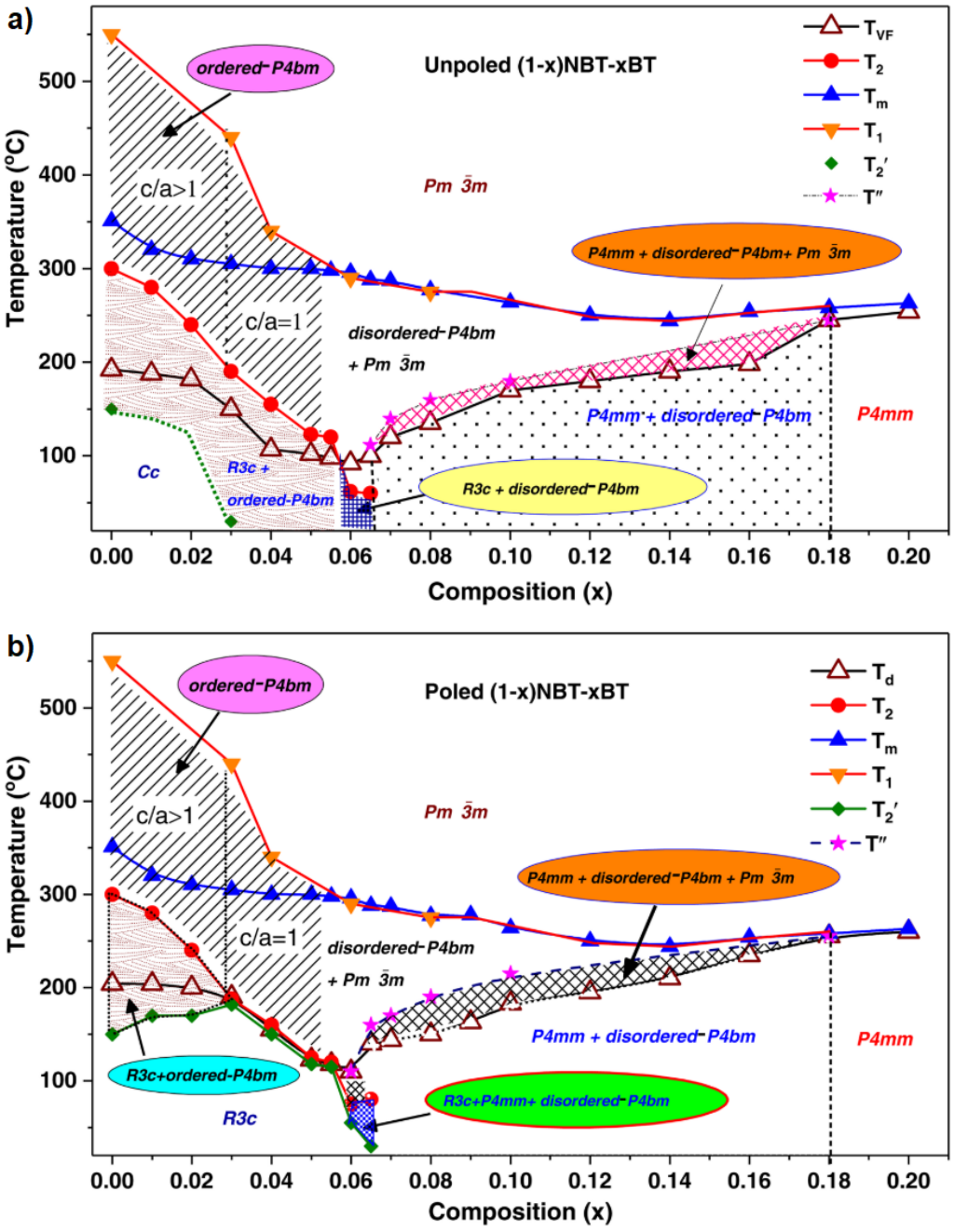

Figure 15: Phase diagram of unpoled (a) and poled (b) (1-x)NBT-xBT. T_{VF} = Vogel-Fulcher temperature, T_2 =transition temperature from rhombohedral *R*3*c* to tetragonal *P*4*bm*, T_m = temperature at the permittivity maximum, T_1 = transition temperature from tetragonal *P*4*bm* to cubic *Pm*$\bar{3}$*m*, T_2' = temperature corresponding to the onset of in-phase octahedral tilt, *T*" = transition temperature from tetragonal P4mm to cubic *Pm*$\bar{3}$*m*, T_d =depolarization temperature. (reprinted from ref. [129] with permission from American Physical Society).

NBT-xBT compositions in the vicinity of the MPB are ergodic relaxors, and below the transition temperature, they are in a non-ergodic relaxor state.[130] In the non-ergodic state, a sufficiently strong electric field introduces a ferroelectric order which remains after removing the field. The field-induced phase transition coincidences with volume expansion of the unit cell and oxygen octahedral tilting.[131, 132] The ferroelectric order can be destroyed by temperature and return into the relaxor phase. The low transition temperature of $T_{F\text{-}R}$ (transition temperature from ferroelectric to relaxor state) of around 100 °C for NBT-6BT, is a significant downside of the NBT-xBT system.[133] The transition temperature manifests as a sharp increase in permittivity with respect to increasing temperature (Figure 16). Above the transition temperature, the material exhibits the typical frequency dispersion of a relaxor. From the application perspective, the depolarization temperature (T_d) is more often used instead of $T_{F\text{-}R}$. At the depolarization temperature, the piezoelectric constant vanishes. Both temperatures are similar but can differ across materials with the randomization of the domain orientation, as occurs in the ferroelectric phase.[134]

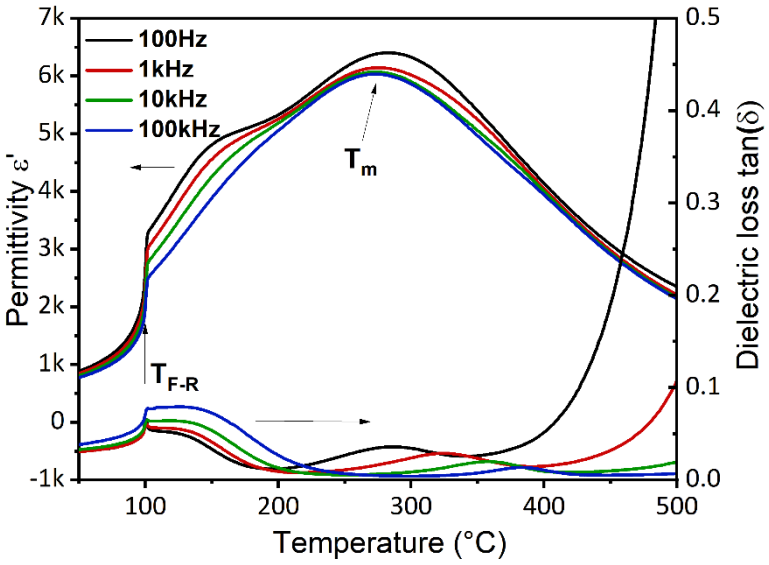

Figure 16: Temperature and frequency dependent permittivity (ε´) and dielectric loss (*tan*(δ)) of NBT-6BT.

The polarization and strain loops exhibit the typical behavior of non-ergodic relaxors (Figure 8). [135] The reported remanent polarization (P_{rem}) ranges from 20-40 µC/cm^2 and the coercive field (E_c) from 2.6-4.27 kV/mm.[115, 136-138] A high coercive field is normally attributed to a high mechanical quality factor (Q_m). In the compositions close to the MPB, Q_m values lie around 150.[82] However, the value is quite stable with increasing vibration velocity and hence makes the material a suitable candidate for high-power applications. The initial, significantly higher Q_m

of PZT drops below the NBT values even in the low vibration velocity regime (Figure 17). The better fracture toughness and thermal conductivity additionally support the high-power properties of the NBT-xBT compositions.[139, 140] When considering mechanical power density (U_m), the benefit of the lead-free material is lost to a small extent, since the density is lower resulting in a slightly smaller U_m for the same vibration velocity.[59] The origin for the higher stability of Q_m with increasing vibration velocity was observed by Slabki et al. [114], showing that, the strain in the lead-free NBT-xBT system is predominantly generated by intrinsic contributions and, more precise lattice distortion. The extrinsic non-180° domain wall motion is in the range of 5 % and does not increase with increasing vibration velocity up to 1.2 m/s.[114] Extrinsic contributions are expected to be the main source of losses leading to heat generation and lower Q_m.[68]

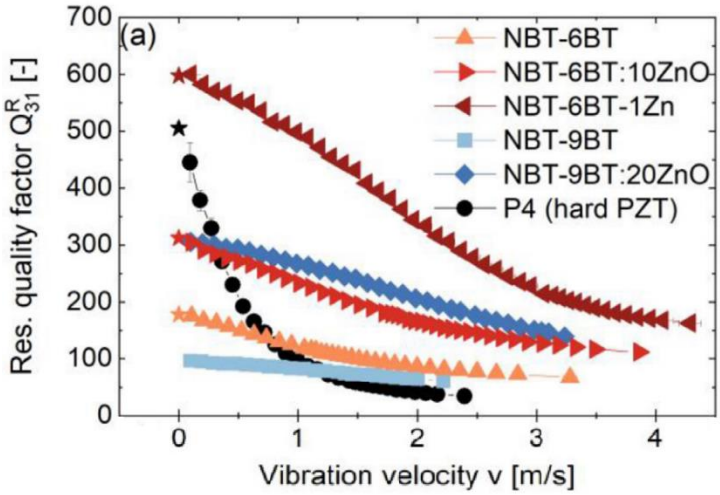

Figure 17: Electromechanical quality factor in resonance in 31-mode $\mathbf{Q}_{31}^R$ as a function of vibration velocity for different NBT-based compositions in comparison to hard PZT (redrawn after ref. [114] with permission from ScienceDirect).

3.1.1 Dopants in (1-x)$Na_{1/2}Bi_{1/2}TiO_3$-x$BaTiO_3$

Different approaches exist to tailor the electromechanical properties of NBT-xBT compositions. Most often, Q_m, d_{33} and T_d are targeted. Common approaches include chemical modification [141-143], grain size engineering [144], formation of a composite [82, 85] and quenching [145, 146]. Relevant techniques include Zn-doping and the formation of a composite with ZnO secondary phase. Both show a significant increase in T_d and Q_m.[82, 85, 141, 147] Therefore, the composite and doping approach are of primary interest for this work. This section provides a broad overview of dopants.

Many dopants have been investigated in the past (Table 1). Although this gives a broad overview, it is difficult to see any tendencies toward acceptor-doping or donor-doping in the PZT system. Acceptor-doping in PZT leads to ferroelectric hardening, and donor-doping leads to ferroelectric softening.[9] Depending on the literature, Co^{2+}-doping in the NBT-xBT system once increases d_{33} and maintains Q_m and once decreases d_{33} and increases Q_m. Similar, Mn-doping results in different observations from different groups. The increase in T_d via Zn-doping appears consistent in the literature. Mg doping, which in principle should be very similar (same charge and almost identical ionic radius), does not show the same hardening effect, such as the increase of Q_m.[IV] A-site dopants, including Bi excess (valency of 3+), could have a softening effect when doped in small amounts. In many prior studies, rare earth elements were used as A-site dopants. However, rare earth elements are not favorable for practical use, as they are often expensive and their production is associated with negative environmental impacts.[108, 148] Nevertheless, the studies on rare earth substitution confirm that A-site disorder can increase the piezoelectric performance.[128] An origin for the unclear picture given by the B-site dopants can be the different approaches of doping. Some groups substitute the dopants, while others add them. Some add them before calcination and some after. Some give the numbers in weight percentages, while others give them in mole percentages. The NBT-xBT system itself is very sensitive to various processing conditions. A broad range of properties exists in the MPB compositions NBT-6BT and NBT-7BT. The piezoelectric coefficient ranges from about 80 to ~200 pC/N, T_d from about 80 to 115 °C and Q_m from about 100 to 270. When plotting the properties of all NBT-6BT and NBT-7BT variants some trends are visible (Figure 18). The maximum achievable Q_m decreases with higher valency on the B-site (Figure 18c1). The maximum achievable d_{33} is also influenced by the ionic radius (Figure 18b1). A larger ionic radius of the dopant is associated with lower d_{33}. Nevertheless, the overall picture is still unclear when considering only the changes from individual publications; there is vast disagreement across results. Overall, this highlights the complexity of the NBT-xBT system. Knowledge from the PZT system cannot easily be transferred, and a general rule for doping has not yet been established.

[IV] In this work the opposite is shown. Mg doping leads to ferroelectric hardening and increases Q_m by several times. It is very similar to Zn doping. The results are published in a separate article: “Characterization of crystal structure, electrical and electromechanical properties of Mg-doped 0.94Na1/2Bi1/2TiO3-0.06BaTiO3”. Journal of European Ceramic Society, D. Bremecker, M. Slabki, J. Koruza, J. Rödel

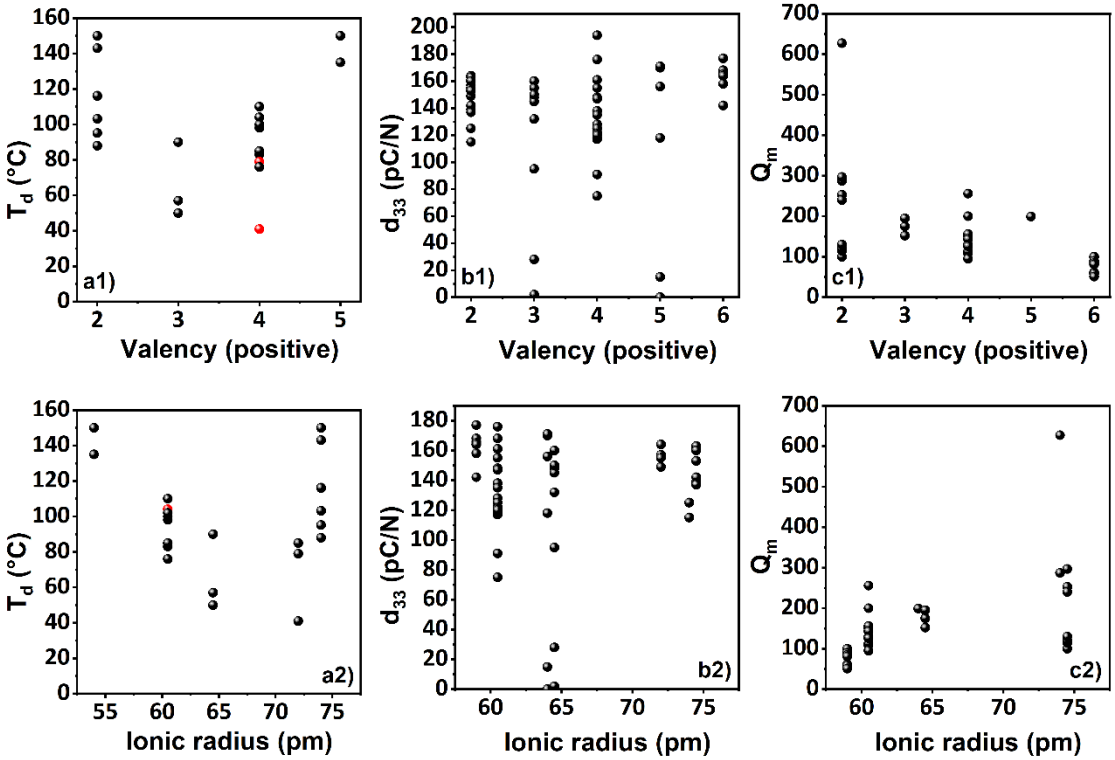

Figure 18: a1) and a2) Depolarization temperature (T_d). b1) and b2) Piezoelectric constant (d_{33}). c1) and c2) Mechanical quality factor (Q_m) against B-site dopants with different valences (a1-c1) and different ionic radii (a2-c2). Only NBT-6BT and NBT-7BT compositions were considered. All undoped compositions are listed at the valency four (Ti^{4+}). Zr^{4+}-doping is highlighted in red.

Table 1: Overview of B-site dopants in the NBT-xBT system. The amount is given in mol% unless otherwise noted. Ionic radii are taken from ref. [149, 150].

NBT-xBT	Dopant	Ionic radius (pm), (CN6)	Amount (mol%)	T_d/T_{F-R} (°C)	d_{33} (pC/N)	Q_m	Ref.
	B-site						
4BT	Fe^{3+}	64.5	1	155	n/a	n/a	[151]
6BT	Fe^{3+}	64.5	1	90	n/a	n/a	
15BT	Fe^{3+}	64.5	1	215	n/a	n/a	
6BT	-	60.5		110	125	n/a	[152]
	Fe^{3+}	64.5	3	90	145	n/a	
7BT	-	60.5		n/a	161	108	[153]
	Mo^{6+}	59	0.1	n/a	177	90	
6BT	-	60.5		n/a	117	256	[154]
	La^{3+}	103.2	1	n/a	125	182	
	Nb^{5+}	64	1	n/a	118	199	
	Co^{2+}	74.5	1	n/a	139	253	
	La^{3+}/Nb^{5+}	103.2/64	1/1	n/a	135	127	
	La^{3+}/Co^{2+}	103.2/74.5	1/1	n/a	127	263	
7BT	-	60.5	wt%	100	176	95	[155]
	Co^{2+}	74.5	0.8	n/a	137	297	
6BT	-	60.5	wt%	102	168	143	[156]
	$Ca^{2+}/Mn^{2+/3+}$	100/83/64.5	4/1	95	179	169	
	$Ca^{2+}/Mn^{2+/3}$	100/83/64.5	1/4	106	170	178	
6BT	-	60.5		n/a	120	200	[157]
	$Mn^{2+/3+}$	83/64.5	0.3	n/a	160	152	
3BT	$Mn^{2+/3+}$	83/64.5	0.5	152	100	n/a	[158]
6BT	$Mn^{2+/3+}$	83/64.5	0.5	57	155	n/a	
9BT	$Mn^{2+/3+}$	83/64.5	0.5	97	150	n/a	
8BT	-	60.5	wt%	n/a	116.3	90.7	[159]
	$Mn^{2+/3}$	83/64.5	0.3	n/a	150	185	
6BT	-	60.5		104	n/a	n/a	[160]
	V^{5+}	54	1	150	n/a	n/a	
6BT	-	60.5		n/a	155	n/a	[161]
	Ta^{5+}	64	1	n/a	171	n/a	
6BT	-	60.5		83	n/a	n/a	[162]
	Zr^{4+}	72	0.3	85	n/a	n/a	
6BT	-	60.5		104	138	130	[147]
	Zn^{2+}	74	1	150	115	627	
9BT	-	60.5		169	140	75	
	Zn^{2+}	74	1	196	95	156	
6BT	-	60.5		85	n/a	n/a	[141]
	Zn^{2+}	74	6	116.2	n/a	n/a	
6BT	-	60.5		n/a	122	n/a	[163]
	Mg^{2+}	72	0.5	n/a	164	n/a	

Table 2: Overview of A-site dopants in the NBT-xBT system. The amount is given in mol% unless otherwise noted. Ionic radii are taken from ref. [149, 150].

NBT-xBT	Dopant	Ionic radius (pm), (CN6)	Amount (mol%)	T_d/T_{F-R} (°C)	d_{33} (pC/N)	Q_m	Ref.
	A-site						
6BT	-	104.45		110	148	n/a	[164]
	Ba^{2+}	135	30	230	41	n/a	
6BT	-	104.45	wt%	n/a	147	143	[165]
	Dy^{3+}	91.2	1.2	n/a	170	102	
6BT	-	104.45	wt%	n/a	147	143	[166]
	Sm^{3+}	95.8	0.6	n/a	202	101	
6BT	-	104.45		76	118	n/a	[167]
	Er^{3+}	89	2	42	9	n/a	
6BT	-	104.45		n/a	121	n/a	[168]
	Eu^{3+}	94.7	0.25	n/a	149	n/a	
6BT	-	104.45	wt%	n/a	120	126	[169]
	Ce^{3+}	101	0.4	n/a	128	215	
6BT	-	104.45	wt%	n/a	147	143	[170]
	Nd^{3+}	98.3	0.8	n/a	175	118	
6BT	-	104.45		n/a	117	256	[171]
	La^{3+}	103.2	1.5	n/a	133	161	
8BT	-	104.45		n/a	121.3	n/a	[172]
	La^{3+}	103.2	0.2	n/a	10	n/a	
	La^{3+}	103.2	1.5	n/a	143	n/a	
7BT	-	104.45		n/a	194	n/a	[173]
	Er^{3+}	89	7	n/a	4.1	n/a	

Table 3: Overview of non-stoichiometric variations in the NBT-xBT system. The amount is given in mol% unless otherwise noted. Ionic radii are taken from ref. [149, 150].

NBT-xBT	Dopant	Ionic radius (pm), (CN6)	Amount (mol%)	T_d/T_{F-R} (°C)	d_{33} (pC/N)	Q_m	Ref.
	Non-stoichiometry						
20BT	-	104.45		n/a	91	n/a	[174]
	Na^{1+}	102	-4	n/a	115	n/a	
	Bi^{3+}	103	2	n/a	114	n/a	
3BT	-	104.45		n/a	75	n/a	[175]
	Na^{1+}	102	-4	n/a	94	n/a	
	Bi^{3+}	103	2	n/a	80	n/a	
5.5BT	-	104.45		n/a	128	113	[176]
	Bi^{3+}	103	4	n/a	137	106	
	Na^{1+}	102	2	n/a	81	246	
6BT	-	104.45		n/a	125	150	
	Bi^{3+}	103	4	n/a	142	69	
	Na^{1+}	102	2	n/a	82	323	
7BT	-	104.45		n/a	148	156	
	Bi^{3+}	103	4	n/a	197	67	
	Na^{1+}	102	2	n/a	44	196	
6BT	-	104.45	50/50	98	135	n/a	[142]
	Na^{1+}/Bi^{3+}	102/103	50/51	75	140	n/a	
	Na^{1+}/Bi^{3}	102/103	51/50	90	142	n/a	
	Na^{1+}/Bi^{3}	102/103	50/49	120	90	n/a	
7BT	-	104.45		85	176	n/a	[177]
	Bi^{3+}	103	51	65	101	n/a	

3.1.2 $(1-x)Na_{1/2}Bi_{1/2}TiO_3$-$xBaTiO_3$ Composites

In the ferroelectric community, the composite approach was first discussed by Shrout et al. in 1980.[178] This approach is used to design properties which are not achieved by the end members alone, like large strain [179-182], fatigue resistance against electric field loading [178], tailoring of the dielectric [183], the piezoelectric and pyroelectric constants [184] and temperature stability [185]. Lately, additional properties, such as the thermal depolarization or the mechanical quality factor, were addressed by the composite approach. Zhang et al. [85] observed the delay of the depolarization temperature in a 0-3 type composite with NBT-xBT as matrix material and ZnO as a secondary phase. “0-3 type composite” is a classification according to the connectivity pattern of a matrix and secondary phase, in which inclusions are embedded in a 3D connected matrix.[186] Although the increased depolarization temperature has been confirmed across different groups, the mechanism responsible is still under debate.[86, 187, 188]

The first explanation by Zhang et al. [85] is based on the semiconductor behavior of ZnO. The poling field induces free charges in ZnO, which reduce the depolarization field (Figure 19a). This mechanism was supported by the investigation of the same matrix material with the insulating ZrO_2 secondary phase, which does not increase the depolarization temperature of NBT-6BT. Riemer et al. [188] argue that considerable stress is induced during the post-sintering cooling process caused by different thermal expansion coefficients of the matrix and the secondary phase (Figure 19b). Stress can stabilize the ferroelectric order in NBT-6BT.[189] Mahajan et al. [187] claim that the incorporation of Zn into the matrix material drives the observed changes. Fan et al. [86] conducted transmission electron microscopy studies but could not rule out one of the suggested mechanisms. The effect of delayed thermal depolarization from ZnO incorporation is not only present in NBT-6BT but also in NBT-9BT and pure NBT.[190, 191]

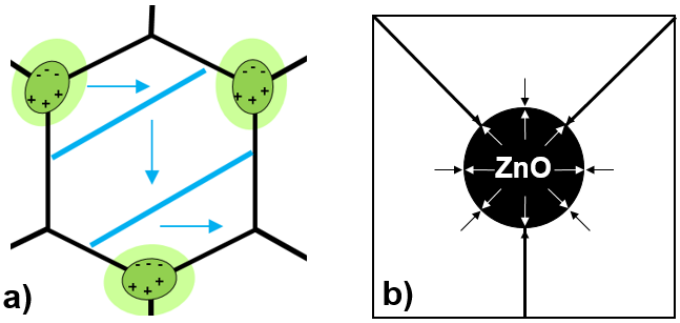

Figure 19: a) Charges induced in the ZnO inclusions by the poling field reduce the depolarization field (redrawn after ref. [85]). b) Stress field around ZnO inclusions caused by thermally induced mismatch (redrawn after ref. [188]).

Table 4: Overview of different NBT-xBT composites and their electromechanical properties. Some literature mentioned in the text does not quantify the given properties and thus is not included in the table.

Matrix	Secondary phase	Amount	T_{F-R} (°C)	d_{33} (pC/N)	Q_m	Ref.
NBT-6BT-3KNN	NBT-7BT	0 (vol %)	n/a	365 (d_{33}*)	n/a	[192]
	NBT-7BT	20	n/a	566	n/a	
NBT-6BT	ZnO	0 (mol%)	98	94	n/a	[85]
	ZnO	0.2	150	83	n/a	
	ZnO	0.4	n/a	106	n/a	
NBT-6BT	ZnO	0 (mole ratio)	99	142	146	[82, 188]
	ZnO	0.1	136	125	320	
NBT-6BT	ZnO	0 (mol%)	97	130	n/a	
	ZnO	0.3	130	78	n/a	
NBT-6BT	$CoFe_2O_4$	0 (mole ratio)	90	120	n/a	
	$CoFe_2O_4$	0.1	120	41-46	n/a	

3.2 (1-x)$Na_{1/2}Bi_{1/2}TiO_3$-x$K_{1/2}Bi_{1/2}TiO_3$

$Na_{1/2}Bi_{1/2}TiO_3$-x$K_{1/2}Bi_{1/2}TiO_3$ (NBT-xKBT) is a solid solution of NBT and $K_{1/2}Bi_{1/2}TiO_3$ (KBT) and is often compared with NBT-xBT. This solution was discovered by Elkechai et al. [193] in 1996 through the observation of a broad range of phases between 0.08 < x < 0.3 mol KBT. Other researchers, including Sasaki et al., [194] reported large electromechanical coupling factors in the MPB region caused by A-site disorder. Values like a d_{33} of 157 pC/N and a depolarization temperature of 174 °C are comparable to or larger than those associated with the NBT-xBT system, making NBT-xKBT a good candidate for piezoelectric applications.[195] The MPB falls around 0.16-0.22 mol KBT.[194, 196-199] The crystal structure has been widely studied. A phase coexistence of rhombohedral and tetragonal crystal structure is generally reported around the MPB region.[199-201] Jones et al., [202] however, reported a single *R*3*c* phase transforming into *R*3*m* at x = 0.45 and into *P*4*mm* phase at x = 0.7. In contrast to most other studies, Jones et al. investigated single crystals. Anton et al. [134] used transmission electron microscopy, neutron diffraction and Raman spectroscopy to reveal a monoclinic *Cc* and tetragonal *P*4*bm* phase coexistence in the NBT-20KBT composition at room temperature. These varied results on the

NBT-xKBT structure show the complexity of the system and the dependence on the method of investigation. The relaxor behavior, however, is commonly accepted, since the permittivity exhibits a frequency dispersion.[203] The electromechanical properties at the MPB range from a d_{33} of 100-167 pC/N, a T_{F-R} of 134-174 °C and a E_c from 3.0-4.4 kV/mm (Table 5). Q_m is reported rarely in the binary NBT-xKBT system and falls between 100-150 in NBT-20KBT. The ternary system NBT-xKBT-yLBT, however, has a stable Q_m against vibration velocity and small-signal Q_m values of around 900 when doped with Mn.[6, 204]

Few publications have investigated the effects of dopants or secondary phases in polycrystalline NBT-xKBT. This therefore, precludes any common assumptions based on it. Ce-doping can increase the piezoelectric constant in NBT-12KBT by approximately 34%.[205] Alumina as a secondary phase can increase T_d from 116 °C in pure NBT-20KBT to 227 °C. The piezoelectric coefficient will decrease simultaneously to a value of approximately 76 pC/N. The d_{33} of pure NBT-20KBT is not provided in the reference.[206] Other secondary phases, such as ZrO_2, HfO_2 and $(Hf_xTi_{1-x})O_3$ shift the depolarization temperature to room temperature.

Table 5: Overview of different NBT-xKBT composites and their electromechanical properties.

Composition	T_{F-R} (°C)	d_{33} (pC/N)	Q_m	E_c (kV/mm)	Ref.
NBT-20KBT	174	167	n/a	n/a	[207]
NBT-16KBT	n/a	134	n/a	n/a	[208]
NBT-18KBT	n/a	144	n/a	n/a	
NBT-20KBT	n/a	141	n/a	n/a	
NBT-10KBT	181	~98	n/a	n/a	[209]
NBT-20KBT	134	100	n/a	n/a	
NBT-40KBT	242	n/a	n/a	n/a	
NBT-16KBT	n/a	n/a	195	n/a	[194]
NBT-20KBT	n/a	n/a	109	3.0	
NBT-17KBT	n/a	112	n/a	4.6	[198]
NBT-20KBT	155	134	n/a	4.4	
NBT-22KBT	n/a	126	n/a	3.5	
NBT-25KBT	n/a	107	n/a	3.6	
NBT-16KBT	160	132	n/a	~4.6	[195]
NBT-18KBT	128	149	n/a	~4	

NBT-20KBT	174	157	n/a	3.6	
NBT-16KBT	~122	112	171	4.9	[210]
NBT-12KBT	n/a	98	n/a	n/a	[205]
0 Ce (wt%)					
0.2 Ce	n/a	132	n/a	4.76	
NBT-20KBT	116	n/a	n/a	n/a	[206]
+0.15 Al_2O_3	227	74	n/a	n/a	
+0.15 ZrO_2	<25	9-12	n/a	n/a	
+0.15 HfO_2	<25	3-5	n/a	n/a	
NBT-22KBT	110	n/a	n/a	n/a	[211]
+0.03 $BiAlO_3$	~25	n/a	n/a	n/a	
NBT-20KBT	140	n/a	n/a	n/a	[212]
+$(Hf_xTi_{1-x})O_3$	~25	n/a	n/a	n/a	

4 Experimental Methodology

This chapter provides all information about the processing conditions and measuring techniques to ensure reproducibility of the results. First, ceramic processing and the sample preparation are introduced. Second, electrical and electromechanical measurement methods are described. The fatigue measurement setup is customized and described in more detail in the end of this section

4.1 Powder Processing

The first processing step was the production of powders in the desired stoichiometry.

All NBT-based compositions were produced using the conventional solid state synthesis route.[V] A schematic description is given in Figure 20. Additional processing steps for the composites are given in red. The synthesis route will be explained in detail by using $0.94Na_{1/2}Bi_{1/2}TiO_3$-$0.06BaTiO_3$ (NBT-6BT) and NBT-6BT composite with ZnO (NBT-6BT:xZnO) as examples. Doped compositions and NBT-xKBT have slightly different conditions. Deviations from the processing route are given in brackets.

The following powders were dried at 100 °C for 24 h before weighing, to get rid of moisture: Na_2CO_3 (99.5%), $BaCO_3$ (99.8%), Bi_2O_3 (99.975%), TiO_2 (Anatase, 99.6%), ZnO (99.99%), MgO (99.99%). All powders were taken from Alfa Aesar (Alfa Aesar GmbH & Co. KG, Germany). $KHCO_3$ (99.93%, Alfa Aesar) was dried in vacuum at room temperature. The powders were weighed according to their stoichiometry with the accuracy of ±0.3 mg (Satorius TE214S, Satorius GmbH, Göttingen, Germany): $(1-x)Na_{1/2}Bi_{1/2}TiO_3$-$xBaTiO_3$ with x=0.06 for NBT-6BT and $(1-x)Na_{1/2}Bi_{1/2}TiO_3$-$xK_{1/2}Bi_{1/2}TiO_3$ with x=0.21 for NBT-21KBT. Dopants on the B-site were substituted for titanium. The subsequent milling took place in ethanol and homemade polyamide container with yttria-stabilized zirconia milling balls for 24 h at 250 rpm with a powder to ball ratio of: Pure NBT-xBT → 1:5, NBT-xKBT and doped compositions → 1:4. Milling ball diameter: Pure NBT-xBT 3 mm, NBT-xKBT and doped 10 mm (Muehlmeier GmbH & Co. KG, Bärnau, Germany). A planetary ball mill was used (Fritsch Pulverisette 5, Idar-Oberstein, Germany). After drying the powders for 24 h at 105 °C (Labor Frischluftwärmeschrank FT6060, Thermo Electric LED GmbH, Langenselfold, Germany) they were crushed with a mortar.

[V] A big part of the powder processing, sample preparation, density measurements and poling was conducted by Siegfried Teuber. The exact compositions produced by Siegfried Teuber can be found in Table S7.

Afterwards, the powders were calcined in closed alumina crucibles (Z50, Giess-Technische-Sonderkeramik GmbH & Co. KG, Düsseldorf, Germany) at 900 °C for 3 h with a heating rate of 5 °C/min (P320, Nabertherm GmbH, Germany). The milling, drying and crushing steps were repeated for a second time.

The prepared NBT-6BT powder was used further for the composite compositions. NBT-6BT was coarsened at 1100 °C for 3 h with a heating rate of 5 °C/min (NBT-xKBT: 1060 °C 2 h). Agglomerates were reduced by sieving the powder with a 160 µm mesh (LINKER Industrie-Technik GmbH, Kassel, Germany). NBT-6BT and the secondary phase (ZnO) were weighted according to the mole ratio: NBT-6BT:xZnO. The milling and drying were conducted under the same conditions like for pure NBT-6BT but with a powder to ball ratio of 1:6.

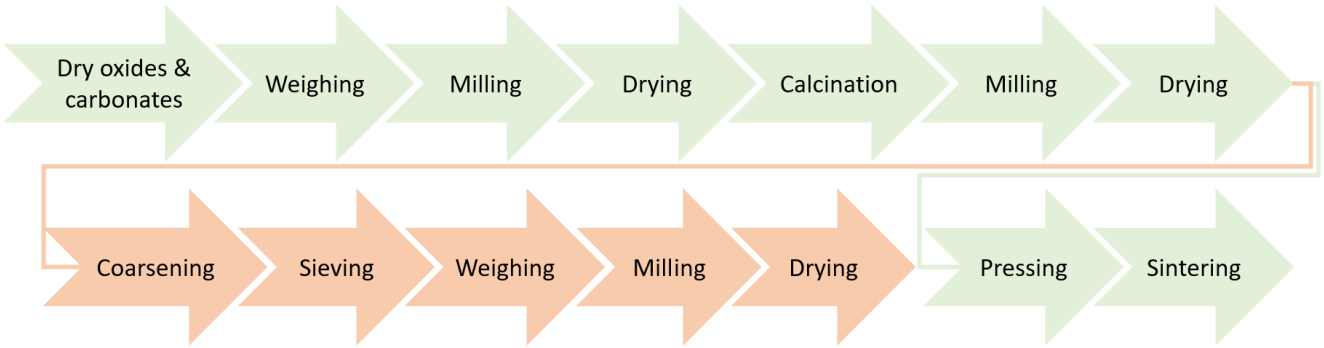

Figure 20: Illustration of the powder processing route.

4.2 Sample Preparation

The powders were used to form green bodies which were densified during sintering.

The produced powders were used to fabricate green bodies. For samples with a diameter of 10 mm, 0.3 g (15 mm, 0.7 g) powder was uniaxially pressed with approximately 40 MPa. Samples were vacuum sealed in latex, followed by an isostatic pressing step in oil (KIP 100E, Paul-Otto Weber GmbH, Remshalden, Germany) with about 350 MPa for 1.5 min (composites 200 MPa). All samples were sintered in closed alumina crucibles with sacrificial powder of the same composition. The sacrificial powder minimizes evaporation of volatile elements by increasing the gas pressure of such elements in the sintering atmosphere. Different sintering conditions were used. Pure NBT-xBT compositions were sintered at 1150 °C for 3 h with a heating rate of 5 °C/min (Nabertherm L16/14, Nabertherm GmbH, Lilienthal, Germany). Pure NBT-xKBT compositions were sintered at 1150 °C for 2 h with a heating rate of 5 °C/min.

Doped compositions were sintered at 1100 °C for 1 h (NBT-xKBT doped: 2 h) with the same heating rate. NBT-xBT composites were sintered at 1012 °C for 1 h (NBT-xKBT composites 1100 °C 2 h). The sintered samples were ground on both sides to have parallel surfaces and a thickness in the range of 0.6-1 mm. The samples were annealed at 450 °C for 30 min (heating rate 5 °C/min) to minimize possible mechanical stress stemming from mechanical sample preparation.

All lead-based ceramics were received from CeramTec GmbH in the final geometry and in poled state.

4.3 Density

A high relative density verifies successful processing and is required for electrical characterization.

The density was determined using the Archimedes method. The sample weight was measured in air (W_{air}). Afterwards, the samples were exposed to a vacuum in water to fill all pores with water and suck the air out. The samples were weighed in water in this condition (W_{fl}). The density of the air was assumed to be ρ_{air}= 0.0012 g/cm^3. The temperature dependent density of the water ρ_{fl} was determined (ρ_{fl}= 0.099768 at 22.5 °C). Following equation gives the sample density:

$$\rho = \frac{W_{\mathrm{air}} \times (\rho_{\mathrm{fl}} - \rho_{\mathrm{air}})}{0.99983 \times (W_{\mathrm{air}} - W_{\mathrm{fl}})} + \rho_{\mathrm{air}} \qquad (16)$$

4.4 Electrical Characterization

Electrodes on the sample surface are needed for electrical and electromechanical characterization. In many cases poled samples are investigated. Both processes are described here.

For most of the electrical measurements silver electrodes were sputtered onto the surfaces. For measurements above 500 °C platinum electrodes were sputtered onto the surface. Each side was sputtered 2 x 4 min at 40 mA in Argon atmosphere at 2 x 10^{-2} mBar. Electrodes on the edge of the samples were hand ground with sand paper (P1200 SiC Grinding Paper, ATM Qness GmbH, Mammelzen, Germany).

Several characterization methods were carried out on poled samples. Samples were poled in a heatable silicon oil bath (Oil: AK200, Wacker Chemie GmbH, München, Germany; Poling machine: PL, Lauda Dr R Wobser GmbH & Co. KG, Lauda-Königshofen, Germany). The poling conditions were optimized, resulting in the following poling conditions: All NBT-xBT-based compositions were poled at 30 °C for 15 min at 6 kV/mm. All NBT-xKBT-based compositions were poled at 120 °C for 10 min at 5 kV/mm. The electric field was maintained when cooling the samples down to *RT* with a cooling rate of 2 °C/min.

4.4.1 Temperature-Dependent Permittivity and Loss

Permittivity and loss against temperature gives insight into phase transitions and defect driven conductivity.

The samples were placed between two Pt electrodes in a box furnace for the dielectric permittivity and dielectric loss measurement (LE4/11/R6, Nabertherm GmbH, Lilienthal, Germany). A LCR impedance analyzer (HP 4284A and HP4192A, Hewlett Packard Corporation, Palo Alto, USA) determined the dielectric response at 100 Hz, 1 kHz, 10 kHz, 100 kHz, 1 MHz with an AC voltage of 1 V from *RT* up to 500 °C. The heating rate was 2 °C/min. The automatic data capture was ensured by a custom LabVIEW program. The real part of the permittivity ε' was calculated from the capacitance of the sample. The measuring error of the sample geometry led to an uncertainty of about 1% in the permittivity. The transition temperature $T_{F\text{-}R}$ was determined from the first derivative of ε' with an uncertainty of about 1 °C.

4.4.2 Thermally Stimulated Depolarization Current

The pyroelectric current contains information about the depolarization behavior and relaxation processes of defects.

The depolarization temperature T_d was determined by measuring the thermally stimulated depolarization current (TSDC). Poled samples were placed between two Pt electrodes in a box furnace (LE4/11/R6, Nabertherm GmbH, Lilienthal, Germany). The samples were heated up to 200 °C with a heating rate of 2 °C/min. The pyroelectric current was logged with an electrometer connected with a custom LabVIEW program (6517B, Keithley, Solon, USA). T_d was determined from the peak in the obtained current.

4.4.3 Polarization and Strain Measurements

The polarization and strain response to a large electric field are fundamental electromechanical characteristics of ferroelectric ceramics.

The polarization and strain hysteresis loops were measured using a modified Sawyer-Tower circuit.[213] The signal was generated by a function generator (HP 33120A, Agilent Technologies Inc., Santa Clara, CA, USA) and amplified with a high voltage amplifier (20/20C, TREK Inc., Lockport, NY, USA). The strain was measured simultaneously with an optical displacements sensor (D63, Philtec, Inc., Annapolis, MD, USA). The signal processing was carried out by a custom LabVIEW program. If not specified differently, a triangular signal[VI] at 1 Hz was used. The measurements were performed in silicon oil to prevent electrical breakdown of the samples.

The remanent polarization was quantified as a function of the poling field by measuring complete P-E loops of partially polarized samples. The negative and positive remanent polarizations of fully poled samples exhibit symmetry with respect to the x-axis. This symmetry enables the quantification of the remanent polarization in initially partially polarized samples (Figure 21).

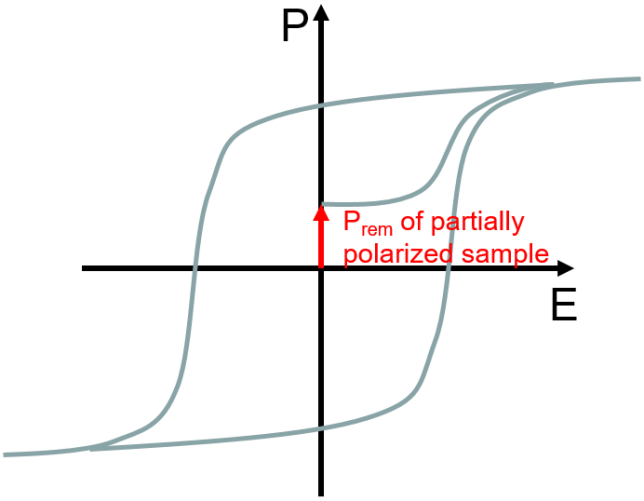

Figure 21: Schematic of the process used to determine the remanent polarization of partially polarized samples.

[VI] Triangular fields have a constant field change, which is desired for frequency dependent large signal measurements.

4.4.4 Temperature-Dependent Impedance Spectroscopy

The temperature dependent DC-conductivity (DC= direct current) can be extracted by temperature-dependent impedance spectroscopy. It helps in the discussion of the conductivity mechanisms and the mobility of defects.

The impedance *Z* is the resistance to an alternating current AC. It is a complex quantity in which the real part is given by the resistance *R* and the imaginary part is given by the reactance X.[214]

$$Z = R + \mathrm{j}X \tag{17}$$

The impedance of a capacitor is frequency dependent. It can be modeled by the bricklayer model to gain information about different conductivity mechanism present in the material. Typical conductivity contributions in capacitor ceramics stem from the bulk, the grain boundary and the space charge at the ceramic-electrode interface.[215] Here, the impedance was determined from 150 °C to 600 °C at constant temperature with a step size of 25 °C. The samples were placed between two platinum plates in a tube furnace (HTM Reetz GmbH, Berlin, Germany). It was measured with 1 Volt applied by an impedance analyzer from Novocontrol (Alpha-A impedance analyzer, Novocontrol Technologies, Germany). The measuring frequencies ranged from 0.1 Hz to 3 MHz with a logarithmic step size of 1.3 (67 frequencies). The post processing of the data was done with RelaxIS software (rhd instruments, Darmstadt, Germany).

4.5 Electromechanical Characterization

All measurements of poled samples which do not preliminary investigate the temperature behavior are considered here as electromechanical measurements.

4.5.1 Piezoelectric Constant d_{33} Off-Resonance

The piezoelectric activity is one of the most desired electromechanical property in ferroelectrics and a necessity when used in high-power applications. d_{33} is the standard coefficient to be determined.

The piezoelectric coefficient was determined using a Berlincourt meter (PiezoMeter System PM300, Piezotest Pte Ltd., Singapore). A static force of 2 N and a dynamic force of 0.25 N was applied at 110 Hz.

4.5.2 Small-signal Resonance Analysis

The resonance analysis is used to determine a bunch of electromechanical properties in resonance along different geometrical directions.

The electrical and mechanical behavior are coupled in piezoelectrics. When piezoelectric ceramics are electrically excited at a certain frequency, the mechanical response gets amplified. The frequency with the highest response is called the resonance frequency. The resonance behavior is determined by the material properties like the electromechanical coupling, the compliance, losses or the geometry of the sample. Four different geometries with different vibration modes have been investigated in this study. Disk-like samples were investigated in the thickness k_t and planar resonance mode k_p. In the thickness mode the mechanical vibration happens mainly along the thickness of the disk. In the planar mode the vibration happens mainly perpendicular to the thickness. In both cases the electric field is applied along the poling direction which is along the thickness of the sample. Bar-shaped samples were investigated in the transversal k_{31} and the longitudinal k_{33} length mode. In the transversal mode the electric field is applied perpendicular to the dominant vibration direction. In the longitudinal mode the electric field is applied along the dominant direction of vibration. The piezoelectric resonator can be represented by a modified Butterworth-Van Dyke electrical equivalent circuit (Figure 22).[216] The dynamic branch L_d, C_d and R_d represents the vibration of the resonator. The resistance R_d correlates with the elastic losses. The other branch C_0 and R_0 represents the off-resonance behavior. C_0 is denoted as “clamped” capacitance. R_0 correlates with the dielectric loss. The electrical circuit can be adapted by an additional LCR brunch to address the piezoelectric component and account for the piezoelectric loss.

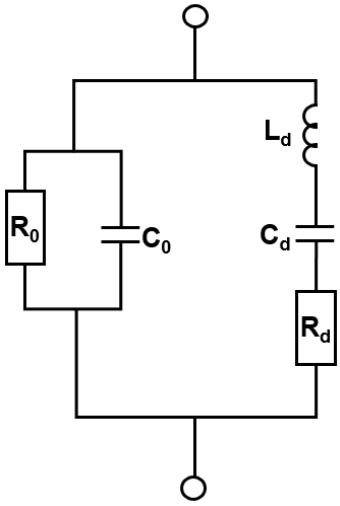

Figure 22: Equivalent electric circuit for a piezoelectric resonator in 31 vibration mode.

Since the electrical and mechanical behavior is coupled and can be represented by an equivalent electrical circuit, several mechanical, piezoelectrical and dielectric properties can be determined by measuring the purely electrical response of the sample.

The impedance *Z* was measured against frequency using an impedance analyzer (Alpha-A impedance analyzer, Novocontrol Technologies, Germany). In the first step the sample was scanned over a broad frequency range to determine the position of the resonance- and anti-resonance peaks. The peaks were measured again from high to low frequencies with a resolution of 3-25 Hz. The measuring voltage was chosen to be as low as possible to prevent the sample from vibration (v = 0). The electric field was 0.01 V/mm (V_p) or lower which is the reason to name it ”small”-signal measurement. The capacitance C_0 was determined at 1 kHz. The sample should be in mechanical free conditions. Hence, the samples were measured in a custom sample holder with very low clamping force. A detailed description of the overall measuring conditions, sample geometries and formulas is given by the European Standard EN-50324.[53] A typical impedance curve of a polarized sample near resonance is give in Figure 23. The resonance is defined as the minimum in the absolute impedance. The maximum in the absolute impedance is defined as anti-resonance. The phase angle changes from almost -90° to almost 90° between both resonance peaks. In the resonance and anti- resonance the phase angle is close to zero. An unpoled sample would not show any resonance peaks.

In some experiments the effect of clamping on the electromechanical properties in resonance was investigated. The samples were mechanically clamped with different stresses. A modified tensile testing device was used to apply uniaxial compressive stress onto the samples.

Conductive stamps were used and electrically connected to the impedance analyzer. All other measuring conditions were the same as described above.

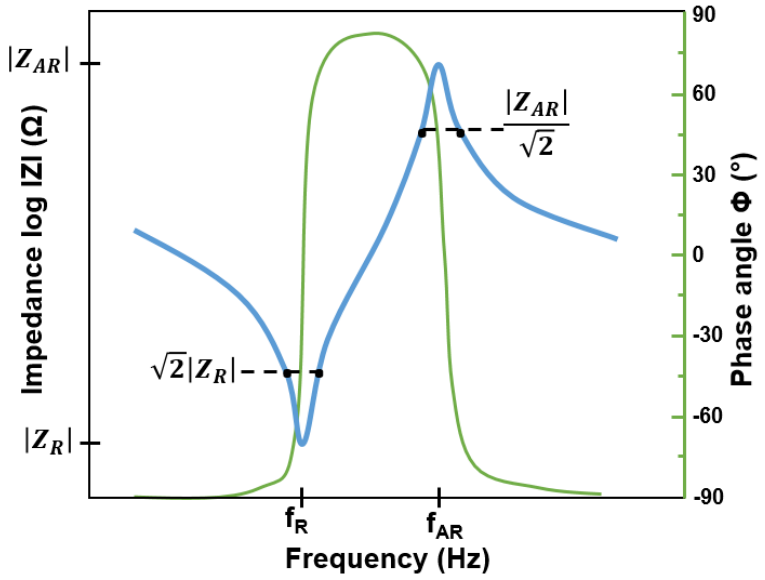

Figure 23: Illustration of the impedance I*Z*I and phase angle as a function of frequency *f*. Depicted are the resonance frequency f_R, the anti-resonance frequency f_{AR}, and the corresponding impedance IZ_RI and IZ_{AR}I. The values multiplied or divided by $\sqrt{2}$ are used for the determination of the quality factor according to the 3dB method.

4.5.3 High-power Resonance Analysis with Burst Excitation

The electromechanical coefficients depend on the mechanical stress level, the electric field strength and temperature. Large electric field results in a non-linear amplitude response. Small-signal parameters do not account for the non-linearity. A customized high-power measuring setup was used to determine the electromechanical properties at high-power driving conditions.

The setup was designed and built by the former PhD student Mihail Slabki. A detailed instruction is given in his thesis.[217] The most important information about the setup and measuring conditions are explained here. The setup is based on reports from Umeda et al. [218]. An AC voltage signal was generated by a function generator (Agilent 33220A, Agilent Technologies Inc., USA). The signal was amplified by 20 times with a high-voltage amplifier (HAS-4052, NF Corp., Japan). The sample was placed in a customized sample holder with needle shaped, gold coated, spring loaded electrodes (1015/G, PTR Messtechnik GmbH, Germany). The spring has a preload of 0.4 N and a diameter of 0.64 mm with a flat contact

surface. The contact to the sample was at the node point. The placement and the sample holder assured a minimum of mechanical clamping to allow quasi-free vibration. The voltage drop at the resonator was measured in parallel with a custom made passive voltage probe. The generated current was measured with an inductive current probe (60 Msamp/s[VII] sampling frequency; PCI-5105, National Instruments, USA). An electromechanical relay was used to apply open-circuit conditions. Coaxial cables were used in the entire setup for an optimal signal to noise ratio. The vibration velocity (vibrational displacement) was measured by a laser vibrometer (OFV-5000 or OFV-505, Polytec GmbH, Germany). The corresponding software VibSoft 5.4 was used (Polytec GmbH, Germany). All measuring signals were recorded with a high-speed oscilloscope (PCI-5105, National Instruments, Austin, USA). The accurate positioning of the Laser was crucial to ensure a stable and clear signal. It was placed on an XYZ precision stage at the optimal focus distance of 484 mm. The Laser as well as the sample holder were mechanically decoupled from their environment to avoid external vibrations. The laser was positioned at the sample surface which was polished beforehand to ensure a better reflectivity. Two different lasers were used in this study. The model OFV-505 was limited to a maximum of 0.8 m/s and the model OFV-5000 was limited to 10 m/s. Samples with a 33 geometry required Ag-wires (silver wire 0.05 mm, Thermo Fisher Scientific, Waltham, MA USA) as electric connection. They were attached with an Ag-glue to the electrode surface (Silberleitlack 530042, Ferro GmbH, Frankfurt/M, Germany).

All the measurements were controlled using a customized LabVIEW program. To characterize a sample the resonance frequency was determined first with a small-signal measurement. Secondly, the large-field resonance frequency region was identified. The time/cycles needed to reach steady state N_1 and the time/cycles needed for the decay of the response N_2 were determined. The measurement was performed using burst excitation to prevent sample heating (total measuring time < 100 ms). A voltage was applied for N_1 cycles. After N_1 cycles the resonator was short circuited. The data were collected for $N_1 + N_2$ cycles (Figure 24). When being short circuited the sample immediately jumps to the resonance frequency. In open circuit the sample jumps into anti-resonance. The collected data was processed in another customized LabVIEW program. The extrema (minimum and maximum) of the cycles in the decay were determined. The decay was segmented into several pieces of displacement attenuation (Figure 24). Each segment was fitted by an exponential expression and correlated with a decay coefficient e. The material properties were assumed constant for each segment

[VII] Msamp/s = Mega-samples per second = 1.000.000 measuring points per second.

to calculate the vibration velocity and mechanical quality factor according to the Equations (18) and (19) with the dimensionless-normalized resonance frequency N_i and the strain S_i.

$$v_i = \pi N_i S_i \tag{18}$$

$$Q_{ij} = \frac{2\pi f_R}{e} \tag{19}$$

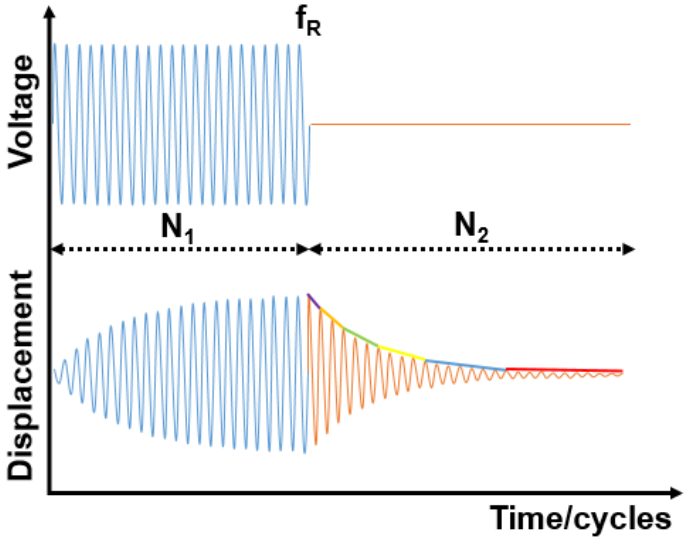

Figure 24: Burst measurement in resonance with N_1 cycles of excitation and N_2 cycles of decay. Typical cycle numbers were N_1=500-2000 and N_2=1000-3000. The segments to determine the decay coefficient are schematically shown in different colors.

4.5.4 High-power Fatigue Measurement

Piezoelectrics in high-power devices are usually continuously driven. They experience a large number of cycles in the order of 10^{11} cycles and higher. Electrical, mechanical or electromechanical fatigue is expected to occur. Hence, it is necessary to gain some information about the fatigue behavior of a material before transferring it into real applications. Different issues are overcome when testing the material in laboratory environment. The testing time can be reduced significantly. The production time and costs can be reduced. The fatigue can be tracked isolated for the material.

A device was developed to fulfill these requirements: Different sample geometries, continuous drive at defined vibration velocity, continuous drive at resonance frequency, tracking of different variables (voltage, current, temperature, vibration velocity, frequency), automatic control.

A schematic description of the setup is given in Figure 25. A function generator generated an AC voltage signal (Agilent 33220A, Agilent Technologies Inc., USA). The voltage was amplified 20 times by a high voltage amplifier (HAS-4052, NF Corp., Japan). The sample was placed in a similar sample holder as described in the chapter “High-power Resonance Analysis with Burst Excitation”, with an additional fixation to the side of the sample. The voltage was measured in parallel with a voltage probe (Passiver Koaxialtastkopf SP500C, National Instruments Germany GmbH, Munich, Germany). The current was measured with an inductive current probe (CT2 High-frequency Current Probe, Tektronix GmbH, Köln, Germany). The same laser vibrometer from the high-power burst measurements was used (OFV-5000, Polytec GmbH, Germany). The temperature was monitored with an IR-laser sensor (CTL-CF1-C3 Hochleistungs-Pyrometer, Micro-Epsilon Messtechnik GmbH & Co. KG, Ortenburg, Germany). All measuring signals were logged with a high-speed measuring card (oscilloscope) (PicoScope 4824, Pico Technology, Cambridgeshire, United Kingdom).

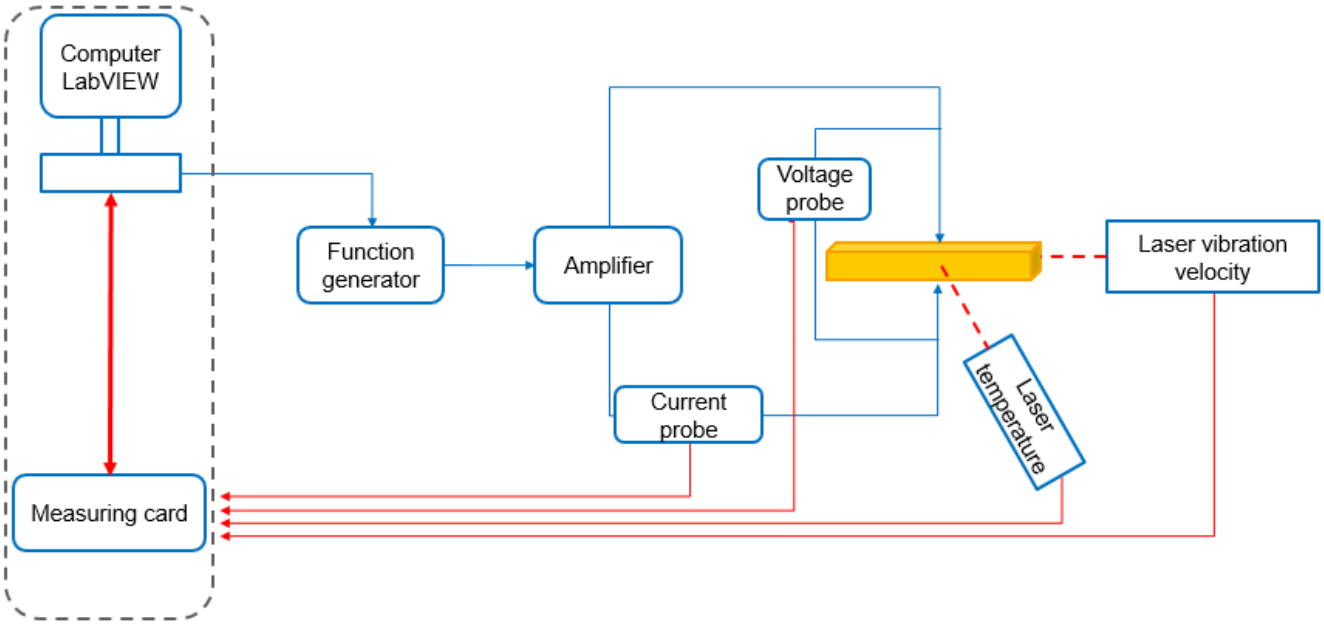

Figure 25: Schematic illustration of the setup to measure fatigue. Blue lines represent the applied signal and red lines represent the measuring signal.

The software will be explained here in more detail since it is a major part of the setup and not commercial available. The measuring card (oscilloscope) tracked the data from the current probe (current *I*), voltage probe (voltage *V*), laser vibrometer (vibration velocity *v*) and temperature laser (temperature *T*) with a frequency of 40 MHz. The data were sent from the measuring card to the computer in packages of 1000 measuring points for each variable.

Hereby, about 80 packages per second were sent from the measuring card to the computer. The data packages (1000 measuring points per variable) were processed in a customized LabVIEW program[VIII] on the computer in the following way: the maximum of the absolute values of each variable were calculated. A variable proportional to the absolute value of the impedance I*Z*I was calculated by dividing the voltage by the current. Additionally, the applied voltage *U*, the time *t*, the frequency *f* and the changed frequency ±*f* were tracked on the computer. The frequency change is explained later. All nine calculated numbers (*I*, *V*, *v*, *T*, *U*, *t*, *f*, ±*f*, I*Z*I) were saved in a TDMS-file at desired saving frequency[IX].

As a result of the described process, the data points were cut down from 9000 points to 9 points without losing the important information (1000 points per variable → 1 point per variable). One purpose of this data processing technique was to reduce the amount of data points but still be able to track all changes. Initial saving of all data points led to huge data files of several hundred Mbyte/minute. This slowed down the program and eventually crashed the program. On top to the described process, every few minutes (~10 min) a complete data package with 1000 data points per variable was saved, which is roughly the equivalent of three vibration cycles.

Apart from tracking all changes during the cycling of the sample, the collected data was also used to keep the sample vibrating in resonance. The vibration in resonance is necessary to reach and maintain a desired vibration velocity. Hence the vibration velocity can be controlled by the frequency and the voltage amplitude. The following steps were performed about 80 times per second to keep the sample vibrating in resonance:

$$\text{If } |Z|_{\mathrm{n}} < |Z|_{\mathrm{n-x}} \text{ then } \pm f \times 1 \tag{20}$$

$$\text{If } |Z|_{\mathrm{n}} > |Z|_{\mathrm{n-x}} \text{ then } \pm f \times -1 \tag{21}$$

The frequency was changed in every tracking cycle (about 80 Hz) by a desired amount (usually ±10 Hz). The absolute value of the impedance at this measuring cycle n was compared to the absolute impedance x measuring cycles before. If the value was higher than before, the frequency is further away from the resonance frequency, since at the resonance frequency the impedance is the lowest. The frequency change ±*f* was multiplied by -1. In the other case, the absolute impedance of this measuring cycle n is lower than the absolute impedance x measuring cycles before. The frequency is getting closer to the resonance frequency. Hence, ±*f* is multiplied by 1 and the direction of the frequency change maintains the same. This

[VIII] In close collaboration with the college Patrick Breckner.

[IX] The usual measuring frequency was 0.2 Hz.

controlling step was optimized and resulted in a comparison of the current measuring cycle n to the fourth measuring cycle before, x = 4. It was influenced by the controlling frequency, the frequency change ±*f* and the measuring accuracy. In a second controlling step the voltage was changed to get the desired vibration velocity.

$$\text{If } v_0 > v_{\text{desired}} + 0.05\ \text{m/s} \text{ then } U - 0.1\ \text{V} \quad (22)$$

$$\text{If } v_0 < v_{\text{desired}} - 0.05\ \text{m/s} \text{ then } U + 0.1\ \text{V} \quad (23)$$

If the measured vibration velocity v_0 was larger than the desired vibration velocity v_{desired} plus a certain threshold (mostly 0.05 m/s), the applied voltage was reduced by a defined voltage (mostly 0.1 V). If v_0 was smaller than the v_{desired} minus a certain threshold, the applied voltage was increased by a defined voltage. The controlling step 2 was performed after the controlling step 1 was performed 1000 times (ratio was optimized).

The measuring procedure itself was performed as follows: The sample surface was polished with a grinding paper (P4000 SiC Grinding Paper, ATM Qness GmbH, Mammelzen, Germany) to increase the reflectivity. In the case of samples in 33 geometry, silver wires (silver wire 0.05mm, Thermo Fisher Scientific, Waltham, MA USA) were glued with silver paste (Silberleitlack 530042, Ferro GmbH, Frankfurt/M, Germany) onto the electrodes. The samples were placed inside the customized sample holder. Their unfatigued resonance characteristics were determined by a small-signal impedance measurement. In the next step, the position of the laser was optimized. Initial testing showed a movement of some samples which was prevented by bringing two outer pins close to the samples without contacting it. A voltage signal in sinus form was applied at the small-signal resonance frequency. The voltage was increased stepwise. Simultaneously, the frequency was adapted to stay in resonance. Close to the desired vibration velocity the control was started. In some cases the control was not reliable. The controlling was done by hand in this case. Similar to the automatic control, first the frequency was changed and in a second step the voltage was adapted. In some cases the voltage was increased continuously to max out the vibration velocity (maximum of continuous drive). Small-signal measurements were performed again after the fatigue process.

4.6 Structural and Microstructure Characterization

4.6.1 Scanning Electron Microscopy and Microstructure

A scanning electron microscope (SEM) was used to obtain information about the microstructure, secondary phases and the topography.

For microscopic investigations the samples were polished using different diamond paste with a particle size of 15 µm, 6 µm, 3 µm, 1 µm and 0.25 µm (machine: Phoenix 4000, Jean-Wirtz GmbH & Co.KG, Düsseldorf, Germany; diamond paste: DP Paste, STRUERS GmbH, Willich, Germany; polishing cloth: DP DUR STRUERS GmbH, Willich, Germany). Some samples were finished with a colloidal silica polishing suspension (Buehler Mastermet, Buehler GmbH, Düsseldorf, Germany).

For topographical investigations, the samples were thermally etched at 900 °C for 8 min. Either gold or carbon was sputtered as a conductive layer on top of the samples. Gold was sputtered 40 sec at 40 mA in Argon atmosphere at 2 x 10^{-2} mBar. Carbon was sputtered with 2-4 pulsed at 2 A. The sample topography was investigated with an SEM (Philips XL3000 FEG, FEI Company, Eindhoven, Netherlands) using the secondary electron mode (SE-mode) and gold as a conductive layer on the sample surface. Secondary phases were investigated using the back-scattered electron mode (BSE-mode) and a conductive carbon layer on the sample surface. The grain size was determined using an automated graphical analysis LabVIEW program. The program registers the grain boundaries and determines the area of each grain. It calculates a grain diameter from the grain area assuming spherical grain shape. At least 150 grains were taken into account. Assuming an isometric grain shape, a numerical multiplication factor of 1.56 was used to determine the 3d average grain size.[219]

4.6.2 Laboratory X-Ray Diffraction

Standard laboratory X-ray diffraction was performed on sintered, crushed and unpoled samples to investigate the phase structure and phase purity.

Samples were annealed for 30 min at 400 °C after being crushed. For the standard measurements a conventional laboratory X-ray diffractometer was used (Bruker AXS D8 Advance, Karlsruhe, Germany) with Cu K_α radiation (wavelength Cu $K_{\alpha 1}$ λ = 1.5406 Å and Cu

$K_{\alpha 2}$ λ = 1.5444 Å). The recorded step size was 0.02°. Some XRD measurements were performed with a Guinier diffractometer (Guinier-Camera G670, Guinier Monochromator 611, X-Huber diffraction and positioning equipment) with a Cu-source and monochromator (Cu $K_{\alpha 1}$ λ = 1.5409 Å). It was measured in transmission geometry. A standard silicon sample (NIST SRM640e) was mixed to the samples, to obtain the instrumental parameter. The data from the second setup was used for Rietveld refinement (Topas V6).

4.6.3 Synchrotron X-Ray Diffraction

Synchrotron X-ray diffraction is usually combined with a 2d detector. The detector type and the transmission geometry (due to the very high intensity) makes it suitable to get orientation dependent structural information of poled bulk samples.

High energy X-ray diffraction data were collected at DESY (Hamburg, Germany) on Beamline P02.1. The beam energy was ~59.8 keV (λ = 0.20718 Å). A 2d detector (16-inch XRD 1621N ES Series PerkinElmer) with a resolution of 2048 x 2048 pixels was used. The detector pixel size was 200 µm^2. A higher angular resolution was obtained by placing the beam center on the corner of the detector. The second synchrotron setup was used at the ESRF in Grenoble. The beam energy was ~ 60 keV (λ = 0.20664 Å).

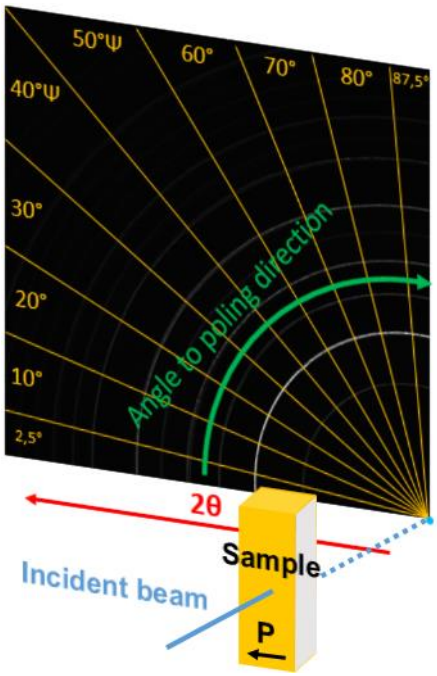

Figure 26: Experimental high-energy XRD setup. Diffraction patterns are measured as a function of poling direction.

The beam was centered onto the detector (Pilatus3 X CdTe 2M). The DAWN software version 2.15.0 was used to integrate the 2d pattern into 1d pattern.[220] The following angles were integrated to obtain a specific angle Ψ (middle of integrated range) which is the angle in relation to the poling direction (only true for poled samples): 0-5°, 5-15°, 15-25°, 25-35°, 35-45°, 40-50°, 45-55°, 55-65°, 65-75°, 75-85°, 85-90° (Figure 26). The obtained 1d patterns were summed up according to Equation (24). It gives randomized XRD pattern without texture such as in an unpoled state. (In = intensity, $\propto_i/\propto_j$= low/high boundaries of respective angle range).[221]

$$\langle I \rangle = \sum_{\propto=0°}^{90°} \mathrm{In}(\propto)\left[\cos(\propto_i) - \cos(\propto_j)\right] \tag{24}$$

The degree of texture was determined for some samples. Two separate methods were used to calculate the texturing degree. In the classical approach the 111_{pc} and 200_{pc} reflections were each fitted with three single peaks. In the case of the 111_{pc} reflection it is composed of 111_R, $11\bar{1}_R$ and 111_T reflections. In the case of the 200_{pc} reflection it is composed of the 002_T, 200_T and 200_R reflections. The peaks were fitted with a pseudo-Voigt shape function (Figure 27). Based on the integrated intensity the texturing factor was calculated like given by Daniels et al.[222]. In another approach the STRAP model (Strain, Texture and Rietveld Analysis for Piezoceramics) was used to calculate the texturing factor in a multiphase system (performed by Manuel Hinterstein).[223, 224] The program package MAUD (Materials Analysis Using Diffraction) was used for the STRAP method.[225]

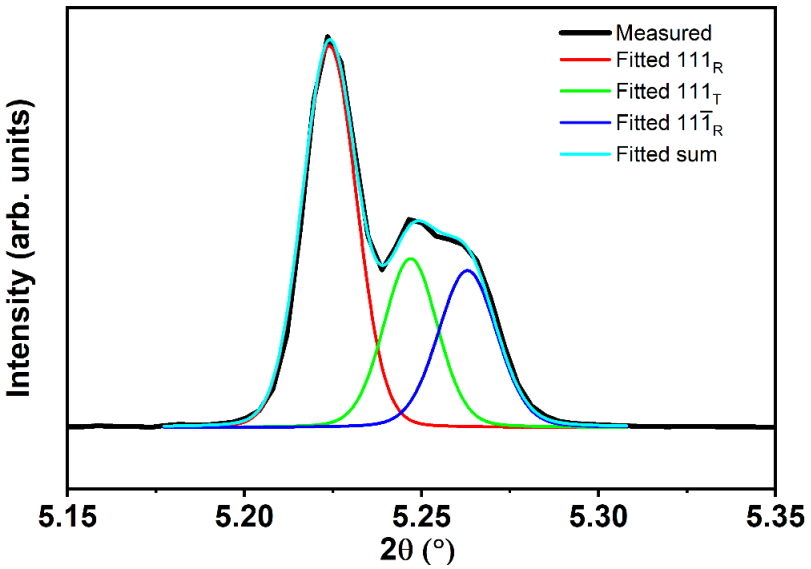

Figure 27: Measured 111_{pc} reflection fitted with the 111_R, $11\bar{1}_R$ and 111_T reflections.

5 (1-x)$Na_{1/2}Bi_{1/2}TiO_3$-x$BaTiO_3$

In the first part of this chapter, the results obtained from chemical modification of NBT-xBT are discussed. Then, NBT-based materials are compared to hard PZT (P4) in conditions related to high-power applications in resonance, such as at high vibration velocities with burst excitation and in continuous drive. Furthermore, the fatigue and the behavior under uniaxial compressive stress in resonance are investigated.

5.1 NBT-xBT: Doping

In the literature, many different dopants have been investigated for the NBT-xBT system (Table 1). However, no clear rule has been established for tailoring the properties in NBT-xBT with dopants, as is the case for PZT or BT. This section aims to lay a basis for a general understanding of doping in the NBT-xBT system. Further, the electromechanical properties of NBT-xBT, with a focus on the piezoelectric coefficient, mechanical quality factor, and depolarization temperature, were optimized according to the needs in high-power applications.

5.1.1 Influence of Zn doping on the Morphotropic Phase Boundary in NBT-xBT

Zn doping shifts the MPB to a lower BT content by stabilizing the tetragonal phase and lattice distortion. Zn doping further leads to a remarkable increase in the mechanical quality factor, up to seven times higher.

Sintered samples feature a relative density of 93.8–97.8% (Table S1). The grain size is between 1.2 µm and 2.1 µm in NBT-5BT to NBT-8BT. Zn doping increases the average grain size to 9.4-15.6 µm in NBT-5BT-0.5Zn to NBT-8BT-0.5Zn (Table S1). Both a lower sintering time and a lower temperature of the Zn-doped compositions suggest that Zn^{2+} acts as a sintering aid. Zn doping leads to an increased oxygen vacancy concentration, which impacts the grain boundary energy and leads to boosted grain growth.[226] An increase in grain size from 1 µm to 18 µm can stabilize the rhombohedral phase *R*3*c* and alter the depolarization temperature.[144] The stabilization of the rhombohedral phase *R*3*c* cannot be confirmed here. The change in grain size is smaller than that observed by Khatua et al. [144]. Hence, the observed changes in the structure and properties are mainly correlated with the Zn-doping effect.

All compositions show a single-phase perovskite structure, according to XRD (Figure S1). The 111_{pc} and 200_{pc} reflections are given in Figure 28 for all compositions in the unpoled state. Detailed transmission electron microscopy (TEM) studies have revealed a phase mixture of *R*3*c*, *P*4*mm*, and *P*4*bm* with no cubic phase.[227] However, since no *P*4*bm* superlattice refection is noticeable in these XRD patterns, the *P*4*mm* phase with higher symmetry is chosen for the refinement. A cubic $Pm\bar{3}m$ phase is needed to obtain considerably good fits. This phase was previously reported as a second phase too.[228] The dissimilarity between this study and the literature might be correlated with the higher resolution of the TEM measurement or with the fact that very thin samples are measured in the TEM study, which can affect the structure.[229] The highest cubic phase fraction is present in the undoped NBT-6BT. This maximum in the cubic phase fraction shifts toward NBT-5.5BT when NBT-xBT is doped with Zn. From NBT-5BT to NBT-6BT, a rhombohedral shoulder is observed in the 111_{pc} reflection on the lower 2θ side (marked with R). The superlattice reflection at 38.3° indicates the *R*3*c* symmetry (marked with an asterisk). The same rhombohedral phase is present in NBT-5BT-0.5Zn to NBT-6BT-0.5Zn but with a smaller phase fraction. The undoped compositions from NBT-6BT to NBT-8BT reveal a splitting in the 200_{pc} reflection (marked with T), indicating a tetragonal phase *P*4*mm*. With increasing BT content (Figure 29), not only the tetragonal phase fraction but also the tetragonal lattice distortion increases (Figure 30). The rhombohedral lattice distortion is unaffected by the BT content. The tetragonal lattice distortion δ_T is given by the ratio from c to a: $\delta_T = \frac{c}{a} - 1$.[230] The rhombohedral lattice distortion δ_R is given by the lattice spacings d_{111} and $d_{11\bar{1}}$: $\delta_R = \frac{d_{111}}{d_{11\bar{1}}} - 1$.[230]

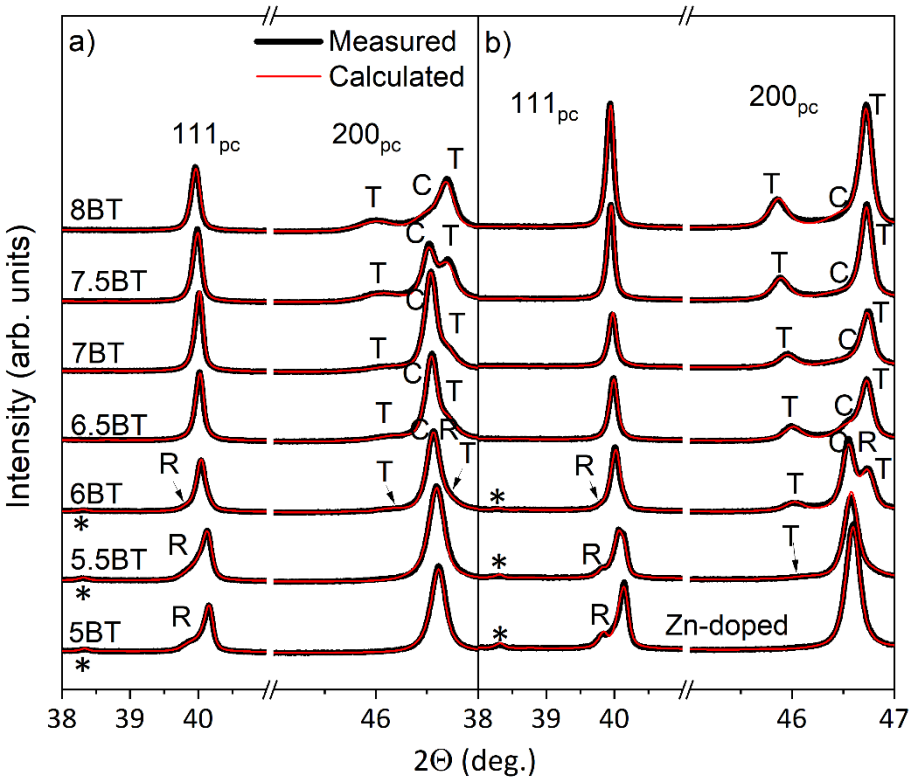

Figure 28: X-ray diffraction profile of 111_{pc} and 200_{pc} reflections of pure NBT-5BT to NBT-8BT (a) and NBT-5BT-0.5Zn to NBT-8BT-0.5Zn (b) (measured: black, calculated: red). Superlattice reflections are marked with an asterisk *. The rhombohedral, tetragonal, and cubic peaks are marked with R, T, and C, respectively.

The Zn-doped compositions show the same tendencies in the phase fraction and tetragonal distortion as the undoped compositions. Nevertheless, the tetragonal phase *P4mm* is present in NBT-5.5BT-0.5Zn up to NBT-8BT-0.5Zn. Furthermore, Zn doping increases the tetragonal phase fraction and the tetragonal distortion (Figure 29 and Figure 30). The increase in lattice distortion results from Zn^{2+} having a larger ionic radius and ionic polarizability than Ti^{4+}, leading to a larger distortion of the BO_6 octahedra.[141] By contrast, the rhombohedral distortion is almost unaffected by the Zn doping. The stabilization of the tetragonal phase by Zn doping leads to a shift of the morphotropic phase boundary (MPB). When the MPB is defined by the highest disorder in the structure, it is located at NBT-5.5BT-0.5Zn and at NBT-6BT in the undoped compositions. The effect of Zn doping on the tetragonality was previously noted in Bi_2ZnTiO_6, exhibiting a large c to a ratio of 1.211.[231] Similarly, Zn doping was found to increase the tetragonality in NBT-6BT and NBT-9BT.[147] A shift of the MPB has been investigated in other systems as well, but it is not known for the NBT-xBT system yet.[134, 232]

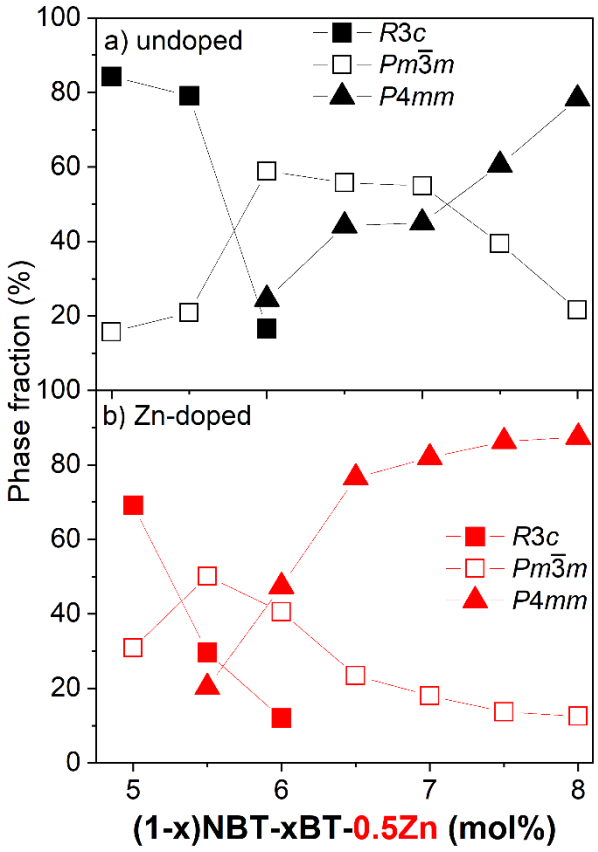

Figure 29: Phase fractions across the morphotropic phase boundary from unpoled NBT-5BT to NBT-8BT without Zn doping (a) and with 0.5 mol% Zn doping (b). The phase fractions were obtained by Rietveld refinement. Detailed information about the refinement is provided in Table S2. The error given by Topas is in the range of ±2%.

The transition temperatures $T_{F\text{-}R}$ are depicted in Figure 31a for all MPB compositions. Both the undoped and the Zn-doped compositions exhibit a minimum in $T_{F\text{-}R}$ at the compositions with the highest cubic phase fractions in the unpoled state, namely NBT-6BT and NBT-5.5BT-0.5Zn. The basic trend of $T_{F\text{-}R}$ is a function of BT content. However, the minimum shifts not only toward a lower BT content with Zn doping but also to a higher temperature: 103 °C in NBT-6BT to 119 °C in NBT-5.5BT-0.5Zn. The shift in $T_{F\text{-}R}$ is rationalized by the non-cubic distortion, which follows a common trend in NBT-based piezoceramics. The increase in lattice distortion is proportional to increased temperature stability.[143] Zn doping has previously been found to improve the temperature stability of NBT-6BT and NBT-9BT.[141, 147]

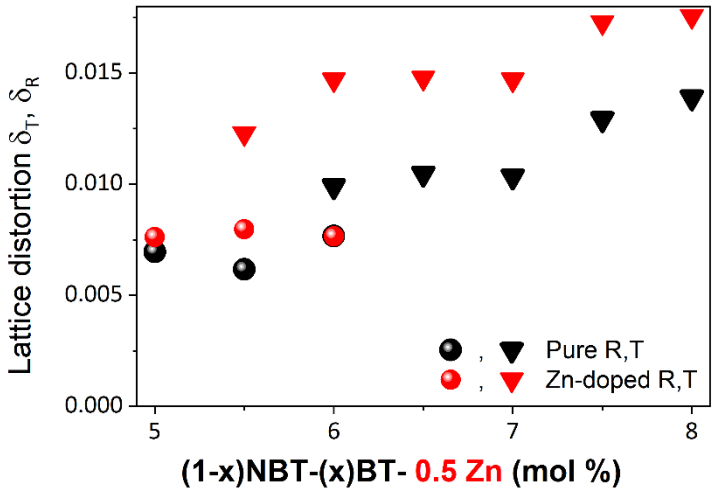

Figure 30: Rhombohedral (circle) and tetragonal (triangle) lattice distortion δ_R (rhombohedral), δ_T (tetragonal) of undoped (black), and Zn-doped (red) NBT-5BT to NBT-8BT.

Other properties also mimic the MPB shift and the enhanced ferroelectric stability found by Zn doping. The maximum in the piezoelectric constant d_{33} is located at a higher BT content than the minimum in $T_{F\text{-}R}$. The maximum d_{33} is located at NBT-7BT in the undoped compositions. The maximum of the piezoelectric constant is often found at the tetragonal side of the MPB.[233, 234] However, Zn doping shifts the maximum in d_{33} to a lower BT content: NBT-6.5BT-0.5Zn. The maximum d_{33} decreases from 164 pC/N to 131 pC/N upon Zn doping. The d_{33} of NBT-5BT is unaffected by Zn doping, whereas the decrease in d_{33} amplifies with increasing BT content. The coupling coefficient k correlates with the piezoelectric constant, see Equation (10). Therefore, a shift of the maximums in k_p and k_t to a lower BT content and their decrease on the tetragonal side upon Zn doping are expected (Figure 31c and d). Higher piezoelectric activity at the MPB is attributed to a flattening of the free energy profile, which promotes polarization rotation.[235] A flattened free energy profile usually correlates with a more cubic-like structure.[64] Hence, an increase in lattice distortion by Zn doping has the opposite effect. Luo et al. [143] previously correlated the c/a ratio with an increase in depolarization temperature T_d and a decrease in d_{33}.

A significant increase is observed in the mechanical quality factor Q_m^p by a factor of three to seven with Zn doping (undoped: 105-201, Zn-doped: 565-744, Figure 31c). The mechanical quality factor Q_m^t is less sensitive to Zn doping than Q_m^p and experiences a minor increase (Figure 31d). An increase in Q_m is related to ferroelectric hardening, which can be verified by the internal bias field E_{bias}. The E_{bias} of undoped NBT-xBT is in the range of 0.08-0.25 kV/mm. Zn doping increases the E_{bias} to a range of 0.45-0.66 kV/mm. Hence, Zn doping ferroelectrically

hardens NBT-xBT compositions around the MPB. The mechanism leading to ferroelectric hardening is unclear from these results and will be discussed in detail in the following chapters. However, the main defects introduced by Zn doping are Zn^{2+} ions on the Ti^{4+} side and oxygen vacancies.[141] A shift of the polarization hysteresis loop along the electric field axes (measured by E_{bias}) is usually associated with the pinning of domain wall movements by defects. Furthermore, Q_m^p notably decreases across the MPB toward the tetragonal side in pure NBT-xBT. In PZT, the opposite behavior is observed: compared with the rhombohedral compositions, the tetragonal compositions have higher Q_m values in PZT. These higher values are rationalized by a higher coercive field, which impedes domain wall motion.[100] The same explanation could be true for NBT-xBT, which exhibits a higher coercive field on the rhombohedral side of the MPB than on the tetragonal side. In Zn-doped compositions, no clear trend can be observed in E_{bias}.

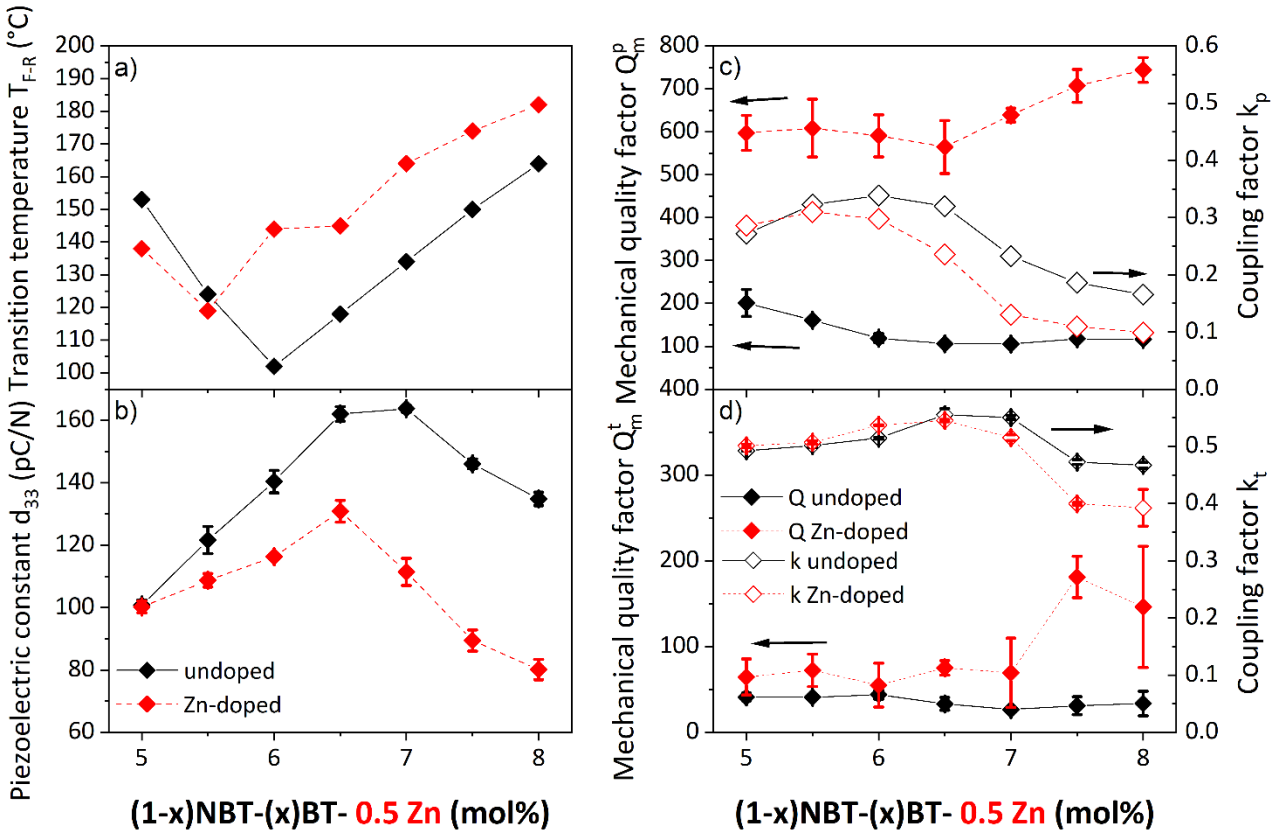

Figure 31: Electromechanical properties across the MPB from NBT-5BT to NBT-8BT without (black) and with (red) Zn doping. a) Transition temperature T_{F-R} determined from temperature-dependent permittivity (Figure S2). b) Piezoelectric constant d_{33}. c) Mechanical quality factor Q_m^p and electromechanical coupling factor k_p in planar mode. d) Mechanical quality factor Q_m^t and electromechanical coupling factor k_t in thickness mode.

5.1.2 NBT-6BT: Comparison of Mg and Zn Doping

In this chapter, Mg and Zn are discussed as acceptor dopants in NBT-6BT. The focus is on Mg doping, which exhibits similar behavior to Zn doping apart from an even higher Q_m in Mg-doped NBT-6BT. Similarities are found in the stabilization of the tetragonal phase and lattice distortion in the unpoled state. The tetragonality in the poled state does not depend on doping.

NBT-6BT was doped with 0.1, 0.3, 0.5, and 1 mol% Mg and Zn. The composition doped with 1 mol% Mg revealed a high conductivity, making it impossible to polarize and obtain electromechanical properties. For this reason, it is excluded from the discussion.

No secondary phases were detected in the microstructure or the XRD profile (Figure 32 and Figure 33). The dark areas in Figure 32h and bright spots in Figure 32g are artifacts from thermal etching. Unetched samples do not exhibit these features. The relative density of all Mg-doped and Zn-doped samples are in the range of 94.5-95.5%. The densities do not depend on the doping concentration. The grain size increases with increasing doping concentration from 1.7 ± 0.8 µm in pure NBT-6BT to 10.4 ± 4.3 µm in NBT-6BT-0.5Mg (other grain sizes are listed in Table S3). The increase in grain size with rising acceptor-doping concentration results from a simultaneous rise in oxygen vacancy concentration. Oxygen vacancies are likely to form in acceptor-doped compositions to maintain charge neutrality (M = metal such as Mg or Zn):

$$\mathrm{MO} \rightarrow M''_{Ti} + V_O^{\circ\circ} + O_O^X$$

The oxygen vacancy concentration could influence the grain boundary structure from faceted to rough. The roughening enhances the grain boundary movement, which itself leads to grain growth. This has been reported for non-stoichiometric NBT-6BT and BT ceramics.[142, 236]

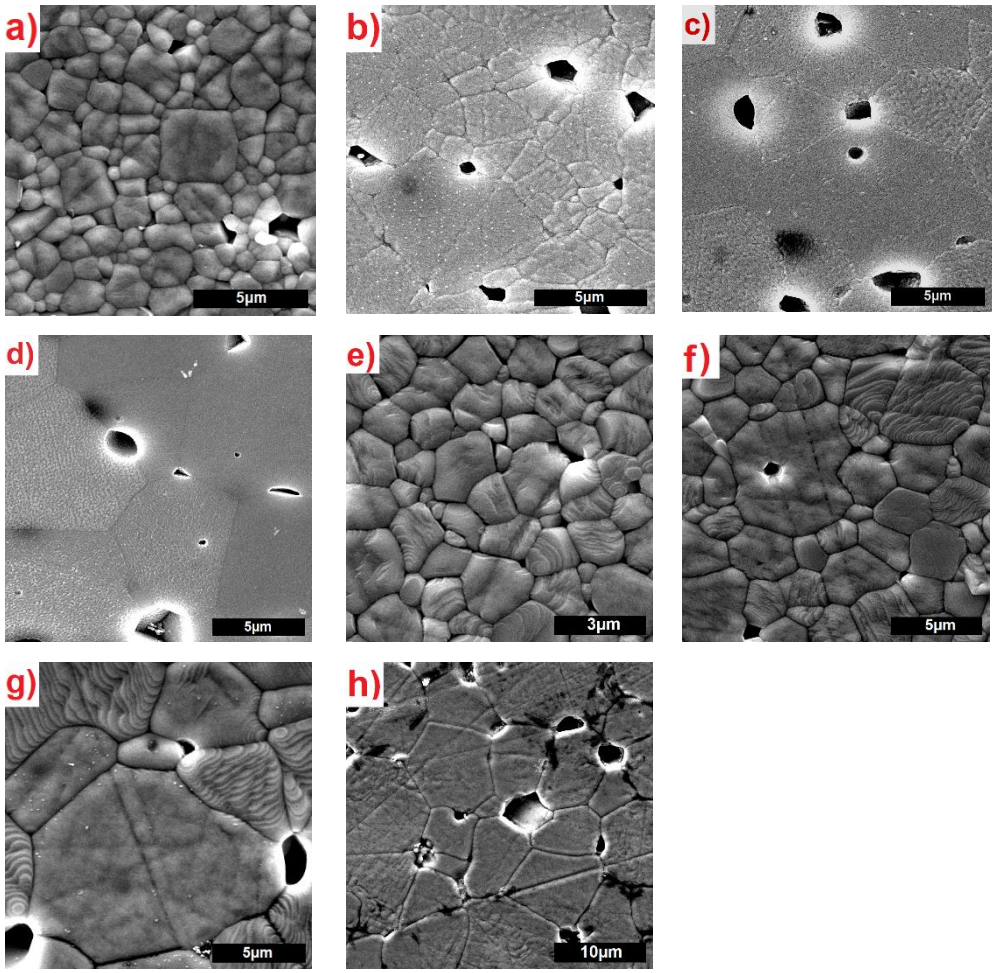

Figure 32: Microstructure obtained by SEM from ground, polished, and thermally etched NBT-6BT (a), NBT-6BT-0.1Mg (b), NBT-6BT-0.3Mg (c), NBT-6BT-0.5Mg (d), NBT-6BT-0.1Zn (e), NBT-6BT-0.3Zn (f), NBT-6BT-0.5Zn (g), and NBT-6BT-1Zn (h).

The complete XRD-profiles of unpoled NBT-6BT and NBT-6BT with Mg doping are displayed in Figure 33a (obtained from crushed and annealed powder with laboratory X-ray diffraction: 4.6.2). In addition, the XRD-profile of NBT-6BT-0.5Zn is depicted as reference material. Figure 33b presents the reflections 111_{pc} and 200_{pc} with measured (black) and calculated (red) XRD profiles (detailed Rietveld-refinement information is provided in Table S5). All compositions have a perovskite structure with tetragonal *P*4*mm* and cubic *Pm*$\bar{3}$*m* crystal structure (Table 6). The rhombohedral phase fraction *R*3*c* decreases with increasing Mg doping concentration from 16.6% in pure NBT-6BT to 0% in NBT-6BT-0.5Mg. Similarly, the cubic phase fraction decreases from 58.9% in NBT-6BT to 38.9% in NBT-6BT-0.5Mg. The tetragonal phase fraction, on the other hand, increases with increasing doping concentration from 24.5% in NBT-6BT to 61.1% in NBT-6BT-0.5Mg. The tetragonality also increases with Mg doping.

Next, the results from unpoled powder are contrasted with phase fractions and lattice distortions obtained from poled bulk ceramics, measured in synchrotron; see Table 6 (measured at DESY, see Subchapter 4.6.3). This comparison must be handled with care, since bulk ceramics are compared to ceramic powder. The higher surface-to-bulk ratio of the powder might influence the structure, as pointed out by Kong et al. [229]. No cubic phase fraction is present in the poled ceramics. In comparison with NBT-6BT, the acceptor-doped compositions maintain the higher tetragonal phase fraction when poled. In the unpoled state, the *P*4*mm* phase is the dominant phase in the doped compositions, while in the poled state, the rhombohedral *R*3*c* phase is dominant in all compositions. The minor difference in phase fractions obtained for NBT-6BT-0.5Mg and NBT-6BT-0.5Zn in the unpoled state is not present in the poled state. Moreover, the tetragonal distortion in the poled state is the same for all investigated compositions.

Overall, the same trends are observed for the Mg-doped and the Zn-doped NBT-6BT (Table 6): In the unpoled state, the same doping concentration leads to a larger non-cubic phase fraction in the Mg-doped NBT-6BT in comparison to Zn-doped NBT-6BT. Structurally and microstructurally, Mg-doped NBT-6BT and Zn-doped NBT-6BT are similar. Both lead to an increase in grain size, non-cubic phase fraction, and tetragonality (unpoled state). In the poled state, both compositions are also structurally identical.

The increase in the tetragonality of unpoled samples correlates with an increase in the depolarization temperature T_d. This correlation was established by Luo et al. [143] and is discussed in Subchapter 5.1.1. Notably, this correlation cannot be adapted to the poled state since undoped NBT-6BT and Mg- and Zn-doped NBT-6BT have the same tetragonality. However, the higher tetragonal phase fraction in the unpoled state reveals a higher stability when doped with Mg or Zn. The exact depolarization temperatures are listed in Table 7. Additionally, the transition temperature from the ferroelectric to the relaxor state $T_{F\text{-}R}$ was determined from permittivity measurements against temperature. In some cases, T_d and $T_{F\text{-}R}$ differ since thermal fluctuations can lead to a randomization of the domain orientation already in the ferroelectric state. This would lead to a depolarization before the transition to the relaxor state.[237] The higher T_d in comparison to $T_{F\text{-}R}$ in the NBT-6BT cannot be explained.

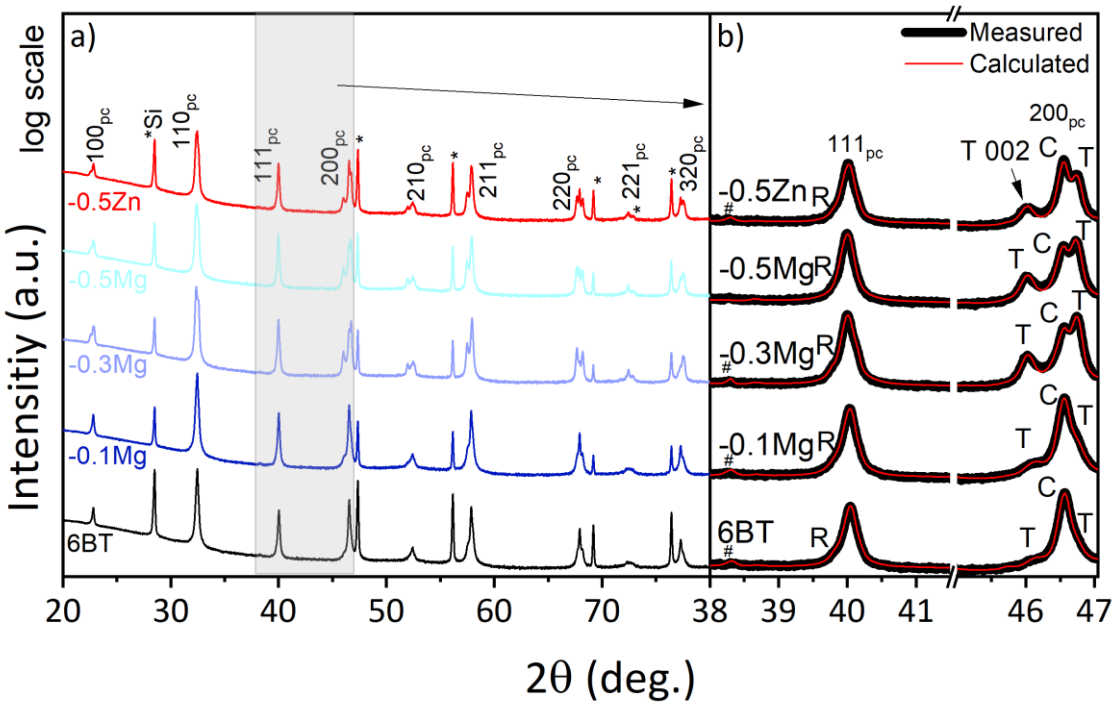

Figure 33: (a) X-ray diffraction profile, from 20° to 80°, of NBT-6BT, both undoped and doped with 0.1, 0.3, and 0.5 mol% Mg and 0.5 mol% Zn. The silicon standard is marked by *Si. (b) 111_{pc} and 200_{pc} reflections (originating from the pseudocubic $\{111\}_{pc}$ and $\{200\}_{pc}$ planes) representing the rhombohedral R and tetragonal distortion T. The cubic peak is marked with C, and the superlattice reflections of the *R*3*c* structure are marked by a hashtag #.

The polarization and strain response under a large electric field are illustrated in Figure 34. The Mg-doped samples were measured up to a field of 7 kV/mm. NBT-6BT and NBT-6BT-0.5Zn were measured up to 6 kV/mm since at a higher field, they experienced electrical breakdown. The poling field E_{pol} and the coercive field E_c increase with doping concentration and are lower in the Zn-doped composition in comparison to the Mg-doped composition for the same doping concentration. NBT-6BT-0.5Mg has the highest E_c: 4.8 kV/mm, which is 1.5 kV/mm higher than in pure NBT-6BT (Figure 35a and Table 7). An increase in E_c is usually correlated with ferroelectric hardening.[9] The remanent polarization P_{rem} is approximately the same in all doped compositions except for NBT-6BT-0.5Mg and NBT-6BT-1Zn, which have a higher P_{rem}. The first loop of the strain (Figure 34a) reveals a poling-induced offset of the butterfly-shaped strain loop in all samples.

Table 6: Phase fractions and tetragonal and rhombohedral lattice distortion (δ_T, δ_R) of unpoled and poled NBT-6BT with Mg and Zn doping. X-ray diffraction patterns and detailed refinement information of the poled samples are provided in Figure S3 and Table S5, respectively.[X] The error given by Topas is in the range of ±2% for the phase fraction and below the given digits in the lattice distortion.

Composition - unpoled -	*Pm*$\bar{3}$*m* (%)	*P*4*mm* (%)	*R*3*c* (%)	δ_T	δ_R
NBT-6BT	58.9	24.5	16.6	0.0117	0.0077
-0.1Mg	52.5	32.8	14.7	0.0122	0.0076
-0.3Mg	32.3	61.7	6	0.0146	0.0086
-0.5Mg	38.9	61.1	-	0.0145	-
-0.5Zn	40.6	47.4	12.0	0.0147	0.0077
- Poled -					
NBT-6BT	-	16	84	0.0144	-
-0.5Mg	-	26	74	0.0145	-
-0.5Zn	-	25	75	0.0142	-

This is a typical behavior for non-ergodic relaxors due to the field-induced phase transition from the non-ergodic to the ferroelectric phase. After the first poling process, all samples have a butterfly-shaped strain loop, thus indicating ferroelectric behavior. Especially the Mg-doped compositions exhibit a small poling strain S_{pol} (Figure 35b and Table S4). A lower S_{pol} can be caused by a smaller phase transformation strain from the relaxor to the ferroelectric phase. The total poling strain is a mixture of phase transformation strain and domain switching strain.[132] The negative strain S_{neg} (Figure 35b and Table S4) also decreases with Mg doping concentration. Furthermore, S_{neg} correlates with the domain switching strain; hence, the larger irreversible strain (difference in: negative strain to zero strain in the first loop) should be caused by the lower domain switching strain. The total strain response is lower when NBT-6BT is doped with Mg or Zn. This is not only observed in the third strain loop (Figure 34b) but also evidenced by decreasing piezoelectric coefficients d_{33} and d_{33}^* (Table 7). In summary, the stabilization of the ferroelectric phase by acceptor-doping, observed by Rietveld-refinement, is reflected in the electromechanical large-signal properties. It also ferroelectrically hardens the materials and hence leads to a lower strain response. The correlation between ferroelectric

[X] The poled samples were investigated and refined in collaboration with Andreas Wohninsland.

hardening and reduced strain response is reflected in Figure 35a. The coercive field and d_{33} demonstrate an opposite trend.

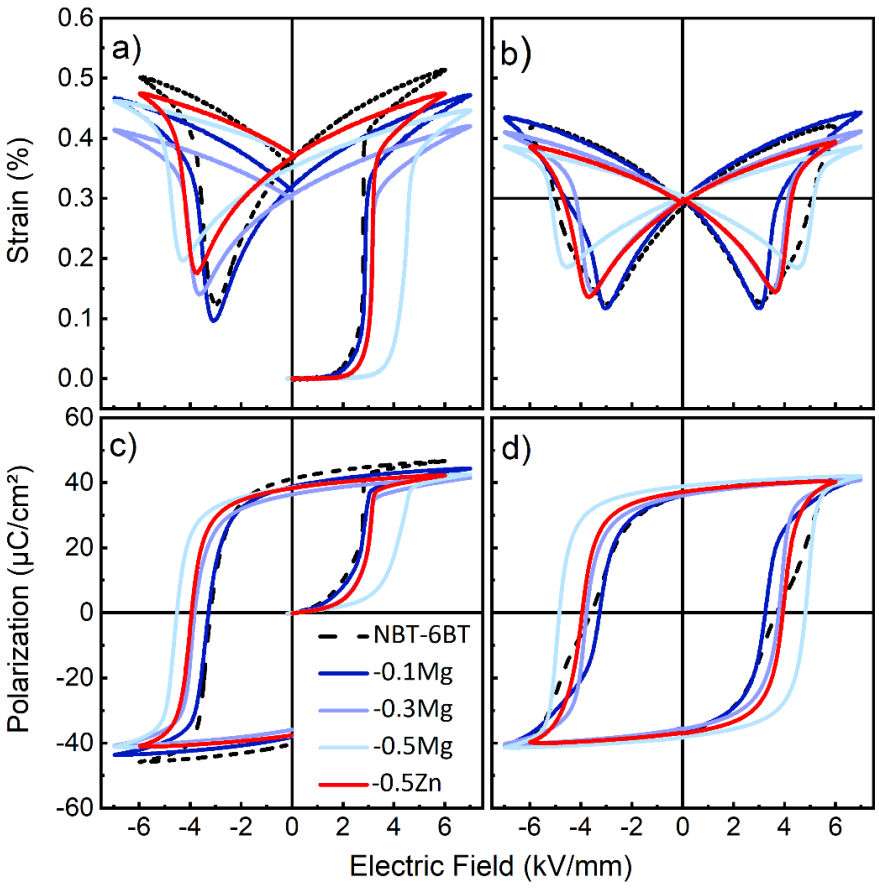

Figure 34: Strain and polarization against the electric field of NBT-6BT doped with 0.1, 0.3, and 0.5 mol% Mg and 0.5 mol% Zn. a) and c) Display the first loop, while b) and d) display the third loop.

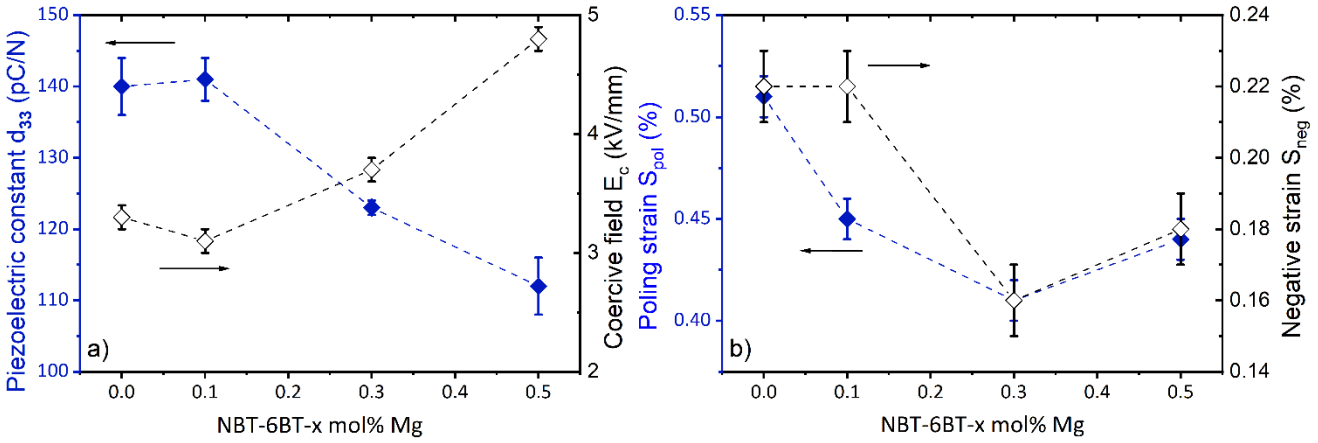

Figure 35: a) Piezoelectric constant d_{33} (blue) and coercive field E_c (black, hollow) against Mg doping concentration in NBT-6BT. b) Poling strain S_{pol} (blue) and negative strain S_{neg} (black, hollow) against Mg doping concentration in NBT-6BT.

Table 7: Electromechanical properties of Mg- and Zn-doped NBT-6BT. T_{F-R} = transition temperature from ferroelectric to relaxor state determined by temperature-dependent permittivity (Figure S4 and Figure S5), T_d = depolarization temperature (determined by thermally stimulated depolarization current; Figure S6), d_{33}/d_{33}^* = small-/large-signal piezoelectric coefficient, E_c = coercive field, E_{pol} = poling field, and P_{rem} = remanent polarization.

Composition	T_{F-R} (°C)	T_d (°C)	d_{33} (pC/N)	d^*_{33} (pm/V)	E_c (kV/mm)	E_{pol} (kV/mm)	P_{rem} (μC/cm²)
NBT-6BT	102	111	140 ± 4	226 ± 8	3.3 ± 0.1	2.8	35.7 ± 0.7
-0.1Mg	120	121	141 ± 3	213 ± 4	3.1 ± 0.1	2.9	37.1 ± 1.2
-0.3Mg	146	149	123 ± 1	163 ± 2	3.7 ± 0.1	3.1	35.7 ± 0.6
-0.5Mg	146	148	112 ± 4	122 ± 2	4.8 ± 0.1	4.4	39.3 ± 0.9
-0.1Zn	111	105	130 ± 4	217 ± 18	3.3 ± 0.1	2.6	36.1± 0.8
-0.3Zn	140	139	124 ± 3	210 ± 4	3.4 ± 0.1	2.4	36.3 ± 0.6
-0.5Zn	146	142	117 ± 3	166 ± 2	4.1 ± 0.1	3.2	36.7 ± 0.6
-1Zn	149	147	113 ± 3	142 ± 3	4.5 ± 0.1	3.8	42.3 ± 0.6

Figure 36 reveals the mechanical quality factor in planar mode Q_m^p up to a vibration velocity of 2 m/s. Q_m^p is highly stable with increasing vibration velocity. The stability stems from very low and stable extrinsic contributions to the strain.[114] NBT-6BT-0.1Mg experiences only a minor change in Q_m^p compared with pure NBT-6BT. By contrast, a significant increase in Q_m^p is observed with increasing Mg doping concentration up to a value of 826 for NBT-6BT-0.5Mg. It

is the highest value known for the NBT-xBT system in polycrystalline samples. The same doping concentration of Zn also increases Q_m^p by several times. However, Mg doping is more effective at reducing the mechanical loss than Zn doping, although the reason for this difference is unknown. The very high and stable Q_m^p makes Mg-doped NBT-xBT an ideal candidate for high-power applications. In comparison, PZT materials have an even higher Q_m^p but experience a sharp drop of approximately 75% at 0.8 m/s, for example (also see Figure 50b).[238] NBT-6BT-0.5Mg still has a Q_m of almost 800 at 2 m/s (Table 8). Despite the drop in d_{33} with Mg and Zn doping, the coupling coefficients k_p in planar mode, as well as k_t in thickness mode, remain almost the same or even slightly increase in NBT-6BT-0.5Zn. The coupling coefficient and the mechanical quality factor are both important variables when considering Equation (12) for the vibration velocity.

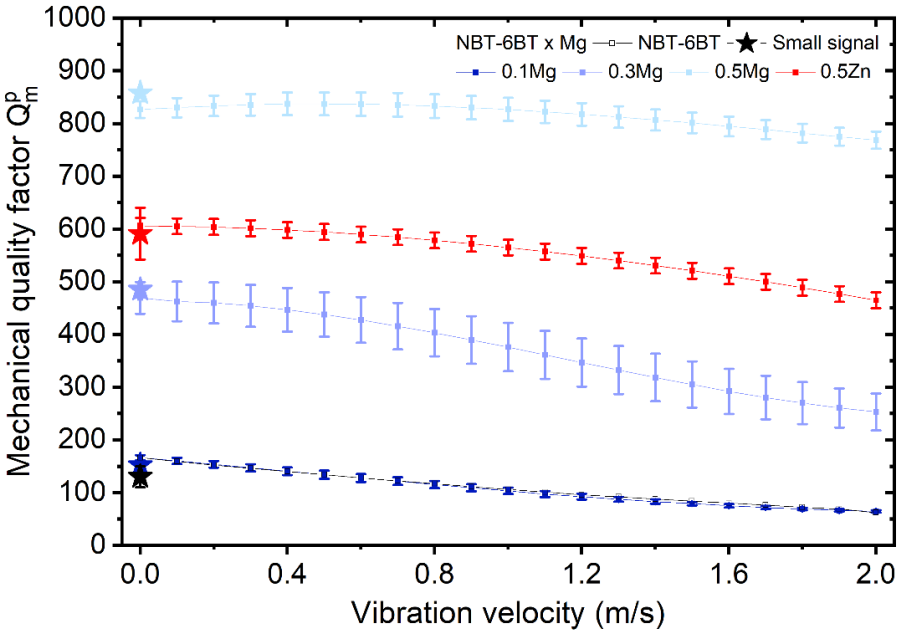

Figure 36: Mechanical quality factor Q_m^p in planar mode as a function of vibration velocity *v* for NBT-6BT and NBT-6BT doped with 0.1, 0.3, and 0.5 mol% Mg and 0.5 mol% Zn. Stars represent Q_m^p at *v* = 0 obtained by small-signal resonance measurements.

Table 8: Coupling coefficient k_p in planar mode and k_t in thickness mode obtained by small-signal resonance measurements. And mechanical quality factor at v = 0 and 2 m/s.

Composition	k_p	Q_m^p (v = 0 m/s)	Q_m^p (v = 2 m/s)	k_t
NBT-6BT	0.32 ± 0.02	119 ± 11	65 ± 4	0.51 ± 0.002
-0.1 Mg	0.34 ± 0.01	166 ± 5	64 ± 2	0.47 ± 0.005
-0.3 Mg	0.32 ± 0.01	469 ± 30	253 ± 35	0.48 ± 0.008
-0.5 Mg	0.29 ± 0.01	826 ± 16	768 ± 17	0.5 ± 0.012
-0.5 Zn	0.3 ± 0.01	590 ± 49	460 ± 14	0.54 ± 0.001

Although ferroelectric hardening is noticeable in the Mg- and Zn-doped NBT-6BT, the mechanism responsible for it has not yet been clarified in the literature. Usually, the hardening mechanism known from PZT and BT is used for all other piezoelectric materials too. In the following, the suitability of this mechanism for NBT-xBT is discussed. In PZT and BT, acceptor dopants on the B-site lead to oxygen vacancies to maintain charge neutrality.[9] The B-site defect and the oxygen vacancy result in defect complexes in the form of defect dipoles, which align according to their surrounding polarization and stress field. Since this alignment is diffusion based, it is a time- and temperature-dependent process. It will stabilize the surrounding polarization hence domain configuration. Domain walls are clamped and hindered from movement. This results in lower losses and hence a higher Q_m.[73] At the same time, the higher oxygen vacancy concentration leads to higher conductivity.[239]

Figure 37 illustrates the bulk conductivity[XI] σ of NBT-6BT with Mg and Zn doping. Pure NBT-6BT and a 0.1 mol% acceptor concentration have a low conductivity. A higher doping concentration leads to a rise in conductivity by approximately three orders of magnitude. This change in σ is explained by the change in association energy of the defect couple between the B-site dopant and oxygen vacancy.[240] The association strongly correlates with the distance between B-site defects. With an increasing doping concentration, the association energy decreases. Similarly, the activation energy for oxygen vacancy migration is lower at a high doping concentration: It is in the range of 0.42-0.68 eV in the low-conductive compositions and 0.11-0.21 eV in the high-conductive compositions. Notably, the concentration of defect dipoles should be very low in compositions with increased conductivity—that is, NBT-6BT with 0.3-1 mol% Mg or Zn. By contrast, in PZT, the existence of defect dipoles is not questioned. The

[XI] DC conductivity: extracted from fitting frequency dependent AC resistance in the Nyquist plots

alignment process and the number of defect dipoles change with acceptor-doping concentration in PZT.

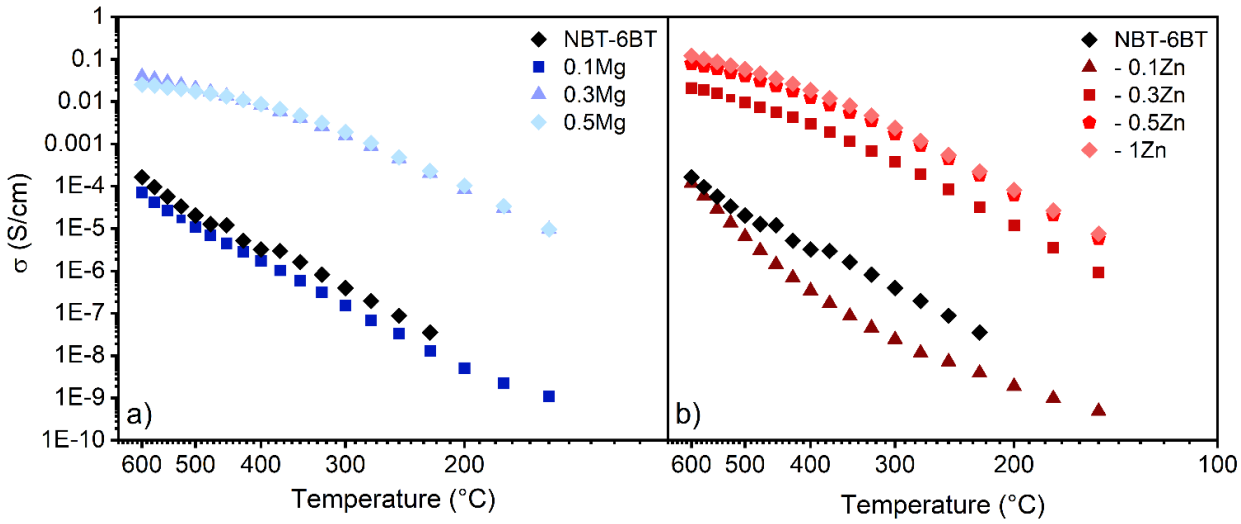

Figure 37: Arrhenius-type plots obtained by impedance spectroscopy. The bulk conductivity is given for pure NBT-6BT and NBT-6BT doped with 0.1, 0.3, and 0.5 mol% Mg and Zn as well as 1 mol% Zn.

When the room temperature bulk conductivity σ[XII] and Q_m are plotted next to each other against the acceptor-doping concentration, a similar trend becomes apparent (Figure 38). A low Mg and Zn doping concentration (0.1 mol%) does not change σ, and Q_m remains almost the same as in pure NBT-6BT. A higher doping concentration (0.3-1 mol%) leads to an increase in σ, and Q_m increases non-linearly. The simultaneous increase in σ and Q_m suggests that the defect dipoles of $Mg''_{Ti} - V_O^{\circ\circ}$ do not play a major role in ferroelectric hardening in NBT-xBT since the hardening effect occurs at the doping concentration when defect dipoles are less likely to form. It implies the importance of the mobility of the oxygen defects. The described behavior is true for two different acceptor dopants in NBT-xBT, implying a universal underlying mechanism. Although the defect complexes of acceptor dopants and oxygen vacancies are unlikely to contribute to ferroelectric hardening in the same manner as in PZT or BT, point defects can accumulate at domain walls or grain boundaries and harden the material.[80] The hardening could further be related to the modulated relaxor state and the phase transformation during the poling process or to different types of defect complexes.

[XII] Extrapolated from Arrhenius-type plots

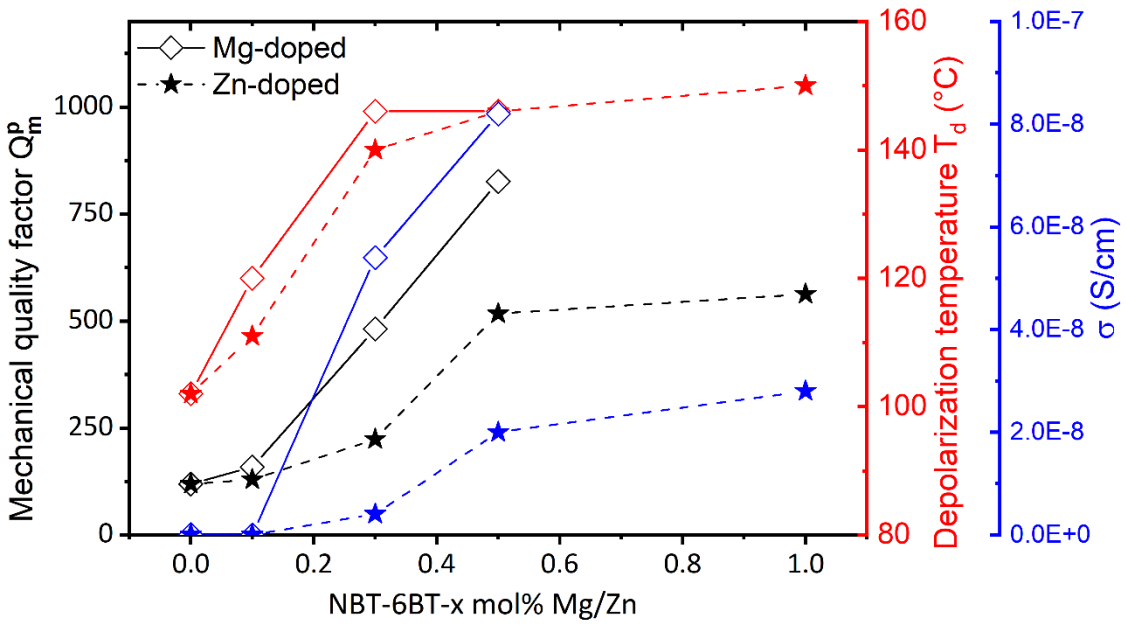

Figure 38: Mechanical quality factor Q_m^p in planar mode (black), depolarization temperature T_d (red), and bulk conductivity σ at RT (blue) of NBT-6BT doped with Mg (rectangular, solid line) in comparison with NBT-6BT doped with Zn (star, dotted).

The aging behavior was investigated to further confirm the difference in the hardening mechanism of PZT/BT and NBT-xBT. Aging is a time- and temperature-dependent process in which ferroelectric properties change under constant boundary conditions, such as temperature or electric field. One character that can change due to the aging process is Q_m. Therefore, the room temperature Q_m of NBT-6BT doped with Mg was measured directly after poling[XIII] and again after 5 days of annealing at 100 °C.[XIV] On the one hand, Q_m remained the same, verifying that either no aging process occurred at all or that a rapid aging process took place already during the poling process. On the other hand, d_{33} decreased during the aging process (Figure S7). Normally, ferroelectric hardening is related to a simultaneous increase in Q_m and a decrease in d_{33}.[239, 241] A separate effect on both properties further confirms that the ferroelectric hardening mechanism in NBT-xBT differs from the known mechanism in PZT and BT. It is suggested that the decrease in d_{33} correlates with the reduction of intrinsic polarization in the *R*3*c* phase below the depolarization temperature. This phenomenon was observed by Adhikary et al. [129] and is described as a transition temperature from *R*3*c* to *P*4*bm* at around 70 °C in NBT-6BT.

[XIII] The usual poling conditions were used.

[XIV] 100 °C was chosen as the aging temperature to speed up the aging process. 100 °C is still below the depolarization temperature.

Defect complexes can be detected by electron paramagnetic resonance (EPR) spectroscopy.[242] Unpaired electrons in an atom are a necessity for detection with EPR. Neither Mg^{2+} nor Zn^{2+} fulfill this requirement and are not EPR active. Thus, the use of Cu^{2+} or Al^{3+} as an acceptor dopant is suggested in future studies to investigate defect dipoles via EPR. Sapper et al. [151] examined the formation of defect complexes and the aging behavior in Fe-doped NBT-1BT, NBT-4BT, NBT-6BT, and NBT-15BT. Their EPR studies reported the formation of defect complexes only in predominantly tetragonal NBT-15BT. Additionally, aging was most pronounced in NBT-15BT.

Contrasts between the most important electromechanical properties for high-power applications (Figure 39) reveal that acceptor-doped NBT-6BT is superior to pure NBT-6BT. Apart from a lower d_{33}, all other depicted properties are in the same range or higher when doped with Mg or Zn. In literature, Zn-doped NBT-xBT is treated as an ideal candidate to replace PZT in high-power applications, and Mg-doped NBT-xBT seems to be an even better candidate because of its higher Q_m. The reason for the higher Q_m by Mg doping is not clear, as the charge and the ionic radii of Mg^{2+} and Zn^{2+} are similar. Several factors are suggested as the cause for such a difference in Q_m: First, the magnitude of the dipole moment might affect the stabilization of the surrounding polarization. The higher electronegativity of Zn results in a more covalent bond and hence a lower dipole moment compared with Mg.[243] Moreover, the higher ionic polarizability of Zn^{2+} compared with Mg^{2+} results in a smaller dipole moment (the center of charge of two ions becomes closer with higher polarizability).[244] Second, the different defect energy levels of Zn^{2+} and Mg^{2+} could impact the charge compensation mechanism, resulting in, for example, differing numbers of oxygen vacancies at the same doping concentration.

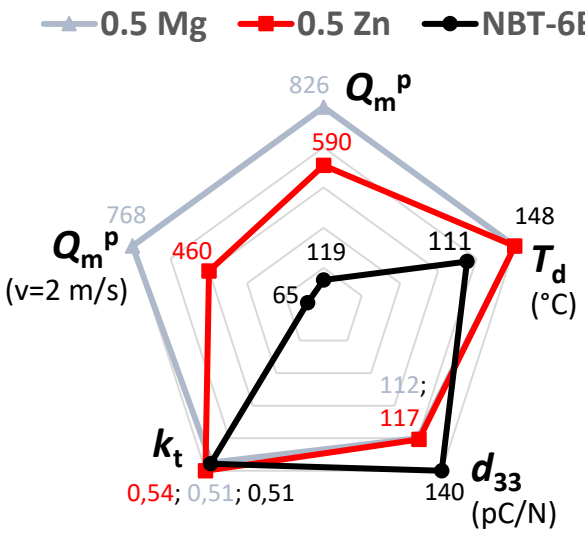

Figure 39: Comparison of pure NBT-6BT (black) and NBT-6BT doped with 0.5 mol% Mg (blue) and Zn (red). Electromechanical properties that are of high importance for high-power applications are depicted, such as the mechanical quality factor at 0 m/s and 2 m/s, the depolarization temperature T_d, the piezoelectric constant d_{33}, and the coupling factor in thickness mode k_t.

5.1.3 NBT-6BT: Non-stoichiometry and Zn Doping

In this chapter the influence of A-site stoichiometry on the crystal structure and electromechanical properties of Zn-doped NBT-6BT is investigated by changing the Bi-stoichiometry. This change allows for some statements to be made regarding the role of oxygen vacancies and B-site acceptor dopants in this material.

NBT-6BT was doped with 0.5 and 1 mol% Zn. Both compositions were produced with 1 mol% Bi deficiency and 1 mol% Bi excess in addition to the stoichiometric composition. The density of all samples was determined to be 93.8% or higher. No secondary phases were observed by XRD (Figure 40a). The used lab-XRD has a low signal-to-noise ratio and consists of $K_{\alpha1}$ and $K_{\alpha2}$ radiation. This increases the difficulty and reduces the reliability of a Rietveld refinement. Nevertheless, some qualitative statements can be made from the raw XRD patterns. Figure 40b compares the 111_{pc} and 200_{pc} reflections of NBT-6BT doped with 0.5 and 1 mol% Zn with Bi excess, Bi deficiency, and stoichiometric Bi. The split of the 200_{pc} reflection into a 200 and 002 peak is evident for NBT-6BT-0.5Zn and -1Zn. This confirms the increased tetragonal phase fraction described in the previous chapters. The same peak splitting is also present with Bi deficiency. However, it is less pronounced with Bi excess, thus indicating a lower tetragonal phase fraction. The 111_{pc} reflection is similar for all compositions. Apart from that, no

quantitative and qualitative statements can be made about the rhombohedral or cubic crystal structure based on the XRD patterns from Figure 40.

The number of B-site acceptor dopants is the same regardless of the Bi-stoichiometry. Hence, it is believed that acceptor-doping and Bi-stoichiometry indirectly influence the crystal structure by tailoring the oxygen vacancy concentration. A considerable amount of Bi evaporates during the processing steps (calcination or sintering) leading to oxygen vacancies to maintain charge neutrality (25).[142, 245]

$$2Bi_{Bi}^{X} + 3O_{O}^{X} \rightarrow 2V_{Bi}^{'''} + 3V_{O}^{\circ\circ} + Bi_2O_3\ (\uparrow). \qquad (25)$$

Bi excess, by contrast, can reduce the oxygen vacancy concentration either because less Bi evaporates during sintering or Bi partly substitutes Na or Ba. In NB_{51}T-6BT-0.5Zn and -1Zn, the creation of oxygen vacancies by Zn doping and the compensation of oxygen vacancies by Bi excess are competing. Structurally, Bi excess could compensate for the creation of oxygen vacancies and lead to a similar crystal structure to that in undoped, stoichiometric NBT-6BT.

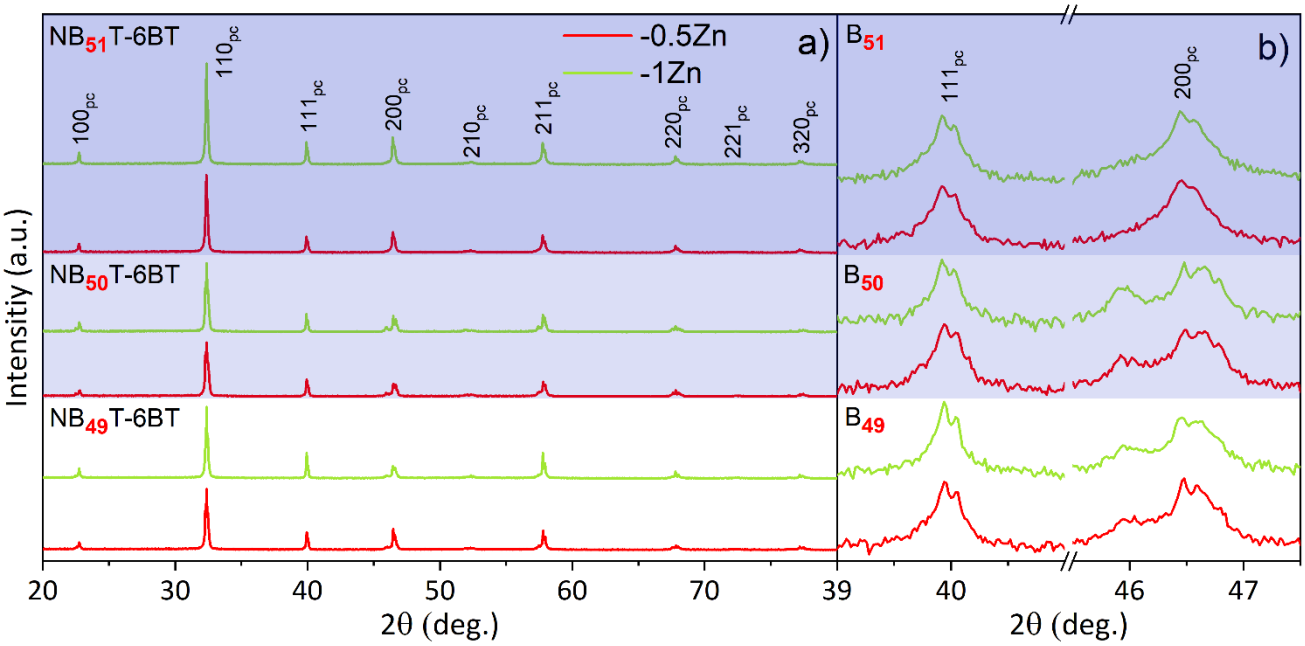

Figure 40: X-ray diffraction patterns of NBT-6BT doped with 0.5 and 1 mol% Zn with Bi excess (B_{51}), Bi deficiency (B_{49}), and stoichiometric Bi (B_{50}). a) Full XRD pattern. b) 111_{pc} and 200_{pc} reflections.

NB_{49}T-6BT-1Zn is excluded from the discussion since it showed leaky behavior in the P-E loop measurements and was not possible to pole. Figure 41 compares the polarization and strain against the electric field of pure NBT-6BT and non-stoichiometric, Zn-doped NBT-6BT. The

poling strain S_{pol} (Figure 41a) is lower in all non-stoichiometric compositions than in pure NBT-6BT. The lower poling strain is either based on a lower phase transformation strain or lower domain switching strain. The phase transformation strain correlates with the offset strain after the first loop (Figure 6). No clear overall trend is present with changing Bi-stoichiometry (Figure 41a). However, Bi excess leads to a lower offset strain, suggesting a lower phase transformation strain in these compositions. Additionally, the third strain loop (Figure 41b) reveals a similar positive strain of NBT-6BT and NB_{51}T-6BT, indicating comparable domain switching strains. The third loop is butterfly shaped for all compositions apart from NB_{51}T-6BT-0.5Zn. It shows less negative strain, which is characteristic for partly ergodic-relaxor behavior. The ergodic-relaxor behavior is confirmed by a tilted polarization loop with much lower remanent polarization P_{rem}. Bi excess decreases P_{rem}, but Bi deficiency does not alter P_{rem}, see Figure 42b.

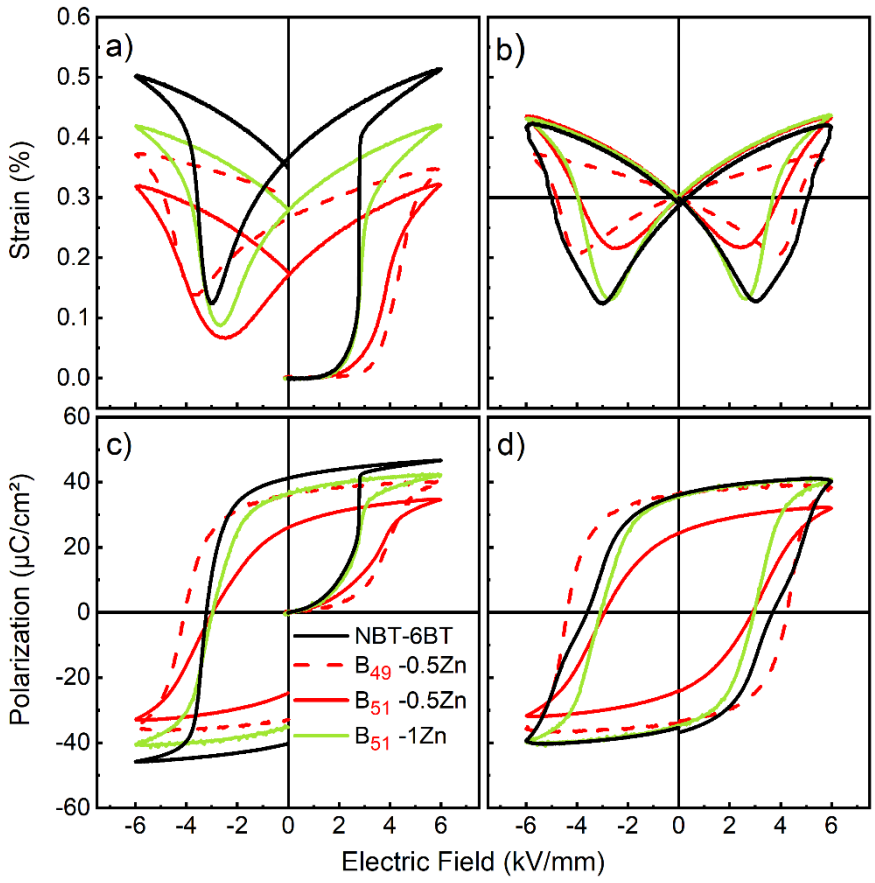

Figure 41: Strain and polarization against the electric field of NBT-6BT, NB_{49}T-6BT-0.5Zn, NB_{51}T-6BT-0.5Zn, and NB_{51}T-6BT-1Zn. a) and c) Display the first loop while, b) and d) display the third loop.

NB_{49}T-6BT-0.5Zn has a moderate strain response (third strain loop; Figure 41b) but a higher coercive field E_c (third P-E loop, Figure 41d), indicating ferroelectric hardening in this composition. A comparison with pure NBT-6BT reveals a two-step switching process in the NBT-6BT. Sapper also observed this process from 50 °C and higher.[246] A partly ergodic material can cause such discontinuity in polarization under field.

Figure 42c illustrates a dependency of E_c not only on the Zn doping concentration but also on the Bi-stoichiometry. Bi excess reduces E_c whereas Bi deficiency increases E_c. The opposite trend is present in the large-signal piezoelectric coefficient d_{33}^*. An increasing Bi amount strongly increases d_{33}^* and can tailor it to a comparable magnitude, like Zn doping. Although E_c and d_{33}^* show the opposite trend, it cannot be correlated qualitatively. For example, the composition with the lowest d_{33}^* is not the one with the highest E_c, and the composition with Bi excess has the lowest E_c but not the highest d_{33}^*. The small-signal d_{33} suggests the same trend as in d_{33}^*. An exception is NB_{51}T-6BT-0.5Zn, which has a lower d_{33} than NBT-6BT, probably due to its partial ergodicity.

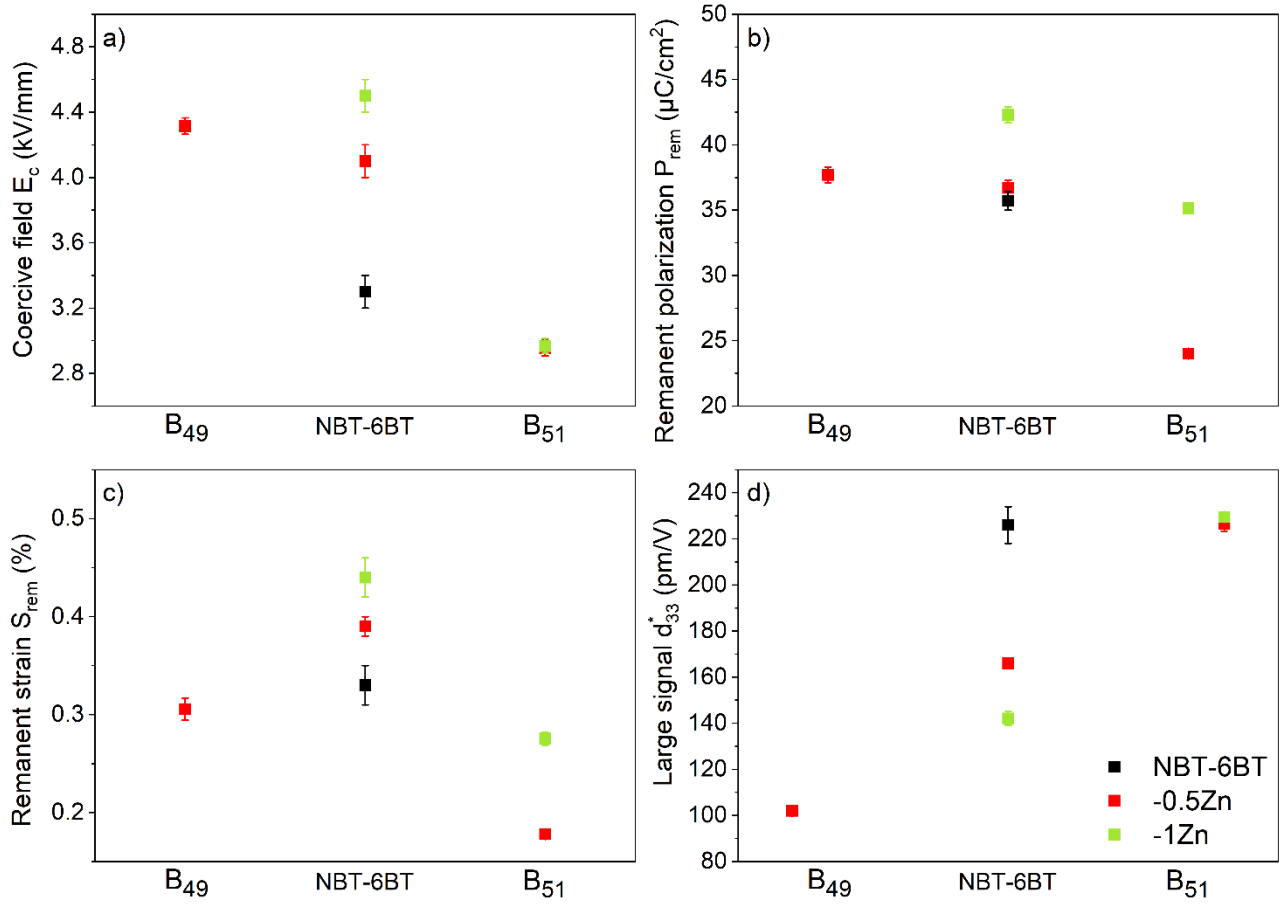

Figure 42: Large-signal electromechanical properties obtained from polarization and strain measurements against the electrical field of NBT-6BT doped with 0.5 and 1 mol% Zn and Bi deficiency (B_{49}) and Bi excess (B_{51}). a) Coercive field E_c. b) Remanent polarization P_{rem}. c) Remanent strain S_{rem}. d) Large-signal piezoelectric coefficient d^*_{33}.

From an application point of view the mechanical quality factor Q_m and transition temperature $T_{F\text{-}R}$ are very interesting (Figure 43a, Table 9). The mechanical quality factor in planar mode (Q_m^p) strongly depends on the Bi amount and Zn doping concentration. Bi deficiency can further increase the already high Q_m of NBT-6BT-0.5Zn to a value of 734. By contrast, Bi excess eliminates the effect of Zn doping on Q_m completely. The Bi-stoichiometry does not tailor the defects on the B-site but rather the oxygen vacancy concentration. Nevertheless, it has a significant impact on Q_m, thus revealing the importance of oxygen vacancies in the ferroelectric hardening process. Seo et al. [142] investigated different A-site stoichiometry in NBT-6BT. They found that E_c does not change considerably with the Bi amount when changed in the range of ±1 mol%. This finding emphasizes that a change in oxygen vacancies alone has no effect on ferroelectric hardness. In summary, it is unlikely that B-site acceptor dopants alone or oxygen vacancies alone are responsible for ferroelectric hardening in NBT-xBT. Rather, the concurrent

presence of both is necessary to observe evidence of ferroelectric hardening. From the previous investigation on Mg- and Zn-doped NBT-6BT, it is suggested that the classical defect dipole is not the main mechanism of ferroelectric hardening. Further investigation is required to determine whether the accumulation of defects at the domain wall or grain boundary is responsible for ferroelectric hardening in NBT-xBT.

Bi deficiency does not affect $T_{F\text{-}R}$ any further, whereas Bi excess decreases $T_{F\text{-}R}$ close to the undoped NBT-6BT. It has been observed that $T_{F\text{-}R}$ is proportional to the lattice distortion.[143] This correlates with the qualitative changes observed in the crystal structure: First, increasing the oxygen vacancy concentration by Bi deficiency does not alter the crystal structure additionally to Zn doping. Second, Bi excess decreases the oxygen vacancy concentration and counteracts the increased tetragonal phase fraction and tetragonality induced by Zn doping. To recap, the lattice distortion caused by oxygen vacancies appears to be limited and will not further increase or lead to a higher $T_{F\text{-}R}$ from a certain threshold, which is in the range of 150 °C in NBT-6BT. Reducing the oxygen vacancy concentration, however, will reduce the lattice distortion and hence $T_{F\text{-}R}$, independently of what causes the oxygen vacancies in the first place. This is supported by Seo et al. [142], who found a strong dependency between $T_{F\text{-}R}$ and Bi-stoichiometry in undoped NBT-6BT.

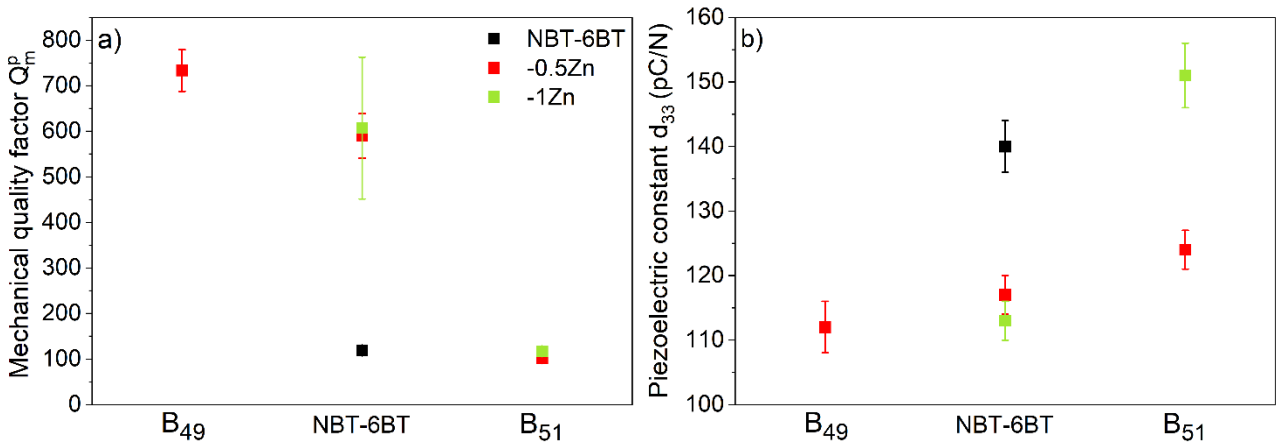

Figure 43: (a) Mechanical quality factor Q_m^p in planar mode and (b) piezoelectric constant d_{33} of NBT-6BT doped with 0.5 and 1 mol% Zn and Bi deficiency (B_{49}) and Bi excess (B_{51}).

Table 9: Overview of electromechanical properties of NBT-6BT doped with 0.5 and 1 mol% Zn and Bi deficiency (B_{49}) and Bi excess (B_{51}). T_{F-R} = transition temperature from ferroelectric to relaxor state determined by temperature-dependent permittivity (Figure S8), d_{33} = small-signal piezoelectric constant, d_{33}^* = large-signal piezoelectric constant, Q_m^p = mechanical quality factor in planar mode, E_c = coercive field, P_{rem} = remanent polarization, and S_{rem} = remanent strain.

Composition	T_{F-R} (°C)	d_{33} (pC/N)	Q_m^p (v = 0 m/s)	d_{33}^* (pm/V)	E_c (kV/mm)	P_{rem} (µC/cm²)	S_{rem} (%)
NBT-6BT	102	140 ± 4	119 ± 11	226 ± 8	3.3 ± 0.1	35.7 ± 0.7	0.33 ± 0.02
NB_{49}T-6BT-0.5Zn	144	112 ± 4	734 ± 46	102 ± 2	4.3 ± 0.1	37.7 ± 0.6	0.31 ± 0.01
NB_{50}T-6BT-0.5Zn	146	117 ± 3	590 ± 49	166 ± 2	4.1 ± 0.1	36.7 ± 0.6	0.39 ± 0.1
NB_{51}T-6BT-0.5Zn	93	117 ± 3	102 ± 2	227 ± 3	3 ± 0.05	24 ± 0.4	0.18 ± 0.01
NB_{50}T-6BT-1Zn	149	113 ± 3	607 ± 156	142 ± 3	4.5 ± 0.1	42.3 ± 0.6	0.44 ± 0.02
NB_{51}T-6BT-1Zn	105	151 ± 5	117 ± 1	230 ± 2	3 ± 0.05	35.1 ± 0.2	0.28 ± 0.01

5.2 NBT-6BT:xZnO Composite

The composite of NBT-xBT with the ZnO secondary phase has already been widely investigated in the literature.[82, 85, 86, 188] Here, the picture is extended by the investigation of compositions with a lower ZnO amount.[XV] The properties are close to the expectations from the literature and show a minor dependency on the secondary phase amount.

Composites with 0.025, 0.05, 0.075, and 0.1 mole ratio ZnO, equivalent to approximately 1, 2, 3, and 3.9 Vol% ZnO, were investigated. For comparison, the lowest amount in the literature is 0.1 mole ratio ZnO.[85, 188] The sintered samples have densities of 94.5% or higher. The grain size was determined from the microstructure, taken with SEM (Figure 44). Interestingly, the grain size in the composites is slightly higher than in pure NBT-6BT with 1.7 ± 0.8 µm but does not depend on the ZnO amount. The grain size varies from 3.6 ± 1.4 µm in NBT-6BT:0.1ZnO to 4.4 ± 2.1 µm in NBT-6BT:0.025ZnO. Two factors might have influenced the grain size of the composites. First, the coarsening step could have resulted in a larger particle size, although a milling step followed the coarsening. Second, the larger grain size might have originated from

[XV] In this work, composites with other secondary phases such as Al_2O_3 and Yttria-stabilized ZrO_2 were synthesized. They are not included in this work, but results can be provided to the interested reader, if requested.

a partial Zn incorporation into the matrix lattice and hence an increased oxygen vacancy concentration. Indeed, Zn incorporation was noticed by Fan et al. [86].

The microstructure of thermally etched NBT-6BT:xZnO (x = 0.025, 0.05, 0.075, and 0.1) is depicted in Figure 44a–d (measured in secondary electron mode [SE]). Figure 44e–f depicts the microstructures of NBT-6BT:0.025ZnO and NBT-6BT:0.1ZnO in the backscattering mode (BSE). The ZnO secondary phase can be identified as dark isolated grains within a bright matrix. The number of ZnO particles increases as the ZnO amount increases. Moreover, the size seems to increase with an increasing ZnO amount. ZnO is distributed equally and is present in the grains as well as at the grain boundaries. Some studies have reported ZnO particles predominantly at the grain boundaries, whereas others have reported them in the grains as well. The position of the ZnO secondary phase has no influence on the properties. [85, 188]

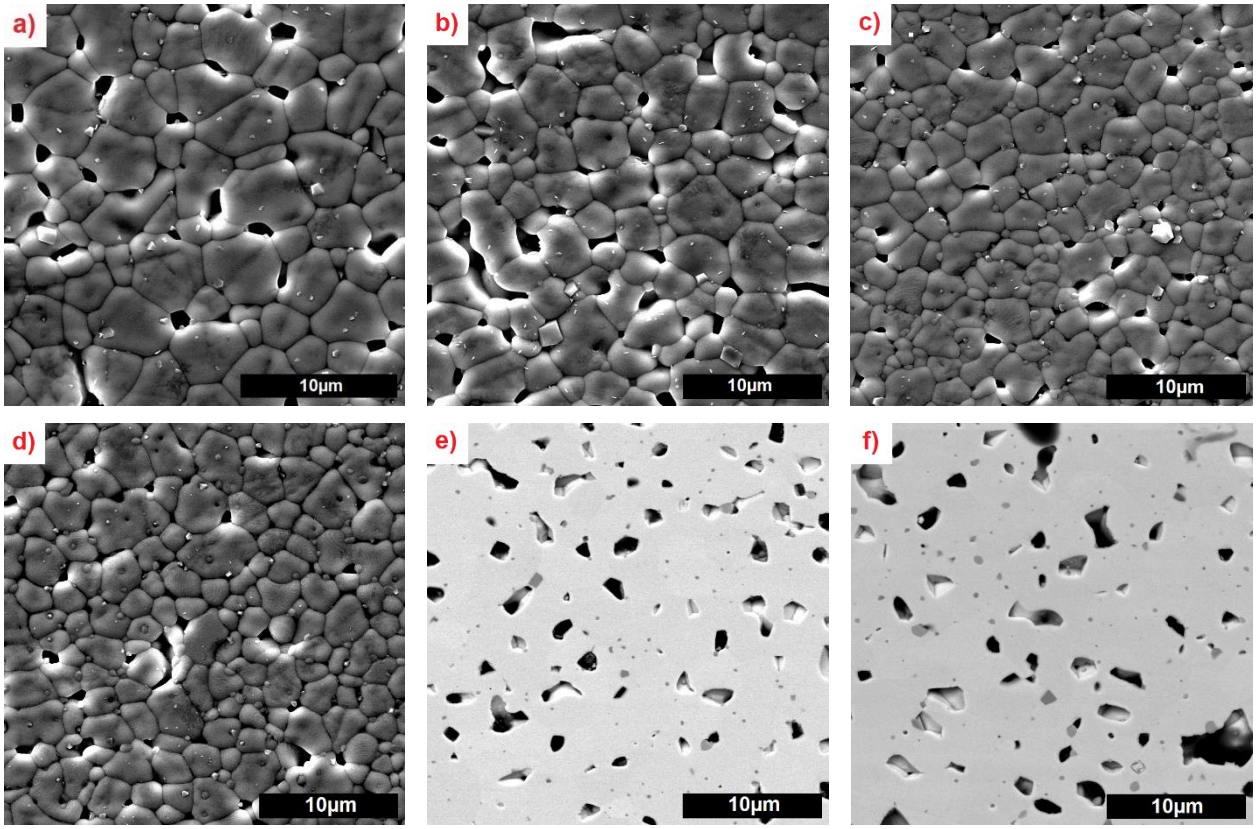

Figure 44: Microstructures obtained by SEM in secondary electron mode from ground, polished, and thermally etched NBT-6BT:xZnO with a) x = 0.025, b) x = 0.05, c) x = 0.075, and d) x = 0.1. Microstructures e) and f) were taken in backscattering mode from ground, polished, and unetched NBT-6BT:0.025ZnO and NBT-6BT:0.1ZnO, respectively.

The X-ray diffraction profiles reveal a perovskite structure in all compositions with some additional peaks at around 35-36° (Figure 45). The peaks are related to ZnO as a secondary phase. It is possible that small amounts of $TiZn_2O_4$ or $ZnTiO_3$ secondary phase formed during the calcination or sintering step. Such low amounts of phase fractions are difficult to detect via XRD.

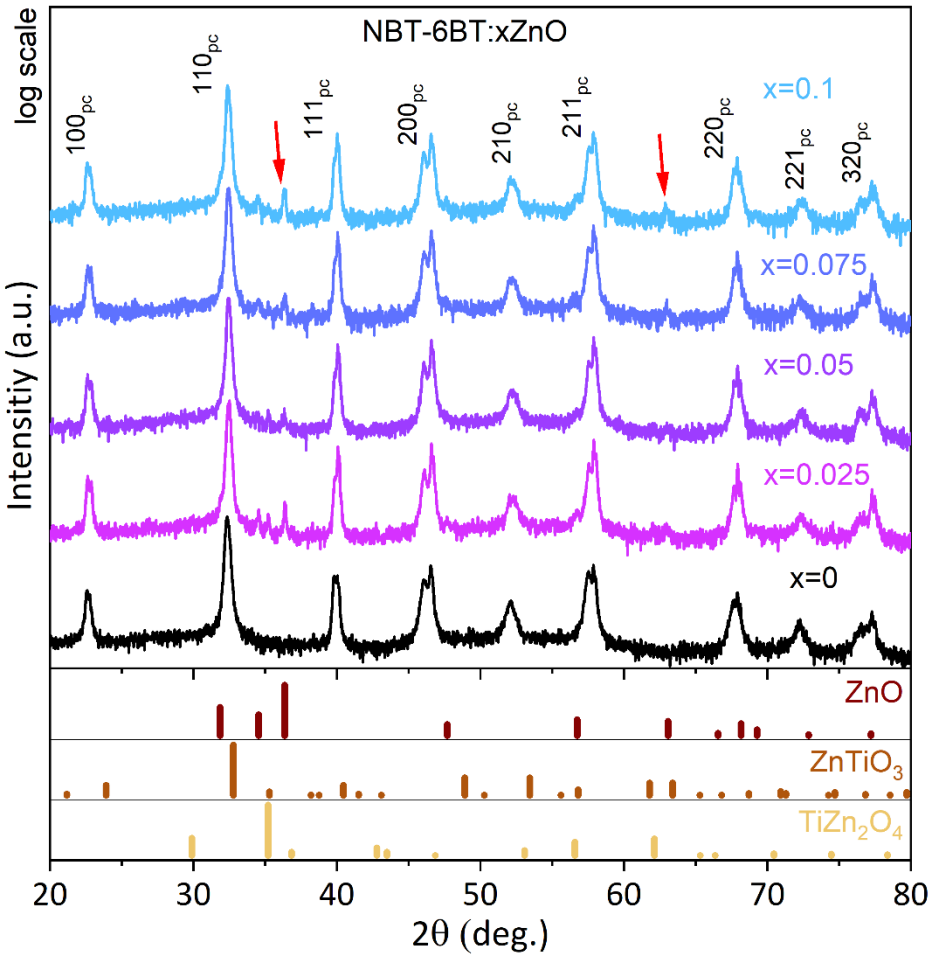

Figure 45: X-ray diffraction pattern of NBT-6BT:xZnO with x = 0, 0.025, 0.05, 0.075, and 0.1. The theoretical diffraction peak positions and intensity ratios are given for expectable secondary phases such as ZnO (red arrow), $ZnTiO_3$, and $TiZn_2O_4$.[247, 248]

The large-signal polarization and strain reveal a decreasing poling strain S_{pol} with increasing ZnO amount as well as a lower remanent strain S_{rem} (Figure 46a). This is expected from a composite in which the non-ferroelectric vol% increases. Although ZnO is piezoelectric, it does not contribute to the overall strain, due to its random distribution within the matrix. However, it prohibits the ferroelectric matrix from fully expanding due to a mechanical mismatch.[82] Despite a smaller S_{pol} and S_{rem}, the strain offset is not reduced with ZnO. The strain offset relates to a lower overall strain and lower S_{neg} noticeable in the third strain loop of all samples with a ZnO

secondary phase in comparison to the undoped NBT-6BT (Figure 46b). The strain response in the third loop is independent of the ZnO amount or is in the error range. A lower strain response cannot be confirmed by the small-signal piezoelectric coefficient d_{33}, whose value decreases from 129 pC/N in NBT-6BT:0.025ZnO to 117 pC/N in NBT-6BT:0.1ZnO. The coupling coefficient k_p displays similar behavior. The remanent polarization P_{rem} is lower in the composites in relation to the undoped NBT-6BT. Within the composite compositions, there is no clear tendency in P_{rem}. The coercive field E_c is approximately 0.4 kV/mm higher when ZnO is added than it is in pure NBT-6BT. A higher coercive field indicates ferroelectric hardening. This is confirmed by a higher mechanical quality factor in planar mode Q_m^p. The values obtained here fit well with the existing literature.[82] In the literature, compositions with even higher ZnO amounts were investigated, revealing the same tendencies observed here but to a stronger extent.

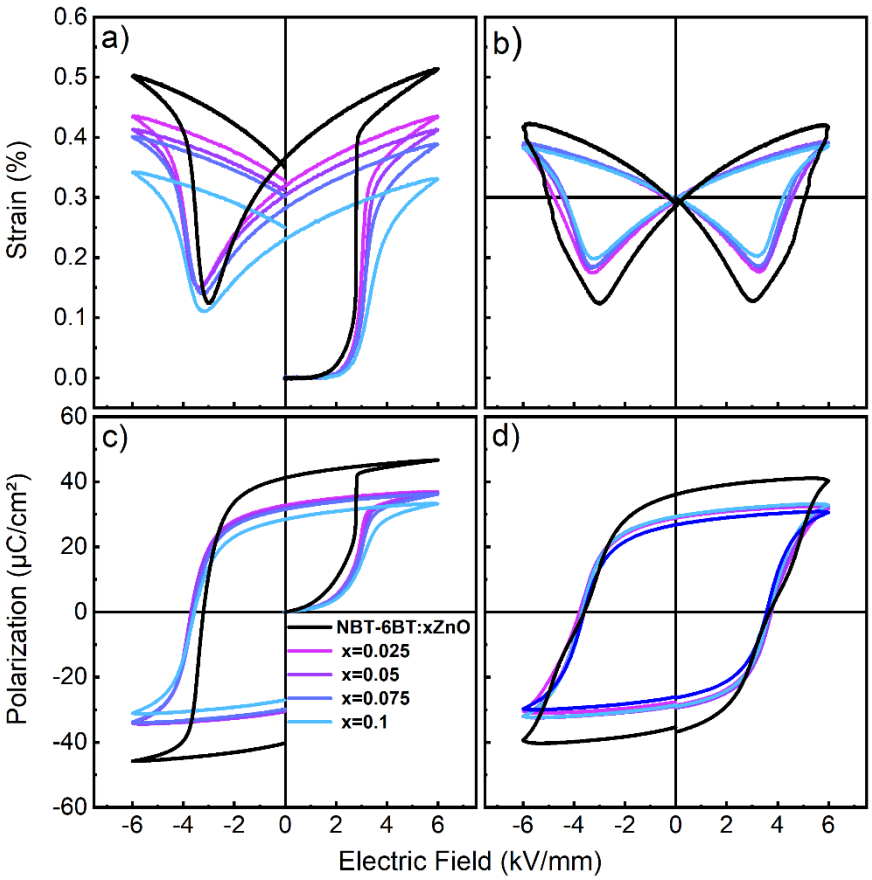

Figure 46: Strain and polarization against the electric field of NBT-6BT:xZnO with x = 0, 0.25, 0.05, 0.075, and 0.1. a) and c) Display the first loop, while c) and d) display the third loop of strain and polarization, respectively.

Table 10: Electromechanical properties of NBT-6BT:xZnO with x = 0, 0.025, 0.05, 0.075, and 0.1. $T_{F\text{-}R}$ = transition temperature from ferroelectric to relaxor state, d_{33} = small-signal piezoelectric constant, Q_m^p = mechanical quality factor in planar mode, k_p= coupling coefficient in planar mode, E_c = coercive field, P_{rem} = remanent polarization, and S_{rem} = remanent strain.

Composition NBT-6BT:xZnO	$T_{F\text{-}R}$ (°C)	d_{33} (pC/N)	Q_m^p (v = 0 m/s)	k_p	E_c (kV/mm)	P_{rem} (μC/cm^2)	S_{rem} (%)
x = 0	102	140 ± 4	119 ± 11	0.32 ±0.02	3.3 ± 0.1	35.7 ± 0.7	0.33 ± 0.02
x = 0.025	131	129 ± 3	265 ± 13	0.28 ± 0.003	3.7 ± 0.1	28.5 ± 0.4	0.32 ± 0. 01
x = 0.05	133	124 ± 3	269 ± 14	0.28 ± 0.008	3.7 ± 0.1	29.2 ± 0.5	0.31 ± 0.1
x = 0.075	124	123 ± 3	199 ± 23	0.26 ± 0.013	3.7 ± 0.1	29.0 ± 0.4	0.30 ± 0.01
x = 0.1	136	117 ± 3	241 ± 17	0.25 ± 0.02	3.6 ± 0.1	26.5 ± 0.6	0.25 ± 0.01

The transition temperature $T_{F\text{-}R}$ can be determined from temperature-dependent permittivity around 136 °C for NBT-6BT:0.1ZnO (Figure 47). All composites experience an increase in $T_{F\text{-}R}$ by approximately 30 °C except NBT-6BT:0.075ZnO, which experiences a $T_{F\text{-}R}$ increase of approximately 20 °C. The reason for this difference is not known. Figure 47 presents the permittivity and dielectric loss against temperature for NBT-6BT:0.1ZnO. The other composites exhibit a similar behavior and thus are not shown here. The strong increase in permittivity and loss above ~200 °C originates from increased bulk conductivity due to mobile charges. The increase in the loss is not the case in undoped NBT-6BT but in acceptor-doped NBT-6BT (Figure S5). Hence, the incorporation of Zn^{2+} ions into the matrix phase of the composite, leading to oxygen vacancy formation, is likely. At around 100 °C, there is a kink in the permittivity, which, in the literature, is correlated with a partial depolarization, predominantly of the rhombohedral phase.[129, 249][XVI]

[XVI] An insightful comparison between Zn doping and the ZnO composite approach can be found in the work of Mihail Slabki.[217]

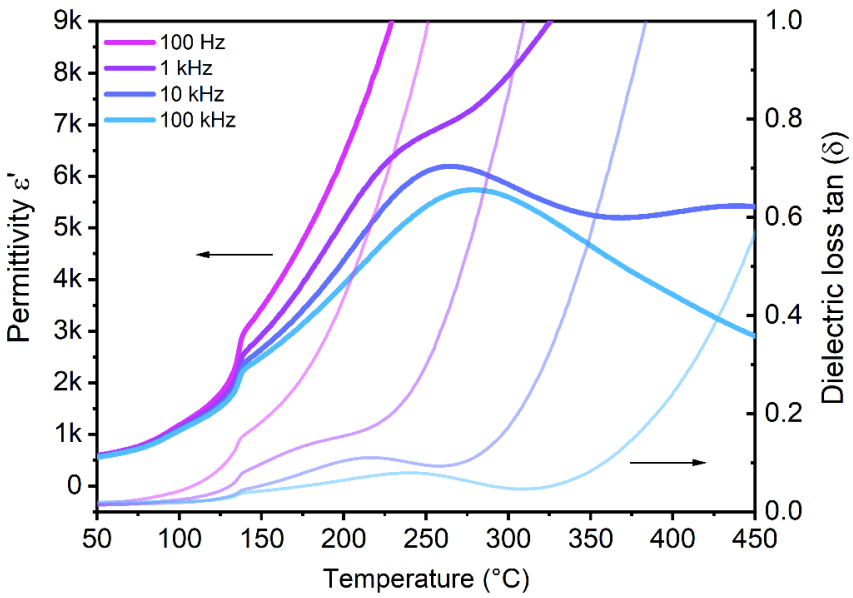

Figure 47: Real part of the permittivity *ε´* and dielectric loss *tan*(δ) against temperature for poled NBT-6BT:0.1ZnO at different frequencies.

5.3 Application-oriented Measurements

Most frequently used standard measurements do not represent the conditions a ferroelectric ceramic experiences during high-power applications. This chapter concerns measurements related to the conditions in real high-power applications such as high vibration velocity, mechanical pre-stress, and continuous drive.

5.3.1 Mechanical Loss at High Vibration Velocity

In this section, the vibration velocity-dependent Q_m is investigated for different lead-free NBT-xBT compositions modified by Zn and Mg doping, the ZnO secondary phase, or Bi-non-stoichiometry. The v-dependent slope of Q_m seems unaffected by the chemical modification with the exception of the BT content.

NBT-xBT is known for the stability of the mechanical quality factor against increasing vibration velocity.[250] Predominantly NBT-6BT and NBT-9BT variations have been investigated in literature in terms of their high power stability.[114] Figure 48 illustrates (a) the mechanical quality factor in resonance in the planar mode of NBT-5BT to NBT-8BT and (b) the same compositions with 0.5 mol% Zn acceptor-doping. Compositions on the rhombohedral side of the MPB exhibit

a higher Q_m at low vibration velocities compared with the tetragonal compositions. This finding confirms the results obtained from small-signal properties (Section 5.1.1).

A higher Q_m on the rhombohedral side has also been observed in other lead-free systems.[204] In PZT, however, the tetragonal side shows a higher Q_m.[251] Q_m correlates with a higher coercive field for both PZT and NBT-xBT.[100] The reason for the different coercive fields on the tetragonal and rhombohedral sides of PZT and NBT-xBT is unknown but could be associated with PZT classified as a rotator and NBT-xBT classified as an extender.[252][XVII]

The decrease of Q_m is approximately 54% in the NBT-5BT from 0.1 m/s to 1.2 m/s. By contrast, NBT-8BT decreases by about 18%. Hence, the tetragonal side is more stable than the rhombohedral side against an increasing v. This observation is still valid in the Zn-doped compositions. In the same v range, Q_m in the Zn-doped compositions decreases by 28% and 0% in NBT-5BT-0.5Zn and NBT-8BT-0.5Zn, respectively. Since the extrinsic loss is highly stable against v in the NBT-6BT and NBT-9BT, the behavior of Q_m against v is mainly determined by the intrinsic loss.[114] Two reasons might explain the varying stability of the rhombohedral compositions. First, the intrinsic losses are higher on the rhombohedral side than on the tetragonal side. Second, extrinsic losses contribute more to the overall loss behavior in the predominantly rhombohedral compositions than in predominantly tetragonal compositions. It should be noted, that there is no clear guideline for determining the stability of Q_m(v). The slope of $Q_m(v)$ is in the same range for undoped and Zn-doped NBT-5BT.

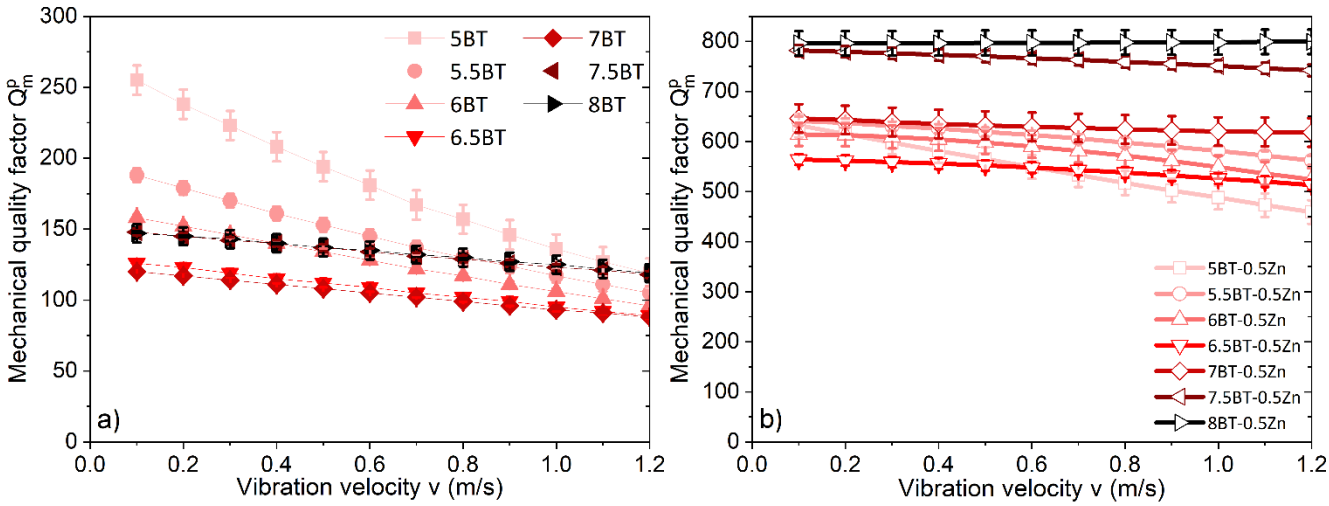

Figure 48: Mechanical quality factor in resonance in planar mode, Q_R^p, against increasing vibration velocity, v, of a) NBT-xBT with x = 5, 5.5, 6, 6.5, 7, 7.5, and 8 and b) NBT-xBT-0.5Zn with x = 5, 5.5, 6, 6.5, 7, 7.5, and 8.

[XVII] The classification into rotator or extender is based on the d_{12}/d_{33} ratio. This ratio is greater in rotator ferroelectrics.

NBT-6BT-0.5Mg and NB_{49}T-6BT-0.5Zn both experience a decrease in Q_m of less than 8% from 0.1 m/s to 2 m/s (Figure 49). In contrast, NBT-6BT drops by 58% and NB_{51}T-6BT-0.5Zn by 30% in the same range. These changes seem considerably high, but in comparison to all PZT-based materials, Q_m is much more stable, even in the undoped NBT-6BT. P4, for example, drops by 70% from 0.1 m/s to 0.8 m/s and experiences the same 58% decrease already at 0.5 m/s (Figure 50b). Although the stability of P4 and NBT-6BT-0.5Zn is vastly different, the incline is similar, thus suggesting a related loss mechanism. In high-power applications, *v* is in the range of 0.2-1 m/s, thus demonstrating the benefit of the lead-free material. Moreover, NBT-based new applications could emerge with a higher *v* and hence a higher mechanical output.

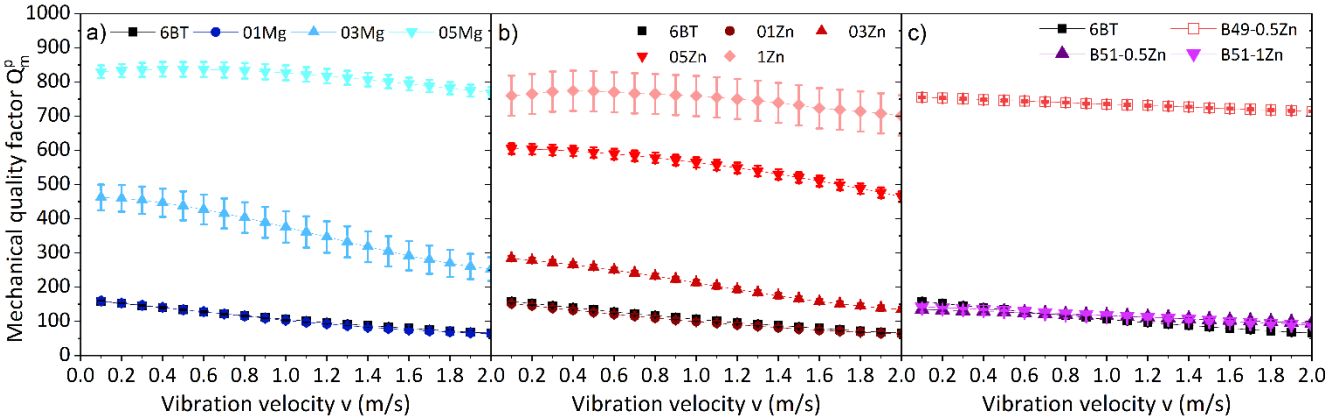

Figure 49: Mechanical quality factor in planar mode in resonance, Q_R^p, up to a vibration velocity of *v* = 2 m/s of a) NBT-6BTxMg with x = 0, 0.1, 0.3, and 0.5; b) NBT-6BTxZn with x = 0, 0.1, 0.3, 0.5, and 1; and c) NB_{49}T-6BT-0.5Zn, NB_{51}T-6BT-0.5Zn, and NB_{51}T-6BT-1Zn.

Thus far, the behavior of Q_m against *v* was mainly discussed on the planar vibration mode, which is of minor relevance for the application usage. Mostly the 33-vibration mode or a mixture of the 33 and 31 modes are relevant in application. The planar, 33, and 31 vibration modes were compared in NBT-xBT[XVIII] and hard PZT (P4). Overall, the results from Slabki et al. [98] are confirmed. Hard PZT reveals a distinct difference between the 33 and 31 geometries and the planar resonance mode. The lower Q_m in the planar resonance is based on the stress distribution in the sample. The maximum strain in the planar resonance mode is approximately one third higher than in the 33 and 31 geometries at the same vibration velocity, resulting in higher losses and hence a lower Q_m. The higher strain in the planar mode does not affect the Q_m of NBT-xBT, probably due to the lower stress sensitivity in the relatively low *v* range of

[XVIII] The exact composition is held secret by the industry partner.

0.8 m/s. Similar to Slabki et al.'s finding, a lower Q_m is observed with attached silver wires. To prohibit this effect, samples with a minimum length of 12 mm are used in the 33 geometry.

Figure 50a contains measurements performed on pure NBT-xBT and NBT-xBT with Zn doping and ZnO as a secondary phase.[XIX] A comparison of these two different strategies to increase Q_m in the NBT-xBT system suggests that doping with Zn and ZnO as a secondary phase are both highly effective. The values obtained from the industry samples are even higher than the compositions produced during this work. This can occur due to different BT contents, purities of initial powders, processing routes, and doping or secondary phase amounts.[XX] Despite the slightly higher Q_m values, the same stability of Q_m against v is observed in the Zn-doped and ZnO composites. This finding confirms that the stability of $Q_m(v)$ is an intrinsic material property, which others have previously studied.[114]

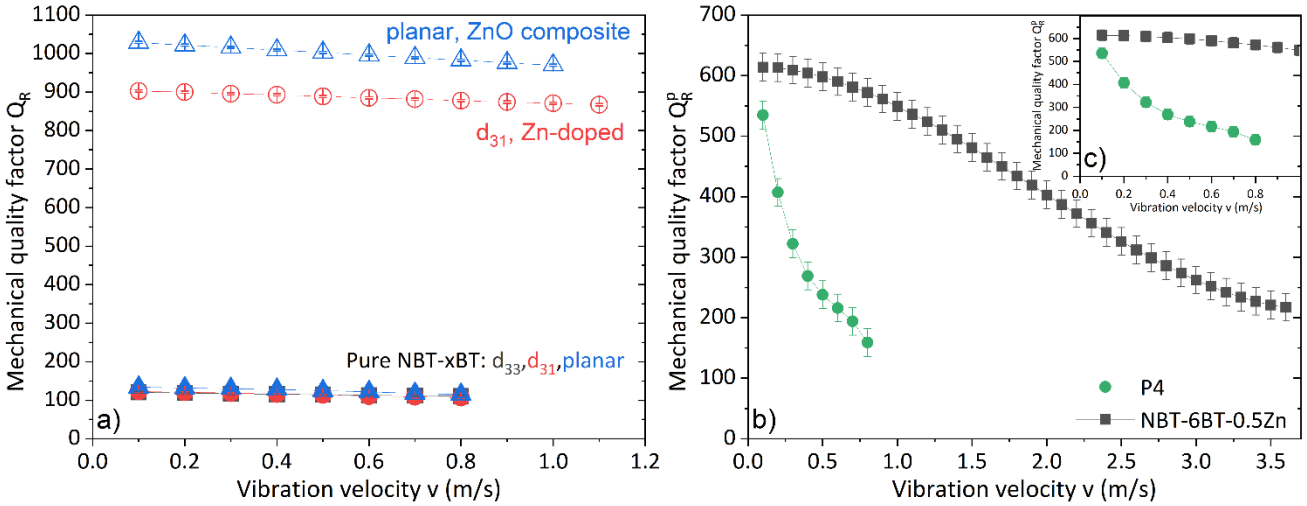

Figure 50: Mechanical quality factor in 33, 31, and planar resonance modes against vibration velocity. a) NBT-xBT with Zn doping and a ZnO secondary phase. b) Hard PZT (P4) and NBT-6BT-0.5Zn.

Plotting the required electric field strength against the vibration velocity provides a trend for the undoped NBT-xBT and the NBT-xBT Zn-doped compositions (Figure 51). The black and red lines serve as guidance for the eye. The slope of the Zn-doped compositions is higher than that of undoped NBT-xBT. With Equation (12) for vibration velocity, the higher required electric field strength is explained by the difference in Q_m. The compliance s and the piezoelectric coefficient d both change less than the mechanical quality factor Q_m when NBT-xBT is doped

[XIX] The exact composition is held secret by the industry partner. The composite and the acceptor doped material are based on the same NBT-xBT composition as the pure one. They all contain the same BT content.

[XX] During the experiments, it seemed that a different sample size could also have an influence. This was not further investigated.

with Zn. Interestingly, both trends are non-linear. The non-linear increase relates to the non-linear decrease of Q_m against v (Figure 50b). Additionally, the maximum achievable v is higher in the Zn-doped compositions, reflected by a saturation at different vibration velocities. This finding indicates that a higher Q_m is maintained up to a high v in the Zn-doped NBT-xBT than in the undoped NBT-xBT.

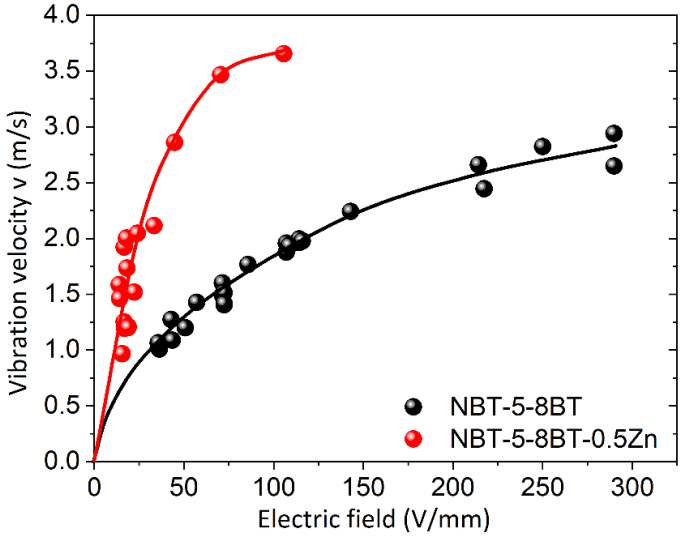

Figure 51: Vibration velocity against electric field strength for undoped NBT-5BT to NBT-8BT (black) and NBT-5BT-0.5Zn to NBT-8BT-0.5Zn (red).

5.3.2 Electromechanical Fatigue in Resonance

The high-power measurements described in the Subchapter 5.3.1 are closer to the application than small-signal measurements but are performed in only a few ms. Time is an important factor that can lead to aging or fatigue of the material. This chapter focuses on changes with time under high vibration velocity in resonance. A lead-free NBT-xBT:ZnO composite is tested and referenced to hard PZT (P4). A comparison of fatigued, recovered, freshly poled, and aged samples suggests a different underlying fatigue and aging mechanism in both material systems.

The electric field required to reach vibration velocities of 0.5 m/s, 1 m/s, and 1.5 m/s has been recorded in the 31 and 33 resonance modes (Figure 52a). The NBT-xBT:ZnO and hard PZT (P4) samples were driven several minutes until stable conditions were reached. Lead-free NBT-xBT:ZnO requires a higher electric field than hard PZT to reach 0.5 m/s. This changes at 1 m/s and 1.5 m/s. Hard PZT requires a higher electric field to reach 1 m/s and 1.5 m/s.

Considering Equation (12), this finding is expected: Hard PZT has a d_{31} of approximately 120 pm/V in relation to approximately 22 pm/V for NBT-xBT:ZnO. The higher d_{31} of PZT cannot compensate the disadvantage from the drastic decrease of Q_{m}^{31} in PZT with increasing v. The stability of Q_{m}^{31} against v in NBT-xBT:ZnO outperforms that in hard PZT, resulting in a lower required electric field, even though d_{31} is about 80% lower. It is surprising that hard PZT can be driven continuously at 1 m/s or even 1.5 m/s. Most literature does not measure at these velocities and predicts a failure of PZT due to the sharp temperature increase observed at a lower v.[55, 253] Several reasons are believed to play a role in these contradicting observations. First, the small samples have a high surface-to-volume ratio, leading to significant heat dissipation. Second, Q_{m} increases with temperature, partly compensating for the sharp drop in Q_{m} with an increasing v.[114]

In comparison to the 31 geometry samples, samples in the 33 geometry require a much lower electric field to reach 0.5 m/s and 1 m/s. This is expected due to the higher piezoelectric coefficient d_{33}. NBT-xBT:ZnO and hard PZT were driven at the same electrical field strength; the same explanation for Q_{m} and d_{33} as in the 31 geometry is valid. The difference in the piezoelectric coefficient is lower: approximately 98 pm/V and 300 pm/V for NBT-xBT:ZnO and hard PZT, respectively. Samples in the 33 geometry could not be driven at 1.5 m/s. This finding is discussed in detail later in this chapter.

The power input takes the current into account in addition to the voltage (Figure 52b). Similar trends as those for the electric field are present. The current flow is much lower in NBT-xBT:ZnO than in hard PZT, resulting in a lower power input. The current flow is geometry-dependent since the power input in the 33 geometry increases relative to the required electric field. The temperature is not 100% proportional with the power input, as the samples in the 33 geometry exhibits a higher temperature even though less power was applied to the sample in comparison to the 31 geometry (Figure 52c). This finding can be rationalized by a lower heat dissipation due to the lower area-to-volume ratio of the 33 geometry samples compared with that of the 31 geometry samples.

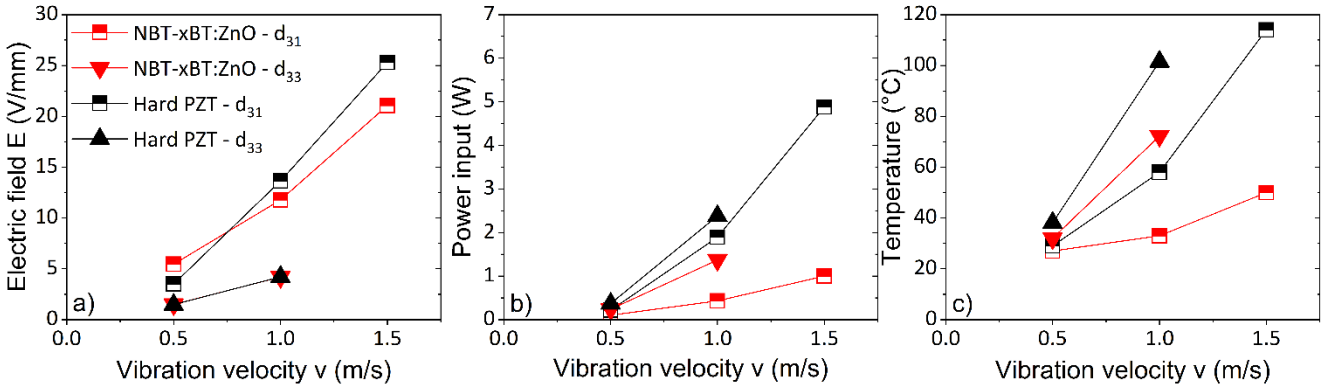

Figure 52: a) Electric field, b) power input, and c) temperature of NBT-xBT:ZnO and hard PZT (P4) at 0.5, 1, and 1.5 m/s vibration velocities. Samples are compared in the 31- and 33-resonance modes.

Figure 53 reveals the frequency, temperature, and vibration velocity over time in continuous drive mode. The difference between manual and automatic control of the vibration velocity is apparent in Figure 53a$_1$.[XXI] Manually controlling the vibration velocity by changing the applied voltage and frequency resulted in a variance of about 1 ± 0.05 m/s, whereas automatic control resulted in a variance of about 1 ± 0.13 m/s. The transition between both methods is visible at approximately 4x10^8 cycles in Figure 53a$_1$. Notably, the method of visualization leads to a distorted perception of the variance. For 93% of the time, the vibration velocity is in the range of 1 ± 0.1 m/s. Although *v* is stable, both the resonance frequency and the temperature changes over time. The resonance frequency of the pristine hard PZT sample is close to 81 kHz (Figure 53a$_2$ and b$_2$). Increasing the v from initially 0 m/s to 1 m/s shifts the resonance to lower frequencies close to 78 kHz and to 76.5 kHz in the case of hard PZT driven at 1.5 m/s. This effect is known from the literature and is characterized by non-linear electromechanical properties. The stiffness decreases because of a non-linear dielectric response with an increasing *v*.[250, 254] A similar observation was made by Slabki et al.[98], who measured dielectric response and elastic compliance against *v* and observed an increase in both. The measurements were taken with the burst method, which generally prevents sample heating. By contrast, the continuous drive used in the present study leads to a temperature rise which further increases elastic compliance, thereby promoting non-linear behavior. The temperature profile (Figure 53a$_3$) is the opposite of the frequency profile. This is also true for hard PZT at 1.5 m/s and NBT-xBT:ZnO at both depicted *v* values (Figure 53a$_2$-d$_3$).

[XXI] Please find details about the control in Subchapter 4.5.4.

In general, NBT-xBT:ZnO demonstrates a much more stable behavior than hard PZT, and it does not need time to reach a stable state. The vibration velocity is in the range of 1.01-1.03 m/s and 1.5 ± 0.04 m/s, except for two times in which the sample jumps out of resonance (Figure 53d). There are fewer changes in the resonance frequency of NBT-xBT:ZnO than of hard PZT, and the temperature is more stable. The temperature increase is also much lower, with a stable temperature of approximately 34 °C and 50 °C at 1 m/s and 1.5 m/s, respectively. By contrast, hard PZT rises to a stable temperature of 58 °C and 113 °C when resonating at 1 m/s and 1.5 m/s, respectively. The lower temperature in the NBT-xBT:ZnO is expected and originates from the higher Q_m at these vibration velocities.

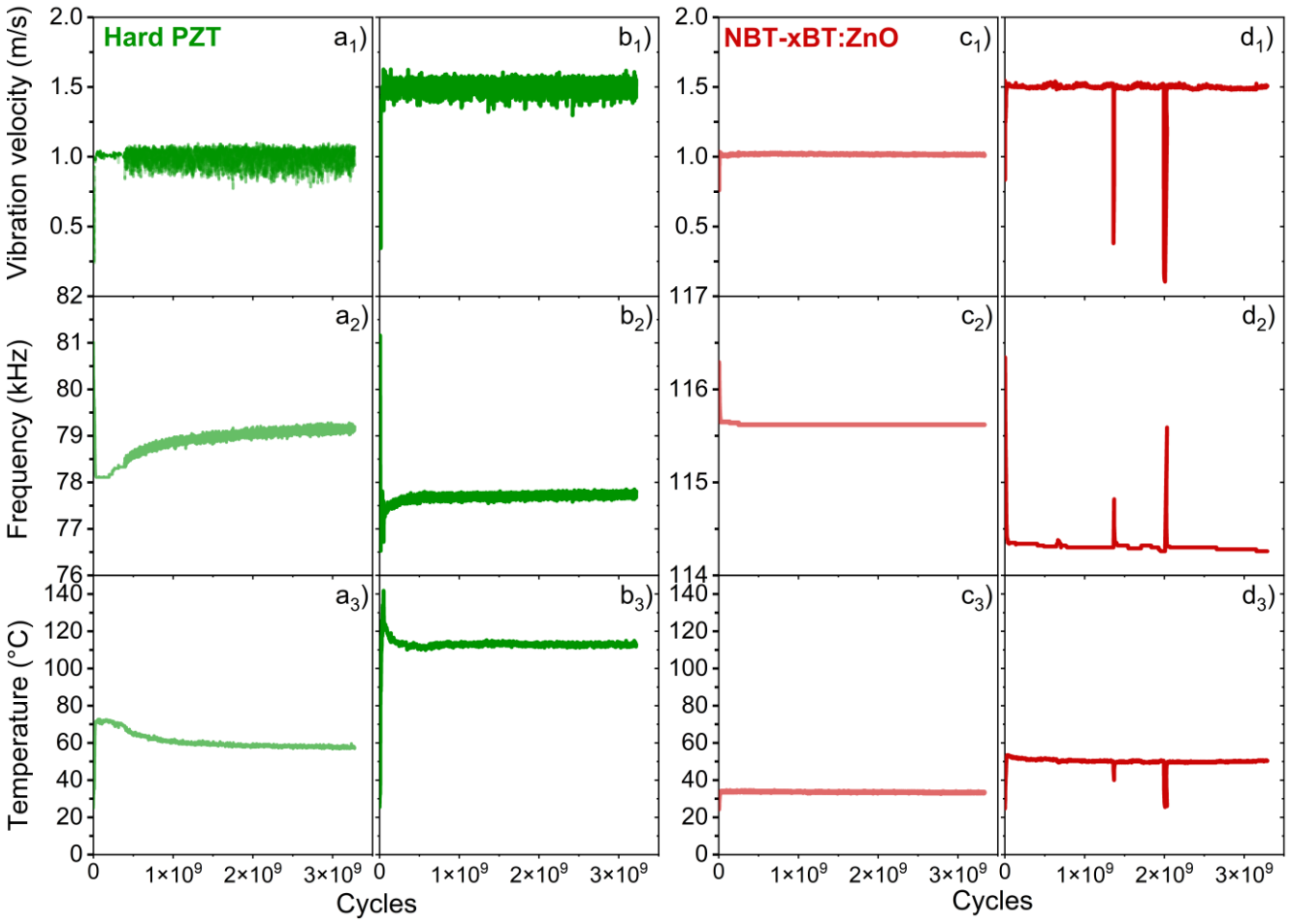

Figure 53: Recorded vibration velocity a_1-d_1, frequency (driven in resonance) a_2-d_2, and temperature a_3-d_3 of hard PZT and NBT-xBT:ZnO *in situ* of the electromechanical loading. Depicted measurements were performed in 31-resonance mode. a_1-a_3) Hard PZT at 1 m/s. b_1-b_3) Hard PZT at 1.5 m/s. c_1-c_3) NBT-xBT:ZnO at 1 m/s. d_1-d_3) NBT-xBT:ZnO at 1.5 m/s. Additional values, such as voltage, current, input power, and impedance, are depicted in Figure S9 and Figure S10.

Figure 54 depicts several full cycles of (a) hard PZT and (b) NBT-xBT:ZnO in the 31-resonance mode. The vibration velocity, current, and voltage are given. The measured voltage is a smooth sine signal in both cases. The voltage signal and the current are lower for the NBT-xBT:ZnO, which was already observed and discussed in Figure 52. The shift in time between voltage/current and velocity is due to measurement inaccuracy and is not considered in the discussion.[XXII] Hard PZT reveals a distorted vibration velocity, which also results in a distorted current. Guyomar et al. [56] studied this phenomenon in 1994 and rationalized it as follows: The stiffness depends non-linearly on the electric field. The saturation of the fundamental vibration leads to the generation of overtones. The higher-order harmonics interfere with the fundamental level and result in a distortion of the vibration velocity.

NBT-xBT:ZnO does not show a distortion in the vibration velocity or current. Hence, no higher-order harmonics are generated. The energy of the vibration is fully contained in the fundamental level, allowing for the assumption that the stiffness is still in the linearly dependent regime at this *v*. Two main advantages result from the behavior of the lead-free material. First, the energy transfer to a medium is higher without higher harmonics. Higher harmonics disturb the fundamental vibration and hence reduce the overall amplitude, even though the energy input into the transducer is the same. Second, operation and control become difficult in a system that changes depending on the input power. This must be compensated for by a more complex controlling system.[255] These advantages of the lead-free material should be considered when designing new applications.

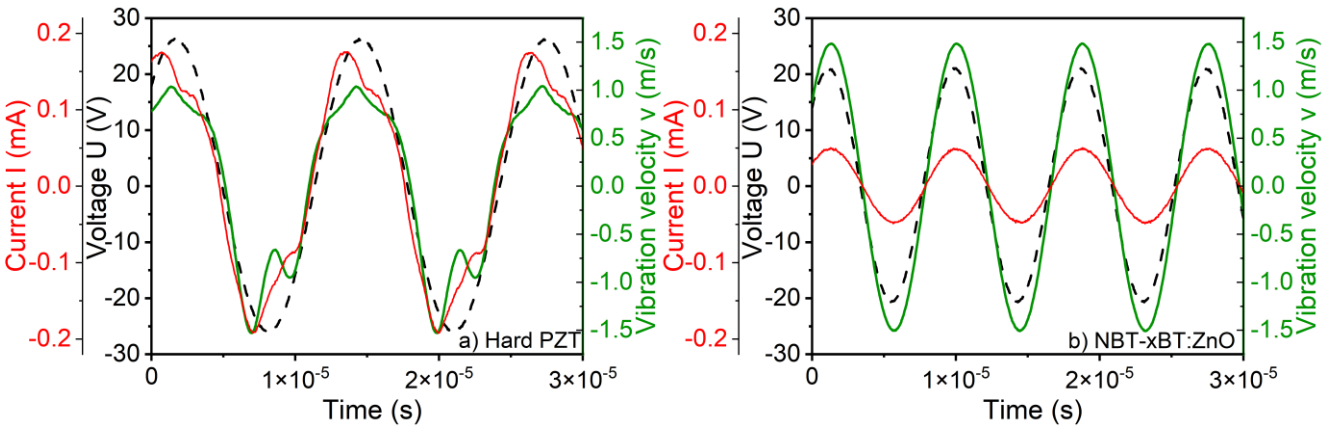

Figure 54: Voltage (black dotted), current (red), and vibration velocity (green) of hard PZT (a) and NBT-xBT:ZnO (b) against time.

[XXII] The voltage and current signal are obtained directly from the measurement probe and hence have a very small time delay. The vibration velocity is measured by a laser with a processing step of the laser signal itself. The depicted signal is an output signal from the laser setup and has a time delay of roughly 6.8 µs. The graph is shown with corrected values.

Hard PZT samples in 31-resonance mode that are fatigued for 3.3×10^9 cycles do not show any changes in the small-signal properties when fatigued at 0.5 m/s (Figure 55a-c). The same is true for NBT-xBT:ZnO (Figure 55d-f). The fatigue or change in properties increases with an increasing *v* in both materials but is lower in the lead-free NBT-xBT:ZnO. A reasonable assumption is that the temperature is the main driving force in the property change. Therefore, samples were annealed at 120 °C (hard PZT) and 50 °C (NBT-xBT:ZnO) for the same time period. The temperature shifts the properties in the same direction but to a smaller extent, suggesting that additional factors lead to the fatigue. Additional factors are likely stress and the electrical field. Distinct differences are revealed between both investigated materials. The piezoelectric coefficient d_{31}, the mechanical quality factor Q_{m}^{31}, and the coupling factor k_{31} decrease in NBT-xBT:ZnO, whereas in hard PZT, Q_{m}^{31} and k_{31} also decrease, but d_{31} increase at the same time. The percentage decreases in d_{31} and k_{31} are in the same order of magnitude at 1.5 m/s for both materials. The decrease in Q_{m}^{31} is considerably higher in hard PZT. A decrease in Q_{m} is mostly attributed to ferroelectric softening. This is supported by an increase in d_{31} in hard PZT, which usually correlates with a similar behavior of k_{31}. The opposite trends for d_{31} and k_{31} are a result of the increase in elastic compliance and permittivity. In PZT, ferroelectric hardening is caused by defect complex formation and alignment.[80] A higher temperature will facilitate the alignment process, which is called aging. Since the opposite behavior is observed here, it is suggested that existing defect complexes will reorient at elevated temperatures and soften the material. After the sample was left at room temperature for 37 days, values close to the initial d_{31} and Q_{m}^{31} are observed (Figure 57a and b). This supports the hypothesis of an aging and reverse-aging process in hard PZT. In NBT-xBT:ZnO, a different behavior is observed: Q_{m}^{31} and d_{31} both decrease, thus excluding a defect-dipole-associated hardening or softening mechanism as in PZT or indicating a second overlapping effect. Indeed, leaving the sample for 37 days at room temperature recovers Q_{m} (Figure 57a). The changes are much lower than in PZT but should still be related to a defect-driven mechanism. By contrast, d_{31} remains unchanged (Figure 57b), implying that two different mechanisms are responsible for the changes in Q_{m} and d_{31}. The decrease in d_{31} and the missing recovery could be caused by a partial depolarization of the rhombohedral phase, as observed by Adhikary et al. [129]. The described differences in hard PZT and NBT-xBT:ZnO support the hypothesis from other chapters that defects behave differently and have different impacts on the lead-free NBT-xBT than on PZT.

Fatigue measurements in resonance at high vibration velocities are rare in the literature. Hill et al. [96] investigated the formation of microcracks in very hard PZT (P8) and found that the microcrack density decreased with increasing cyclic loading. Additionally, at very high electric loading, leading to a temperature rise of 180 °C, partial depolarization occurred, which is not observed in this work. Hill et al. found a correlation of the temperature with the stress, which was the highest in the middle of the sample. A similar finding was revealed by measuring the temperature at different sample positions during a steady state.

Measurements in the 33-resonance mode reveal the same trend as in the 31-resonance mode: Q_{m}^{33} and k_{33} decrease, and d_{33} increases in hard PZT after cycling. In NBT-xBT:ZnO, all properties decrease. The change is higher in the samples fatigued at higher v, with the exception of Q_{m} in NBT-xBT:ZnO, which cannot be explained but might originate from the small number of samples investigated in the 33 geometry.

Note that the samples in the 33 geometry were contacted via a thin silver wire. This wire fatigued and broke significantly faster than the ceramics. Hence, the wire had to be renewed frequently, making it impossible[XXIII] to take measurements for the same number of cycles as in the 31 geometry. Samples in the 33 geometry were cycled for about 0.8×10^9 cycles. In addition, it was not possible to reach a higher vibration velocity than 1.15 m/s. The determination of the maximum driving velocity is discussed in detail at the end of this chapter.

[XXIII] Impossible due to limited time. The measurements would have taken months instead of hours.

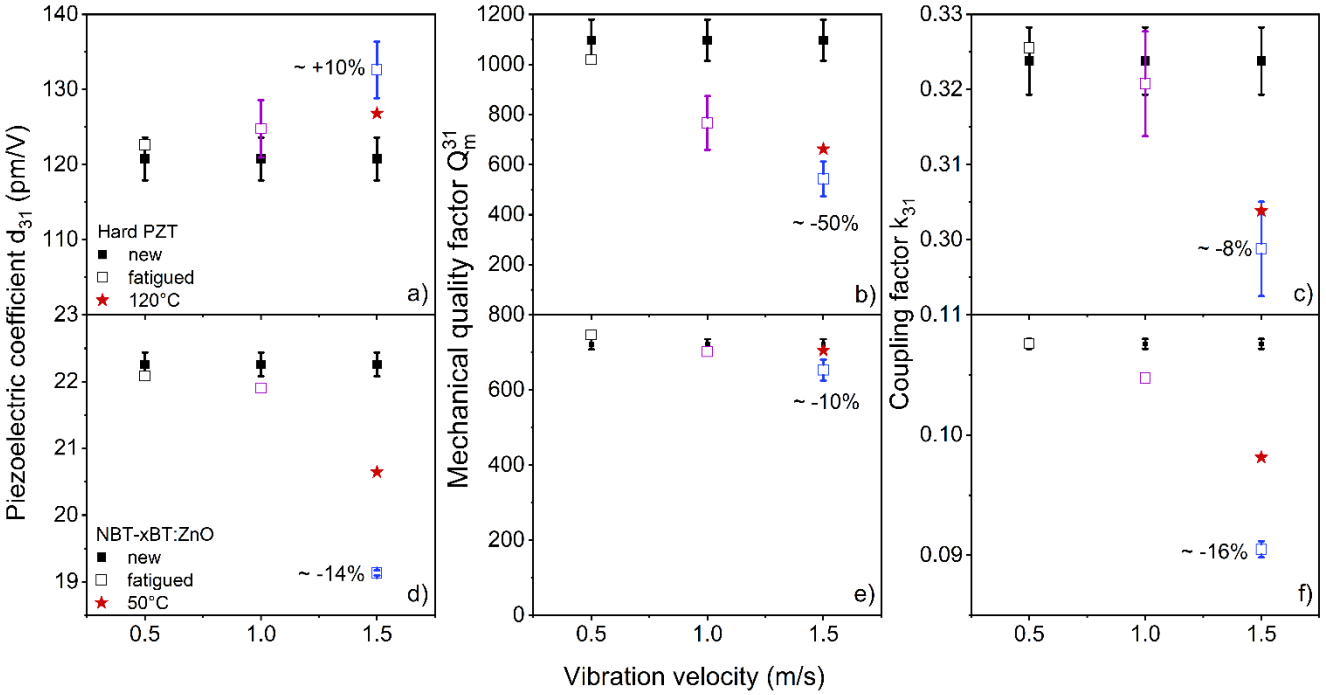

Figure 55: Small-signal properties such as piezoelectric coefficient d_{31}, mechanical quality factor Q_m^{31}, and coupling coefficient k_{31} of hard PZT and NBT-xBT:ZnO. Values of both materials are given before (black) and after (colored) the fatigue at 0.5, 1, and 1.5 m/s for about 3.3×10^9 cycles. Additional properties, such as compliance, capacitance, and permittivity, can be found in Figure S11 and Figure S12.

Table 11: Small-signal properties such as piezoelectric coefficient d_{33}, mechanical quality factor Q_m^{33}, and coupling coefficient k_{33} of hard PZT and NBT-xBT:ZnO before and after the materials were fatigued (~0.8×10^9 cycles).

	Hard PZT			**NBT-xBT:ZnO**		
	New	1 m/s	1.15 m/s	New	1 m/s	1.15 m/s
$\boldsymbol{Q_m^{33}}$	955 ±76	607	283	448 ±38	213	355
$\boldsymbol{k_{33}}$	0.71 ±0.01	0.7	0.67	0.5 ±0.01	0.47	0.28
$\boldsymbol{d_{33}}$ (pm/V)	301 ±3	315	341	98 ±1	91	58

A comparison of the changes in the properties over short time intervals of the measurement (v = 1.5 m/s) yields some interesting insights (Figure 56). The mechanical quality factor Q_m^{31} drops immediately in both PZT and NBT-xBT:ZnO (Figure 56a and d). Moreover, the coupling coefficient reveals a similar behavior in both materials: It decays in a logarithmic manner, which is faster in PZT (Figure 56b and e). The logarithmic decay originates from the reorientation of defect dipoles.[256] The piezoelectric response d_{31} is revealed as a similar decay to that of k_{31}

in NBT-xBT:ZnO, whereas in the PZT, d_{31} first increases from 122 pm/V to 142 pm/V and thereafter decreases again to approximately 137 pm/V. The initial increase of d_{31} should originate from the increase in elastic compliance and permittivity. Both elastic compliance and permittivity are constant after the first change in the hard PZT. By contrast, the changes are not saturated in the same number of cycles in the NBT-xBT:ZnO. Changes are an order of magnitude lower but alter in the same direction (Figure 56c and f). This time-dependent measurement of the electromechanical properties confirms the overall higher stability of the NBT-xBT:ZnO in comparison with hard PZT against vibration velocity.

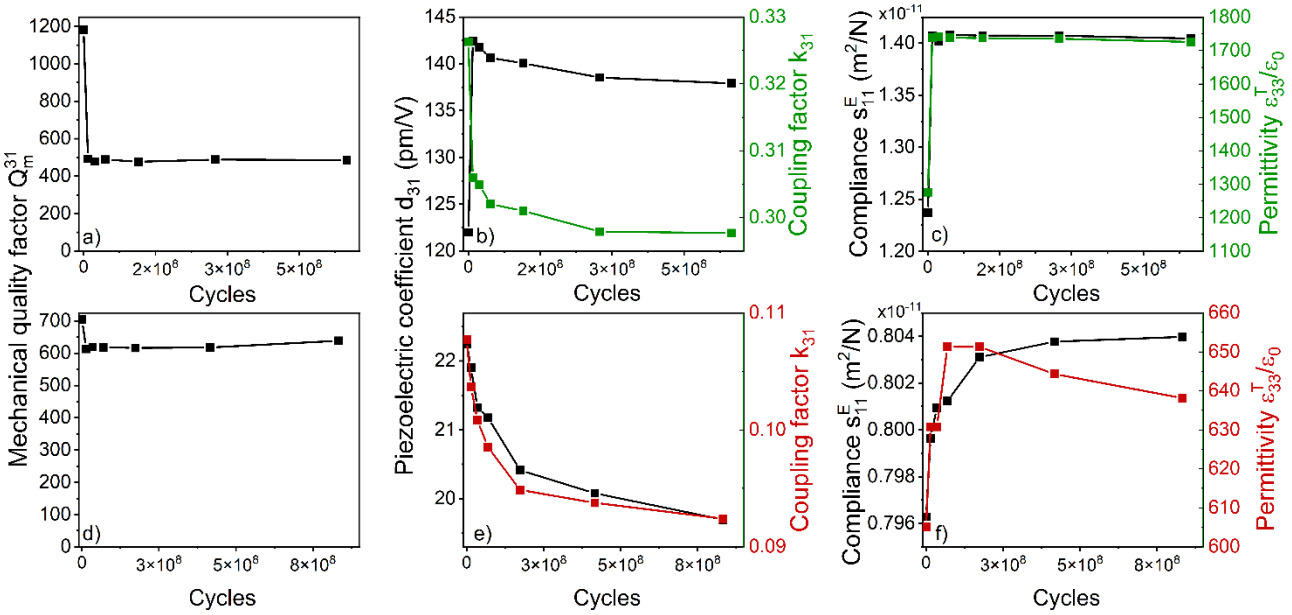

Figure 56: a) and d) Mechanical quality factor Q_m^{31}. b) and e) Piezoelectric coefficient d_{31} and coupling coefficient k_{31}. c) and f) Elastic compliance s_{11}^E and permittivity ε_{33}^T of hard PZT (a–c) and NBT-xBT:ZnO (d–f) against the number of cycles at a vibration velocity of 1.5 m/s.

Figure 57 compares Q_m and d_{31} of hard PZT and NBT-xBT:ZnO at different states of aging, poling, and fatigue. To understand Figure 57, steps 1–5 must be explained (marked in a color scheme). In condition 1, the samples are poled, aged at room temperature for more than 5 weeks, and not fatigued. The resulting values of Q_m and d_{31} are referred to as reference values. The second values were taken after 3.3×10^9 cycles at 1.5 m/s, which correlates with 8 h for the hard PZT samples and 11.5 h for the NBT-xBT:ZnO samples. Hard PZT reveals a process that leads to the opposite trend of aging, indicated by the simultaneous increase in d_{31} and decrease in Q_m. NBT-xBT:ZnO reveals a mixture of depolarization and a lower Q_m. The third measurement was conducted after step two at 37 days of aging at room temperature. Hard PZT almost regains its initial values within this aging process, whereas NBT-xBT:ZnO

has an unchanged d_{31} but a Q_m that recovers. This could be correlated with the partial aging process, which affects Q_m but does not compensate for the lost piezoelectric response due to partial unpoling in the rhombohedral phase. If the change in Q_m in NBT-xBT:ZnO is a result of aging, it is an order of magnitude lower than in hard PZT. In Figure 57-4, samples were poled again, and Q_m and d_{31} values were taken 1 h after poling. The properties of hard PZT are similar to those in the state after fatigue (2): a high d_{31} and a low Q_m. Aging of the samples at room temperature for 18 days reveals the expected increase in Q_m and decrease in d_{31} (Figure 57-5). The mechanical quality factor and the piezoelectric activity correlate strongly in hard PZT. This phenomenon is explained in literature by the formation, destruction, and reorientation of defect complexes between the acceptor dopant and an oxygen vacancy, and it is normally referred to as ferroelectric hardening.[80, 256, 257] The piezoelectric activity is affected to a strong extent, but Q_m changes even more by up to a twofold increase or decline.

Poling NBT-xBT:ZnO again (Figure 57-4) does not change Q_m considerably, but the initial value of d_{31} is regained. Aging at room temperature for 43 days increases Q_m by approximately 6%, which is much lower compared to the changes observed in hard PZT. The changes in d_{31} are even lower. The overall behavior of NBT-xBT:ZnO clearly demonstrates the low correlation between d_{31} and Q_m, suggesting the presence of a different defect mechanism in the lead-free material. Hence, the well-established ferroelectric hardening mechanism for PZT and BT should be handled with care when transferring it to NBT-xBT.

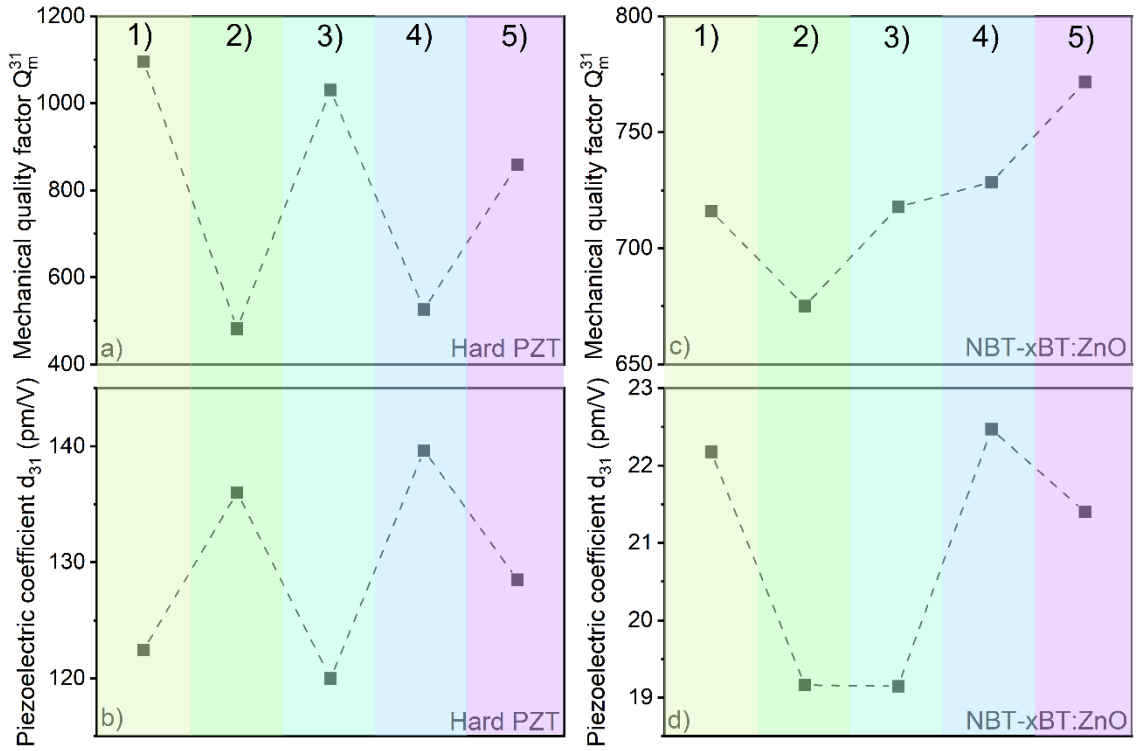

Figure 57: Mechanical quality factor Q_m and piezoelectric coefficient d_{31} of hard PZT (a and b) and NBT-xBT:ZnO (c and d) at different states: 1) poled, aged at RT for 5 weeks, and not fatigued; 2) fatigued at 1.5 m/s for 3.3×10^9 cycles; 3) recovered at RT for 37 days; 4) 1 h after new poling; and 5) aged for 18 or 43 days (hard PZT and NBT-xBT:ZnO) at RT.

During attempts to reach the maximum vibration velocity at which the samples mechanically break, the limit of the amplifier was reached before breaking. Hard PZT did not fail until 2.7 m/s, and NBT-xBT:ZnO did not fail until 4.8 m/s. Others have reported mechanical fracture in hard PZT at 2.6 ±0.3 m/s and in NBT-xBT-based material at 4.4 ±0.2 m/s[217], which correspond to a fracture strength of 63 ±7 MPa and 128 ±6 MPa, respectively. The observed maximum vibration velocities are within the boundaries of the reported dynamic fracture strength, which itself is in good agreement with the reported static fracture strength.[258] NBT-xBT-based compositions also have a much higher fracture toughness in comparison to PZT.[259] Both, a higher fracture strength and a higher fracture toughness, are beneficial in terms of applications since higher vibration velocities can be reached before mechanical failure.

Testing of the maximum reachable vibration velocity under continuous drive yielded some interesting findings. Hard PZT has a limit of approximately 1.7 m/s (Figure 58a), which cannot be overcome even when the input voltage increases further (Figure 58b). Furthermore, the current increases along with the voltage, resulting in a linear increasing power input (Figure 58 c). The temperature rises proportionally to the power input. Even though the *v* remains constant

at 1.7 m/s, the temperature rises until approximately 175 °C. Figure 53 indicates that the resonance frequency first increases with the temperature of the sample but then decreases again above approximately 105 °C. Hard PZT became more difficult to control when the voltage is increased, which resulted in a jump out of resonance frequency. Hence, it was not possible to further increase the power input above 7 W.

NBT-xBT:ZnO, by contrast, is more stable even at the maximal attainable *v*, which is around 1.8 m/s (Figure 58d). Surprisingly, this is close to the value of hard PZT despite the higher mechanical fracture toughness and strength and the higher stability of Q_m against increasing *v*. This is an important observation for the use of NBT-xBT in applications. Burst analyses suggest a high possible operation vibration velocity for NBT-based materials, which was not reached in continuous drive. As with hard PZT, the input voltage for NBT-based materials can be increased further, which leads to an increase in the current and the power input. The temperature also increases since it is proportional to the power input. When the depolarization temperature is reached, a sharp drop in *v* is observed. Interestingly, *v* does not drop to 0 but remains considerably larger than 0. The findings indicate that polarized regions still exist above the depolarization temperature, as reported previously.[133] By further increase of the power input, the temperature also increases. Close to 200 °C, the power input and the temperature increase exponentially until the sample melts (Figure 59, quantifiable temperature was limited to 500 °C) and *v* eventually drops to 0.

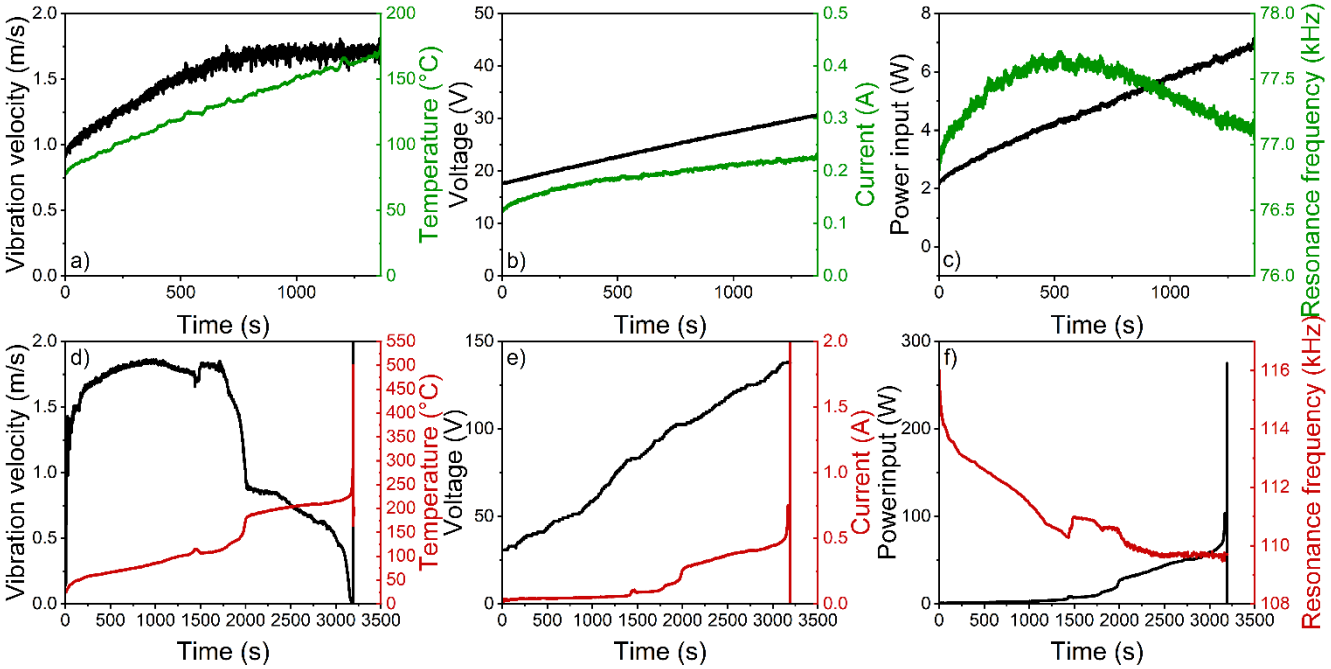

Figure 58: *In situ* a) and d) vibration velocity and temperature, b) and e) voltage and current, d) and f) power input and resonance frequency of hard PZT (a-c) and NBT-xBT:ZnO (d-f) during the test of maximum attainable vibration velocity.

Figure 59: Molten NBT-xBT:ZnO sample due to self-heating.

In addition to fatigue with a defined number of cycles, attempts were made to drive the samples until failure, but the state of failure was never reached. Hard PZT was driven continuously in the 31 mode at 1.5 m/s for 465 h, which corresponds to approximately 1.31×10^{11} cycles. NBT-xBT:ZnO was driven continuously in the 31 mode at 1.5 m/s for 164 h, which corresponds to approximately 6.8×10^{10} cycles. Both materials were stable during this long measuring time.[XXIV] Although the sample geometry and the conditions are different compared with those in the real application, both materials exhibit high persistence.

[XXIV] Since these two measurements took 1 month, the decision was made not to wait for failure. Instead, the samples were measured for a defined number of cycles at different vibration velocities.

5.3.3 Electromechanical Properties in Resonance under Uniaxial Compressive Stress

In many high-power applications, ceramics are mechanically pre-stressed to ensure mechanical coupling to the system and to drive the ceramic under compressive stress. By contrast, when the resonance method is used to determine the electromechanical properties, the sample should be in free boundary conditions, as in Figure 60-1. Here, the resonance method is used with mechanical pre-stress to achieve the same conditions as (or as close as possible to) those in the application.

The Q_m obtained in free boundary conditions is around 1,000 for hard PZT. This experimental setup is difficult since wires must be glued to the sample. Instead, the sample is often clamped between two electrodes with very low clamping force and spring constant. This setup is reproduced in Figure 60-4 and results in a Q_m of approximately 200. Hence, depending on the measurement setup, there is a fivefold difference in Q_m. The low Q_m must be handled with care, as Q_m is determined from the whole system and not independently from the sample. Two other measurement setups confirm the high dependency of Q_m on the mounting. In Figure 60-2, the sample is horizontally placed on the knot point; Q_m is almost the same as it is for the free boundary conditions (Figure 60-1). This is the method used in this work. In Figure 60-3, the sample has free boundary conditions but is placed vertically; hence, the weight of the sample is on the sample itself, resulting in a Q_m of approximately 650.

The harsh drop in Q_m with the small load is reproducible when the sample is placed into a mechanical load frame (Figure 61). The drop in the pure NBT-xBT composition is the lowest, likely due to the overall lower Q_m. A further increase in compressive stress does not alter the Q_m of the NBT-xBT-based compositions—it remains constant within the range of error. Up to about 25 MPa, NBT-xBT:ZnO reveals a higher Q_m than the undoped composition. Hard PZT, by contrast, experiences an increase in Q_m from 1 MPa and higher to values as high as the initial value. Although the measured Q_m is influenced by the setup, intrinsic differences exist between the two material systems. Furthermore, d_{33} and the compliance exhibit similar behavior: They decrease in all materials logarithmically to approximately the same level (Figure 61a and c). Based on Equation (10), since piezoelectric activity correlates with elastic compliance, a decrease in d_{33} is expected when s_{33} decreases. Hard PZT experiences the largest drop in d_{33} from about 300 pm/V at 0 MPa to about 20 pm/V at 50 MPa. From 30 MPa and higher, the piezoelectric activity seems to be higher in the NBT-xBT-based materials than in hard PZT, especially in the composite. The permittivity is constant with increasing pressure

in the NBT-based materials except for the increase from 0 MPa to 1 MPa. This increase should be related to the measuring condition discussed in Figure 60, which is also seen in Q_m. Hard PZT, however, reveals a slight increase in permittivity with a further increase in compressive stress. This increase is believed to be related to a change in the domain structure.

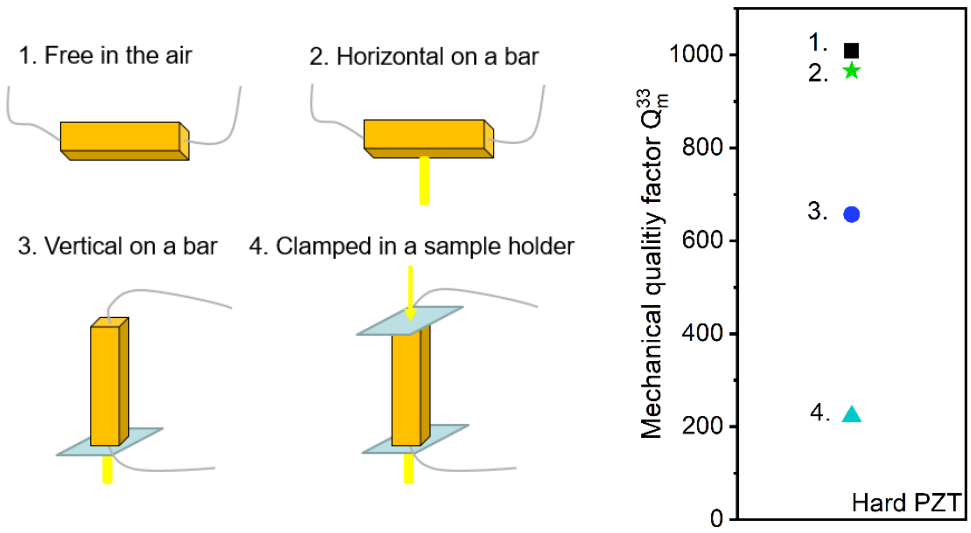

Figure 60: Samples in the 33 geometry placed in different ways to measure small-signal resonance properties and the resulting mechanical quality factor Q_m. 1. Thin silver wires keep the sample hanging in the air. 2. The sample is placed horizontally on a bar. 3. The sample is placed vertically. 4. The sample is placed between two needle-shaped electrodes. The samples were contacted with silver wires as electrodes in all cases to exclude influences from the electrical contact.

In the literature, the piezoelectric response has been investigated in dependence of the uniaxial compressive stress a few times but never in resonance. On the one hand, Daneshpajooh et al. [260] investigated piezoelectric soft PZT rings in a transducer setup. They found an almost constant d_{33} with increasing compressive stress and increasing elastic losses. On the other hand, Ochoa et al. [261] and Schader et al. [189] observed an increase in d_{33} with increasing compressive stress in hard PZT. They both investigated the direct piezoelectric effect. Schader et al. measured up to higher stress levels and found a decline in d_{33} from 80 MPa and higher. Above 80 MPa, the domain walls are mechanically clamped again, and depolarization occurs, thereby reducing d_{33}. Aside from PZT, Schader et al. also investigated NBT-3, -6, -9, and -12BT under compressive stress. They found that d_{33} decreased in all compositions with increasing stress. Zhang et al. [262] used a different setup in which they adapted to the dynamic stress to keep it constant. They measured the inverse and direct piezoelectric effects at 10 Hz

and found that d_{33} decreased, whereas d_{31} increased.[XXV] This finding is explained by the facilitation of non-180° DW and a reverse-aging effect. All reported results highlight the sensitivity of the piezoelectric activity to a uniaxial compressive stress, although the findings strongly depend on the exact measuring conditions, such as the frequency, the inverse or direct effect, or the dynamic stress.

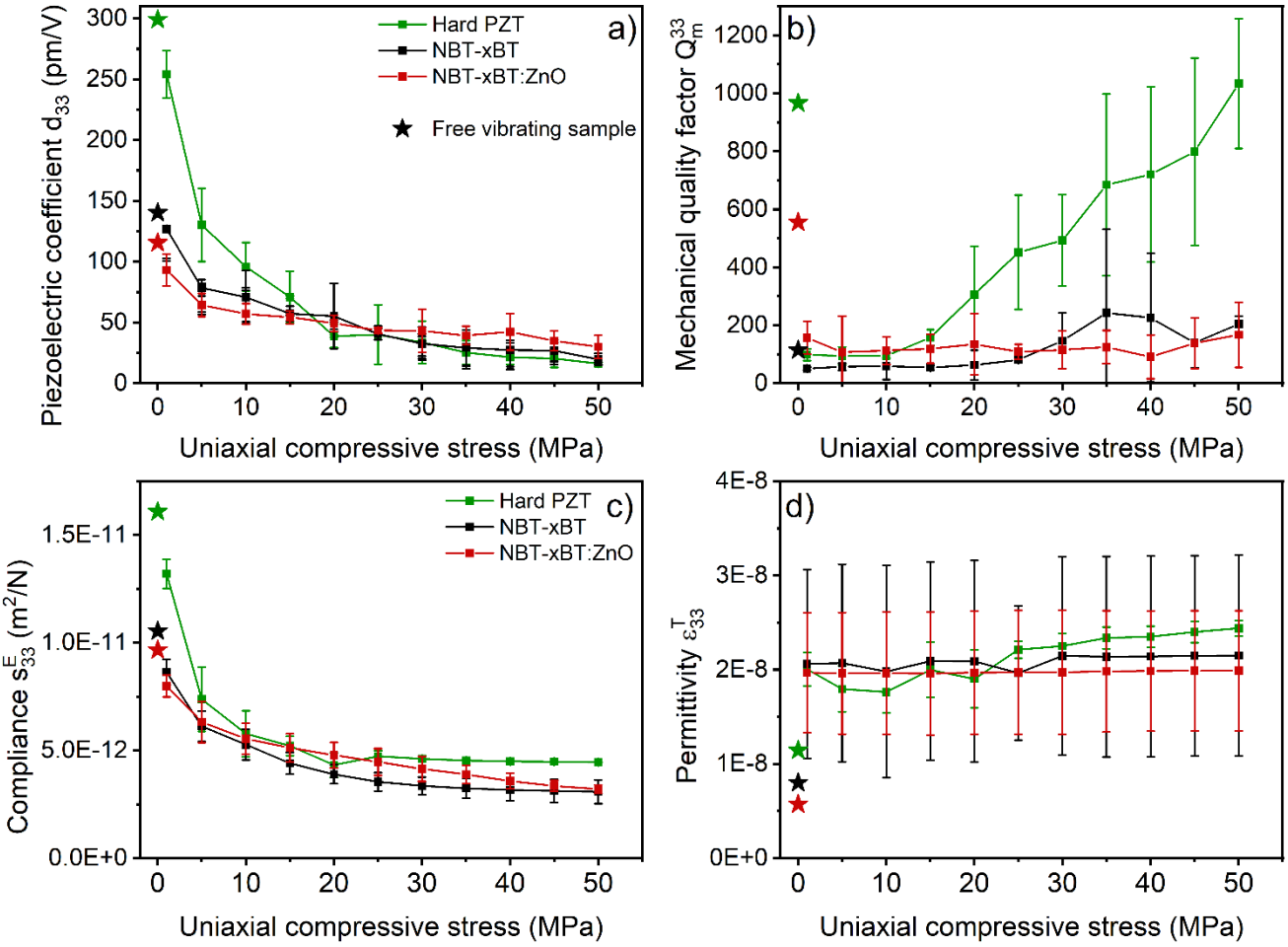

Figure 61: a) Piezoelectric coefficient d_{33}, b) mechanical quality factor Q_{m}^{33}, c) compliance s_{33}^{E}, and d) permittivity $\varepsilon_{33}^{\mathrm{T}}$ depending on mechanical compressive stress for NBT-xBT, NBT-xBT:ZnO, and hard PZT (P4).

In the literature, mostly mechanical pre-stress and the direct piezoelectric effect are measured, whereas in the present study, mechanical pre-stress and the indirect piezoelectric effect are investigated. Mechanical stress counteracts the indirect piezoelectric effect and acts as a clamping force. With increasing mechanical load, the material approaches the blocking force.

[XXV] Note that d_{31} is given in negative values.

The pre-stress should not antagonize additional stress when the direct piezoelectric effect is measured. Mechanical stress will lead to domain reorientation and depinning of DWs from defects, which would alter the piezoelectric response. Hence, the piezoelectric activity can increase to a certain stress level.

It is suggested that the different behavior of NBT-xBT/NBT-xBT:ZnO and hard PZT originates from their different intrinsic and extrinsic contributions to the piezoelectric response.[114] In PZT, extrinsic contributions are higher and might be suppressed by an increasing mechanical compressive stress. Lower extrinsic contributions simultaneously decrease the piezoelectric response and reduce the losses originating from domain wall movement. In NBT-xBT-based materials, the extrinsic contributions are lower and more stable against mechanical load.[114] Hence, Q_m is more stable against mechanical stress and the decrease in d_{33} is lower in NBT-xBT:ZnO than in hard PZT.

6 $(1-x)Na_{1/2}Bi_{1/2}TiO_3$-$xK_{1/2}Bi_{1/2}TiO_3$

Low piezoelectric coefficients are an issue in the NBT-xBT system, but in principle they can be compensated for by a higher electric driving field. However, the high-voltage AC-field needs to be produced by a generator, which can be challenging for it and increase the cost of the generator. Furthermore, the electromechanical properties might depend on the applied electric field. Therefore, a higher piezoelectric activity is desired for high-power applications. Since, in the NBT-xBT system, a higher piezoelectric coefficient always results in a lower Q_m and T_d, another system was investigated to meet the desired requirements. The NBT-xKBT system is known for higher piezoelectric activity than the NBT-xBT system. Nevertheless, NBT-xKBT has a stable Q_m with increasing vibration velocity.

6.1 Morphotropic Phase Boundary in $(1-x)Na_{1/2}Bi_{1/2}TiO_3$-$xK_{1/2}Bi_{1/2}TiO_3$

Optimization of the sintering and poling conditions leads to a d_{33} of 178 pC/N in NBT-22KBT, which is the highest d_{33} of the investigated compositions. T_d is the lowest in NBT-20KBT with 97 °C. All the compositions, especially those close to the MPB, reveal partial ergodicity.

The relative density of NBT-xKBT strongly depends on the sintering temperature (Figure 62a). Sintering temperatures of 1125 °C and 1150 °C result in the highest relative densities for all compositions (about 96.5-97%). An increase in the sintering temperature by 25 °C to 1175 °C leads to a severe drop in the relative density below 94.5%. When sintered at 1100 °C, the density remains considerable, but it results in lower piezoelectric activity. The piezoelectric activity is depicted in Figure 62b. The maximum in d_{33} is found, depending on the sintering temperature, at NBT-21KBT when sintered at 1125 °C and at NBT-22KBT when sintered at 1150 °C. Usually, d_{33} is measured 24 h after poling. A comparison of 0 h and 24 h after poling reveals a strong decrease in d_{33} with time. On average, d_{33} falls by 15 pC/N in the first 24 h after poling. However, Figure 62b displays values with non-optimized poling conditions.

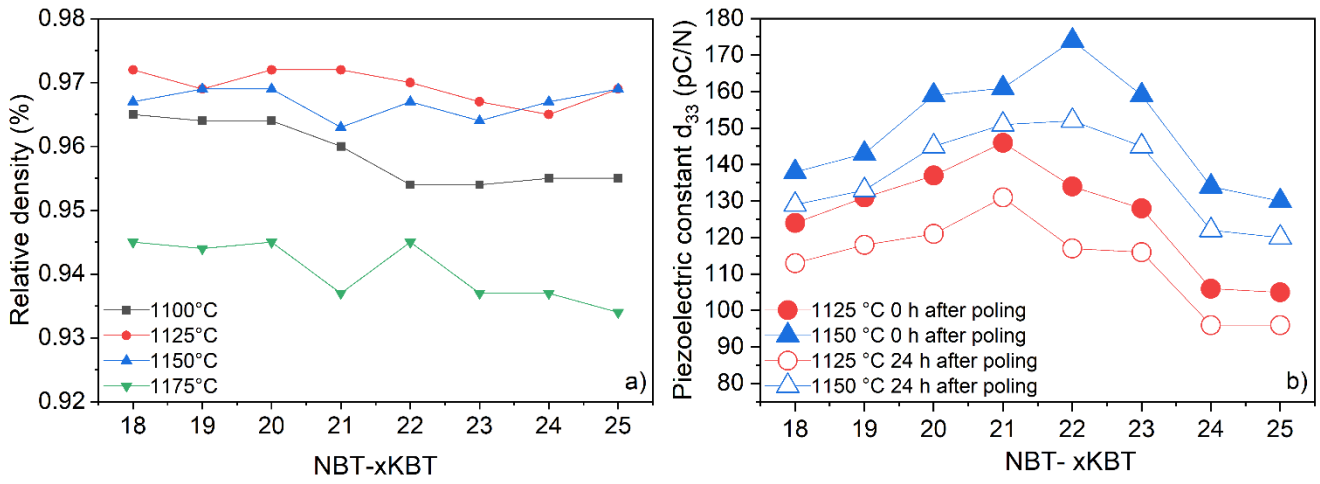

Figure 62: a) Relative density of NBT-xKBT with x = 18, 19, 20, 21, 22, 23, 24, and 25 mol% at 1100 °C, 1125 °C, 1150 °C, and 1175 °C sintering temperatures. b) Piezoelectric constant d_{33} directly after poling and 24 h after poling of the same compositions sintered at 1125 °C and 1150 °C. Poling conditions: 30 °C, 15 min, 5 kV/mm.

Zhang et al. [263] obtained the highest d_{33} of 192 pC/N for NBT-22KBT at 1150 °C sintering temperature. Optimization of the poling conditions leads to a comparable d_{33} of 186 pC/N directly after poling and 178 pC/N 24 h after poling (Figure 63a, sintered at 1150 °C).[XXVI] The discrepancy of the results presented here to the results of Zhang et al. might originate from different measuring conditions: d_{33} was usually determined at 110 Hz and a dynamic force of 0.25 N in this work. When increasing the frequency to 300 Hz and the dynamic force to 2 N, values of 215 pC/N were measured, revealing a strong dependency on the measuring conditions too. Poling at 30 °C reveals considerably lower d_{33} values (Figure 63a). An increased poling temperature reduces the potential well of domain orientation or polarization rotation in general. The better aligned domains maintain their configuration when cooling with an electrical field.[264] Li et al. [265] reported charge accumulation at grain boundaries, (leading to an internal bias field) to be the main responsible effect on the piezoelectric properties in $Ba(Zr_{0.2}Ti_{0.8})O_3$–$x(Ba_{0.7}Ca_{0.3})TiO_3$ (BZT–BCT). Additionally, cooling under field increased the lattice distortion in BZT-BCT, which could also tailor the temperature stability. The same effect might occur in the investigated NBT-xKBT too, since cooling under field also leads to an increase of T_d (Figure 63b). In general, the lowest T_d of the NBT-xKBT compositions is at NBT-20KBT (about 97 °C). Similar to the NBT-xBT system, the minimum of T_d and the maximum of d_{33} are not in the same composition. In both cases, the maximum of d_{33} is located at lower NBT

[XXVI] Poling conditions: 10 min at 140 °C and 5 kV/mm, cooling to 30 °C with 2 °C/min and 5 kV/mm.

content and thus, on the tetragonal side of the MPB. Compared with NBT-xBT, the maximum d_{33} is about 9% higher in the NBT-xKBT, whereas the minimum in T_d is about 5% lower.

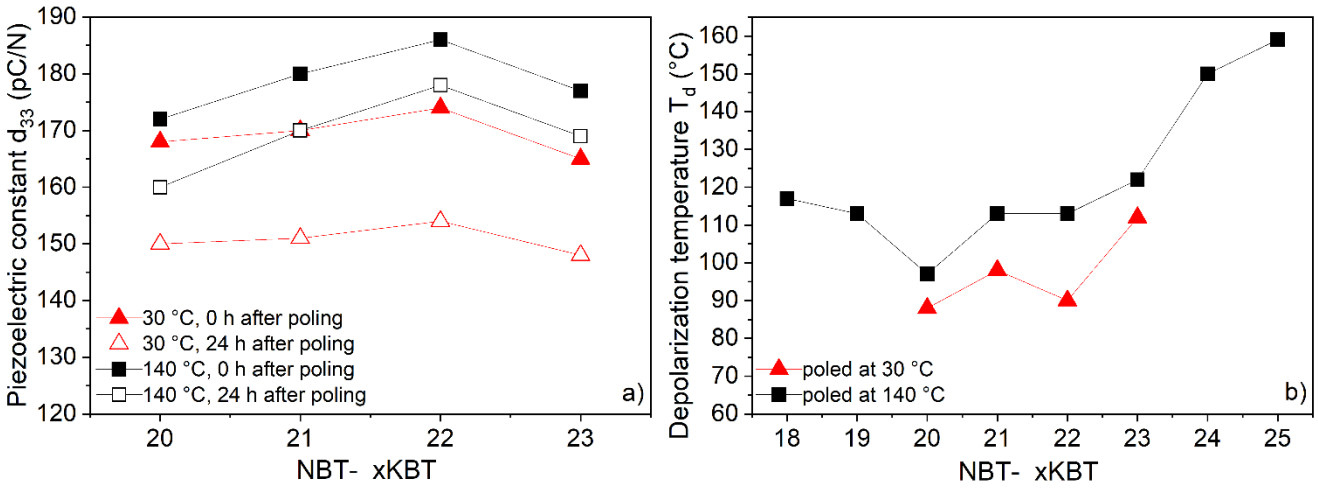

Figure 63: a) Piezoelectric constant d_{33} and b) depolarization temperature T_d of NBT-18KBT to NBT-25KBT poled at 30 °C (black) and 140 °C (red). Sintering temperature: 1150 °C. The corresponding TSDC measurements are presented in Figure S14.

When investigating the depolarization behavior of NBT-21KBT poled at 30 °C and 140 °C, the maximum in the depolarization current shifts to a higher temperature when poled at 140 °C (Figure 64). In both cases, the depolarization current does not have a sharp peak but rises continuously from room temperature, which indicates a partial depolarization of the material prior to T_d. A maximum defines the depolarization temperature, after which the current drops immediately. For the sample poled at 140 °C, the current does not drop to zero up to 200 °C. This finding indicates that, although the depolarization is defined at the current maximum, depolarization happens over a broad temperature range even above T_d. Similar behavior occurs in the permittivity against temperature behavior (Figure 65b). A strong frequency dispersion is present, which is an indication of relaxor behavior. Although Figure 65 illustrates poled samples, a clear transition from the ferroelectric to the relaxor phase is not visible in the NBT-21KBT. This transition is much more defined in the NBT-18KBT (Figure 65a). A small frequency dispersion below T_{F-R} is present in the NBT-18KBT, too. Frequency dispersion indicates the ergodicity of the material, which could explain the strong decrease of d_{33} over time. T_{F-R} is found at 124 °C and 127 °C for NBT-18KBT and NBT-21KBT, respectively. These temperatures are higher than the depolarization temperatures, likely due to the randomization of the domain configuration in the ferroelectric phase.

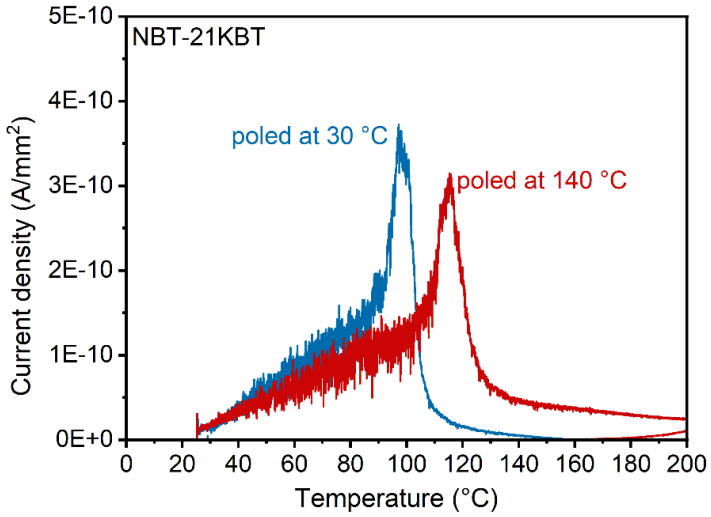

Figure 64: Thermally stimulated depolarization temperature (TSDC) of NBT-21KBT poled at 30 °C (blue) and 140 °C (red).

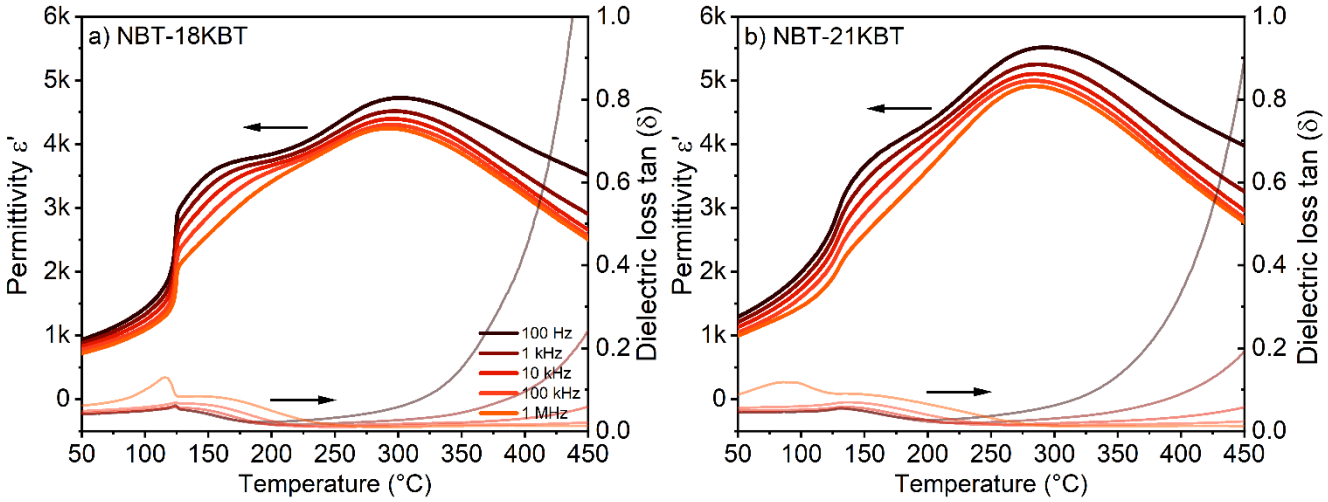

Figure 65: Permittivity *ε*' and dielectric loss *tan*(δ) at different frequencies against temperature of poled NBT-18KBT (a) and NBT-21KBT (b).

The X-ray diffraction patterns were collected from the sintering- and poling-optimized samples. Rietveld refinement of unpoled NBT-20KBT to NBT-23KBT reveals a pure cubic $Pm\bar{3}m$ crystal structure in all compositions. A small tetragonal or rhombohedral distortion may be present, but it cannot be reliably resolved with the given 2θ resolution (Figure S15). However, when poled, no cubic phase is necessary to refine NBT-20KBT to NBT-23KBT (the data file of poled NBT-22KBT was corrupted and hence could not be refined). The rhombohedral *R*3*c* phase decreases with increasing KBT content, and the tetragonal *P*4*mm* phase increases simultaneously. A similar trend was observed by Jing et al. [199] in unpoled powder. However, the lattice distortion increases in the tetragonal phase and decreases in the rhombohedral

phase with increasing KBT content. The powder diffraction data of Jing et al. [199] also revealed an increase in rhombohedral lattice distortion with increasing KBT content. However, the tetragonal lattice distortion remains unaffected by the KBT content in their observations. On the other hand, Otonicar et al. [198] confirmed the results found in this work. As in NBT-xBT, the lattice distortion of the tetragonal phase in NBT-xKBT correlates with the thermal stability, which is the lowest for NBT-20KBT.

Table 12: Phase fraction and lattice distortion (δ_R = rhombohedral, δ_T = tetragonal) of poled NBT-20KBT, NBT-21KBT, and NBT-23KBT. The data were collected at ESRF in Grenoble. The file of NBT-22KBT was corrupted and hence not refined.[XXVII]

Composition - poled -	*P*4*mm* (%)	*R*3*c* (%)	δ_R	δ_T
NBT-20KBT	22	78	0.0068	0.0105
NBT-21KBT	65	35	0.0059	0.0123
NBT-23KBT	69	31	0.0047	0.0126

6.2 NBT-xKBT: Doping and Composites

Similar to the NBT-xBT system, the NBT-xKBT compositions need to be tailored to obtain lower mechanical losses and higher temperature stability.
Modification by doping can increase the depolarization temperature, but with the drawback of lower piezoelectric activity. The ZnO secondary phase does not shift T_d but defines it in a smaller temperature range, reducing the ergodicity. The mechanical losses are not affected considerably by different types of chemical modifications, such as doping, ZnO secondary phase, or K-non-stoichiometry.

The X-ray diffraction pattern of NBT-21KBT doped with 0.5 mol% Mg exemplary reveal the changes in the crystal structure caused by acceptor doping (Figure S16). In the unpoled state, NBT-21KBT-0.5Mg consists of 18% tetragonal *P*4*mm* and 82% cubic $Pm\bar{3}m$. The tetragonal lattice distortion is relatively low, with δ_T = 0.0113. The increase in the tetragonal phase fraction by doping is known from the NBT-xBT system. However, Mg doping seems less impactful at increasing the tetragonal phase fraction, increasing it by about 20% in NBT-21KBT-0.5Mg, compared with roughly 40% in NBT-xBT. In NBT-xBT, the increase in the tetragonal phase

[XXVII] The measurements in Grenoble at the synchrotron were performed by Jurij Koruza. The Rietveld refinement was performed by Andreas Wohninsland.

fraction is correlated with a shift in the MPB (Subchapter 5.1.1), which seems possible in NBT-xKBT too, but was not investigated. When NBT-21KBT-0.5Mg is poled, the phase ratio shifts toward similar values to those in the undoped, poled NBT-21KBT, with about 63% *R*3*c* and 37% *P*4*mm*. The lattice distortion slightly increases in the *R*3*c* and *P*4*mm* phases when doped and poled, from δ_R = 0.0059 to δ_R = 0.0063 and from δ_T = 0.0123 to δ_T = 0.0134. Overall, Mg doping increases the non-cubic phase fraction in the unpoled state and the lattice distortion in the poled state while maintaining the same phase ratio in the poled state.

The increases of T_d via acceptor doping by about 20-30 °C in the NBT-20KBT and NBT-21KBT (Figure 66a) is believed to originate from the increased lattice distortion. Zn and Mg doping both revealed a comparable effect, whereas 0.5 mol% Zn and 1 mol% Mg increase T_d by about the same amount in NBT-20KBT. Introducing an additional ZnO secondary phase does not tailor T_d any further, but decreases it again. This outcome suggests that either the doping and the effect of a secondary phase are not adding up in NBT-xKBT or the ZnO secondary phase does not produce the same effect as in NBT-xBT. In the literature, Al_2O_3, ZrO_2, and HfO_2 have been investigated as secondary phases, with Al_2O_3 increasing T_d and the others decreasing it.[206] Changing the stoichiometry on the A-site by reducing the K amount does tendentially decrease T_d. Adding ZnO does not increase the depolarization temperature but changes the depolarization behavior below T_d. Figure 67 reveals the thermally stimulated depolarization current of NBT-21KBT:ZnO composites compared with the same compositions without ZnO secondary phase. Clearly, ZnO influences the overall depolarization behavior. With ZnO secondary phase, the current peak is more pronounced. In contrast, the compositions without the ZnO secondary phase (Figure 67a) have a broader depolarization current peak in the temperature range below T_d, which is attributed to partial depolarization of the material.

All the investigated compositional changes in NBT-20KBT and NBT-21KBT lead to a decrease in piezoelectric activity. Increasing the Mg doping concentration results in a performance loss of up to 41% in d_{33} in NBT-20KBT (e.g., see Figure 66b). Adding ZnO reduces d_{33} further. A ZnO secondary phase does not contribute to the piezoelectric activity; hence, the overall piezoelectricity decreases. Usually, an increase in T_d and a simultaneous decrease of d_{33} are correlated with an increased lattice distortion, as known from the related NBT-xBT system.[143]

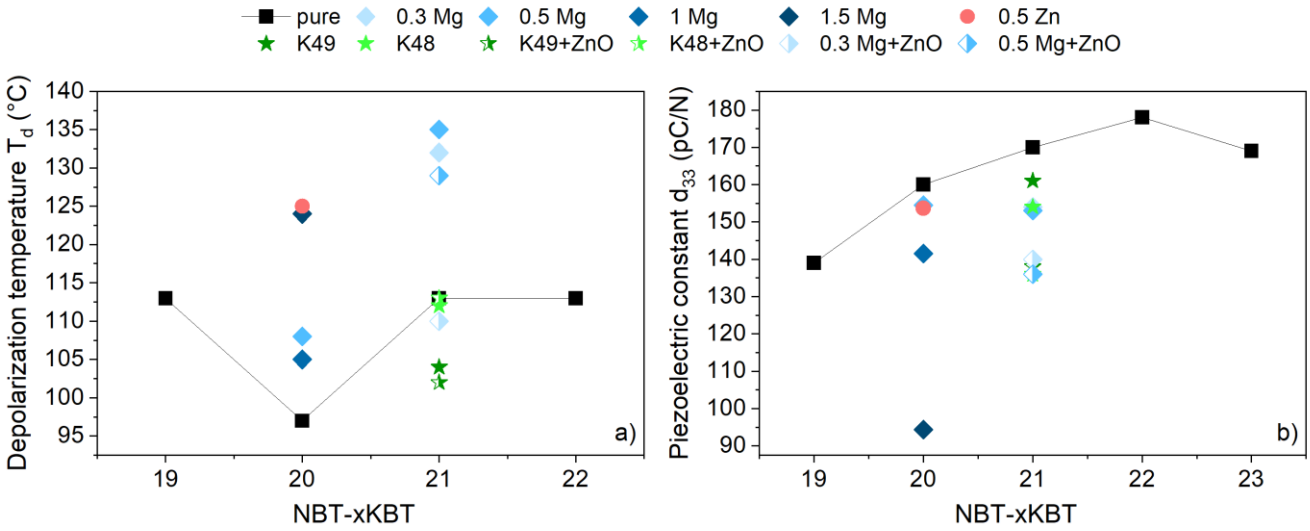

Figure 66: a) Depolarization temperature T_d and b) piezoelectric constant d_{33} of NBT-19KBT to NBT-23KBT with Mg and Zn doping, K non-stoichiometry, and ZnO secondary phase.

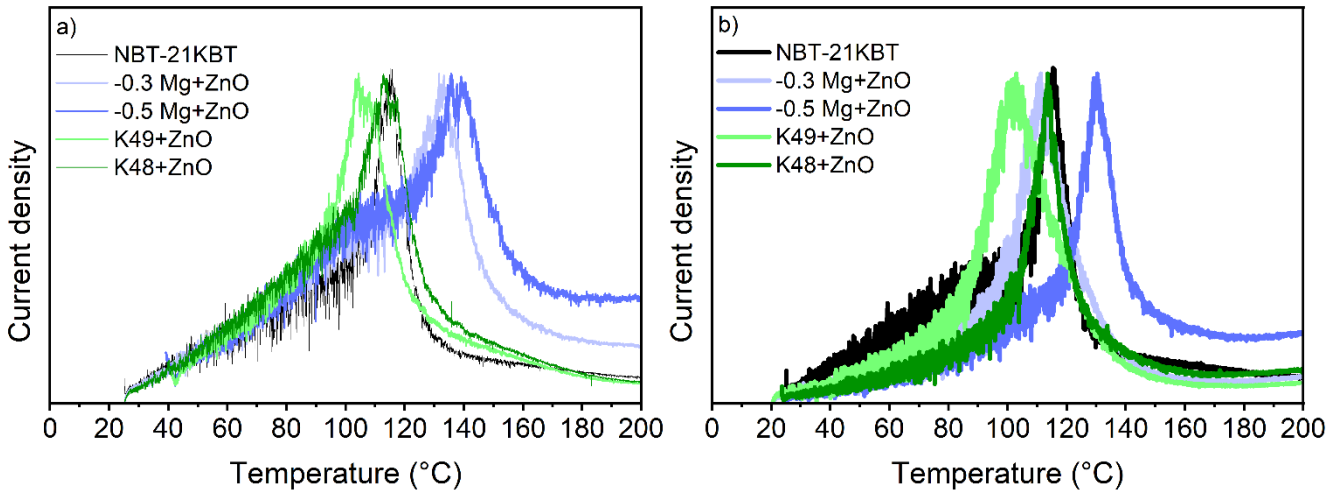

Figure 67: Thermally stimulated depolarization current of a) NBT-21KBT doped with 0.3, 0.5 mol% Mg, and 1, 2 mol% K deficiency and b) the same modified NBT-21KBT compositions with the ZnO secondary phase. As a comparison, the unmodified NBT-21KBT is depicted. The depolarization currents are normalized to unity for better comparison.

In addition to tailoring the depolarization temperature in NBT-xKBT, a reduction of mechanical losses is also within the scope of chemical modification (doping, non-stoichiometry, composite). Figure 68 compares the mechanical quality factor in planar (a) and thickness (b) resonance modes. In both cases, no significant increase in Q_m is observed, especially when compared with the sevenfold increase in Q_m in NBT-xBT caused by Mg doping. Therefore, it is argued that acceptor-doping and the introduction of ZnO secondary phases do not affect the mechanical losses in NBT-xKBT. No change in the coercive field or internal bias field are

obtained from P-E measurements of the NBT-20KBT modified samples. This behavior is unexpected, since the same chemical modifications hugely impacted the very similar NBT-xBT system.

Zhang et al. [266] investigated the modification of the ternary system NBT-xBT-yKBT with Mn and observed a huge increase in Q_m. This finding might hint at Ba playing a major role in the ferroelectric hardening of NBT-based ceramics: NBT-based materials containing Ba, such as NBT-xBT and NBT-xBT-yKBT, experience ferroelectric hardening via acceptor doping, whereas NBT-xKBT, which does not contain Ba, shows no signs of ferroelectric hardening via acceptor doping. The role of Ba in ferroelectric hardening in these compositions is suggest as a future research question.

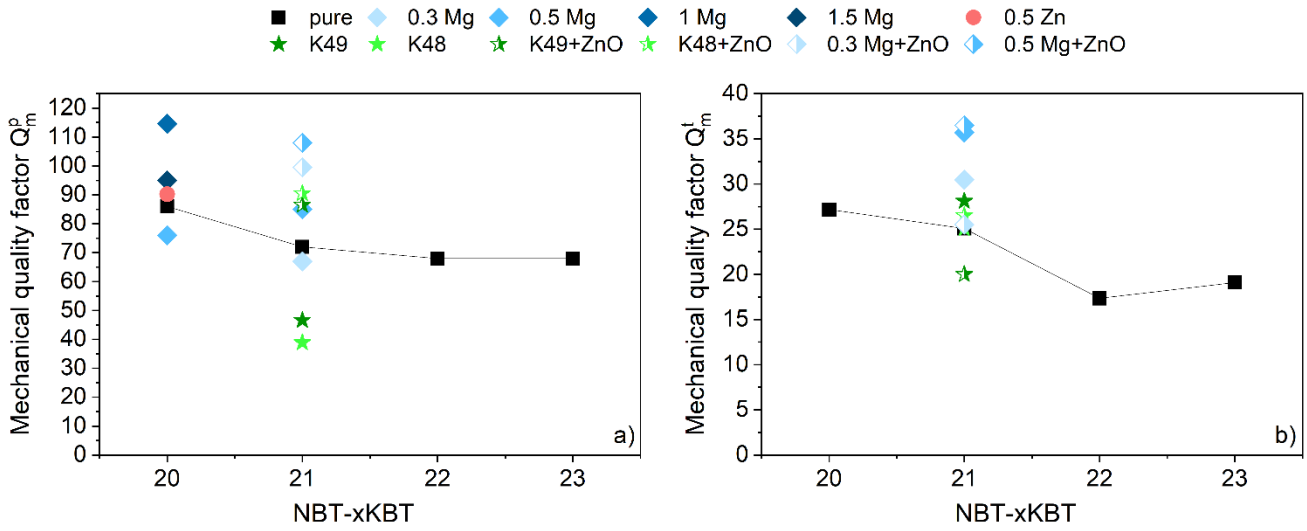

Figure 68: a) Mechanical quality factor Q_m^p in planar mode and b) mechanical quality factor Q_m^t in thickness mode of NBT-20KBT to NBT-23KBT modified by Zn and Mg doping, K-non-stoichiometry and ZnO as a secondary phase.

The coupling factor k_p in planar resonance mode decreases with increasing KBT content. In contrast, the coupling factor k_t in thickness mode displays no dependency on the KBT content (Figure 69). Doping does not change k_p significantly in NBT-20KBT and NBT-21KBT, apart from 1.5 mol% Mg doping. This decrease is related to the drop in d_{33}. On the other hand, a more or less constant k_p and a small increase of k_t with chemical modification are not expected, since d_{33} decreases in the same compositions, which should also result in a drop of k. Based on Equation (10), the behavior of k and d signifies a simultaneous decrease of the permittivity and/or the compliance. Overall, the coupling coefficient cannot be modified considerably by the investigated strategies.

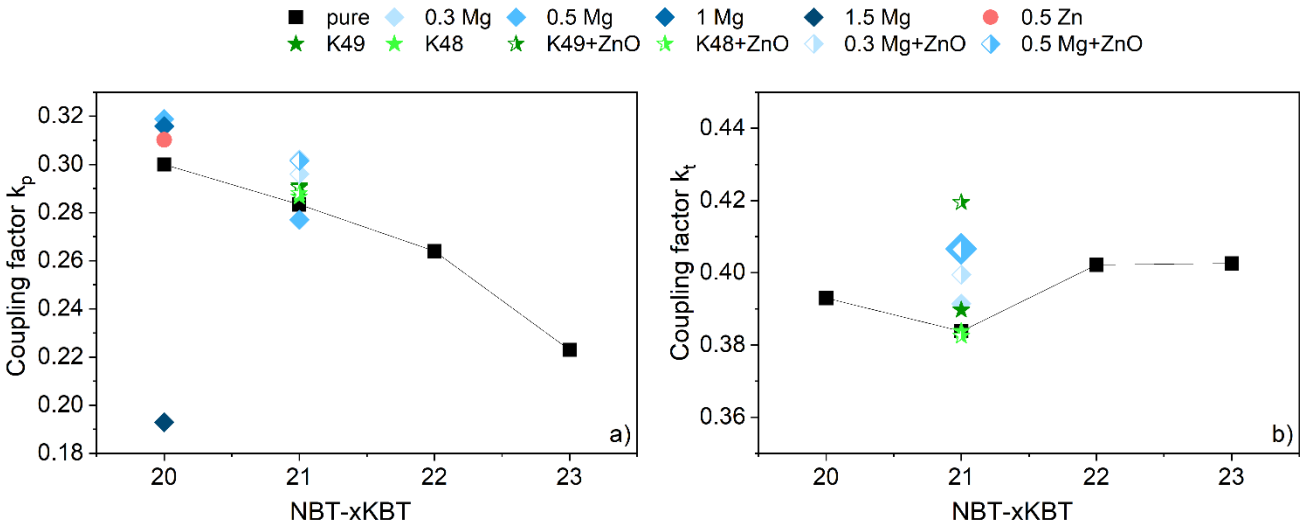

Figure 69: a) Coupling factor k_p in planar mode and b) coupling factor k_t in thickness mode of NBT-20KBT to NBT-23KBT modified by Zn and Mg doping, K non-stoichiometry, and ZnO as a secondary phase.

7 (1-x)$Na_{1/2}Bi_{1/2}TiO_3$-x$BaTiO_3$ versus (1-x)$Na_{1/2}Bi_{1/2}TiO_3$-x$K_{1/2}Bi_{1/2}TiO_3$

The material systems with the main focus in this work are the NBT-xBT and NBT-xKBT solid solutions. Both are investigated and discussed individually in Chapters 5 and *6, respectively. In this chapter, the main differences and similarities are highlighted. This discussion includes not only the electromechanical and structural properties, but also the processing and usability for applications.*

Both material systems have an MPB between the rhombohedral R3c and tetragonal P4mm phases. The minimum T_d is found on the NBT-rich side, whereas the maximum in d_{33} is found on the NBT-lean side of the MPB. Acceptor-doping increases T_d and decreases d_{33}. A major difference is the effect on the mechanical loss, which is significantly influenced by acceptor-doping or the ZnO secondary phase in the NBT-xBT but displays no considerable change in the NBT-xKBT system. The NBT-xKBT compositions at the MPB are partly ergodic when poled. This outcome is not the case for the NBT-xBT compositions near the MPB.

In the literature, NBT-xKBT is often produced using hygroscopic K_2CO_3.[195, 198, 209] Several strategies exist to avoid humidity while weighing the initial powders: Using a protective atmosphere, using non-hygroscopic $KHCO_3$, or rapid weighing (rather imprecise). When using the second method, as in this work, there is no major difference in the processing route between NBT-xBT and NBT-xKBT. The sintering conditions vary depending on the modification of the composition. Pure NBT-xBT is sintered at 1150 °C for 3 h, and pure NBT-xKBT possesses the best electromechanical properties when sintered at 1150 °C for 2 h. Doped compositions are sintered at 1100 °C for 1 h and 2 h (NBT-xBT and NBT-xKBT, respectively). Regarding polarization and depolarization, the material systems reveal distinct differences. Poling with temperature has no effect on the temperature stability or magnitude of the piezoelectric activity of NBT-xBT, whereas poling NBT-xKBT at 120-140 °C increases d_{33} and T_d significantly.

A major consensus in both materials systems is the formation of an MPB between the rhombohedral *R*3*c* phase and the tetragonal *P*4*mm* phase (Figure 29 and Table 13). However, the position of the MPB is different in each system. The lowest depolarization temperatures are found for NBT-6BT and NBT-20KBT. On the other hand, the highest piezoelectric constant, d_{33}, is located at a higher tetragonal phase content, at around NBT-7.5BT and NBT-22KBT. Mg acceptor doping increases the tetragonal phase fraction in both solid solutions in the unpoled state but only in the poled state for the NBT-xBT system. Mg doping increases the

lattice distortion of the poled NBT-xKBT but not of the poled NBT-xBT. The lattice distortion is higher in the undoped and poled NBT-xBT as compared to the undoped and poled NBT-xKBT.

Comparing the polarization against an increasing electric field reveals a higher E_{pol} of the NBT-20KBT (Figure 70b), not only for the first polarization process, but also the switching from positive to negative polarization is less steep. Consequently, the polarization loop of the NBT-6BT has a more square-like shape, which is attributed to a higher level of ferroelectricity. NBT-6BT displays a higher S_{pol}, S_{rem}, and S_{offset} than NBT-20KBT (Figure 70a). This finding is likely due to a higher phase transformation strain (strain in the first polarization process, in which phases transform from, e.g., cubic into tetragonal).

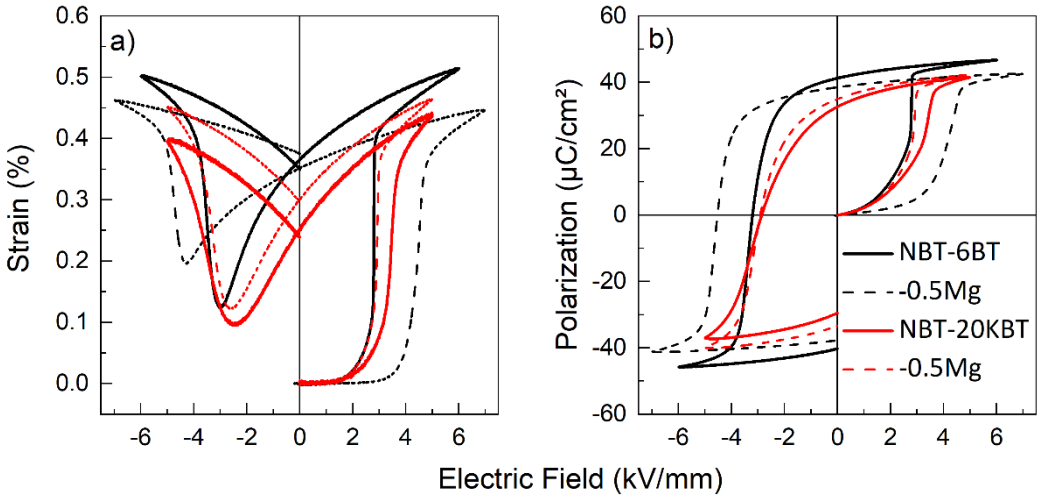

Figure 70: Strain (a) and polarization (b) against the electric field of the first loop of NBT-6BT, NBT-6BT-0.5Mg, NBT-20KBT, and NBT-20KBT-0.5Mg.

Like discussed, the P-E loops reveal a higher level of ferroelectricity in the NBT-6BT composition compared with the NBT-20KBT. The permittivity against temperature in the poled and unpoled states of both compositions is supplied in Figure 71. In the unpoled state (Figure 71b and d), no phase transitions occur, whereas in the poled state, NBT-6BT reveals sharp phase transitions at around 100 °C (Figure 71a). The sample is in the ferroelectric state below this temperature, as indicated by the absence of frequency dispersion. NBT-20KBT behaves different. Although a phase transition is located at around 100 °C, the transition is not as defined and happens across a temperature range. Moreover, a frequency dispersion is present below the transition temperature, indicating ergodicity. Similar to the permittivity plots, the TSDC measurements reveal a defined depolarization peak for NBT-6BT, whereas NBT-20KBT exhibits a very broad depolarization peak (Figure 72).

In summary, NBT-6BT fully transforms from a non-ergodic relaxor into a ferroelectric material during poling, whereas NBT-20KBT is partly ergodic within the observed temperature range. Poling NBT-20KBT at 140 °C induces a higher degree of ferroelectricity in the material. A higher level of ergodicity is true in general for all NBT-xKBT compositions near the MPB, in comparison with the NBT-xBT compositions near the MPB.

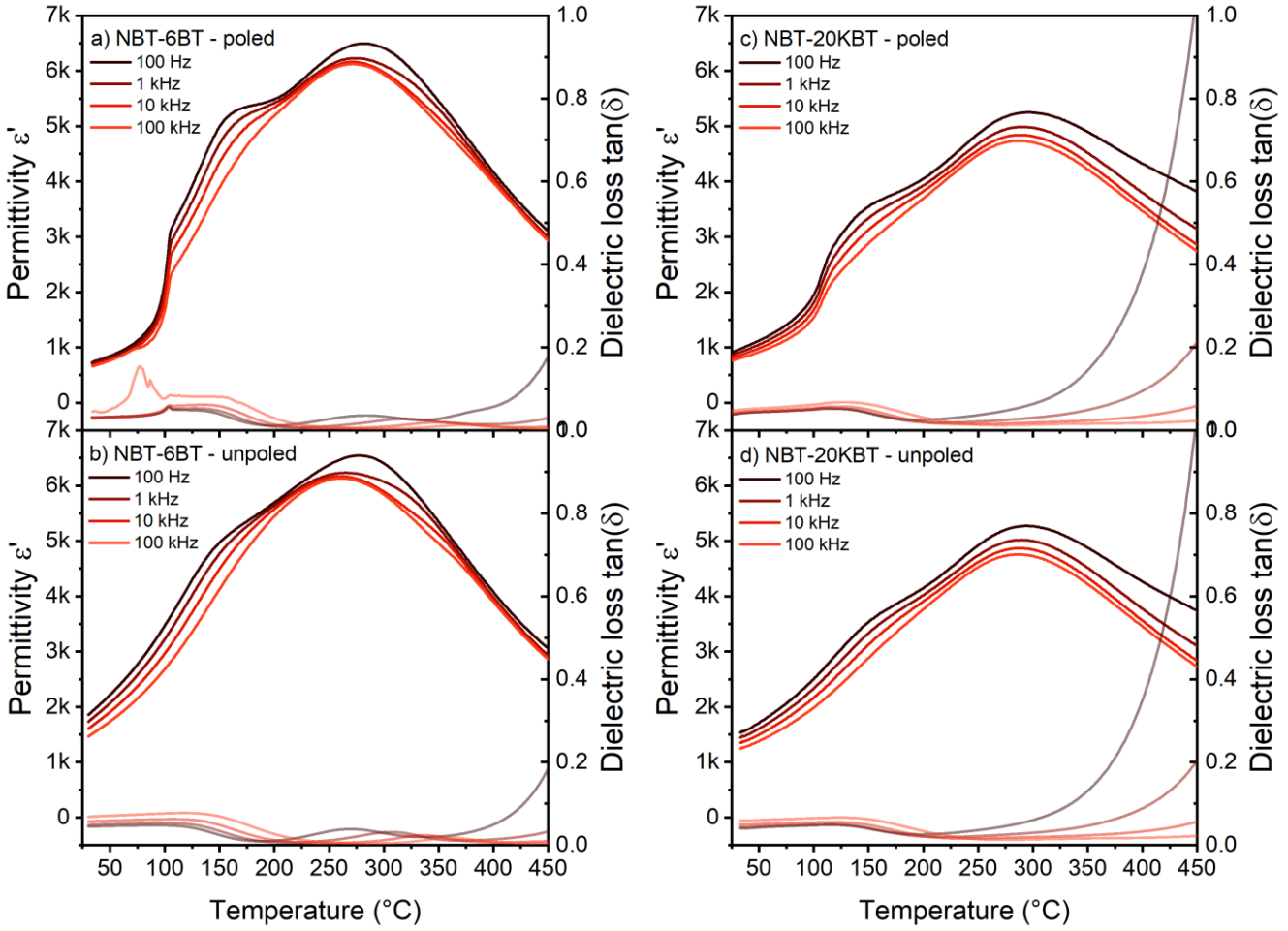

Figure 71: Permittivity *ε´* and dielectric loss *tan*(δ) against temperature of NBT-6BT and NBT-20KBT in the poled state (a and c) and in the unpoled state (b and d) at different frequencies.

Acceptor-doping at the MPB (e.g., with Mg) can shift T_d in both material systems to higher temperatures. Acceptor doping is more effective in the NBT-xBT system, with an increase of about 40 °C, in contrast to about 20 °C in NBT-xKBT. The depolarization behavior itself remains unchanged in NBT-20KBT. However, a broad depolarization peak is measured when doped with Mg (Figure 72). The TSDC of NBT-6BT-0.5Mg reveals not only the main depolarization peak at 148 °C, but also an additional smaller peak at around 80-90 °C. This

finding is attributed to the depolarization of the rhombohedral phase.[129] Hence, Mg doping predominantly impacts the tetragonal phase. The increasing current density above 100 °C in NBT-6BT-0.5Mg is caused by the conductivity of the material.[267]

Another interesting difference between both solid solutions is the effect of acceptor doping, such as Mg, on the ferroelectric hardness. NBT-20KBT-0.5Mg exhibits a slightly higher P_{rem} and a more square-shaped polarization loop than NBT-20KBT (Figure 70b). E_{pol} is lower, but the coercive field, E_c, does not change. When extrapolating the results from the P-E loops, it is clear that Q_m maintains the same value in NBT-xKBT when doped with an acceptor. In stark contrast, doping NBT-6BT with Mg leads to a significantly higher E_c and E_{pol}, a lower total strain, and a much higher Q_m, all indicating ferroelectric hardening. A few interesting hypotheses can be taken down from this outcome. First, the increases in depolarization temperature and ferroelectric hardening are not correlated in NBT-based materials. This hypothesis is supported by reports of an increase in T_d via quenching but no change in Q_m.[147] This outcome is attributed to the correlation of the depolarization temperature to the lattice distortion[143] and the phase mixture. In contrast, only a very minor correlation of the phase mixture to Q_m was observed in Subchapter 5.1.1, and no correlation of the lattice distortion to Q_m is known in the NBT-based materials.

A second hypothesis is that ferroelectric hardening due to acceptor doping might be correlated with Ba in NBT-based materials. NBT-xBT and NBT-xKBT are very similar in their microstructure, crystal structure, and electromechanical properties. Both display a similar reaction to acceptor doping, apart from ferroelectric hardening, which is only present in the solid solution with Ba. In agreement with hypothesis, ferroelectric hardening by acceptor doping was found for the ternary system NBT-xBT-yKBT.[266] From the investigation with Mg doping, Zn doping, and Bi non-stoichiometry, it is known the number of oxygen vacancies and the mobility of the defects dictate ferroelectric hardening in NBT-xBT. It is suggested that, Ba can influence either the concentration of oxygen vacancies or their mobility. Incorporating the acceptor into the lattice of NBT-xKBT is assumed, since the depolarization behavior and piezoelectric activity were tailored. Additionally, the NBT-xKBT system is very similar to the NBT-xBT system, in which the incorporation of acceptor dopants is widely accepted. NBT-xKBT was doped with large amounts of acceptor dopants; hence, the concentration of oxygen vacancies is likely comparable to that in NBT-xBT. Therefore, it seems plausible that Ba influences the mobility of the oxygen vacancies. This is an interesting topic for further research but cannot be answered in detail from the results obtained here.

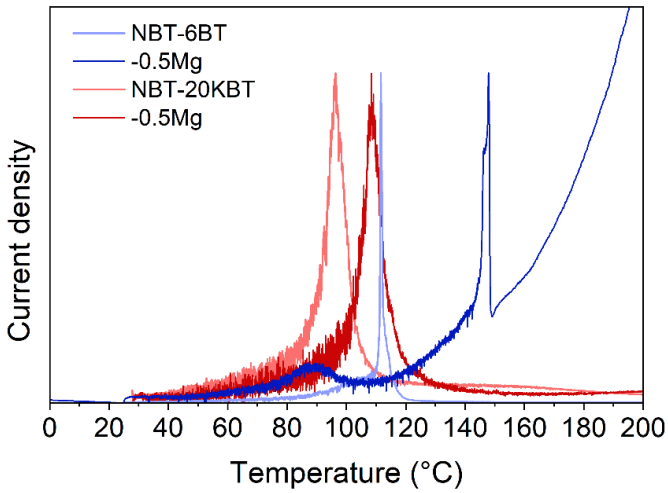

Figure 72: Thermally stimulated depolarization current of poled NBT-6BT, NBT-6BT-0.5Mg, NBT-20KBT, and NBT-20KBT-0.5Mg. The depolarization currents are normalized to unity for better comparison.

For the use of ferroelectric materials in high-power applications, the main requirements are high T_d, d_{33},and Q_m as well as high stability of Q_m against vibration velocity. A higher T_d is found in the NBT-xBT compared to NBT-xKBT. However, NBT-21KBT-0.5Mg still has a T_d of around 135 °C, which could be sufficient for most use cases. An issue for both materials is the partial depolarization, and hence loss, of piezoelectricity before T_d. In NBT-xBT, the partial depolarization is caused by a transformation of the poled rhombohedral phase into an untextured tetragonal phase.[129] The piezoelectric activity is superior in the NBT-xKBT system, with a d_{33} of still 153 pC/N when doped with Mg. In NBT-6BT-0.5Mg, d_{33} is 27% lower with 112 pC/N. d_{33} is expected to be a few points higher when taking NBT-6.5BT as a base composition instead of NBT-6BT (see Figure 31b). When only considering thermal stability and piezoelectricity, NBT-xKBT seems the favorite solid solution. Nevertheless, considering the mechanical loss, it is clear that NBT-xBT is, overall, a more suitable choice for use in high-power applications. The mechanical loss cannot be tailored considerably in the NBT-xKBT system, whereas in NBT-xBT it is increased via acceptor doping by several times and is about 10 times higher than in NBT-xKBT. Other properties, such as permittivity, density, compliance, and mechanical properties, are not considered here, but based on the experience during the experimentation, no considerable differences are expected.

8 Poling-induced Texture and its Correlation to Mechanical Losses

An outstandingly high degree of texture is revealed in NBT-based materials compared with standard materials, such as $Pb(Ti,Zr)O_3$, $BaTiO_3$, and $(K,Na)NbO_3$. The texture correlates with the characteristic intrinsic and extrinsic strain contributions in NBTs.

Some of the discussed microstructural and electromechanical properties have previously been debated. This first paragraph only recaps the necessary information to discuss the texturing degree. The discussed compositions are NBT-6BT, NBT-6BT-0.5Zn, NBT-6BT-0.5Zn-Q (quenched), NBT-21KBT, and NBT-21KBT-0.5Mg.

The relative densities of the investigated samples are 95-97%. No secondary phases were observed. The grain sizes of the undoped compositions are 1.2 ± 0.8 µm. Mg doping does not alter the grain size of NBT-21KBT. Zn doping increases the grain size to 10.4 ± 4.3 µm. The electromechanical properties, such as T_d, d_{33}, and Q_m in the planar mode, are listed in Table 13. The values for NBT-6BT slightly deviate from the values discussed in Chapter 5, since it is another batch.[XXVIII] The quenching of Zn-doped NBT-6BT raises T_d by about 30 °C and decreases d_{33} by about 10 pC/N but does not modify Q_m.

Table 13: Depolarization temperature T_d, mechanical quality factor in planar mode Q_m^p and piezoelectric constant d_{33} of NBT-6BT, NBT-6BT doped with 0.5 mol% Zn furnace cooled and quenched (Q), NBT-21KBT, and NBT-21KBT doped with 0.5 mol% Mg.

Composition	T_d (°C)	$\boldsymbol{Q_m^p}$	d_{33} (pC/N)
NBT-6BT	111	132 ± 11	140 ± 4
NBT-6BT-0.5Zn	142	570 ± 53	117 ± 3
NBT-6BT-0.5Zn-Q	173	516	107 ± 4
NBT-21KBT	114	72	170 ± 4
NBT-21KBT-0.5Mg	135	71 ± 20	154 ± 4

Table 14 depicts the phase fractions and lattice distortions of all compositions in the poled state. A phase mixture of the rhombohedral phase *R*3*c* and the tetragonal phase fraction *P*4*mm* was used for the Rietveld-refinement. The same space groups were used in the literature for NBT-6BT and NBT-22KBT.[124, 131, 268, 269] Zn doping increases the tetragonal phase fraction and the tetragonality δ_T. Quenching the NBT-6BT-0.5Zn does not alter the phase fraction any

[XXVIII] Andreas Wohninsland processed this batch. The same processing conditions as described in this work were used.

further but increases the tetragonal distortion further. The increase in the tetragonal phase fraction by Zn doping originates from a shift in the MPB and is described in Subchapter 5.1.1 for the unpoled compositions. The higher T_d is caused by the increased lattice distortion.[143] It seems the changes due to the doping and the quenching add up and originate from a different mechanism.[147] Moreover, quenching has a stronger effect on the rhombohedral lattice distortion than doping. Mg doping the NBT-21KBT does not change the phase fractions but slightly increases the rhombohedral and tetragonal lattice distortion. Again, the increased lattice distortion correlates with the higher T_d in the doped system. No direct correlation between the lattice distortion or phase composition and Q_m can be established.

Table 14: Rhombohedral (*R*3*c*) and tetragonal (*P*4*mm*) phase fractions and rhombohedral (δ_R) and tetragonal (δ_T) lattice distortions of NBT-6BT, NBT-6BT doped with 0.5 mol% Zn and quenched, NBT-21KBT, and NBT-21KBT-0.5Mg in the poled state.[XXIX] The error for the phase fraction given by Topas is in the range of ±2%. The error for the lattice distortion is smaller than the last given digit.

Composition	*R*3*c* (%)	*P*4*mm* (%)	δ_R	δ_T
NBT-6BT	84	16	0.0078	0.0126
NBT-6BT-0.5Zn	75	25	0.0077	0.0142
NBT-6BT-0.5Zn-Q	77	23	0.0079	0.0158
NBT-21KBT	65	35	0.0059	0.0123
NBT-21KBT-0.5Mg	63	37	0.0063	0.0134

8.1 Calculated Texturing Degrees from X-ray Diffraction

All the investigated NBT-based materials reveal an extreme degree of poling-induced domain texture close to the theoretical maximum in the standard model. A comparison of the texturing degree with $Pb(Zr,Ti)O_3$ (PZT), $BaTiO_3$ (BT), and $(K,Na)NbO_3$ (KNN) underlines the outstandingly high remanent degree of texture in NBT-based materials. The high remanent texture is believed to reduce the possibility of further domain alignment during application due to lower domain wall density. The correlation between domain alignment/piezoelectric activity and the texturing degree is directly proven by a non-linear correlation between d_{33} and the remanent polarization.

[XXIX] These data is also used for a publication with Andreas Wohninsland who conducted these refinements.

The diffraction pattern of poled NBT-6BT-0.5Zn is provided in Figure 73 for different azimuthal angles to the poling direction. The 200_{pc} and 111_{pc} reflections are presented to exemplify the tetragonal and rhombohedral distortion, respectively. Both reflections reveal a very high dependency of the intensities with respect to the azimuthal angle. This finding indicates a very high remanent anisotropy in the material, referred to as the degree of texture (NBT-6BT-0.5Zn is provided as an example, but all other diffraction patterns are listed as supplemental material: Figure S18). The 111_{pc} reflection consists of an overlapping tetragonal 111_T and two rhombohedral reflections, the 111_R and $11\bar{1}_R$ reflections. The 111_R strongly changes with respect to the poling direction and even vanishes at angles perpendicular to the poling direction. The tetragonal 111_T reflection reveals no dependency regarding the poling direction. Similar to the 111_{pc} reflection, the 200_{pc} reflection consists of three individual reflections: the 200_T, 002_T, and 200_R. The intensity of the tetragonal peaks strongly depends on the azimuthal angle, whereas 200_R reveals no anisotropy.

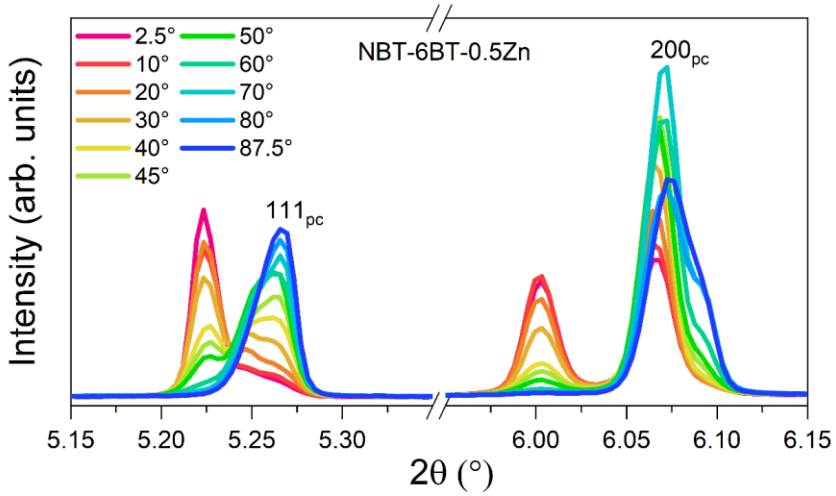

Figure 73: X-ray diffraction pattern of poled NBT-6BT-0.5Zn in the remanent state. Depicted are the 111_{pc} and 200_{pc} reflections for different angles with respect to the poling direction.

From the 111_{pc} and 200_{pc} reflections, the texturing degrees for the rhombohedral and tetragonal phases are calculated. This is defined as the pole figure density (PFD) and given in multiples of the random distribution (MRD). The standard method is described in Subchapter 4.6.3. In this classic approach, each phase is investigated individually and has a maximum PFD of 4 and 3 in the rhombohedral (f_{111}) and tetragonal (f_{002}) phases, respectively.[90] The degree of texture was found to be close to the theoretical maximum in all compositions (Figure 74). The tetragonal phase overall has a higher degree of texture than the rhombohedral phase. This finding is indicated by the high PFD values at angles up to 30°. The texturing degree of

the tetragonal phase of pure NBT-6BT is not given, since a strong overlap of the $002_T/200_T$ doublet and the 200_R singlet led to a large error. At a PFD = 1, the material is randomly oriented, which is the case at around the 45° angle. Values close to zero, which is the minimum, indicate a strong anisotropy, but with the short axis of the unit cell in this direction. When comparing the poling-induced degree of remanent texturing with other materials, in is clear that the observed degree of anisotropy is very high. For comparison, the PFDs for the tetragonal phase range from 1.2-1.5 MRD in PZT and $PbTiO_3$ (PT) and 2 MRD for $K_{0.5}Na_{0.5}NbO_3$ (KNN).[270, 271]

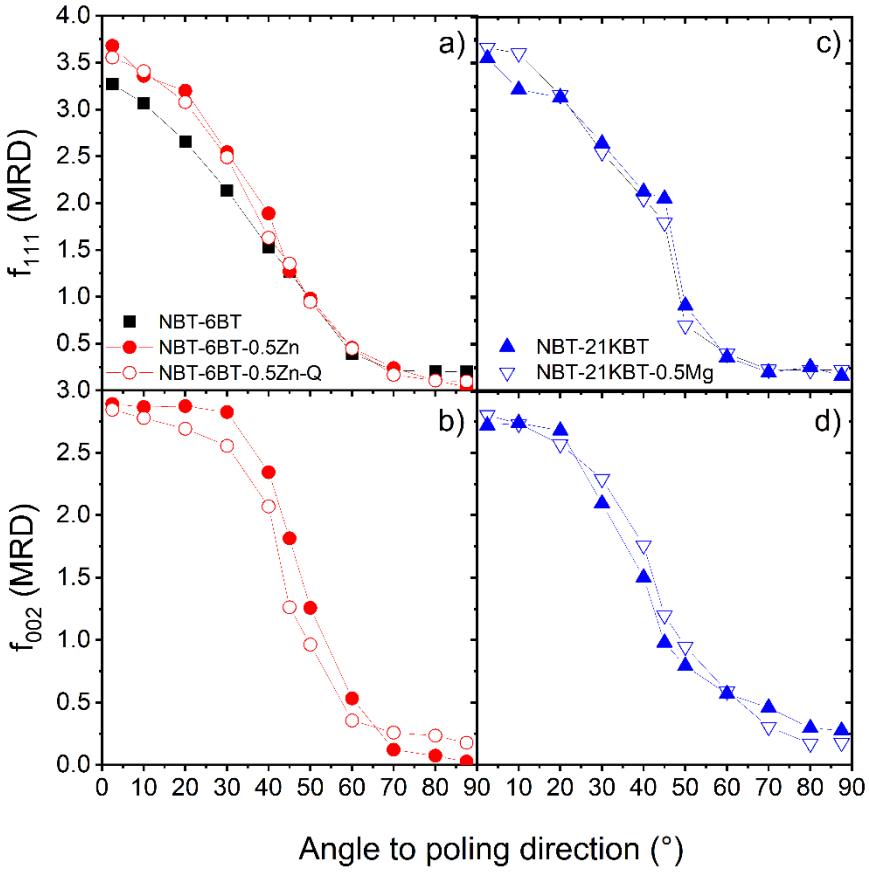

Figure 74: Pole figure densities in multiples of random distribution (MRD) for a) and c) the rhombohedral *R*3*c* (f_{111}) and b) and d) the tetragonal *P*4*mm* (f_{002}) phase of NBT-6BT, NBT-6BT-0.5Zn, NBT-6BT-0.5Zn-Q, NBT-21KBT, and NBT-21KBT-0.5Mg. The values were calculated from the 111_{pc} and 200_{pc} reflections (Figure 73 and Figure S18).

Phase coexistence model

Another model is employed to calculate the degree of texture. The standard model does not consider the phase coexistence of the rhombohedral and tetragonal phases, nor does it consider the phase transformation during the poling process.

It is commonly accepted that the orientation of the grains to the poling direction can influence the evolving crystal structure.[124, 272, 273] For example, a unit cell oriented with the (100) axis along the poling direction can transform into a tetragonal crystal structure, preferably (other crystal symmetries are also possible but are excluded from the discussion here). If the unit cell is oriented with the (111) axis along the poling direction, it transforms, preferably, into a rhombohedral crystal structure. In the unpoled state, NBT-6BT is roughly 60% cubic and 40 % non-cubic. It is expected that even the rhombohedral and tetragonal phases can transform to a certain degree into the respective other phases, depending on their orientation. Figure 75a depicts the resulting phases for all possible directions of the unit cells. The described process results in a theoretical phase ratio of 57.1% rhombohedral and 42.9% tetragonal phase.[124, 274] The observed phase ratio (Table 14) are shifted more toward the rhombohedral side. This outcome might result from chemical pressure, because the symmetry and phase compositions are also influenced by the abundance and quantity of ions on the A-site.

The phase coexistence and the orientation-dependent phase transformation both contribute to the high remanent texturing degree. In the multi-phase system, the three directions of the tetragonal phase and the four directions of the rhombohedral phase add up to a total of seven directions. The theoretical maximum of the PFD in this system changes to roughly seven for both phases, which is considerably higher than in the single-phase model (see Figure 75b).

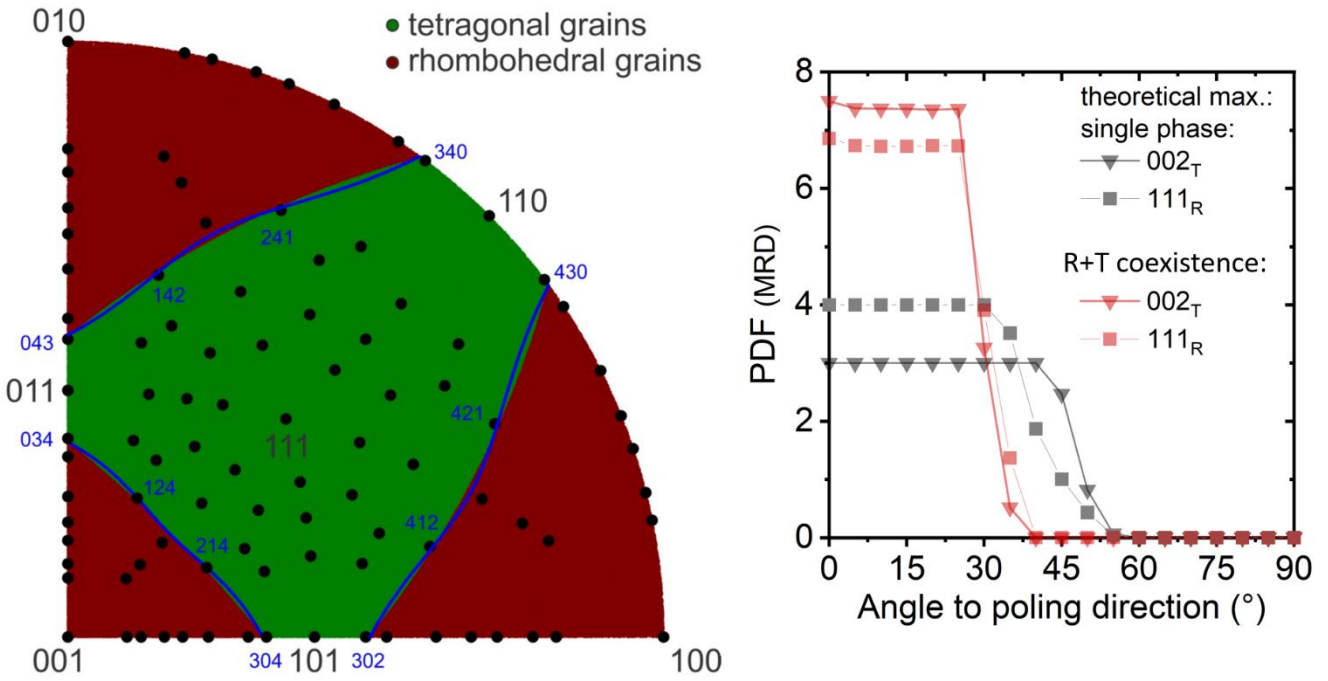

Figure 75: a) Depending on the randomly oriented grains to the polarization field direction, the field induces a rhombohedral (green) or tetragonal (red) phase. The blue lines indicate the exact boundaries between both phases. The theoretical maximum PDF for the two-phase model was calculated using Equations (26)-(31) (supplemental material).[XXX]

The STRAP model (Strain, Texture and Rietveld Analysis for Piezoceramics) was used to consider phase coexistence when determining the PFD.[XXXI] When using the STRAP model, the full diffraction pattern is fitted simultaneously, enabling consideration of phase coexistence, strain, and texture at the same time.[223, 224] Compared with the classic method described previously (Figure 27), the STRAP method results in a smaller error, since the complete diffraction pattern is used instead of just the 111_{pc} and 200_{pc} reflections.

Figure 76 compares the PFD in MRD for all the investigated NBT-based compositions (a and b) with standard PZT, KNN ($(Ka,Na)NbO_3$) and BT ($BaTiO_3$)[XXXII] (c).[270, 271, 275] The revealed degree of texture is extremely high in all NBT-based compositions, whereas the degree of texture is only a little higher in the tetragonal phase than in the rhombohedral phase, with values of 5-6 and 4-5, respectively. The reference materials, however, are considerably lower, in the range of two. Even *In situ* with 2 kV/mm, the degree of texture is not close to the level of the NBT-based compositions at zero field.

[XXX] This model of phase coexistence was established in close collaboration with Manuel Hinterstein, who also performed the calculations.

[XXXI] The refinement, using the STRAP model, was conducted by Manuel Hinterstein.

[XXXII] These data are not published in the references but were kindly shared by the authors.

Both methods for determining the degree of texture reveal extremely high anisotropy in the poled remanent state. Independent of the absolute values, both methods exhibit the same trend. Zn doping further increases the degree of texture, whereas quenching does not alter it any further. The increase in the PFD by Zn doping might originate from the shift in the MPB, which leads to a more energetically equivalent state of the rhombohedral and the tetragonal phases. Hence, Zn doping could result in greater unit cell orientation-dependent phase stabilization and, further, a higher degree of texture. The trend in the texture is also apparent in the mechanical quality factor Q_m. Zn doping increases Q_m, whereas quenching does not tailor it any further. The NBT-21KBT-based compositions exhibit a comparable degree of texture, regardless of Mg doping. Q_m behaves accordingly, which implicates a correlation between the mechanical losses and the remanent degree of texture. This aspect is discussed in a later section.

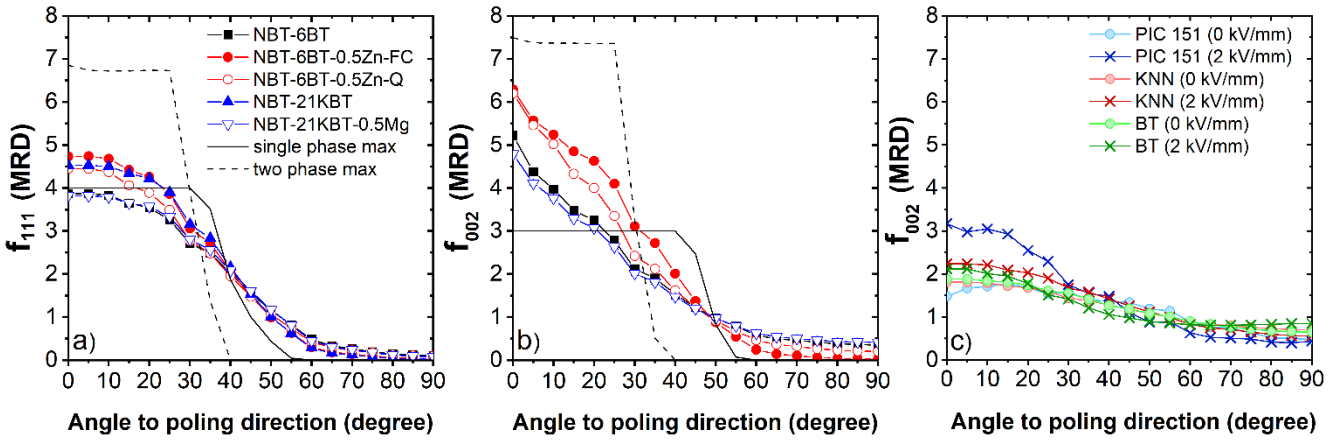

Figure 76: Pole figure densities in multiples of random distribution of a) the rhombohedral phase (f_{111}) and b) the tetragonal phase (f_{002}) of NBT-6BT, NBT-6BT-0.5Zn, NBT-6BT-0.5Zn-Q, NBT-21KBT, and NBT-21KBT-0.5 Mg. PFD in MRD of c) the tetragonal phase (f_{002}) of soft PZT (PIC151), (K,Na)NbO_3, and $BaTiO_3$ *In situ* at 2 kV/mm and in the remanent state. All the values are calculated using the STRAP method, performed by Manuel Hinterstein.

Correlation of strain contributions and poling-induced texturing degree

It is believed the high degree of remanent texture directly influences the electromechanical properties. This correlation is schematically drawn in Figure 77. “NBT-based” represents a material with high remanent texture, and “PZT-based” (PIC151, PI ceramics, Lederhose, Germany) represents a material with low remanent texture. In the unpoled state (Figure 77a), both materials are untextured, and all polarization vectors are randomly oriented. PZT already features a rhombohedral and tetragonal phase mixture in the unpoled state, which does not transform while poling to the same degree as NBT-based materials at the MPB. Poling induces

a remanent anisotropy of the polarization vectors, hence a remanent degree of texture. The degree of texture is significantly higher in the NBT-based materials (Figure 77b). During the application of an external electrical field, domains orient according to the field direction, and the degree of texture increases further (Figure 77c). The difference between the remanent state and the *In situ* state is larger in the soft PZT than in the NBT-based material. A very high degree of texture results in a low number or lower volume percentage of domains, which can align at a smaller angle to the applied electric field. The possibility and probability of domain reorientation decrease above a certain threshold of texture. This point is discussed by Jones et al. [90] in the context of poling and the contribution of domain-switching strain to the overall strain. In other words, the extrinsic contributions during the application of a small-signal decrease upon further increase of remanent texture, if a certain degree of texture is exceeded in the remanent state.

In a perfectly textured material, such as a mono-domain single crystal, the extrinsic contributions are zero. In a polycrystalline multi-domain piezoceramic, the piezoelectric response is a mixture of intrinsic and extrinsic contributions.[64, 66] The intrinsic contributions are classified into polarization rotation and polarization extension. A theoretical angle of the unit cell to the external electric field with the maximum intrinsic contribution exists. The angle depends on the material-specific contribution from the rotation and extension. Materials can be separated into rotators or extenders. NBT-based materials are classified as extenders. The highest intrinsic contribution is found parallel to the polarization direction.[233, 276] On the other hand, extrinsic contributions are defined as domain-switching strain. Domains oriented close to an external field grow at the expense of domains oriented at a larger angle to the electric field. Soft PZT reveals a significant difference in the degree of texture between the remanent state and at 2 kV/mm, which is attributed to the back-switching of domains.[223] In contrast, in NBT-based materials, the degree of texture cannot increase significantly anymore. Hinterstein et al. [124] revealed only a minor back-switching in NBT-6BT when investigated *In situ* at 4 kV/mm and in the remanent state.

The overall extrinsic strain is determined by the total number of domains switching and the strain generated per switching event. The strain per switching event can be approximated using the lattice distortion, which provides the ratio of the long side and short side of the unit cell. The tetragonal lattice distortion of the NBT-6BT and soft PZT (PIC151) is comparable (ref. [223] and Table 14). The rhombohedral lattice distortion is in the range of 0.86-0.93% and 0.5% for NBT-

6BT and soft PZT (PIC151), respectively. Hence, the same strain is generated by fewer switching events in the NBT-6BT. Fewer switching events mean lower losses.

Wohninsland et al. [277] evaluated the degree of texture of NBT-6BT while applying an external electric field. The 111_{pc} and 200_{pc} reflections depended less on the azimuthal angle than observed in this work due to an inferior 2θ resolution.

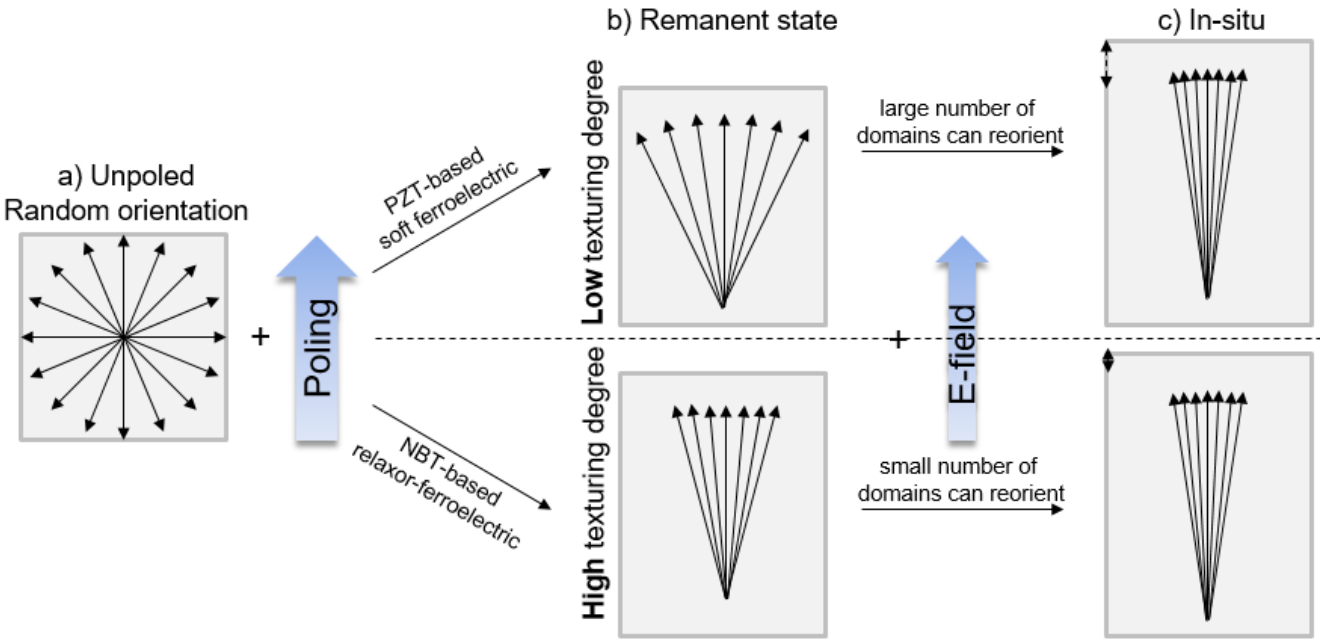

Figure 77: Schematic pole figure density in a) the unpoled state, b) the remanent state, and c) during the application of a small-signal electric field. Soft PZT and NBT-based materials are compared.

8.2 Piezoelectric Activity in Dependence of the Texturing Degree

Remanent polarization is a measure of the degree of texture induced by poling. In contrast to PZT, NBT-based materials reveal a non-linear correlation of the piezoelectric activity in dependence on the remanent polarization. This finding is rationalized by decreasing extrinsic strain contributions at high levels of texture. It is believed that the domain wall movement is not hindered by the alignment of defect dipoles but rather by reduction in domain wall density.

As discussed above, the piezoelectric response, including d_{33}, consists of intrinsic and extrinsic contributions. The intrinsic contributions are assumed to increase linearly with increasing degrees of texture in the NBT-based materials. The extrinsic contributions are believed to

decrease above a certain threshold of remanent degree of texture. The degree of texture is proportional to the remanent polarization. The relationship of the piezoelectric coefficient d_{33} to the remanent polarization P_{rem} is compared for NBT-based materials and soft PZT (PIC151) in Figure 78. A linear relationship between d_{33} and P_{rem} is revealed for soft PZT (Figure 78b). Hence, soft PZT should still be in the linear regime when fully poled. This outcome is also expected from a relatively low degree of texture. On the other hand, all the NBT-based materials deviate from the linear trend at a polarization between 20 and 30 µC/cm² (Figure 78a and b). NBT-6BT-0.5Zn reveals a saturation or even a slight decline of d_{33} at high polarization levels. The extrinsic contributions of NBT-6BT can be evaluated when assuming linear intrinsic contributions (Figure 78c).The intrinsic contributions are 95% in a fully poled ceramic.[114] As a result, decreasing extrinsic contributions at high P_{rem} are revealed.

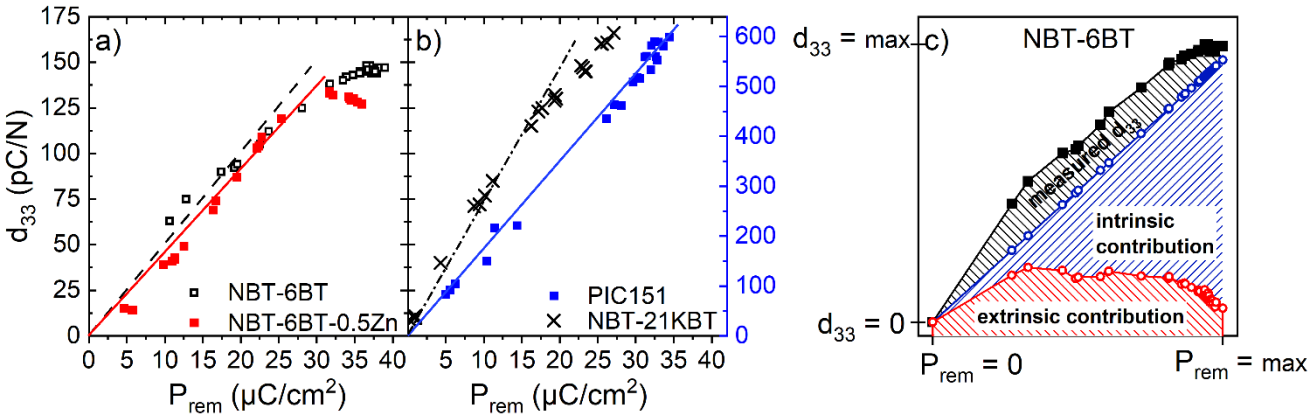

Figure 78: Remanent polarization P_{rem} against the piezoelectric coefficient d_{33} of a) NBT-6BT, NBT-6BT-0.5Zn and b) soft PZT (PIC151) and NBT-21KBT. c) The intrinsic and extrinsic contributions in NBT-6BT to the overall d_{33} in dependence of the polarization state.[XXXIII]

In the following section, the correlation between a high degree of texture and low mechanical loss is discussed in more detail. It was recently discovered, that NBT-based materials have low and stable extrinsic contributions with increasing vibration velocity in resonance.[114] This is the reason for a stable Q_m with increasing vibration velocity. However, the origin of the low extrinsic contributions is not clear yet. In this study, the minor extrinsic contributions were correlated with the extreme degree of poling-induced texture. Hence, it is believed that the well-established ferroelectric hardening mechanism, known from PZT- and BT-based materials, is not valid to the same extent in NBT-based materials. The commonly used mechanism to describe ferroelectric hardening is based on the formation of defect dipoles. Acceptor dopants

[XXXIII] This data was used for a publication together with Andreas Wohninsland who mainly conducted these measurements.

will lead to the formation of oxygen vacancies. Both defects associate and align according to their surrounding polarization directions. The domain walls are trapped in deeper energy levels, which prevents domain wall movement (Figure 79). The association of defects and the alignment are diffusion based and occur after the poling process.[71, 76, 77] Subchapter 5.1.2 discussed how the association of defect couples in the NBT-based materials is unlikely. Hence, this hardening mechanism is unlikely for NBT-based materials. In NBT-based materials, domains are highly aligned during the poling process. With a higher degree of domain alignment, the room for further alignment decreases. This can be imagined as a reduced domain wall density (Figure 79). In the literature, the correlation of domain wall density and domain wall mobility to the piezoelectric response is discussed by Lemos da Silva et al. [275] and Picht et al. [278] for BT and PZT, respectively. Both the domain wall density and mobility depend on the grain size and are opposed, resulting in an optimized grain size at which the piezoelectric response is maximal. Furthermore, the effect of the domain wall density on the mechanical loss is reported in the literature.[279] Figure 79 schematically describes the energy level of the individual domain walls. The energy level does not decrease, but the number of domain walls decreases in the NBT-BT. Note that this is a hypothesis, since no direct measurements of domain wall densities or domain wall energy levels were performed.

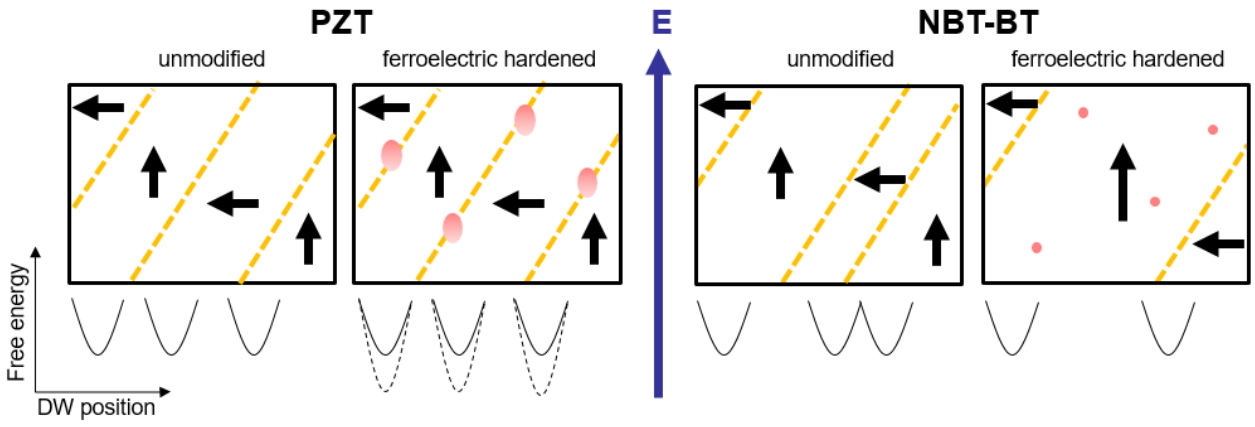

Figure 79: Schematic comparison of the domain/domain wall alignment and the corresponding free energy profile of unmodified and ferroelectric hardened PZT and NBT-BT.

When NBT-based materials are fully poled and the degree of texture is very high, even a strong driving force cannot induce much more domain wall motion. Extrinsic contributions are limited. In high-power devices, the mechanical losses mainly derive from extrinsic contributions.[114] Therefore, it is believed that the excellent high-power properties of NBT-based materials are due to the high degree of poling-induced remanent texture. Note that a higher degree of texture

does not necessarily mean a higher Q_m or a higher stability of Q_m vs. v, however, this can be the case if the degree of texture surpasses a certain threshold.

9 Summary and Conclusions

This study is divided into different topics, as is this summary. First, the solid solutions NBT-xBT and NBT-xKBT and their chemical variations were compared and discussed. Second, the defect structure was examined and related to the ferroelectric hardening in PZT. Third, a new theory was proposed to explain the low and stable extrinsic contributions in NBT-based materials with increasing vibration velocity. Finally, the material's performance in application-relevant high-power measurements was evaluated and compared with the PZT alternative.

In this research project, different chemical modifications are explored to design a piezoelectric material for high-power applications. The investigation results in promising compositions and establishes general rules for future research in this area.

Unpoled NBT-xBT exhibits a gradual decrease in rhombohedral *R*3*c* and an increase in the tetragonal *P*4*mm* phase across the MPB with increasing BT content. Zn and Mg acceptor-doping on the B-site stabilize the tetragonal phase and tetragonal lattice distortion in the unpoled state in a similar fashion. Poled Mg- and Zn-doped NBT-6BT maintain a higher tetragonal phase fraction than undoped samples, but the tetragonality remains the same. Investigating Zn-doped NBT-5BT to NBT-8BT reveals a shift of the MPB towards a higher temperature and the rhombohedral side. This shift is reflected in properties such as higher temperature stability, lower piezoelectric activity, and lower mechanical losses. Mg doping results in similar property changes to Zn doping, but Q_m is higher, making it the highest known value for NBT-xBT.

Moreover, the Bi-stoichiometry can act similarly to acceptor doping if added on top. Bi deficiency is comparable to a higher acceptor doping concentration, resulting in a higher Q_m and a lower piezoelectric coefficient d_{33}. However, temperature stability does not further increase. Bi excess reverses the changes induced by B-site acceptor doping.

The NBT-xKBT system is comparable in many ways to the NBT-xBT system. In the poled state, there is a change in structure from *R*3*c* to *P*4*mm* across the MPB with decreasing NBT content. The maximum value of d_{33} is on the tetragonal side of the MPB, whereas the minimum in $T_{F\text{-}R}$ is located on the rhombohedral side of the MPB. Acceptor doping with Mg or Zn decreases the piezoelectric activity but improves temperature stability. Adding a ZnO secondary phase does not further affect the properties significantly. The piezoelectric response in NBT-xKBT is slightly higher than in NBT-xBT. An ergodic behavior is found in NBT-xKBT, which results in a gradual

depolarization below T_{F-R}. Surprisingly, acceptor doping or the secondary phase ZnO addition does not alter Q_m considerably.

Different doping strategies in NBT-xBT and NBT-xKBT provide insights into the underlying mechanisms of ferroelectric hardening. One key observation is that ferroelectric hardening occurs when there is a jump in conductivity, which has been observed in Mg- and Zn-doped NBT-6BT. This jump in conductivity is caused by a lower association energy of acceptor defect and oxygen vacancy. Hence, the classic explanation of defect complex formation in materials such as PZT and BT cannot explain the phenomenon of ferroelectric hardening in NBT-xBT. Other defect-driven hardening mechanisms, such as the agglomeration of defects at domain walls and grain boundaries, are possible. A different approach to controlling Q_m and ferroelectric hardening is to manipulate the A-site stoichiometry, such as Bi-stoichiometry, to address the oxygen vacancy concentration. In this way, the Bi-stoichiometry only impacts Q_m if the material is already acceptor-doped. Interestingly, ferroelectric hardening does not occur in NBT-xKBT through B-site acceptor-doping, ZnO secondary phase, or K-deficiency. This lack of hardening remains a question for future research, but it may be related to the presence of Ba in NBT-xBT and NBT-xBT-yKBT, which is absent in NBT-xKBT.

Further investigation of samples in the un-fatigued, recovered, and fatigued states reveals a different behavior in PZT and NBT-xBT:ZnO, supporting the idea of a different defect association and ferroelectric hardening mechanism in both materials. In PZT, a strong inverse proportionality of Q_m and the piezoelectric coefficient d_{33} underlines the major impact of defect association, which is not found in NBT-xBT:ZnO, supporting the idea that the association and formation of defect dipoles play a subordinate role.

A theory has been proposed to explain the stability of the extrinsic contributions against changes in vibration velocity. This theory may also provide insights into tailoring Q_m through doping. The modification of mechanical loss in materials such as NBT-xBT and NBT-xKBT due to acceptor-doping does not seem linked to structural changes, such as phase shifts or lattice distortion. Slabki et al. [114] correlated the stable mechanical losses to low and stable extrinsic contributions to the strain in resonance. Although the exact cause remains unknown, it is hypothesized in this study that this phenomenon could stem from a significant level of domain texture induced by poling, which may result from phase transformations and the coexistence of tetragonal and rhombohedral phases. In theory, a high degree of poling-induced texture limits the possibility of the further reorientation of domains in poled samples when applying a

small extrinsic electric field. Consequently, even when the driving force is increased, such as with higher vibration velocity, extrinsic contributions to the strain, and hence mechanical losses induced by domain wall movement, remain low. The high stability of Q_m and the high degree of domain texture appear to be specific to materials such as NBT-xBT and NBT-xKBT, whereas other materials, such as PZT, BT, and KNN, exhibit different behaviors, supporting this hypothesis. Additionally, doping may influence the degree of domain texture and affect the domain wall density and, in turn, Q_m. Further investigation into this theory, particularly in the context of doping, is necessary to understand fully the underlying mechanisms and potential applications.

The stability of mechanical losses in materials is crucial for their suitability in high-power applications. This study examined the stability of Q_m with increasing vibration velocity in NBT-xBT and found it depends on the BT content and is less stable on the rhombohedral side of the MPB. Interestingly, doping does not change this behavior, suggesting it is intrinsic to the material. NBT-xBT and PZT exhibit a similar trend in the decline of Q_m with increasing vibration velocity, with PZT declining four to five times quicker, as demonstrated by the comparison of PZT and a NBT-xBT:ZnO composite.

The lead-free material exhibits higher stability against fatigue at high vibration velocity and requires lower input power to maintain the same level of vibration velocity. The NBT-xBT:ZnO composite also stabilizes at a lower temperature than PZT due to its lower mechanical loss, again correlating with non-linear mechanical properties. These properties result in the excitation of second harmonics in PZT at 1 m/s and above, but they do not occur in NBT-xBT-based composites. Despite the higher losses in PZT, both materials max out in continuous drive mode at a similar vibration velocity of about 1.6-1.8 m/s. These findings indicate that NBT-xBT:ZnO is as suitable as PZT for high-power applications and even outperforms PZT in terms of fatigue resistance.

In most high-power applications, the piezoceramics are mechanically clamped, so there are no free boundary conditions in resonance. Both PZT and NBT-xBT-based materials exhibit a decrease in piezoelectric activity with increasing uniaxial compressive stress to about the same level. Q_m, on the other hand, drops immediately in both material systems and maintains a low level in NBT-xBT-based materials. In PZT, Q_m increases again with stress.

The findings provide valuable insights into the behavior of these materials under high-power conditions and suggest their use in practical applications. Some issues still need to be

addressed, such as the low piezoelectric coefficient in comparison to PZT. It is suggested to drive the lead-free piezoceramic at a higher electric field or change the ceramic's geometry to reach the same performance as PZT. Another issue is thermal stability. Partial depolarization below T_d makes it difficult to have stable and controllable conditions. Chemical modification or processing might address this problem, but a pre-heating process will also result in lower but more stable electromechanical properties. Low mechanical losses are a necessity for use at high vibration velocities. NBT-based materials have low mechanical losses at high vibration velocities, which suggests using them even with more output power than the PZT materials currently used.

Appendix

Table S1: Relative density and grain size of NBT-5BT to NBT-8BT with and without 0.5 mol% Zn doping. The measurement error for the density is 0.75.

	Relative density (%)	**Grain size (µm)**
NBT-5BT	96.8	2.1±2
NBT-5.5BT	97.8	1.4±0.8
NBT-6BT	97.3	1.7±0.8
NBT-6.5BT	97.2	1.2±0.8
NBT-7BT	97.3	1.2±0.7
NBT-7.5BT	96.8	1.8±0.8
NBT-8BT	97.0	1.3±0.7
NBT-5BT-0.5Zn	93.8	14.7±5.5
NBT-5.5BT-0.5Zn	94.7	15.6±6.6
NBT-6BT-0.5Zn	95.0	9.4±4.4
NBT-6.5BT-0.5Zn	94.3	14.1±6.5
NBT-7BT-0.5Zn	93.8	13.1±5.9
NBT-7.5BT-0.5Zn	95.5	12.4±6.1
NBT-8BT-0.5Zn	95.5	14.3±5.4

Table S2: Rietveld refinement details, including the unit cell dimensions, atomic positions, and the quality of the fits of NBT-5BT to NBT-8BT with and without 0.5 mol% Zn.

	R3c	***$Pm\bar{3}m$***	***P4mm***	**Reliability factors**
NBT-5BT	a= 5.4999 (Å) c= 13.5773 (Å) V= 59.28	a= 3.9003 (Å) V= 59.34		Rp: 2.36 Rwp: 3.25 Rexp: 1.65
NBT-5.5BT	a= 5.5033 (Å) c= 13.5739 (Å) V= 59.34	a= 3.9031 (Å) V= 59.46		Rp: 3.08 Rwp: 5.24 Rexp: 1.54
NBT-6BT	a= 5.5023 (Å) c= 13.5939 (Å) V= 59.40	a= 3.9038 (Å) V= 59.49	a= 3.8922 (Å) c= 3.9378 (Å) V= 59.65	Rp: 2.19 Rwp: 3.11 Rexp: 1.60
Site x y z Na 0.00000 0.00000 0.27582 Bi 0.00000 0.00000 0.27582 Ba 0.00000 0.00000 0.27582 Ti 0.00000 0.00000 0.02083 O 0.08893 0.35931 0.08330		Site x y z Na 0.00000 0.00000 0.00000 Bi 0.00000 0.00000 0.00000 Ba 0.00000 0.00000 0.00000 Ti 0.50000 0.50000 0.50000 O 0.50000 0.50000 0.00000		Site x y z Bi 0.00000 0.00000 0.00000 Ba 0.00000 0.00000 0.00000 Na 0.00000 0.00000 0.00000 Ti 0.50000 0.50000 0.45432 O 0.50000 0.50000 -0.15000 O 0.50000 0.00000 0.40000
NBT-6.5BT	**-**	a= 3.9053 (Å) V= 59.56	a= 3.8932 (Å) c= 3.9339 (Å) V= 59.63	Rp: 2.29 Rwp: 3.23 Rexp: 1.57

NBT-7BT	-	a= 3.9058 (Å) V= 59.59	a= 3.8947 (Å) c= 3.9350 (Å) V= 59.69	Rp: 2.31 Rwp: 3.50 Rexp: 1.61
NBT-7.5BT	-	a= 3.9075 (Å) V= 59.66	a= 3.893 (Å) c= 3.9433 (Å) V= 59.76	Rp: 2.54 Rwp: 3.85 Rexp: 1.62
NBT-8BT	-	a= 3.9094 (Å) V= 59.75	a= 3.8934 (Å) c= 3.9475 (Å) V= 59.84	Rp: 2.6 Rwp: 3.93 Rexp: 1.56
NBT-5BT -0.5Zn	a= 5.5013 (Å) c= 13.5908 (Å) V= 59.37	a= 3.8998 (Å) V= 59.31	-	Rp: 2.47 Rwp: 3.76 Rexp: 1.59
NBT-5.5BT -0.5Zn	a= 5.5023 (Å) c= 13.5987 (Å) V= 59.43	a= 3.9023 (Å) V= 59.43	a= 3.8907 (Å) c= 3.9385 (Å) V= 59.62	Rp: 2.21 Rwp: 3.22 Rexp: 1.64
NBT-6BT -0.5Zn	a= 5.5043 (Å) c= 13.5989 (Å) V= 59.47	a= 3.9048 (Å) V= 59.54	a= 3.8895 (Å) c= 3.9467 (Å) V= 59.71	Rp: 2.08 Rwp: 3.09 Rexp: 1.63
NBT-6.5BT -0.5Zn	-	a= 3.9051 (Å) V= 59.55	a= 3.8903 (Å) c= 3.9475 (Å) V= 59.75	Rp: 1.87 Rwp: 2.79 Rexp: 1.64
NBT-7BT -0.5Zn	-	a= 3.9062 (Å) V= 59.6	a= 3.8899 (Å) c= 3.9520 (Å) V= 59.8	Rp: 2.63 Rwp: 4.49 Rexp: 1.72
NBT-7.5BT -0.5Zn	-	a= 3.9077 (Å) V= 59.67	a= 3.8906 (Å) c= 3.9572 (Å) V= 59.9	Rp: 2.39 Rwp: 3.74 Rexp: 1.63
NBT-8BT -0.5Zn	-	a= 3.9087 (Å) V= 59.72	a= 3.8909 (Å) c= 3.9592 (Å) V= 59.94	Rp: 2.44 Rwp: 3.7 Rexp: 1.56

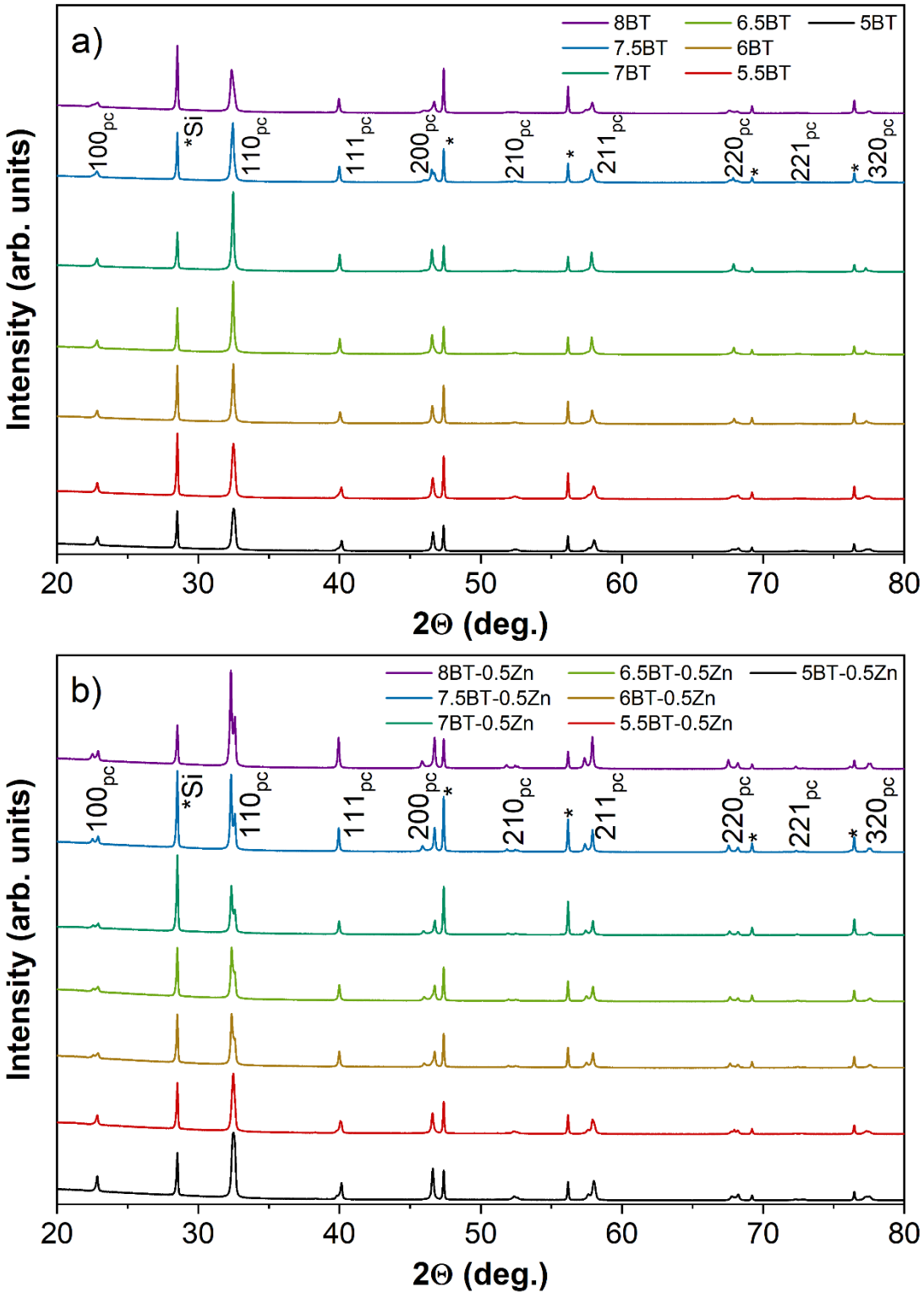

Figure S1: X-ray diffraction profile with a silicon standard (marked by an asterisk *) of a) NBT-5BT to NBT-8BT and b) NBT-5BT-0.5Zn to NBT-8BT-0.5Zn.

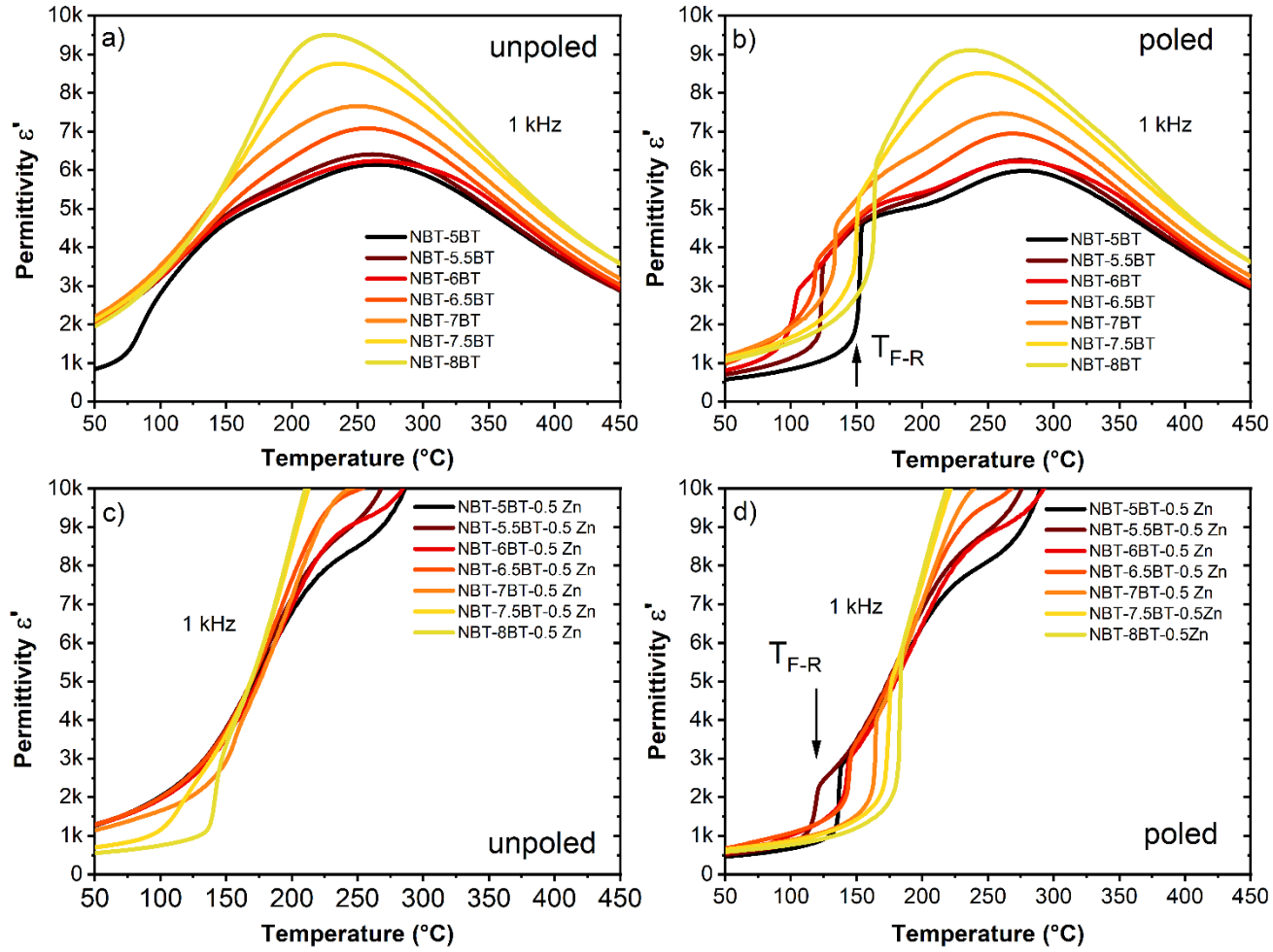

Figure S2: Real part of the permittivity, ε', at 1 kHz of NBT-5BT to NBT-8BT without (a and b) and with (c and d) 0.5 mol% Zn in unpoled (a and c) and poled (b and d) states.

Table S3: Grain size of NBT-6BT doped with 0, 0.1, 0.3, 0.5 mol% Mg, and 0.1, 0.3 mol% Zn.

Composition	Grain size (µm)
NBT-6BT	1.7 ± 0.8
-0.1 Mg	2.8 ± 1.5
-0.3 Mg	9.9 ± 3
-0.5 Mg	10.4 ± 4.3
-0.1Zn	2.1 ± 0.9
-0.3Zn	3.7 ± 1.8
-0.5Zn	9.4 ± 4.5
-1Zn	26 ± 12.5

Table S4: Poling strain S_{pol}, remanent strain S_{rem}, and negative strain S_{neg} of NBT-6BT doped with 0.1, 0.3, 0.5 mol% Mg and 0.1, 0.3, 0.5, 1 mol% Mg.

	S_{pol} (%)	S_{rem} (%)	S_{neg} (%)
NBT-6BT	0.51 ± 0.01	0.33 ± 0.02	0.22 ± 0.01
-0.1 Mg	0.45 ± 0.01	0.31 ± 0.01	0.22 ± 0.01
-0.3 Mg	0.41 ± 0.01	0.31 ± 0.01	0.16 ± 0.01
-0.5 Mg	0.44 ± 0.01	0.38 ± 0 01	0.18 ± 0.01
-0.1Zn	0.49 ± 0.05	0.31 ± 0.01	0.17 ± 0.01
-0.3Zn	0.47 ± 0.01	0.33 ± 0.01	0.15 ± 0.01
-0.5Zn	0.49 ± 0.02	0.39 ± 0.01	0.15 ± 0.01
-1Zn	0.51 ± 0.03	0.44 ± 0.02	0.16 ± 0.01

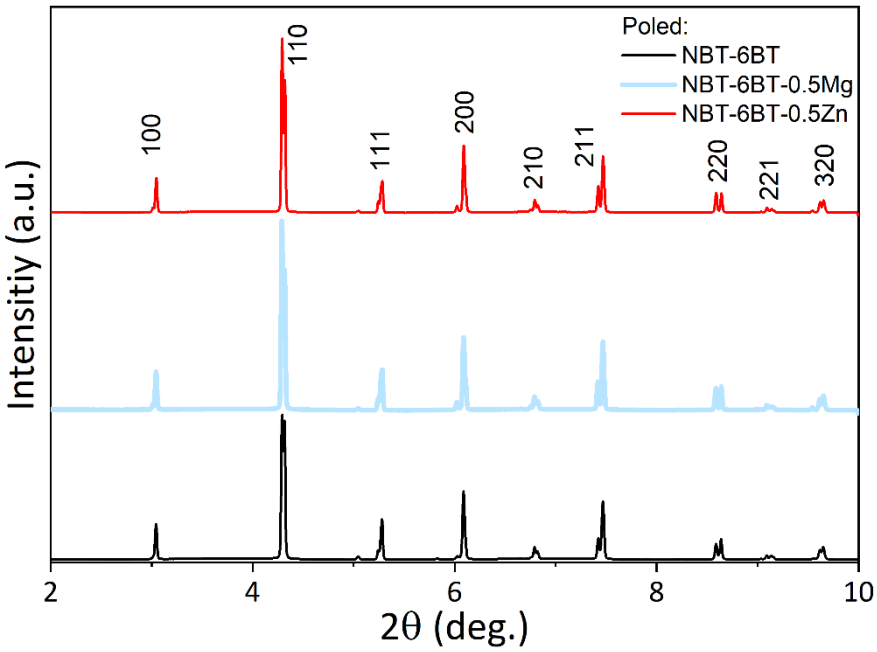

Figure S3: X-ray diffraction pattern of poled bulk samples of NBT-6BT, NBT-6BT-0.5Mg, and NBT-6BT-0.5Zn.

Table S5: Rietveld refinement details, including the unit cell dimensions and the quality of the fits of NBT-6BT doped with 0.1, 0.3, 0.5 mol% Mg.

Composition - unpoled -	***R3c***	$\boldsymbol{Pm\bar{3}m}$	***P4mm***	**Reliability factors**
NBT-6BT -0.1 Mg	a= 5.5039 (Å) c= 13.5969 (Å) V= 59.45	a= 3.9042 (Å) V= 59.51	a= 3.8916 (Å) c= 3.9391 (Å) V= 59.66	Rp: 2.10 Rwp: 2.81 Rexp: 1.67
NBT-6BT -0.3 Mg	a= 5.5036 (Å) c= 13.6113 (Å) V= 59.51	a= 3.9044 (Å) V= 59.52	a= 3.8893 (Å) c= 3.9461 (Å) V= 59.69	Rp: 2.15 Rwp: 3.06 Rexp: 1.64
NBT-6BT -0.5 Mg		a= 3.9053 (Å) V= 59.56	a= 3.8902 (Å) c= 3.9464 (Å) V= 59.72	Rp: 2.57 Rwp: 3.93 Rexp: 1.82
- poled -				
NBT-6BT	a= 5.5 (Å) c= 13.5899 (Å) V= 59.34		a= 3.886 (Å) c= 3.9421 (Å) V= 59.53	Rp: 3.7 Rwp: 5.34 Rexp: 2.47
NBT-6BT -0.5 Mg	a= 5.5 (Å) c= 13.5897 (Å) V= 59.36		a= 3.886 (Å) c= 3.9422 (Å) V= 59.53	Rp: 3.76 Rwp: 5.38 Rexp: 2.47
NBT-6BT -0.5 Zn	a= 5.502 (Å) c= 13.5933 (Å) V= 59.4		a= 3.8883 (Å) c= 3.9435 (Å) V= 59.62	Rp: 2.97 Rwp: 4.31 Rexp: 2.64

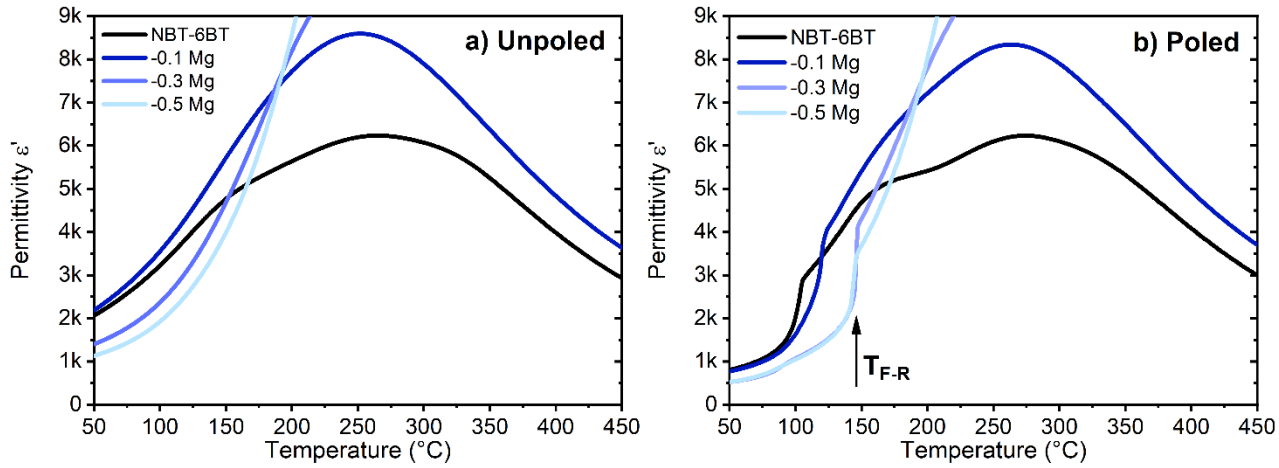

Figure S4: Temperature-dependent real part of the permittivity at 1 kHz of NBT-6BT with 0, 0.1, 0.3, 0.5 mol% Mg in a) unpoled and b) poled states.

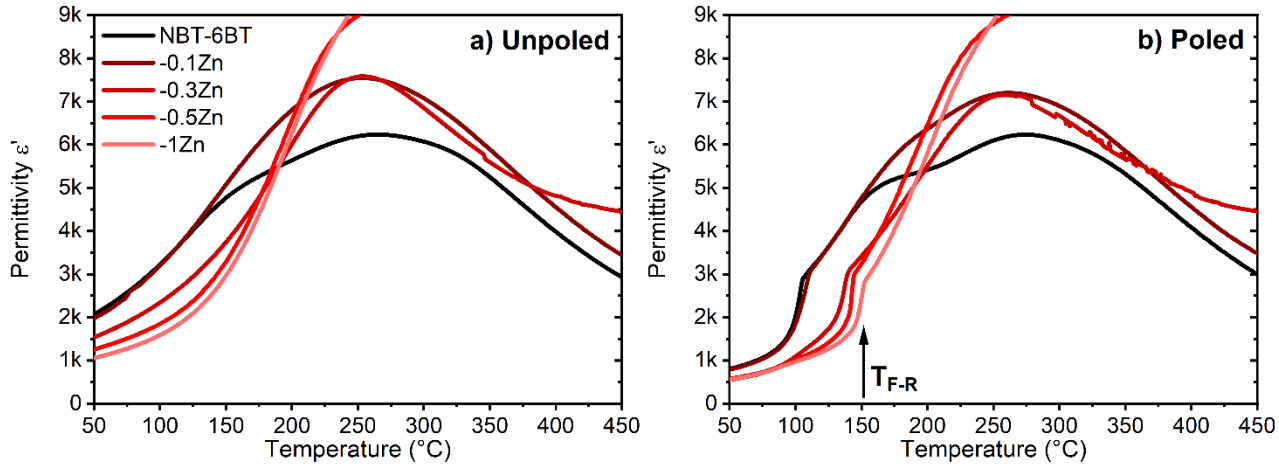

Figure S5: Temperature-dependent real part of the permittivity at 1 kHz of NBT-6BT with 0, 0.1, 0.3, 0.5, 1 mol% Zn in a) unpoled and b) poled states.

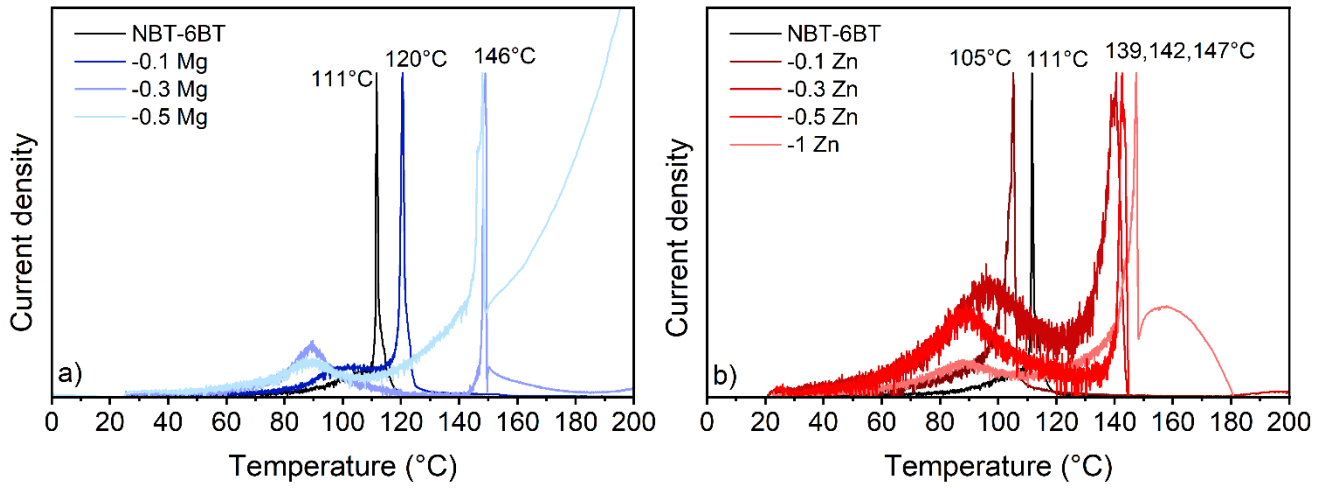

Figure S6: Pyroelectric current against temperature of poled NBT-6BT with 0, 0.1, 0.3, 0.5 mol% Mg (a) and NBT-6BT with 0, 0.1, 0.3, 0.5, 1 mol% Zn (b). The depolarization currents are normalized to unity for a better comparison.

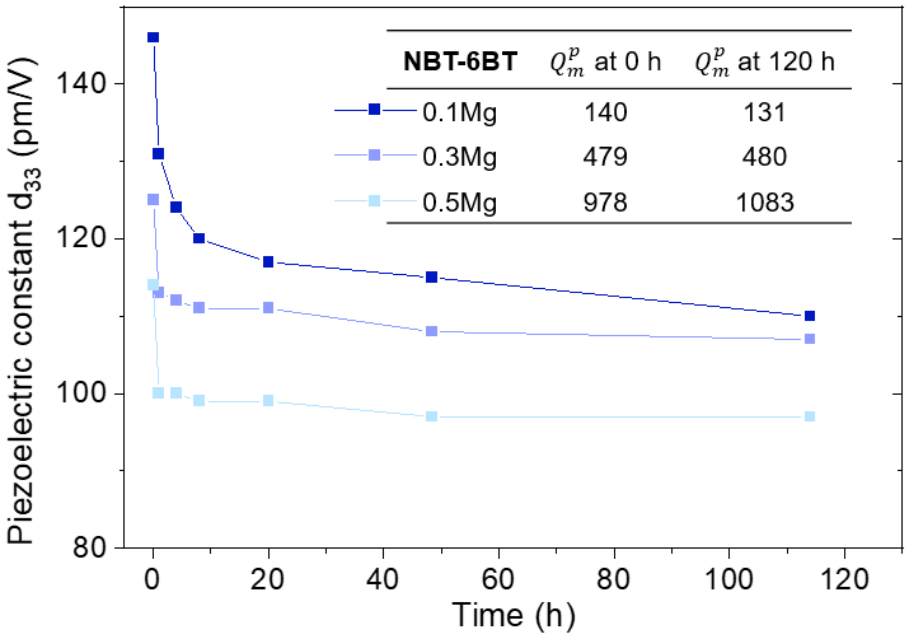

Figure S7: Piezoelectric constant d_{33} over time while annealed at 100 °C. The piezoelectric coefficient was measured at room temperature. The mechanical quality factor in planar mode is given at 0 h and 120 h.

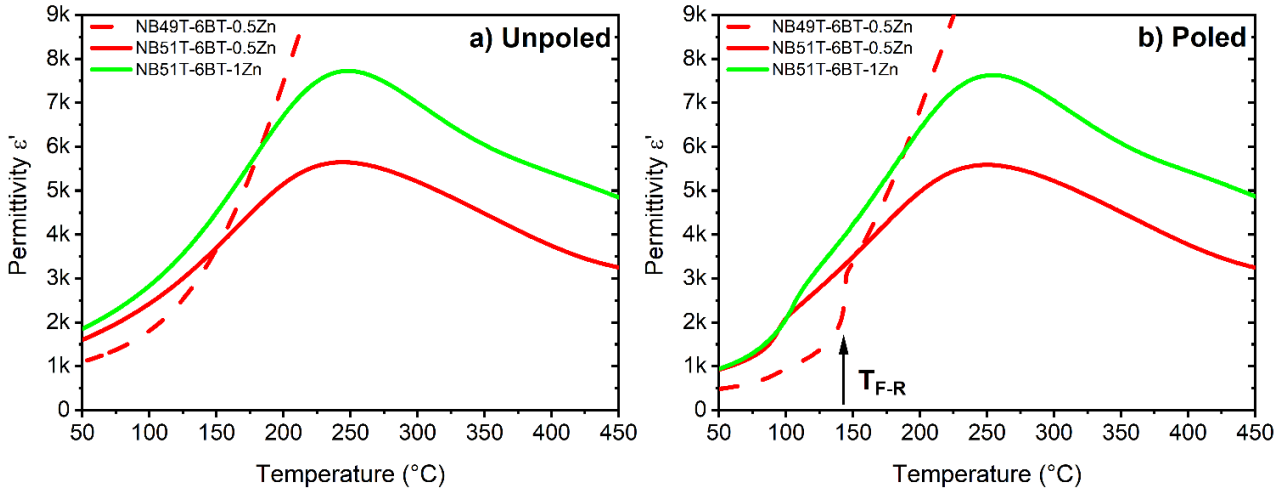

Figure S8: Temperature-dependent real part of the permittivity at 1 kHz of NB_{49}T-6BT with 0.5 mol% Zn and NB_{51}T-6BT with 0.5 and 1 mol% Zn in a) unpoled and b) poled states.

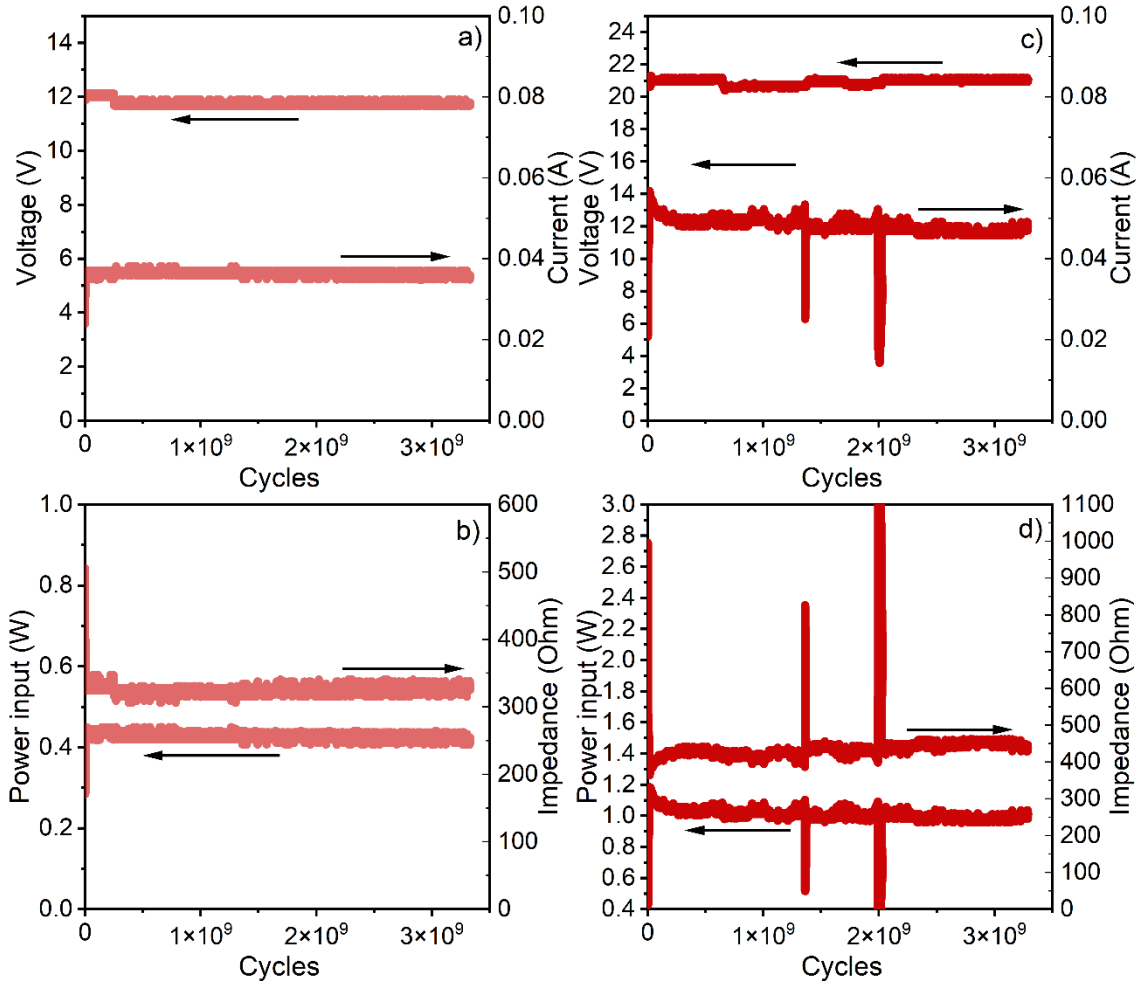

Figure S9: Recorded voltage and current a) and c) and, power input and impedance b) and d) of NBT-xBT:ZnO *In situ* of the electromechanical loading at v = 1 m/s (a and b) and v = 1.5 m/s (c and d). The depicted measurements were performed in 31-resonance mode.

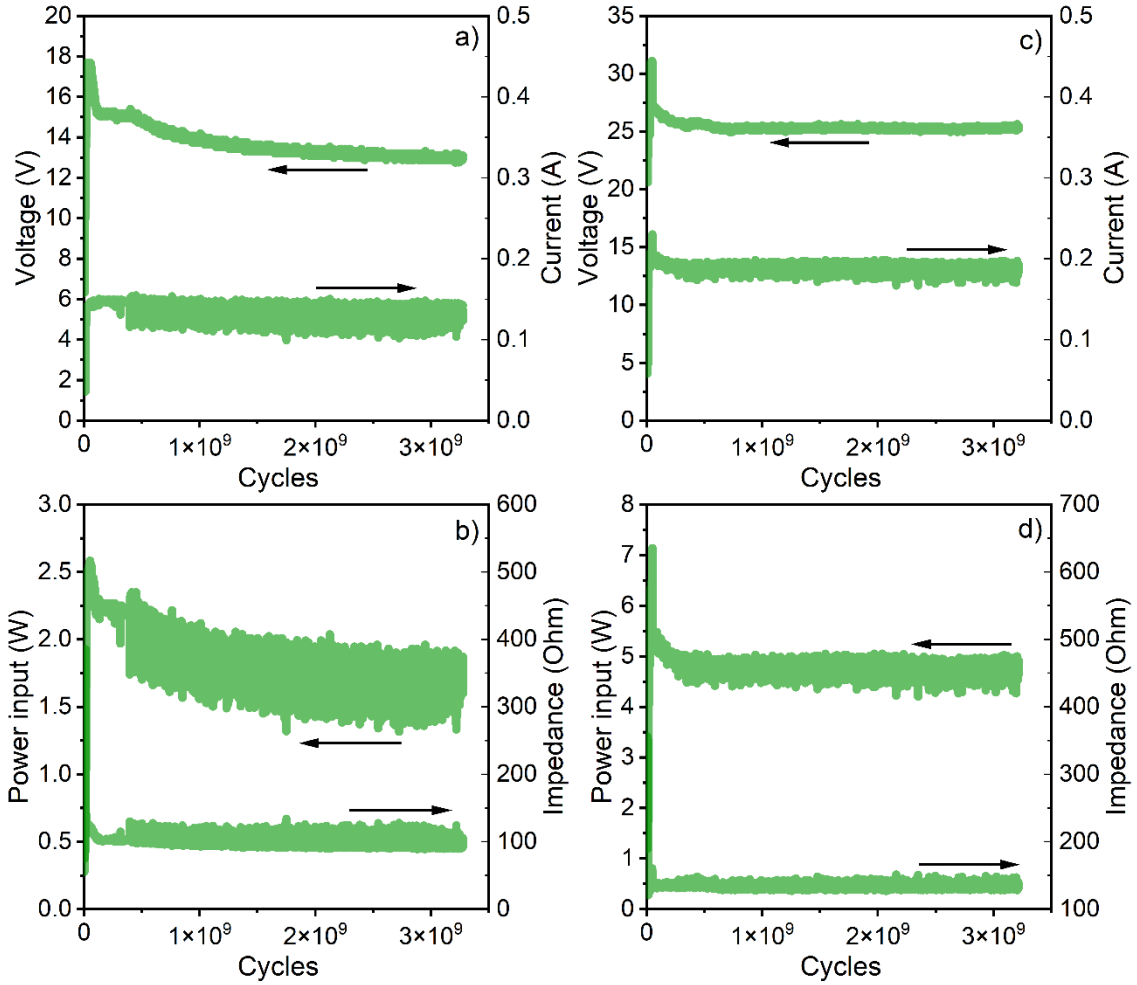

Figure S10: Recorded voltage and current a) and c) and, power input and impedance b) and d) of hard PZT *In situ* of the electromechanical loading at v = 1 m/s (a and b) and v = 1.5 m/s (c and d). The depicted measurements were performed in 31-resonance mode.

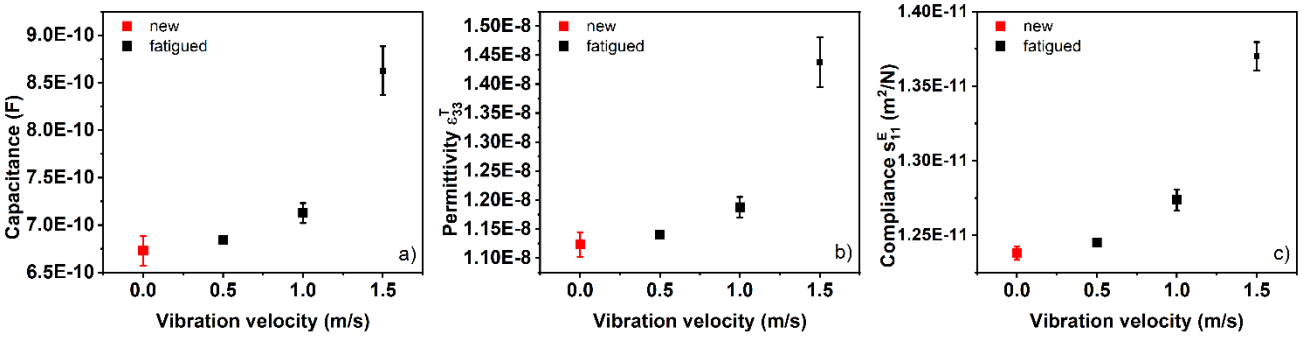

Figure S11: Small-signal properties, including a) the capacitance at 1 kHz, b) the permittivity $\varepsilon_{33}^{\mathrm{T}}$, and c) the compliance s_{11}^{E} of new (red) hard PZT and fatigued (black) at 0.5, 1, and 1.5 m/s for about 3.3×10^9 cycles.

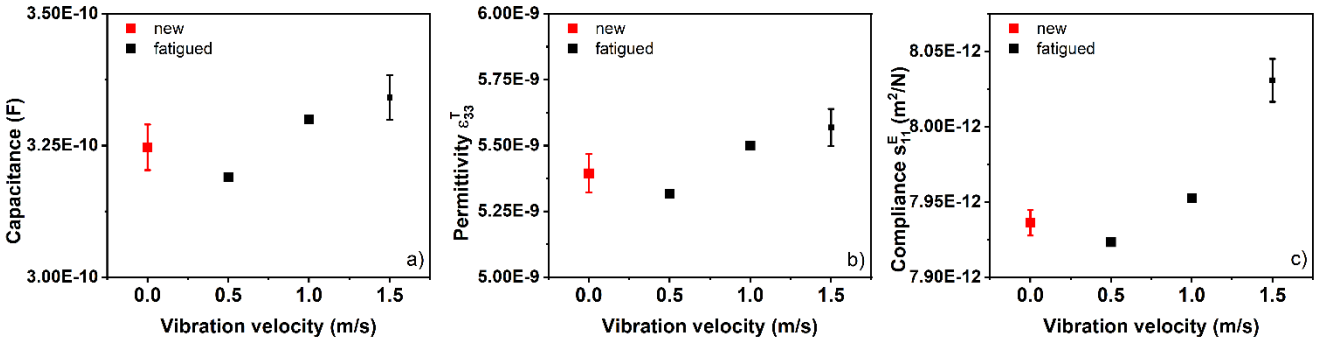

Figure S12: Small-signal properties, including a) the capacitance at 1 kHz, b) the permittivity $\varepsilon_{33}^{\mathrm{T}}$, and c) the compliance s_{11}^{E} of new (red) NBT-xBT:ZnO and fatigued (black) at 0.5, 1, and 1.5 m/s for about 3.3×10^9 cycles.

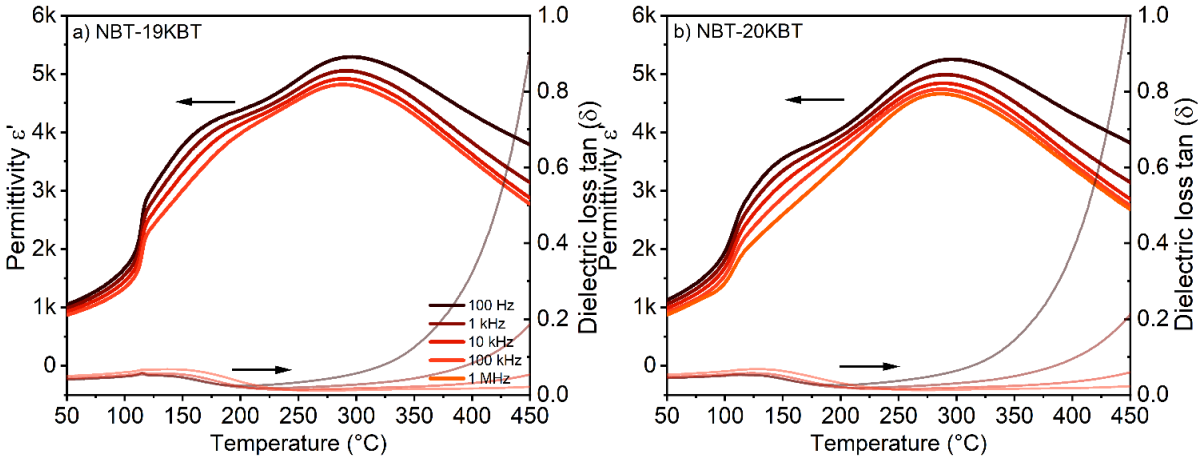

Figure S13: Permittivity *ε*' and dielectric loss *tan*(δ) against temperature of NBT-19KBT and NBT-20KBT in the poled state.

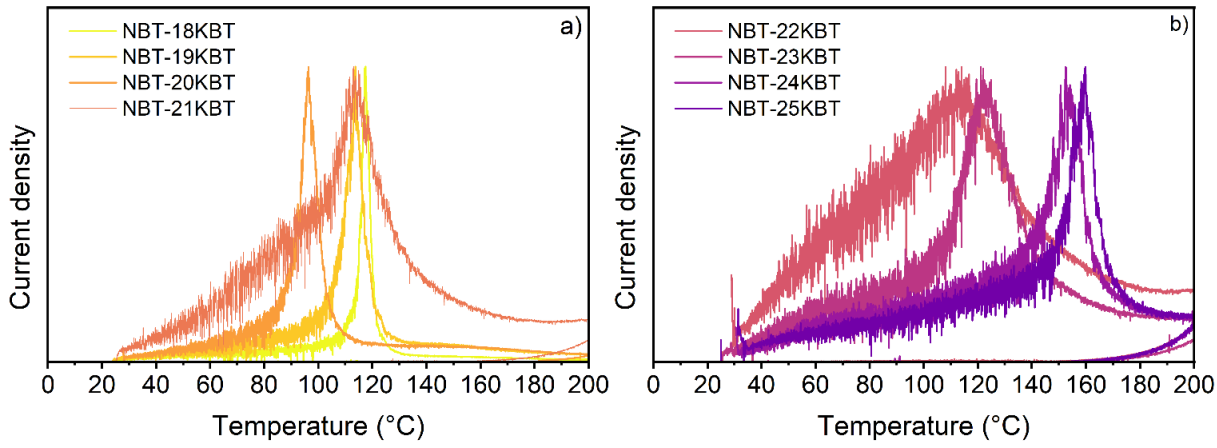

Figure S14: Thermally stimulated depolarization current of poled NBT-xKBT with x = 0.18, 0.19, 0.2, 0.21, 0.22, 0.23, 0.24, and 0.25. The depolarization currents are normalized to unity for better comparison.

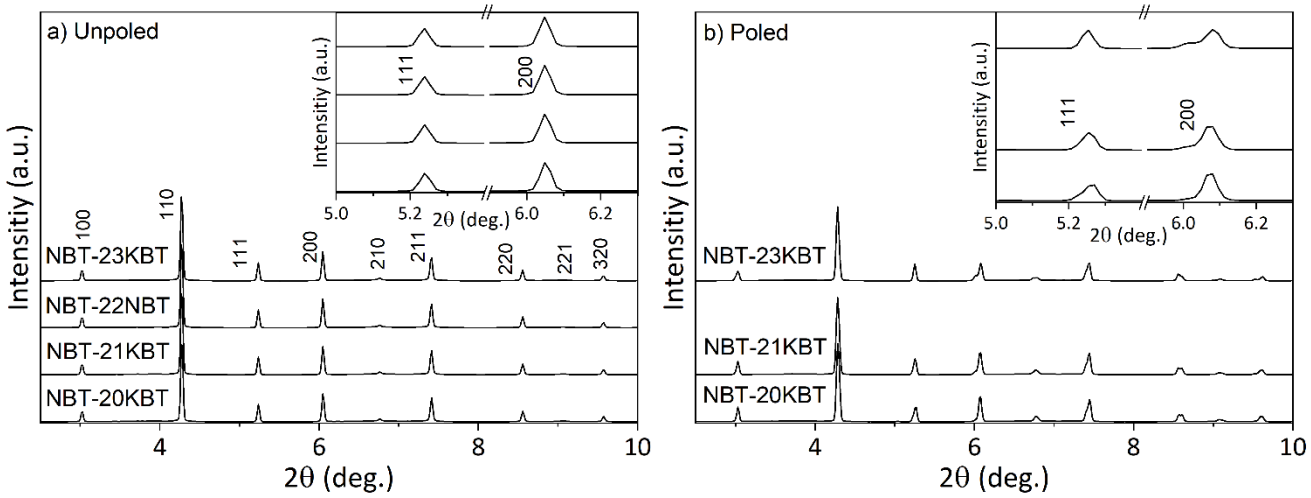

Figure S15: X-ray diffraction profile of unpoled (a) and poled (b) bulk samples of NBT-20KBT, NBT-21KBT, NBT.22KBT, and NBT-23KBT. The data file of the poled NBT-22KBT was corrupted and hence not refined.

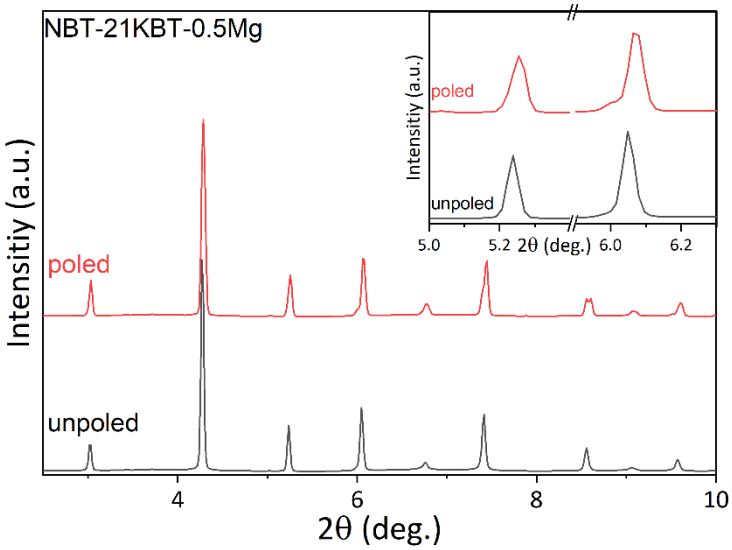

Figure S16: X-ray diffraction profile of unpoled (black) and poled (red) bulk samples of NBT-21KBT-0.5Mg.

Table S6: Rietveld refinement details, including the unit cell dimensions and the quality of the fits of unpoled and poled NBT-20KBT, NBT-21KBT, NBT.22KBT, and NBT-23KBT. The data file of the poled NBT-22KBT was corrupted and hence not refined.

Composition - unpoled -	***R3c***	$\boldsymbol{Pm\bar{3}m}$	***P4mm***	**Reliability factors**
NBT-20KBT		a= 3.9159 (Å) V= 60.05		Rp: 7.09 Rwp: 9.0 Rexp: 4.57
NBT-21KBT		a= 3.9163 (Å) V= 60.07		Rp: 6.64 Rwp: 8.34 Rexp: 4.55
NBT-22KBT		a= 3.9161 (Å) V= 60.06		Rp: 7.46 Rwp: 9.58 Rexp: 4.54
NBT-23KBT		a= 3.9164 (Å) V= 60.07		Rp: 6.4 Rwp: 8.24 Rexp: 4.51
NBT-21KBT-0.5Mg		a= 3.9187 (Å) V= 60.18	a= 3.9088 (Å) c= 3.953 (Å) V= 60.4	Rp: 6.34 Rwp: 8.95 Rexp: 4.48
- poled -				
NBT-20KBT	a= 5.5038 (Å) c= 13.5852 (Å) V= 59.4		a= 3.8927 (Å) c= 3.9335 (Å) V= 59.6	Rp: 4.06 Rwp: 5.44 Rexp: 4.26
NBT-21KBT	a= 5.509 (Å) c= 13.5847 (Å) V= 59.51		a= 3.8914 (Å) c= 3.9396 (Å) V= 59.66	Rp: 3.71 Rwp: 4.86 Rexp: 4.26
NBT-23KBT	a= 5.516 (Å) c= 13.562 (Å) V= 59.56		a= 3.8903 (Å) c= 3.939 (Å) V= 59.62	Rp: 3.63 Rwp: 4.97 Rexp: 4.45
NBT-21KBT-0.5Mg	a= 5.5085 (Å) c= 13.5895 (Å) V= 59.52		a= 3.8914 (Å) c= 3.9427 (Å) V= 59.7	Rp: 3.61 Rwp: 4.8 Rexp: 4.25

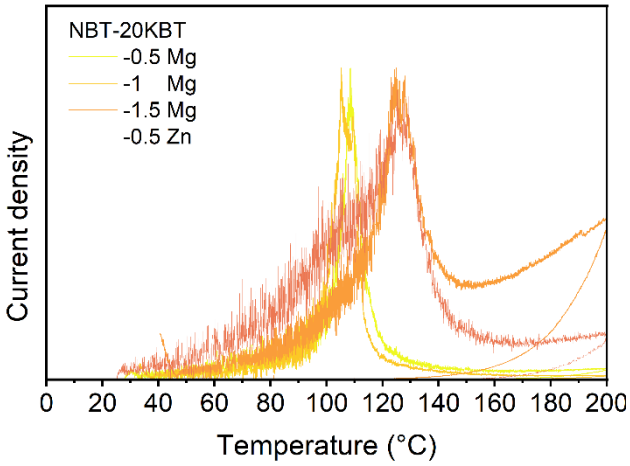

Figure S17: Thermally stimulated depolarization current of poled NBT-20KBT doped with 0.5, 1, 1.5 mol% Mg and 0.5 mol% Zn. The depolarization currents are normalized to unity for better comparison.

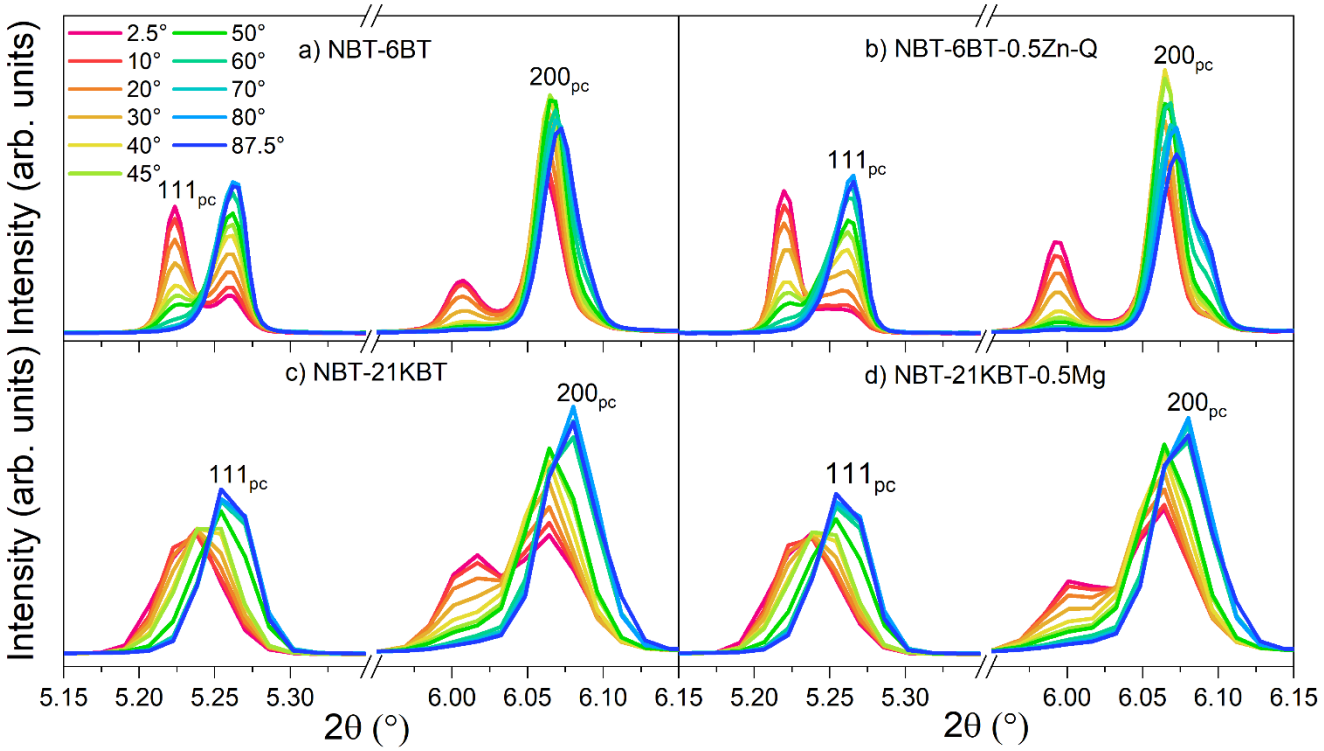

Figure S18: X-ray diffraction pattern of poled NBT-6BT (a), NBT-6BT-0.5Zn-Q (b), NBT-21KBT (c), and NBT-21KBT-0.5Mg (d) in the remanent state. Depicted are the 111_{pc} and 200_{pc} reflections for different angles regarding the poling direction. The NBT-xBT- and the NBT-xKBT-based compositions were measured at different synchrotrons with different setups, resulting in different angular resolutions.

Equations to calculate the boundaries between the rhombohedral and tetragonal phases in the phase coexistence model. The model describes the resulting phase based on the orientation of the unit cell to an external electrical poling field.

$$x_{h=}\frac{\cos\left(\sin^{-1}\left[\frac{k_x}{\sqrt{h_x^2+k_x^2}}\right]\right)}{\tan\left(\frac{\frac{\pi}{2}-\sin^{-1}[l_x]}{2}\right)} \tag{26}$$

$$x_{k=}\frac{\sin\left(\sin^{-1}\left[\frac{k_y}{\sqrt{h_y^2+k_y^2}}\right]\right)}{\tan\left(\frac{\frac{\pi}{2}-\sin^{-1}[l_y]}{2}\right)} \tag{27}$$

$$x_{l=}\frac{\cos\left(\sin^{-1}\left[\frac{k_z}{\sqrt{h_z^2+k_z^2}}\right]\right)}{\tan\left(\frac{\theta_z}{2}\right)} \tag{28}$$

$$y_{h=}\frac{\sin\left(\sin^{-1}\left[\frac{k_x}{\sqrt{h_x^2+k_x^2}}\right]\right)}{\tan\left(\frac{\frac{\pi}{2}-\sin^{-1}[l_x]}{2}\right)} \tag{29}$$

$$y_{k=}\frac{\cos\left(\sin^{-1}\left[\frac{k_y}{\sqrt{h_y^2+k_y^2}}\right]\right)}{\tan\left(\frac{\frac{\pi}{2}-\sin^{-1}[l_y]}{2}\right)} \tag{30}$$

$$y_{l=}\frac{\sin\left(\sin^{-1}\left[\frac{k_z}{\sqrt{h_z^2+k_z^2}}\right]\right)}{\tan\left(\frac{\theta_z}{2}\right)} \tag{31}$$

Table S7: Overview of the electromechanical properties, including the piezoelectric coefficient d_{33}, the depolarization temperature T_d or the transitions temperature from the ferroelectric to the relaxor state $T_{F\text{-}R}$ and the mechanical quality factor in planar mode Q_m^p. Some of the provided compositions were not discussed in this work. Compositions produced mainly by Siegfried Teuber are marked with S.

Composition	d_{33} (pC/N)	T_d/$T_{F\text{-}R}$ (°C)	Q_m^p
NBT-3BT (S)	83	191	240
NBT-5BT (S)	103	153	201
NBT-5.5BT (S)	127	124	161
NBT-6BT	140	102	119
NBT-6.5BT (S)	165	118	106
NBT-7BT (S)	164	134	105
NBT-7.5BT (S)	148	151	118
NBT-8BT (S)	138	164	116
NBT-9BT (S)	139	157	81
NBT-5BT-0.5Zn (S)	103	138	590
NBT-5.5BT-0.5Zn (S)	112	119	564
NBT-6BT-0.5Zn	116	144	516
NBT-6.5BT-0.5Zn (S)	136	145	503
NBT-7BT-0.5Zn (S)	118	164	662
NBT-7.5BT-0.5Zn (S)	94	175	707
NBT-8BT-0.5Zn (S)	85	184	735
NBT-6BT-0.1Zn	130	105	129
NBT-6BT-0.3Zn	124	140	224
NBT-6BT-1Zn	113	147	563
NB49T-6BT-0.5Zn	112	144	734
NB49T-6BT-1Zn	-	-	-
NB51T-6BT-0.5Zn	124	95	102
NB51T-6BT-1Zn	153	108	117
NBT-6BT-0.1Mg	141	120	166
NBT-6BT-0.3Mg	123	148	469
NBT-6BT-0.5Mg	112	147	826
NBT-6BT-1Mg	114	-	-
NBT-6BT-0.1W	146	95	-
NBT-6BT-0.3W	148	82	-
NBT-6BT-0.5W	140	70	-
NBT-6BT:0.025ZnO	129	132	265
NBT-6BT:0.05ZnO	124	133	269
NBT-6BT:0.075ZnO	123	128	199
NBT-6BT:0.1ZnO	117	135	241
NBT-6BT:0.025Al_2O_3	119	97	157
NBT-6BT:0.05Al_2O_3	98	93-107	145
NBT-6BT:0.1Al_2O_3	62	85-117	151
NBT-6BT:0.2Al_2O_3	3	-	124
NBT-3BT:0.1ZrO_2 (S)	83	106	181

NBT-6BT:0.014ZrO_2 (S)	137	50	91
NBT-6BT:0.029ZrO_2 (S)	120	40	88
NBT-6BT:0.058ZrO_2 (S)	70	~40	80
NBT-6BT:0.116ZrO_2 (S)	48	~35	87
NBT-9BT:0.1ZrO_2 (S)	22	~35	-
NBT-18KBT (S)	130	**117**	-
NBT-19KBT (S)	138	**113**	-
NBT-20KBT (S)	160	**97**	86
NBT-21KBT (S)	170	**113**	72
NBT-22KBT (S)	178	**113**	68
NBT-23KBT (S)	169	**122**	68
NBT-24KBT (S)	159	**150**	-
NBT-25KBT (S)	144	**159**	-
NBT-21KBT-0.3Mg (S)	154	**132**	67
NBT-21KBT-0.5Mg (S)	153	**135**	85
NBT-21K48BT (S)	161	**112**	39
NBT-21K49BT (S)	154	**104**	47
NBT-20KBT-0.5Mg	156	**108**	76
NBT-20KBT-1Mg	141	**105**	115
NBT-20KBT-1.5Mg	93	**124**	95
NBT-20KBT-0.5Zn	154	**125**	90
NBT-21KBT-0.3Mg:0.025ZnO (S)	140	**110**	100
NBT-21KBT-0.5Mg:0.025ZnO (S)	136	**129**	108
NBT-21K48BT:0.025ZnO (S)	138	**113**	91
NBT-21K49BT:0.025ZnO (S)	136	**102**	87

Bibliography

[1] K. Uchino, *Ferroelectric devices*. CRC press, 2018.

[2] T. Abraham and B. Gupta, "Piezoelectric ceramic, polymer and ceramic/polymer composite devices—Types, materials, applications, new developments, industry structure and global markets," *Innovative Research and Products, Inc., Stamford,* 2014.

[3] E. Directive, "Restriction of the use of certain hazardous substances in electrical and electronic equipment (RoHS)," *Off. J. Eur. Communities,* vol. 46, pp. 19-23, 2013.

[4] J. Rödel, K. G. Webber, R. Dittmer, W. Jo, M. Kimura, and D. Damjanovic, "Transferring lead-free piezoelectric ceramics into application," *Journal of the European Ceramic Society,* vol. 35, no. 6, pp. 1659-1681, 2015.

[5] J. Koruza, L. K. Venkataraman, and B. Malič, "Lead-free perovskite ferroelectrics," in *Magnetic, ferroelectric, and multiferroic metal oxides*: Elsevier, 2018, pp. 51-69.

[6] M. Hejazi, E. Taghaddos, E. Gurdal, K. Uchino, and A. Safari, "High Power Performance of Manganese-Doped BNT-Based Pb-Free Piezoelectric Ceramics," *Journal of the American Ceramic Society,* vol. 97, no. 10, pp. 3192-3196, 2014.

[7] A. J Moulson, "Electroceramics Second Edition Materials Á Properties Á Applications," ed: John Wiley & Sons Ltd, 2003.

[8] R. Waser, U. Böttger, and S. Tiedke, *Polar oxides*. Wiley Online Library, 2005.

[9] W. Jaffe, "Cook, and H. Jaffe," *Piezoelectric Ceramics,* pp. 271-80, 1971.

[10] D. Damjanovic, "Ferroelectric, dielectric and piezoelectric properties of ferroelectric thin films and ceramics," *Reports on Progress in Physics,* vol. 61, no. 9, p. 1267, 1998.

[11] J. C. M. A. Maxwell, *A Treatise on electricitz and magnetism*. London: Calendon Press Series, Univeristiy of Oxford, 1873, p. 500.

[12] K. W. Wagner, "Erklärung der dielektrischen nachwirkungsvorgänge auf grund maxwellscher vorstellungen," *Archiv für Elektrotechnik,* vol. 2, no. 9, pp. 371-387, 1914.

[13] D. Hall, "Review nonlinearity in piezoelectric ceramics," *Journal of materials science,* vol. 36, no. 19, pp. 4575-4601, 2001.

[14] M. E. Lines and A. M. Glass, *Principles and applications of ferroelectrics and related materials*. Oxford university press, 2001.

[15] J. Valasek, "Piezo-electric and allied phenomena in Rochelle salt," *Physical review,* vol. 17, no. 4, p. 475, 1921.

[16] H. Jaffe, "Piezoelectric ceramics," *Journal of the American Ceramic Society,* vol. 41, no. 11, pp. 494-498, 1958.

[17] A. Von Hippel, R. Breckenridge, F. Chesley, and L. Tisza, "High dielectric constant ceramics," *Industrial & Engineering Chemistry,* vol. 38, no. 11, pp. 1097-1109, 1946.

[18] W. Cherry Jr and R. Adler, "Piezoelectric effect in polycrystalline barium titanate," *Physical Review,* vol. 72, no. 10, p. 981, 1947.

[19] S. Roberts, "Dielectric and piezoelectric properties of barium titanate," *Physical Review,* vol. 71, no. 12, p. 890, 1947.

[20] V. Goldschmidt, "Skrifter Norske Videnskaps-Akad. Oslo, I," *Mat.-Naturv. Kl,* no. 8, 1926.

[21] H. F. Kay and P. Vousden, "XCV. Symmetry changes in barium titanate at low temperatures and their relation to its ferroelectric properties," *The London, Edinburgh, and Dublin Philosophical Magazine and Journal of Science,* vol. 40, no. 309, pp. 1019-1040, 1949.

[22] K. Uchino, E. Sadanaga, and T. Hirose, "Dependence of the crystal structure on particle size in barium titanate," *Journal of the American Ceramic Society,* vol. 72, no. 8, pp. 1555-1558, 1989.

[23] C. Kittel, P. McEuen, and P. McEuen, *Introduction to solid state physics*. Wiley New York, 1996.
[24] A. Sonin and B. Strukow, "Einführung in die Ferroelektrizität, vieweg," ed: Braunschweig, 1974.
[25] L. Gauckler, "Ingenieurskeramik 3-Funktionskeramik," *Swiss Federal Institute of Technology Zurich, Zurich,* 2001.
[26] M. Lente, A. Picinin, J. Rino, and J. Eiras, "90° domain wall relaxation and frequency dependence of the coercive field in the ferroelectric switching process," *Journal of applied physics,* vol. 95, no. 5, pp. 2646-2653, 2004.
[27] D. Fang and C. Li, "Nonlinear electric-mechanical behavior of a soft PZT-51 ferroelectric ceramic," *Journal of Materials Science,* vol. 34, no. 16, pp. 4001-4010, 1999.
[28] A. Von Hippel, "Ferroelectricity, domain structure, and phase transitions of barium titanate," *Reviews of Modern Physics,* vol. 22, no. 3, p. 221, 1950.
[29] G. Jonker, "Nature of aging in ferroelectric ceramics," *J. Am. Ceram. Soc,* vol. 55, no. 1, pp. 57-58, 1972.
[30] S. Priya and S. Nahm, *Lead-free piezoelectrics*. Springer Science & Business Media, 2011.
[31] Z.-G. Ye, *Handbook of advanced dielectric, piezoelectric and ferroelectric materials: Synthesis, properties and applications*. Elsevier, 2008.
[32] W. Kleemann, "The relaxor enigma—charge disorder and random fields in ferroelectrics," in *Frontiers of ferroelectricity*: Springer, 2006, pp. 129-136.
[33] A. Bokov and Z.-G. Ye, "Recent progress in relaxor ferroelectrics with perovskite structure," *Progress in Advanced Dielectrics,* pp. 105-164, 2020.
[34] G. Smolenskii and V. Isupov, "* Segnetoelektricheskie Svoistva Tverdykh Rastvorov Stannata Bariya V Titanate Bariya.," *Zhurnal Tekhnicheskoi Fiziki,* vol. 24, no. 8, pp. 1375-1386, 1954.
[35] L. E. Cross, "Relaxor ferroelectrics," *Ferroelectrics,* vol. 76, no. 1, pp. 241-267, 1987.
[36] G. Burns and F. Dacol, "Glassy polarization behavior in ferroelectric compounds Pb(Mg1/3Nb2/3)O3 and Pb(Zn1/3Nb2/3)O3," *Solid state communications,* vol. 48, no. 10, pp. 853-856, 1983.
[37] R. J. Tilley, *Perovskites: structure-property relationships*. John Wiley & Sons, 2016.
[38] F. Jiang and S. Kojima, "Relaxation mode in 0. 65Pb(Mg1/3Nb2/3)O3−0.35PbTiO3 relaxor single crystals studied by micro-Brillouin scattering," *Physical Review B,* vol. 62, no. 13, p. 8572, 2000.
[39] M. Abplanalp *et al.*, "Scanning force microscopy of domain structures in Pb(Zn1/3Nb2/3)O3-8% PbTiO3 and Pb(Mg1/3Nb2/3)O3-29% PbTiO3," *Journal of applied physics,* vol. 91, no. 6, pp. 3797-3805, 2002.
[40] W. Jo *et al.*, "Giant electric-field-induced strains in lead-free ceramics for actuator applications–status and perspective," *Journal of Electroceramics,* vol. 29, no. 1, pp. 71-93, 2012.
[41] D. Viehland, S. Jang, L. E. Cross, and M. Wuttig, "Deviation from Curie-Weiss behavior in relaxor ferroelectrics," *Physical Review B,* vol. 46, no. 13, p. 8003, 1992.
[42] D. Viehland, M. Wuttig, and L. Cross, "The glassy behavior of relaxor ferroelectrics," *Ferroelectrics,* vol. 120, no. 1, pp. 71-77, 1991.
[43] A. Glazounov, A. Tagantsev, and A. Bell, "Evidence for domain-type dynamics in the ergodic phase of the PbMg1/3Nb2/3O3 relaxor ferroelectric," *Physical Review B,* vol. 53, no. 17, p. 11281, 1996.
[44] A. Glazounov and A. Tagantsev, "A “breathing” model for the polarization response of relaxor ferroelectrics," *Ferroelectrics,* vol. 221, no. 1, pp. 57-66, 1999.
[45] Y. Imry and S.-k. Ma, "Random-field instability of the ordered state of continuous symmetry," *Physical Review Letters,* vol. 35, no. 21, p. 1399, 1975.

[46] W. Kleemann, "Random fields in relaxor ferroelectrics—a jubilee review," *Journal of Advanced Dielectrics,* vol. 2, no. 02, p. 1241001, 2012.
[47] K. Uchino, *Advanced piezoelectric materials: Science and technology*. Woodhead Publishing, 2017.
[48] K. Nakamura, "Ultrasonic motors," in *Ultrasonic Transducers*: Elsevier, 2012, pp. 677-704.
[49] S. Kumar, C. Wu, G. Padhy, and W. Ding, "Application of ultrasonic vibrations in welding and metal processing: A status review," *Journal of manufacturing processes,* vol. 26, pp. 295-322, 2017.
[50] J. Gallego-Juarez, "Piezoelectric ceramics and ultrasonic transducers," *Journal of Physics E: Scientific Instruments,* vol. 22, no. 10, p. 804, 1989.
[51] E. Moreno *et al.*, "Design and construction of a bolt-clamped Langevin transducer," in *2005 2nd International Conference on Electrical and Electronics Engineering*, 2005: IEEE, pp. 393-395.
[52] T. Ikeda, *Fundamentals of piezoelectricity*. Oxford university press, 1996.
[53] E. S. E. 50324-2, "Piezoelectric Properties of Ceramic Materials and Components—Part 2: Methods of Measurement—Low Power," ed: CENELEC European Committee for Electrotechnical Standardization Brussels …, 2002.
[54] K. Negishi, "Jump phenomenon in resonance curve of ferroelectric ceramics," *Journal of the Physical Society of Japan,* vol. 15, no. 3, pp. 534-534, 1960.
[55] E. Hennig, E. Wehrsdorfer, S. Lürtzing, B. Kolle, and W. Plötner, "Large signal characterization of hard PZT materials," *Journal of the European Ceramic Society,* vol. 25, no. 12, pp. 2411-2414, 2005.
[56] D. Guyomar, N. Aurelle, C. Richard, P. Gonnard, and L. Eyraud, "Nonlinearities in Langevin transducers," in *1994 Proceedings of IEEE Ultrasonics Symposium*, 1994, vol. 2: IEEE, pp. 925-928.
[57] V. Ljamov, "Nonlinear acoustical parameters of piezoelectric crystals," *The Journal of the Acoustical Society of America,* vol. 52, no. 1B, pp. 199-202, 1972.
[58] H. Beige and G. Schmidt, "Electromechanical resonances for investigating linear and nonlinear properties of dielectrics," *Ferroelectrics,* vol. 41, no. 1, pp. 39-49, 1982.
[59] H. N. Shekhani, E. A. Gurdal, S. O. Ural, and K. Uchino, "Analysis of high power behavior in piezoelectric ceramics from a mechanical energy density perspective," *arXiv preprint arXiv:1605.06685,* 2016.
[60] A. Mezheritsky, "Quality factor of piezoceramics," *Ferroelectrics,* vol. 266, no. 1, pp. 277-304, 2002.
[61] K. Uchino and S. Hirose, "Loss mechanisms in piezoelectrics: how to measure different losses separately," *IEEE Transactions on Ultrasonics, ferroelectrics, and frequency control,* vol. 48, no. 1, pp. 307-321, 2001.
[62] T. Tsurumi, Y. B. Kil, K. Nagatoh, H. Kakemoto, S. Wada, and S. Takahashi, "Intrinsic elastic, dielectric, and piezoelectric losses in lead zirconate titanate ceramics determined by an immittance-fitting method," *Journal of the American Ceramic Society,* vol. 85, no. 8, pp. 1993-1996, 2002.
[63] S. Li, W. Cao, and L. Cross, "The extrinsic nature of nonlinear behavior observed in lead zirconate titanate ferroelectric ceramic," *Journal of applied physics,* vol. 69, no. 10, pp. 7219-7224, 1991.
[64] D. Damjanovic, "Contributions to the piezoelectric effect in ferroelectric single crystals and ceramics," *Journal of the American Ceramic society,* vol. 88, no. 10, pp. 2663-2676, 2005.
[65] L. Zheng, R. Sahul, S. Zhang, W. Jiang, S. Li, and W. Cao, "Orientation dependence of piezoelectric properties and mechanical quality factors of 0.27Pb(In1/2Nb1/2)O3-

0.46Pb(Mg1/3Nb2/3)O3-0.27PbTiO3: Mn single crystals," *Journal of Applied Physics,* vol. 114, no. 10, p. 104105, 2013.
[66] Q. M. Zhang, H. Wang, N. Kim, and L. E. Cross, "Direct evaluation of domain-wall and intrinsic contributions to the dielectric and piezoelectric response and their temperature dependence on lead zirconate-titanate ceramics," *Journal of Applied Physics,* vol. 75, no. 1, pp. 454-459, 1994, doi: 10.1063/1.355874.
[67] E. Bondarenko, V. Y. Topolov, and A. Turik, "The role of 90 domain wall displacements in forming physical properties of perovskite ferroelectric ceramics," *Ferroelectrics Letters Section,* vol. 13, no. 1, pp. 13-19, 1991.
[68] G. Liu, S. Zhang, W. Jiang, and W. Cao, "Losses in ferroelectric materials," *Materials Science and Engineering: R: Reports,* vol. 89, pp. 1-48, 2015.
[69] D. Damjanovic, "Hysteresis in piezoelectric and ferroelectric materials," Academic Press, 0124808743, 2006.
[70] C. A. Randall, N. Kim, J. P. Kucera, W. Cao, and T. R. Shrout, "Intrinsic and extrinsic size effects in fine-grained morphotropic-phase-boundary lead zirconate titanate ceramics," *Journal of the American Ceramic Society,* vol. 81, no. 3, pp. 677-688, 1998.
[71] H. Baerwald and D. Berlincourt, "Electromechanical response and dielectric loss of prepolarized barium titanate under maintained electric bias. Part I," *The Journal of the Acoustical Society of America,* vol. 25, no. 4, pp. 703-710, 1953.
[72] A. Pramanick, A. D. Prewitt, J. S. Forrester, and J. L. Jones, "Domains, domain walls and defects in perovskite ferroelectric oxides: A review of present understanding and recent contributions," *Critical Reviews in Solid State and Materials Sciences,* vol. 37, no. 4, pp. 243-275, 2012.
[73] M. Morozov and D. Damjanovic, "Charge migration in Pb(Zr,Ti)O3 ceramics and its relation to ageing, hardening, and softening," *Journal of Applied Physics,* vol. 107, no. 3, p. 034106, 2010.
[74] P. Erhart, R.-A. Eichel, P. Träskelin, and K. Albe, "Association of oxygen vacancies with impurity metal ions in lead titanate," *Physical Review B,* vol. 76, no. 17, p. 174116, 2007.
[75] G. Arlt and H. Neumann, "Internal bias in ferroelectric ceramics: origin and time dependence," *Ferroelectrics,* vol. 87, no. 1, pp. 109-120, 1988.
[76] A. Nowick and W. Heller, "Dielectric and anelastic relaxation of crystals containing point defects," *Advances in Physics,* vol. 14, no. 54, pp. 101-166, 1965.
[77] K. Carl and K. Hardtl, "Electrical after-effects in Pb(Ti,Zr)O3 ceramics," *Ferroelectrics,* vol. 17, no. 1, pp. 473-486, 1977.
[78] V. Postnikov, V. Pavlov, and S. Turkov, "Internal friction in ferroelectrics due to interaction of domain boundaries and point defects," *Journal of Physics and Chemistry of Solids,* vol. 31, no. 8, pp. 1785-1791, 1970.
[79] Y. A. Genenko, J. Glaum, O. Hirsch, H. Kungl, M. Hoffmann, and T. Granzow, "Aging of poled ferroelectric ceramics due to relaxation of random depolarization fields by space-charge accumulation near grain boundaries," *Physical Review B,* vol. 80, no. 22, p. 224109, 2009.
[80] Y. A. Genenko, J. Glaum, M. J. Hoffmann, and K. Albe, "Mechanisms of aging and fatigue in ferroelectrics," *Materials Science and Engineering: B,* vol. 192, pp. 52-82, 2015.
[81] A. Benčan *et al.*, "Structure and the electrical properties of Pb(Zr,Ti)O3–Zirconia composites," *Journal of the American Ceramic Society,* vol. 95, no. 2, pp. 651-657, 2012.
[82] L. K.V., L. M. Riemer, J. Koruza, and J. Rödel, "Hardening of electromechanical properties in piezoceramics using a composite approach," *Applied Physics Letters,* vol. 111, no. 2, p. 022905, 2017, doi: 10.1063/1.4986911.

[83] C. Zhao *et al.*, "Precipitation Hardening in Ferroelectric Ceramics," *Advanced Materials,* vol. 33, no. 36, p. 2102421, 2021.
[84] D. Hall, A. Steuwer, B. Cherdhirunkorn, P. Withers, and T. Mori, "Micromechanics of residual stress and texture development due to poling in polycrystalline ferroelectric ceramics," *Journal of the Mechanics and Physics of Solids,* vol. 53, no. 2, pp. 249-260, 2005.
[85] J. Zhang *et al.*, "Semiconductor/relaxor 0–3 type composites without thermal depolarization in Bi0.5Na0.5TiO3-based lead-free piezoceramics," *Nature communications,* vol. 6, no. 1, pp. 1-10, 2015.
[86] Z. Fan, L. Zhou, T.-H. Kim, J. Zhang, S.-T. Zhang, and X. Tan, "Mechanisms of enhanced thermal stability of polarization in lead-free (Bi1/2Na1/2)0.94Ba0.06TiO3/ZnO ceramic composites," *Physical Review Materials,* vol. 3, no. 2, p. 024402, 2019.
[87] Z. Zhang *et al.*, "Preparation and anisotropic properties of textured structural ceramics: A review," *Journal of Advanced Ceramics,* vol. 8, pp. 289-332, 2019.
[88] M. M. Seabaugh, G. L. Messing, and M. D. Vaudin, "Texture development and microstructure evolution in liquid-phase-sintered α-alumina ceramics prepared by templated grain growth," *Journal of the American Ceramic Society,* vol. 83, no. 12, pp. 3109-3116, 2000.
[89] T. Kimura, "Application of Texture Engineering to Piezoelectric Ceramics;A Review&mdash," *Journal of the Ceramic Society of Japan,* vol. 114, no. 1325, pp. 15-25, 2006, doi: 10.2109/jcersj.114.15.
[90] J. L. Jones, M. Hoffman, and K. J. Bowman, "Saturated domain switching textures and strains in ferroelastic ceramics," *Journal of applied physics,* vol. 98, no. 2, p. 024115, 2005.
[91] J. Glaum and M. Hoffman, "Electric fatigue of lead-free piezoelectric materials," *Journal of the American Ceramic Society,* vol. 97, no. 3, pp. 665-680, 2014.
[92] H. Simons *et al.*, "Domain fragmentation during cyclic fatigue in 94%(Bi1/2Na1/2) TiO3-6% BaTiO3," *Journal of Applied Physics,* vol. 112, no. 4, p. 044101, 2012.
[93] W. Warren, D. Dimos, B. Tuttle, G. Pike, and H. N. Al-shareef, "Relationships among ferroelectric fatigue, electronic charge trapping, defect-dipoles, and oxygen vacancies in perovskite oxides," *Integrated ferroelectrics,* vol. 16, no. 1-4, pp. 77-86, 1997.
[94] X. Shi, N. Kumar, and M. Hoffman, "Electrical fatigue behavior of NBT-BT-xKNN ferroelectrics: effect of ferroelectric phase transformations and oxygen vacancies," *Journal of Materials Chemistry C,* 10.1039/C9TC05665C vol. 8, no. 11, pp. 3887-3896, 2020.
[95] M. Okayasu, G. Ozeki, and M. Mizuno, "Fatigue failure characteristics of lead zirconate titanate piezoelectric ceramics," *Journal of the European Ceramic Society,* vol. 30, no. 3, pp. 713-725, 2010.
[96] M. D. Hill, G. S. White, C. S. Hwang, and I. K. Lloyd, "Cyclic damage in lead zirconate titanate," *Journal of the American Ceramic Society,* vol. 79, no. 7, pp. 1915-1920, 1996.
[97] M. Umeda, S. Takahashi, Y. Sasaki, K. Nakamura, and S. Ueha, "Vibration stress and temperature dependence of piezoelectric resonators with lead–zirconate–titanate ceramics," *Electronics and Communications in Japan (Part II: Electronics),* vol. 83, no. 9, pp. 1-7, 2000.
[98] M. Slabki *et al.*, "Anisotropy of the high-power piezoelectric properties of Pb(Zr,Ti)O3," *Journal of the American Ceramic Society,* vol. 102, no. 10, pp. 6008-6017, 2019.
[99] MarketsandMarkets, "Piezoelectric Devices Market—Global Trend & Forecast to 2020," 2015.
[100] T. Yamamoto, "Ferroelectric properties of the PbZrO3–PbTiO3 system," *Japanese Journal of Applied Physics,* vol. 35, no. 9S, p. 5104, 1996.
[101] L. Jin, "Broadband dielectric response in hard and soft PZT," EPFL, 2011.

[102] A. J. Bell and O. Deubzer, "Lead-free piezoelectrics—The environmental and regulatory issues," *Mrs bulletin,* vol. 43, no. 8, pp. 581-587, 2018.
[103] J. Gordon, A. Taylor, and P. Bennett, "Lead poisoning: case studies," *British journal of clinical pharmacology,* vol. 53, no. 5, pp. 451-458, 2002.
[104] W. H. Organization, "Lead poisoning and health fact sheet," *updated August,* 2017.
[105] I. Hertz-Picciotto, "The evidence that lead increases the risk for spontaneous abortion," *American journal of industrial medicine,* vol. 38, no. 3, pp. 300-309, 2000.
[106] E. Commission, "Regulation (EC) No 1907/2006 of the European Parliament and of the Council of 18 December 2006 concerning the Registration, Evaluation, Authorisation and Restriction of Chemicals (REACH), establishing a European Chemicals Agency, amending Directive 1999/45/EC and repealing Council Regulation (EEC) No 793/93 and Commission Regulation (EC) No 1488/94 as well as Council Directive 76/769/EEC and Commission Directives 91/155/EEC, 93/67/EEC, 93/105/EC and 2000/21/EC," *Official Journal of the European Union,* vol. 396, pp. 1-849, 2006.
[107] J. Koruza, A. J. Bell, T. Frömling, K. G. Webber, K. Wang, and J. Rödel, "Requirements for the transfer of lead-free piezoceramics into application," *Journal of Materiomics,* vol. 4, no. 1, pp. 13-26, 2018.
[108] J. Rödel, W. Jo, K. T. Seifert, E. M. Anton, T. Granzow, and D. Damjanovic, "Perspective on the development of lead-free piezoceramics," *Journal of the American Ceramic Society,* vol. 92, no. 6, pp. 1153-1177, 2009.
[109] D. Berlincourt, "Piezoelectric ceramic compositional development," *The Journal of the Acoustical Society of America,* vol. 91, no. 5, pp. 3034-3040, 1992.
[110] X. Xing, X. Zhu, and J. Li, "Structure of Pb(Zr,Ti)O3 (PZT) for power ultrasonic transducer," *Journal of Wuhan University of Technology-Mater. Sci. Ed.,* vol. 33, no. 4, pp. 884-887, 2018.
[111] D. Bochenek and P. Niemiec, "Microstructure and physical properties of the multicomponent PZT-type ceramics doped by calcium, sodium, bismuth and cadmium," *Applied Physics A,* vol. 124, no. 11, pp. 1-7, 2018.
[112] H. J. Lee, S. O. Ural, L. Chen, K. Uchino, and S. Zhang, "High power characteristics of lead-free piezoelectric ceramics," *Journal of the American Ceramic Society,* vol. 95, no. 11, pp. 3383-3386, 2012.
[113] S. T. HIROSE, "Vibration-level characteristics of lead-zirconate-titanate ceramics," *Japanese journal of applied physics,* vol. 31, no. 9S, p. 3055, 1992.
[114] M. Slabki, K. V. Lalitha, J. Rödel, and J. Koruza, "Origin of high-power drive stability in (Na0.5Bi0.5)TiO3-BaTiO3 based piezoceramics," *Acta Materialia,* p. 117703, 2022/02/01/ 2022.
[115] T. Takenaka, K.-i. Maruyama, and K. Sakata, "(Bi1/2Na1/2)TiO3-BaTiO3 system for lead-free piezoelectric ceramics," *Japanese Journal of Applied Physics,* vol. 30, no. 9S, p. 2236, 1991.
[116] W. Jo *et al.*, "Evolving morphotropic phase boundary in lead-free (Bi1/2Na1/2)TiO3–BaTiO3 piezoceramics," *Journal of Applied Physics,* vol. 109, no. 1, p. 014110, 2011.
[117] D. K. Khatua, A. Agarwal, N. Kumar, and R. Ranjan, "Probing local structure of the morphotropic phase boundary composition of Na0.5Bi0.5TiO3–BaTiO3 using rare-earth photoluminescence as a technique," *Acta Materialia,* vol. 145, pp. 429-436, February 2018.
[118] C. Ma and X. Tan, "In situ Transmission Electron Microscopy Study on the Phase Transitionsin Lead-Free (1− x)(Bi1/2Na1/2) TiO3–xBaTiO3 Ceramics," *Journal of the American Ceramic Society,* vol. 94, no. 11, pp. 4040-4044, 2011.
[119] A. R. Paterson *et al.*, "Relaxor-ferroelectric transitions: Sodium bismuth titanate derivatives," *MRS Bulletin,* vol. 43, no. 8, pp. 600-606, 2018.

[120] A. M. Glazer, "The classification of tilted octahedra in perovskites," *Acta Crystallographica Section B: Structural Crystallography and Crystal Chemistry,* vol. 28, no. 11, pp. 3384-3392, 1972.
[121] E. Aksel, J. S. Forrester, J. L. Jones, P. A. Thomas, K. Page, and M. R. Suchomel, "Monoclinic crystal structure of polycrystalline Na0.5Bi0.5TiO3," *Applied Physics Letters,* vol. 98, no. 15, p. 152901, 2011.
[122] R. Beanland and P. Thomas, "Imaging planar tetragonal sheets in rhombohedral Na0.5Bi0.5TiO3 using transmission electron microscopy," *Scripta Materialia,* vol. 65, no. 5, pp. 440-443, 2011.
[123] J. Yao *et al.*, "Role of coexisting tetragonal regions in the rhombohedral phase of Na0.5Bi0.5TiO3-xat.% BaTiO3 crystals on enhanced piezoelectric properties on approaching the morphotropic phase boundary," *Applied physics letters,* vol. 100, no. 1, p. 012901, 2012.
[124] M. Hinterstein *et al.*, "Cyclic electric field response of morphotropic Bi1/2Na1/2TiO3-BaTiO3 piezoceramics," *Applied Physics Letters,* vol. 106, no. 22, p. 222904, 2015.
[125] R. Ranjan and A. Dviwedi, "Structure and dielectric properties of (Na0.50Bi0. 50)1−xBaxTiO3: 0≤ x≤ 0.10," *Solid state communications,* vol. 135, no. 6, pp. 394-399, 2005.
[126] A.-K. Fetzer, A. Wohninsland, K. Hofmann, O. Clemens, L. Kodumudi Venkataraman, and H.-J. Kleebe, "Domain structure and phase evolution in quenched and furnace cooled lead-free Na1/2Bi1/2TiO3–BaTiO3 ceramics," *Open Ceramics,* vol. 5, p. 100077, 2021/03/01/ 2021.
[127] C. Ma, H. Guo, S. P. Beckman, and X. Tan, "Creation and destruction of morphotropic phase boundaries through electrical poling: a case study of lead-free (Bi1/2Na1/2)TiO3−BaTiO3 piezoelectrics," *Physical Review Letters,* vol. 109, no. 10, p. 107602, 2012.
[128] D. Damjanovic, "A morphotropic phase boundary system based on polarization rotation and polarization extension," *Applied Physics Letters,* vol. 97, no. 6, p. 062906, 2010.
[129] G. D. Adhikary, B. Mahale, B. N. Rao, A. Senyshyn, and R. Ranjan, "Depoling phenomena in Na0.5Bi0.5TiO3−BaTiO 3: A structural perspective," *Physical Review B,* vol. 103, no. 18, p. 184106, 2021.
[130] Q. Zhang, X. Zhao, R. Sun, and H. Luo, "Crystal growth and electric properties of lead-free NBT-BT at compositions near the morphotropic phase boundary," *physica status solidi (a),* vol. 208, no. 5, pp. 1012-1020, 2011.
[131] R. Garg, B. N. Rao, A. Senyshyn, P. Krishna, and R. Ranjan, "Lead-free piezoelectric system (Na0.5Bi0.5)TiO3-BaTiO3: Equilibrium structures and irreversible structural transformations driven by electric field and mechanical impact," *Physical Review B,* vol. 88, no. 1, p. 014103, 2013.
[132] W. Jo and J. Rödel, "Electric-field-induced volume change and room temperature phase stability of (Bi1/2Na1/2)TiO3-x mol.% BaTiO3 piezoceramics," *Applied Physics Letters,* vol. 99, no. 4, p. 042901, 2011.
[133] C. Xu, D. Lin, and K. W. Kwok, "Structure, electrical properties and depolarization temperature of (Bi0.5Na0.5)TiO3–BaTiO3 lead-free piezoelectric ceramics," *Solid State Sciences,* vol. 10, no. 7, pp. 934-940, July 2008.
[134] E.-M. Anton *et al.*, "Structure and temperature-dependent phase transitions of lead-free Bi1/2Na1/2TiO3-Bi1/2K1/2TiO3-K0.5Na0.5NbO3 piezoceramics," *Journal of Materials Research,* vol. 27, no. 19, p. 2466, 2012.
[135] H. Simons *et al.*, "Electric-field-induced strain mechanisms in lead-free 94%(Bi1/2Na1/2)TiO3–6%BaTiO3," *Applied Physics Letters,* vol. 98, no. 8, p. 082901, February 2011.

[136] Q. Xu *et al.*, "Synthesis and piezoelectric and ferroelectric properties of (Na0.5Bi0.5)1−xBaxTiO3 ceramics," *Materials Chemistry and Physics,* vol. 90, no. 1, pp. 111-115, 2005.
[137] B.-J. Chu, D.-R. Chen, G.-R. Li, and Q.-R. Yin, "Electrical properties of Na1/2Bi1/2TiO3–BaTiO3 ceramics," *Journal of the European Ceramic Society,* vol. 22, no. 13, pp. 2115-2121, December 2002.
[138] S. T. Zhang, A. B. Kounga, E. Aulbach, and Y. Deng, "Temperature-dependent electrical properties of 0.94Bi0.5Na0.5TiO3–0.06BaTiO3 ceramics," *Journal of the American Ceramic Society,* vol. 91, no. 12, pp. 3950-3954, 2008.
[139] J. Suchanicz, A. Jeżowski, R. Poprawski, and S. Dacko, "Thermal and dielectric behaviour of pure and doped Na0.5Bi0.5TiO3 at low temperatures," *physica status solidi (b),* vol. 221, no. 2, pp. 789-795, 2000.
[140] S. M. Denkhaus, M. Vögler, N. Novak, and J. Rödel, "Short crack fracture toughness in (1−x)(Na1/2Bi1/2)TiO3–xBaTiO3 relaxor ferroelectrics," *Journal of the American Ceramic Society,* vol. 100, no. 10, pp. 4760-4769, October 2017.
[141] L. Li, M. Zhu, K. Zhou, Q. Wei, M. Zheng, and Y. Hou, "Delayed thermal depolarization of Bi0.5Na0.5TiO3-BaTiO3 by doping acceptor Zn^2+ with large ionic polarizability," *Journal of Applied Physics,* vol. 122, no. 20, p. 204104, November 2017.
[142] I.-T. Seo, S. Steiner, and T. Frömling, "The effect of A site non-stoichiometry on 0.94(NayBix)TiO3-0.06 BaTiO3," *Journal of the European Ceramic Society,* vol. 37, no. 4, pp. 1429-1436, 2017.
[143] H. Luo *et al.*, "Simultaneously enhancing piezoelectric performance and thermal depolarization in lead-free (Bi,Na)TiO3-BaTiO3 via introducing oxygen-defect perovskites," *Acta Materialia,* vol. 208, p. 116711, 2021.
[144] D. K. Khatua *et al.*, "A coupled microstructural-structural mechanism governing thermal depolarization delay in Na0.5Bi0.5TiO3-based piezoelectrics," *Acta Materialia,* vol. 179, pp. 49-60, 2019.
[145] H. Muramatsu, H. Nagata, and T. Takenaka, "Quenching effects for piezoelectric properties on lead-free (Bi1/2Na1/2)TiO3 ceramics," *Japanese Journal of Applied Physics,* vol. 55, no. 10S, p. 10TB07, 2016.
[146] L. KV, J. Koruza, and J. Rödel, "Propensity for spontaneous relaxor-ferroelectric transition in quenched (Na1/2Bi1/2)TiO3-BaTiO3 compositions," *Applied Physics Letters,* vol. 113, no. 25, p. 252902, 2018.
[147] L. Kodumudi Venkataraman *et al.*, "Thermal depolarization and electromechanical hardening in Zn2+-doped Na1/2Bi1/2TiO3-BaTiO3," *Journal of the American Ceramic Society,* vol. 104, no. 5, pp. 2201-2212, 2020.
[148] G. Haxel, *Rare earth elements: critical resources for high technology* (no. 2). US Department of the Interior, US Geological Survey, 2002.
[149] R. Shanon, "Revised effective ionic and systematic studies of interatomic distances in halides and chalcogenides," *Acta Crystallogr. A,* vol. 32, pp. 751-767, 1976.
[150] L. H. Ahrens, "The use of ionization potentials Part 1. Ionic radii of the elements," *Geochimica et cosmochimica Acta,* vol. 2, no. 3, pp. 155-169, 1952.
[151] E. Sapper *et al.*, "Aging in the relaxor and ferroelectric state of Fe-doped (1-x)(Bi1/2Na1/2)TiO3-xBaTiO3 piezoelectric ceramics," *Journal of Applied Physics,* vol. 116, no. 10, p. 104102, September 2014.
[152] J. Shi, W. Tian, X. Liu, and H. Fan, "Electric-field induced phase transition and fatigue behaviors of (Bi0.5+x/2Na0.5-x/2)0.94Ba0.06Ti1-xFexO3 ferroelectrics," *Journal of the American Ceramic Society,* vol. 100, no. 3, pp. 1080-1090, March 2017.
[153] J. Jin *et al.*, "Influence of MoO3 on electrical properties and thermal depolarization of Bi0.5Na0.5TiO3-BaTiO3 lead-free piezoceramics," *Journal of Applied Physics,* vol. 127, no. 23, p. 234102, 2020, doi: 10.1063/1.5143641.

[154] H.-d. Li, C.-d. Feng, and W.-l. Yao, "Some effects of different additives on dielectric and piezoelectric properties of (Bi1/2Na1/2)TiO3-BaTiO3 morphotropic-phase-boundary composition," *Materials Letters,* vol. 58, no. 7–8, pp. 1194-1198, March 2004.
[155] Q. Xu, M. Chen, W. Chen, H.-X. Liu, B.-H. Kim, and B.-K. Ahn, "Effect of CoO additive on structure and electrical properties of (Na0.5Bi0.5)0.93Ba0.07TiO3 ceramics prepared by the citrate method," *Acta Materialia,* vol. 56, no. 3, pp. 642-650, February 2008.
[156] M.-S. Yoon, Y.-G. Lee, and S.-C. Ur, "Effects of co-doped CaO/MnO on the piezoelectric/dielectric properties and phase transition of lead-free (Bi0.5Na0.5)0.94Ba0.06TiO3 piezoelectric ceramics," *Journal of electroceramics,* vol. 23, no. 2-4, p. 564, 2009.
[157] X.-J. Li, Q. Wang, and Q.-L. Li, "Effects of MnO2 addition on microstructure and electrical properties of (Bi0.5Na0.5)0.94Ba0.06TiO3 ceramics," *Journal of electroceramics,* vol. 20, no. 2, pp. 89-94, 2008.
[158] E. Sapper, N. Novak, W. Jo, T. Granzow, and J. Rödel, "Electric-field–temperature phase diagram of the ferroelectric relaxor system (1 − x)Bi1/2Na1/2TiO3 − xBaTiO3 doped with manganese," *Journal of Applied Physics,* vol. 115, no. 19, p. 194104, May 2014.
[159] M. Zhu, L. Liu, Y. Hou, H. Wang, and H. Yan, "Microstructure and electrical properties of MnO-doped (Na0. 5Bi0. 5) 0.92 Ba0. 08TiO3 lead-free piezoceramics," *Journal of the American Ceramic Society,* vol. 90, no. 1, pp. 120-124, 2007.
[160] A. Verma *et al.*, "Increase in depolarization temperature and improvement in ferroelectric properties by V5+ doping in lead-free 0.94(Na0.50Bi0.50)TiO3-0.06 BaTiO3 ceramics," *Journal of Applied Physics,* vol. 123, no. 22, p. 224101, 2018.
[161] R. Zuo, C. Ye, X. Fang, and J. Li, "Tantalum doped 0.94Bi0.5Na0.5TiO3–0.06BaTiO3 piezoelectric ceramics," *Journal of the European Ceramic Society,* vol. 28, no. 4, pp. 871-877, 2008.
[162] J. Glaum, H. Simons, M. Acosta, and M. Hoffman, "Tailoring the Piezoelectric and Relaxor Properties of (Bi1/2Na1/2)TiO3–BaTiO3 via Zirconium Doping," *Journal of the American Ceramic Society,* vol. 96, no. 9, pp. 2881-2886, September 2013.
[163] G. Liu *et al.*, "Phase segregation and dielectric, ferroelectric, and piezoelectric properties of MgO-doped NBT-BT lead-free ferroelecric ceramics," *Materials Research Express,* vol. 5, no. 3, p. 036305, 2018.
[164] D. Zhu, H. Liu, H. Luo, S. Sun, and J. Chen, "Tetragonal phase and enhanced depolarization temperature in Ba-rich (Bi,Na)TiO3–BaTiO3 lead-free piezoelectrics," *Ceramics International,* 2019.
[165] P. Fu *et al.*, "Effect of Dy2O3 on the structure and electrical properties of (Bi0.5Na0.5)0.94Ba0.06TiO3 lead-free piezoelectric ceramics," *Journal of Alloys and Compounds,* vol. 508, no. 2, pp. 546-553, 2010/10/22/ 2010.
[166] P. Fu, Z. Xu, R. Chu, W. Li, G. Zang, and J. Hao, "Piezoelectric, ferroelectric and dielectric properties of Sm2O3-doped (Bi0.5Na0.5)0.94Ba0.06TiO3 lead-free ceramics," *Materials Chemistry and Physics,* vol. 124, no. 2-3, pp. 1065-1070, 2010.
[167] B. Hu *et al.*, "Photoluminescence and Temperature Dependent Electrical Properties of Er-Doped 0.94Bi0.5Na0.5TiO3-0.06BaTiO3 Ceramics," *Journal of the American Ceramic Society,* vol. 97, no. 12, pp. 3877-3882, 2014.
[168] X. Ma, J. Yin, Q. Zhou, L. Xue, and Y. Yan, "Effect of Eu doping on structure and electrical properties of lead-free (Bi0.5Na0.5)0.94Ba0.06TiO3 ceramics," *Ceramics International,* vol. 40, no. 5, pp. 7007-7013, 2014.
[169] J. Shi and W. Yang, "Piezoelectric and dielectric properties of CeO2-doped (Bi0.5Na0.5)0.94 Ba0.06TiO3 lead-free ceramics," *Journal of alloys and compounds,* vol. 472, no. 1-2, pp. 267-270, 2009.

[170] P. Fu, Z. Xu, R. Chu, W. Li, G. Zang, and J. Hao, "Piezoelectric, ferroelectric and dielectric properties of Nd2O3-doped (Bi0.5Na0.5)0.94Ba0.06TiO3 lead-free ceramics," *Materials Science and Engineering: B,* vol. 167, no. 3, pp. 161-166, 2010.
[171] H.-D. Li, C.-D. Feng, and P.-H. Xiang, "Electrical properties of La3+-doped (Na0.5Bi0.5)0.94 Ba0.06TiO3 ceramics," *Japanese journal of applied physics,* vol. 42, no. 12R, p. 7387, 2003.
[172] L. Liu, M. Zhu, Y. Hou, H. Yan, and R. Liu, "Abnormal piezoelectric and dielectric behavior of 0.92Na0.5Bi0.5TiO3-0.08BaTiO3 induced by La doping," *Journal of Materials Research,* vol. 22, no. 05, pp. 1188-1192, May 2007.
[173] C. M. Lau, X. W. Xu, and K. Kwok, "Photoluminescence, ferroelectric, dielectric and piezoelectric properties of Er-doped BNT–BT multifunctional ceramics," *Applied surface science,* vol. 336, pp. 314-320, 2015.
[174] A. Mishra, G. Abebe, G. Jafo, G. D. Adhikary, and A. De, "Effect of A-site off-stoichiometry on the microstructural, structural, and electromechanical properties of lead-free tetragonal 0.80Na0.5Bi0.5TiO3–0.20BaTiO3 (NBT–20BT) piezoceramic," *Journal of Materials Science: Materials in Electronics,* pp. 1-16, 2021.
[175] A. Mishra, D. K. Khatua, A. De, and R. Ranjan, "Off-stoichiometry, structural-polar disorder and piezoelectricity enhancement in pre-MPB lead-free Na0.5Bi0.5TiO3-BaTiO3 piezoceramic," *Journal of Applied Physics,* vol. 125, no. 21, p. 214101, 2019.
[176] S. Prasertpalichat and D. P. Cann, "Hardening in non-stoichiometric (1 − x)Bi0.5Na0.5TiO3–xBaTiO3 lead-free piezoelectric ceramics," *Journal of Materials Science,* vol. 51, no. 1, pp. 476-486, September 2015.
[177] Q. Xu, D.-P. Huang, M. Chen, W. Chen, H.-X. Liu, and B.-H. Kim, "Effect of bismuth excess on ferroelectric and piezoelectric properties of a (Na0.5Bi0.5)TiO3–BaTiO3 composition near the morphotropic phase boundary," *Journal of Alloys and Compounds,* vol. 471, no. 1-2, pp. 310-316, 2009.
[178] T. Shrout, W. Schulze, and J. Biggers, "Electromechanical behavior of antiferroelectric-ferroelectric multilayer PZT based composites," *Ferroelectrics,* vol. 29, no. 1, pp. 129-134, 1980.
[179] D. Su Lee, S. Jong Jeong, M. Soo Kim, and J. Hyuk Koh, "Electric field induced polarization and strain of Bi-based ceramic composites," *Journal of Applied Physics,* vol. 112, no. 12, p. 124109, 2012.
[180] C. Groh *et al.*, "Relaxor/ferroelectric composites: a solution in the quest for practically viable lead-free incipient piezoceramics," *Advanced Functional Materials,* vol. 24, no. 3, pp. 356-362, 2014.
[181] N. H. Khansur *et al.*, "Tailoring of unipolar strain in lead-free piezoelectrics using the ceramic/ceramic composite approach," *Journal of Applied Physics,* vol. 115, no. 12, p. 124108, 2014.
[182] H. Zhang, C. Groh, Q. Zhang, W. Jo, K. G. Webber, and J. Rödel, "Large strain in relaxor/ferroelectric composite lead-free piezoceramics," *Advanced Electronic Materials,* vol. 1, no. 6, p. 1500018, 2015.
[183] V. O. Sherman, A. K. Tagantsev, N. Setter, D. Iddles, and T. Price, "Ferroelectric-dielectric tunable composites," *Journal of applied physics,* vol. 99, no. 7, p. 074104, 2006.
[184] T. Takenaka, H. Komiya, and K. Sakata, "PbZrO3-based composite pyroelectric ceramics," in *1990 IEEE 7th International Symposium on Applications of Ferroelectrics*, 1990: IEEE, pp. 370-373.
[185] O. Furukawa, M. Harata, M. Imai, Y. Yamashita, and S. Mukaeda, "Low firing and high dielectric constant X7R ceramic dielectric for multilayer capacitors based on relaxor and barium titanate composite," *Journal of materials science,* vol. 26, no. 21, pp. 5838-5842, 1991.

[186] E. K. Akdogan, M. Allahverdi, and A. Safari, "Piezoelectric composites for sensor and actuator applications," *IEEE transactions on ultrasonics, ferroelectrics, and frequency control,* vol. 52, no. 5, pp. 746-775, 2005.
[187] A. Mahajan, H. Zhang, J. Wu, E. V. Ramana, M. Reece, and H. Yan, "Effect of phase transitions on thermal depoling in lead-free 0.94(Bi0.5Na0.5TiO3)–0.06 (BaTiO3) based piezoelectrics," *The Journal of Physical Chemistry C,* vol. 121, no. 10, pp. 5709-5718, 2017.
[188] L. M. Riemer *et al.*, "Stress-induced phase transition in lead-free relaxor ferroelectric composites," *Acta Materialia,* vol. 136, pp. 271-280, 2017.
[189] F. Schader, "Mechanical Stability of the Electromechanical Properties and Phase Transitions in Lead-Containing and Lead-Free Ferroelectrics," Dr. Ing Dissertation, Material- und Geowissenschaften, Technische Universität Darmstadt, TU Prints, 2016.
[190] J. Zhang *et al.*, "Bi0.5Na0.5TiO3:ZnO lead-free piezoelectric composites with deferred thermal depolarization," *Applied Physics Letters,* vol. 106, no. 23, p. 232904, 2015.
[191] L. K. V. *et al.*, "Spontaneous ferroelectric order in lead-free relaxor Na1/2Bi1/2TiO3-based composites," *Physical Review B,* vol. 101, no. 17, p. 174108, 2020.
[192] C. Groh, W. Jo, and J. Rödel, "Tailoring Strain Properties of (0.94− x) Bi1/2Na1/2TiO3–0.06BaTiO3–xK0.5Na0.5NbO3 Ferroelectric/Relaxor Composites," *Journal of the American Ceramic Society,* vol. 97, no. 5, pp. 1465-1470, 2014.
[193] O. Elkechai, M. Manier, and J. Mercurio, "Na0.5Bi0.5TiO3–K0.5Bi0.5TiO3 (NBT-KBT) system: a structural and electrical study," *physica status solidi (a),* vol. 157, no. 2, pp. 499-506, 1996.
[194] A. Sasaki, T. Chiba, Y. Mamiya, and E. Otsuki, "Dielectric and piezoelectric properties of (Bi0.5Na0.5)TiO3–(Bi0.5K0.5)TiO3 systems," *Japanese Journal of Applied Physics,* vol. 38, no. 9S, p. 5564, 1999.
[195] K. Yoshii, Y. Hiruma, H. Nagata, and T. Takenaka, "Electrical properties and depolarization temperature of (Bi1/2Na1/2)TiO3–(Bi1/2K1/2)TiO3 lead-free piezoelectric ceramics," *Japanese journal of applied physics,* vol. 45, no. 5S, p. 4493, 2006.
[196] Y. Hiruma, K. Yoshii, H. Nagata, and T. Takenaka, "Investigation of phase transition temperatures on (Bi1/2Na1/2) TiO3-(Bi1/2K1/2) TiO3 and (Bi1/2Na1/2) TiO3-BaTiO3 lead-free piezoelectric ceramics by electrical measurements," *Ferroelectrics,* vol. 346, no. 1, pp. 114-119, 2007.
[197] Y. Hiruma, K. Yoshii, H. Nagata, and T. Takenaka, "Phase transition temperature and electrical properties of (Bi1⁄2Na1⁄2)TiO3–(Bi1⁄2A1⁄2)Ti O3 (A= Li and K) lead-free ferroelectric ceramics," *Journal of Applied Physics,* vol. 103, no. 8, p. 084121, 2008.
[198] M. Otoničar, S. Škapin, M. Spreitzer, and D. Suvorov, "Compositional range and electrical properties of the morphotropic phase boundary in the Na0.5Bi0.5TiO3-K0.5Bi0.5TiO3 system," *Journal of the European Ceramic Society,* vol. 30, no. 4, pp. 971-979, 2010.
[199] R. Jing *et al.*, "Phase evolution and relaxor to ferroelectric phase transition boosting ultrahigh electrostrains in (1− x)(Bi1/2Na1/2) TiO3-x (Bi1/2K1/2) TiO3 solid solutions," *Journal of Materiomics,* 2021.
[200] C. F. Buhrer, "Some properties of bismuth perovskites," *The Journal of Chemical Physics,* vol. 36, no. 3, pp. 798-803, 1962.
[201] I. Levin *et al.*, "Local structure, pseudosymmetry, and phase transitions in Na1/2Bi1/2TiO3–K1/2Bi1/2TiO 3 ceramics," *Physical Review B,* vol. 87, no. 2, p. 024113, 2013.
[202] G. Jones, J. Kreisel, and P. Thomas, "A structural study of the (Na1−xKx)0.5 Bi0.5TiO3 perovskite series as a function of substitution (x) and temperature," *Powder diffraction,* vol. 17, no. 4, pp. 301-319, 2002.

[203] S. Saïd and J.-P. Mercurio, "Relaxor behaviour of low lead and lead free ferroelectric ceramics of the Na0.5Bi0.5TiO3–PbTiO3 and Na0.5Bi0.5TiO3–K0.5Bi0.5TiO3 systems," *Journal of the European Ceramic Society,* vol. 21, no. 10-11, pp. 1333-1336, 2001.
[204] Y. Hiruma, T. Watanabe, H. Nagata, and T. Takenaka, "Piezoelectric properties of (Bi1/2Na1/2)TiO3-based solid solution for lead-free high-power applications," *Japanese Journal of Applied Physics,* vol. 47, no. 9S, p. 7659, 2008.
[205] Y. Li, W. Chen, Q. Xu, J. Zhou, Y. Wang, and H. Sun, "Piezoelectric and dielectric properties of CeO2-doped Bi0.5Na0.44K0.06TiO3 lead-free ceramics," *Ceramics International,* vol. 33, no. 1, pp. 95-99, 2007/01/01/ 2007.
[206] J. Yin, Y. Wang, Y. Zhang, B. Wu, and J. Wu, "Thermal depolarization regulation by oxides selection in lead-free BNT/oxides piezoelectric composites," *Acta Materialia,* vol. 158, pp. 269-277, 2018.
[207] Y. Hiruma, H. Nagata, and T. Takenaka, "Phase diagrams and electrical properties of (Bi1/2Na1/2)TiO3-based solid solutions," *Journal of Applied Physics,* vol. 104, no. 12, p. 124106, 2008.
[208] Z. Yang, B. Liu, L. Wei, and Y. Hou, "Structure and electrical properties of (1− x)Bi0.5Na0.5TiO3–xBi0.5K0.5TiO3 ceramics near morphotropic phase boundary," *Materials Research Bulletin,* vol. 43, no. 1, pp. 81-89, 2008.
[209] E.-M. Anton, W. Jo, D. Damjanovic, and J. Rödel, "Determination of depolarization temperature of (Bi1/2Na1/2) TiO3-based lead-free piezoceramics," *Journal of Applied Physics,* vol. 110, no. 9, p. 094108, 2011.
[210] S. Zhao, G. Li, A. Ding, T. Wang, and Q. Yin, "Ferroelectric and piezoelectric properties of (Na,K)0.5Bi0.5TiO3 lead free ceramics," *Journal of Physics D: Applied Physics,* vol. 39, no. 10, pp. 2277-2281, 2006/05/05 2006, doi: 10.1088/0022-3727/39/10/042.
[211] A. Ullah, C. W. Ahn, A. Hussain, S. Y. Lee, H. J. Lee, and I. W. Kim, "Phase transitions and large electric field-induced strain in BiAlO3-modified Bi0.5(Na,K)0.5TiO3 lead-free piezoelectric ceramics," *Current Applied Physics,* vol. 10, no. 4, pp. 1174-1181, 2010/07/01/ 2010.
[212] C. Wang, X. Lou, T. Xia, and S. Tian, "The dielectric, strain and energy storage density of BNT-BKHxT1− x piezoelectric ceramics," *Ceramics International,* vol. 43, no. 12, pp. 9253-9258, 2017.
[213] C. B. Sawyer and C. Tower, "Rochelle salt as a dielectric," *Physical review,* vol. 35, no. 3, p. 269, 1930.
[214] P. A. Tipler and G. Mosca, *Physik: Für wissenschaftler und ingenieure*. Springer-Verlag, 2014.
[215] T. Van Dijk and A. Burggraaf, "Grain boundary effects on ionic conductivity in ceramic GdxZr1–xO2–(x/2) solid solutions," *physica status solidi (a),* vol. 63, no. 1, pp. 229-240, 1981.
[216] K. S. Van Dyke, "The electric network equivalent of a piezoelectric resonator," *Phys. Rev,* vol. 25, no. 6, p. 895, 1925.
[217] M. Slabki, "High-power properties of lead-based and lead-free ferroelectric ceramics," Ph.D. Thesis, 11 Department of Materials and Earth Sciences > Material Science, Technische Universität Darmstadt, TUprints, 21763, 2022.
[218] M. Umeda, K. Nakamura, and S. Ueha, "The measurement of high-power characteristics for a piezoelectric transducer based on the electrical transient response," *Japanese Journal of Applied Physics,* vol. 37, no. 9S, p. 5322, 1998.
[219] M. I. Mendelson, "Average grain size in polycrystalline ceramics," *Journal of the American Ceramic society,* vol. 52, no. 8, pp. 443-446, 1969.
[220] J. Filik *et al.*, "Processing two-dimensional X-ray diffraction and small-angle scattering data in DAWN 2," *Journal of applied crystallography,* vol. 50, no. 3, pp. 959-966, 2017.

[221] J. E. Daniels, W. Jo, J. Rödel, V. Honkimäki, and J. L. Jones, "Electric-field-induced phase-change behavior in (Bi0.5Na0.5)TiO3–BaTiO3–(K0.5Na0.5)NbO3: A combinatorial investigation," *Acta Materialia,* vol. 58, no. 6, pp. 2103-2111, 2010.
[222] J. E. Daniels, W. Jo, J. Rödel, and J. L. Jones, "Electric-field-induced phase transformation at a lead-free morphotropic phase boundary: Case study in a 93%(Bi0.5Na0.5)TiO3–7% BaTiO3 piezoelectric ceramic," *Applied Physics Letters,* vol. 95, no. 3, p. 032904, July 2009.
[223] M. Hinterstein *et al.*, "Interplay of strain mechanisms in morphotropic piezoceramics," *Acta materialia,* vol. 94, pp. 319-327, 2015.
[224] M. Hinterstein *et al.*, "Determining fundamental properties from diffraction: Electric field induced strain and piezoelectric coefficient," *Physical Review B,* vol. 99, no. 17, p. 174107, 2019.
[225] J. Grässlin, L. B. McCusker, C. Baerlocher, F. Gozzo, B. Schmitt, and L. Lutterotti, "Advances in exploiting preferred orientation in the structure analysis of polycrystalline materials," *Journal of Applied Crystallography,* vol. 46, no. 1, pp. 173-180, 2013.
[226] Y. Sung, J. Kim, J. Cho, T. Song, M. Kim, and T. Park, "Effects of Bi nonstoichiometry in (Bi0.5+xNa)TiO3 ceramics," *Applied Physics Letters,* vol. 98, no. 1, p. 012902, 2011.
[227] A.-K. Fetzer, "Microstructural Characterization of Ferroelectric (Na1/2Bi1/2)TiO3-BaTiO3 Ceramics via Transmission Electron Microscopy," Dr. rer. nat, Fachbereich Material- und Geowissenschaften, Technische Universität Darmstadt, 2023.
[228] R. R. McQuade and M. R. Dolgos, "A review of the structure-property relationships in lead-free piezoelectric (1− x)Na0.5Bi0.5TiO3–(x)BaTiO3," *Journal of Solid State Chemistry,* vol. 242, pp. 140-147, 2016.
[229] S. Kong, N. Kumar, S. Checchia, C. Cazorla, and J. Daniels, "Defect-Driven Structural Distortions at the Surface of Relaxor Ferroelectrics," *Advanced Functional Materials,* vol. 29, no. 27, p. 1900344, 2019.
[230] N. Uchida and T. Ikeda, "Electrostriction in perovskite-type ferroelectric ceramics," *Japanese Journal of Applied Physics,* vol. 6, no. 9, p. 1079, 1967.
[231] M. R. Suchomel, A. M. Fogg, M. Allix, H. Niu, J. B. Claridge, and M. J. Rosseinsky, "Bi2ZnTiO6: A lead-free closed-shell polar perovskite with a calculated ionic polarization of 150 μC cm-2," *Chemistry of materials,* vol. 18, no. 21, pp. 4987-4989, 2006.
[232] T. Leist, W. Jo, T. Comyn, A. Bell, and J. Rödel, "Shift in morphotropic phase boundary in La-doped BiFeO3–PbTiO3 piezoceramics," *Japanese Journal of Applied Physics,* vol. 48, no. 12R, p. 120205, 2009.
[233] M. Budimir, D. Damjanovic, and N. Setter, "Piezoelectric anisotropy–phase transition relations in perovskite single crystals," *Journal of Applied Physics,* vol. 94, no. 10, pp. 6753-6761, 2003.
[234] H. Kungl and M. J. Hoffmann, "Temperature dependence of poling strain and strain under high electric fields in LaSr-doped morphotropic PZT and its relation to changes in structural characteristics," *Acta Materialia,* vol. 55, no. 17, pp. 5780-5791, 2007.
[235] D. Damjanovic, "Comments on origins of enhanced piezoelectric properties in ferroelectrics," *IEEE transactions on ultrasonics, ferroelectrics, and frequency control,* vol. 56, no. 8, pp. 1574-1585, 2009.
[236] Y.-I. Jung, S.-Y. Choi, and S.-J. L. Kang, "Effect of oxygen partial pressure on grain boundary structure and grain growth behavior in BaTiO3," *Acta Materialia,* vol. 54, no. 10, pp. 2849-2855, 2006/06/01/ 2006.
[237] W. Jo, J. Daniels, D. Damjanovic, W. Kleemann, and J. Rödel, "Two-stage processes of electrically induced-ferroelectric to relaxor transition in 0.94(Bi1/2Na1/2)TiO3-0.06BaTiO3," *Applied Physics Letters,* vol. 102, no. 19, p. 192903, May 2013.
[238] S. Takahashi, S. Hirose, K. Uchino, and K.-Y. Oh, "Electro-mechanical characteristics of lead-zirconate-titanate ceramics under vibration-level change," in *Proceedings of*

1994 IEEE International Symposium on Applications of Ferroelectrics, 1994: IEEE, pp. 377-382.
[239] U. Robels and G. Arlt, "Domain wall clamping in ferroelectrics by orientation of defects," *Journal of Applied Physics,* vol. 73, no. 7, pp. 3454-3460, 1993.
[240] L. Koch, S. Steiner, K.-C. Meyer, I.-T. Seo, K. Albe, and T. Frömling, "Ionic conductivity of acceptor doped sodium bismuth titanate: influence of dopants, phase transitions and defect associates," *Journal of Materials Chemistry C,* vol. 5, no. 35, pp. 8958-8965, 2017.
[241] H. Dederichs and G. Arlt, "Aging of Fe-doped PZT ceramics and the domain wall contribution to the dielectric constant," *Ferroelectrics,* vol. 68, no. 1, pp. 281-292, 1986.
[242] R. A. Eichel, "Characterization of defect structure in acceptor-modified piezoelectric ceramics by multifrequency and multipulse electron paramagnetic resonance spectroscopy," *Journal of the American Ceramic Society,* vol. 91, no. 3, pp. 691-701, 2008.
[243] W. Gordy and W. O. Thomas, "Electronegativities of the elements," *The Journal of Chemical Physics,* vol. 24, no. 2, pp. 439-444, 1956.
[244] Y. Iwadate, K. Kawamura, K. Murakami, K. Igarashi, and J. Mochinaga, "Electronic polarizabilities of Tl+, Ag+, and Zn2+ ions estimated from refractive index measurements of TlNO3, AgNO3, and ZnCl2 melts," *The Journal of Chemical Physics,* vol. 77, no. 12, pp. 6177-6183, 1982.
[245] X. S. Qiao, X. M. Chen, H. L. Lian, W. T. Chen, J. P. Zhou, and P. Liu, "Microstructure and electrical properties of nonstoichiometric 0.94(Na0.5Bi0.5+x)TiO3–0.06 BaTiO3 lead-free ceramics," *Journal of the American Ceramic Society,* vol. 99, no. 1, pp. 198-205, 2016.
[246] E. Sapper, "Lead-free (1-x)(Bi1/2Na1/2)TiO3-xBaTiO3: The impact of relaxor characteristics and induced long range order on piezoelectric properties," oktor-Ingenieurs Promotion, Material- und Geowissenschaften, Technischen Universität Darmstadt, VVB Laufersweiler, 2014.
[247] S. F. Bartram and R. A. Slepetys, "Compound formation and crystal structure in the system ZnO-TiO2," *Journal of the American Ceramic Society,* vol. 44, no. 10, pp. 493-499, 1961.
[248] R. L. Millard, R. C. Peterson, and B. K. Hunter, "Study of the cubic to tetragonal transition in Mg2TiO4 and Zn2TiO4 spinels by 17O MAS NMR and Rietveld refinement of X-ray diffraction data," *American Mineralogist,* vol. 80, no. 9-10, pp. 885-896, 1995.
[249] E. Sapper, S. Schaab, W. Jo, T. Granzow, and J. Rödel, "Influence of electric fields on the depolarization temperature of Mn-doped (1-x) Bi1/2Na1/2TiO3-xBaTiO3," *Journal of Applied Physics,* vol. 111, no. 1, p. 014105, 2012.
[250] Y. Doshida, H. Shimizu, Y. Mizuno, K. Itoh, S. Hirose, and H. Tamura, "Nonlinear behavior and high-power properties of (Bi,Na,Ba)TiO3 and (Sr,Ca)2NaNb5O15 piezoelectric ceramics," *Japanese Journal of Applied Physics,* vol. 50, no. 9S2, p. 09ND06, 2011.
[251] D. Berlincourt, C. Cmolik, and H. Jaffe, "Piezoelectric properties of polycrystalline lead titanate zirconate compositions," *Proceedings of the IRE,* vol. 48, no. 2, pp. 220-229, 1960.
[252] M. Davis, M. Budimir, D. Damjanovic, and N. Setter, "Rotator and extender ferroelectrics: Importance of the shear coefficient to the piezoelectric properties of domain-engineered crystals and ceramics," *Journal of Applied Physics,* vol. 101, no. 5, p. 054112, 2007.
[253] H. Nagata, K. Takai, Y. Nomura, S. Sato, Y. Hiruma, and T. Takenaka, "Vibration velocities under high-power driving on perovskite-type lead-free ferroelectric ceramics,"

in *2010 IEEE International Symposium on the Applications of Ferroelectrics (ISAF)*, 2010: IEEE, pp. 1-4.
[254] D. Guyomar, B. Ducharne, and G. Sebald, "High nonlinearities in Langevin transducer: A comprehensive model," *Ultrasonics,* vol. 51, no. 8, pp. 1006-1013, 2011.
[255] M. Prokic, "Piezoelectric Transducers Modeling and Characterization, ," ed. Switzerland by MPI, Copyright© by MPI: August, 2004.
[256] Y. Gao, K. Uchino, and D. Viehland, "Time dependence of the mechanical quality factor in “hard” lead zirconate titanate ceramics: development of an internal dipolar field and high power origin," *Japanese journal of applied physics,* vol. 45, no. 12R, p. 9119, 2006.
[257] Y. A. Genenko and D. C. Lupascu, "Drift of charged defects in local fields as aging mechanism in ferroelectrics," *Physical Review B,* vol. 75, no. 18, p. 184107, 2007.
[258] K. Lalitha, D. Isaia, W. Gong, C. Wu, Y. Li, and J. Rödel, "Deformation and bending strength of high-performance lead-free piezoceramics," *Journal of the American Ceramic Society,* vol. 105, no. 5, pp. 3128-3132, 2022.
[259] K. G. Webber, M. Vögler, N. H. Khansur, B. Kaeswurm, J. E. Daniels, and F. H. Schader, "Review of the mechanical and fracture behavior of perovskite lead-free ferroelectrics for actuator applications," *Smart Material Structures,* vol. 26, p. 063001, June 01, 2017 2017, doi: 10.1088/1361-665X/aa590c.
[260] H. Daneshpajooh, M. Choi, Y. Park, T. Scholehwar, E. Hennig, and K. Uchino, "Compressive stress effect on the loss mechanism in a soft piezoelectric Pb(Zr,Ti)O3," *Review of Scientific Instruments,* vol. 90, no. 7, p. 075001, 2019.
[261] D. A. Ochoa, J. E. García, I. Tamayo, V. Gomis, D. Damjanovic, and R. Perez, "Effect of Uniaxial Compressive Stress on Dielectric and Piezoelectric Responses in Lead Zirconate Titanate Based Ceramics," *Journal of the American Ceramic Society,* vol. 95, no. 5, pp. 1656-1660, 2012.
[262] Q. Zhang, J. Zhao, K. Uchino, and J. Zheng, "Change of the weak-field properties of Pb (ZrTi) O3 piezoceramics with compressive uniaxial stresses and its links to the effect of dopants on the stability of the polarizations in the materials," *Journal of materials research,* vol. 12, no. 1, pp. 226-234, 1997.
[263] Y. R. Zhang, J. F. Li, and B. P. Zhang, "Enhancing electrical properties in NBT–KBT lead-free piezoelectric ceramics by optimizing sintering temperature," *Journal of the American Ceramic Society,* vol. 91, no. 8, pp. 2716-2719, 2008.
[264] A. B. Kounga, T. Granzow, E. Aulbach, M. Hinterstein, and J. Rödel, "High-temperature poling of ferroelectrics," *Journal of Applied Physics,* vol. 104, no. 2, p. 024116, 2008.
[265] B. Li, J. E. Blendell, and K. J. Bowman, "Temperature-dependent poling behavior of lead-free BZT–BCT piezoelectrics," *Journal of the American Ceramic Society,* vol. 94, no. 10, pp. 3192-3194, 2011.
[266] S. Zhang, H. J. Lee, and T. R. Shrout, "NBT based lead-free piezoelectric materials for high power applications," ed: Google Patents, 2013.
[267] S. H. Yoon, C. A. Randall, and K. H. Hur, "Effect of acceptor (Mg) concentration on the resistance degradation behavior in acceptor (Mg)-doped BaTiO3 bulk ceramics: II. Thermally stimulated depolarization current analysis," *Journal of the American Ceramic Society,* vol. 92, no. 8, pp. 1766-1772, 2009.
[268] G. D. Adhikary, D. K. Khatua, A. Senyshyn, and R. Ranjan, "Random lattice strain and its relaxation towards the morphotropic phase boundary of Na0.5Bi0.5TiO3-based piezoelectrics: Impact on the structural and ferroelectric properties," *Physical Review B,* vol. 99, no. 17, p. 174112, 2019.
[269] N. H. Khansur, M. Hinterstein, Z. Wang, C. Groh, W. Jo, and J. E. Daniels, "Electric-field-induced strain contributions in morphotropic phase boundary composition of (Bi1/2Na1/2) TiO3-BaTiO3 during poling," *Applied Physics Letters,* vol. 107, no. 24, p. 242902, 2015.

[270] J. L. Jones, B. J. Iverson, and K. J. Bowman, "Texture and anisotropy of polycrystalline piezoelectrics," *Journal of the American Ceramic Society,* vol. 90, no. 8, pp. 2297-2314, 2007.
[271] B. Liu *et al.*, "Simultaneously enhanced piezoelectric response and piezoelectric voltage coefficient in textured KNN-based ceramics," *Journal of the American Ceramic Society,* vol. 101, no. 1, pp. 265-273, 2018.
[272] G. Esteves, C. M. Fancher, S. Röhrig, G. A. Maier, J. L. Jones, and M. Deluca, "Electric-field-induced structural changes in multilayer piezoelectric actuators during electrical and mechanical loading," *Acta Materialia,* vol. 132, pp. 96-105, 2017.
[273] T. Nishikubo *et al.*, "Polarization-and strain-mediated control of negative thermal expansion and ferroelasticity in BiInO3–BiZn1/2Ti1/2O3," *Chemistry of Materials,* vol. 33, no. 4, pp. 1498-1505, 2021.
[274] J. Zhao, S. D. Funni, E. R. Molina, E. C. Dickey, and J. L. Jones, "Orientation-dependent, field-induced phase transitions in soft lead zirconate titanate piezoceramics," *Journal of the European Ceramic Society,* vol. 41, no. 6, pp. 3357-3362, 2021.
[275] L. Lemos da Silva *et al.*, "Uncovering the symmetry of the induced ferroelectric phase transformation in polycrystalline barium titanate," *Journal of Applied Physics,* vol. 130, no. 23, p. 234101, 2021.
[276] H. Liu *et al.*, "Critical role of monoclinic polarization rotation in high-performance perovskite piezoelectric materials," *Physical Review Letters,* vol. 119, no. 1, p. 017601, 2017.
[277] A. Wohninsland, A.-K. Fetzer, R. Broughton, J. L. Jones, and K. Lalitha, "Structural and microstructural description of relaxor-ferroelectric transition in quenched Na1/2Bi1/2TiO3BaTiO3," *Journal of Materiomics,* vol. 8, no. 4, pp. 823-832, 2022.
[278] G. Picht, N. H. Khansur, K. G. Webber, H. Kungl, M. J. Hoffmann, and M. Hinterstein, "Grain size effects in donor doped lead zirconate titanate ceramics," *Journal of applied physics,* vol. 128, no. 21, p. 214105, 2020.
[279] B. Li, M. S. Cao, J. Liu, and D. W. Wang, "Domain structure and enhanced electrical properties in sodium bismuth titanate ceramics sintered from crystals with different morphologies," *Journal of the American Ceramic Society,* vol. 99, no. 7, pp. 2316-2326, 2016.

List of Figures

List of Tables

Acknowledgements

I would like to thank Prof. Jürgen Rödel for the opportunity to work on this project. In addition to the constant scientific support, he encouraged me to find and shift my own limits. I greatly acknowledge his unbroken scientific curiosity and open mind for unconventional and new solutions and for constantly trying to expand the knowledge of electroceramics and ferroelectric ceramics.

I would like also to thank Prof. Andreas Klein for his interest in my work and for being the second reviewer of this study. Similarly, my thanks go to the other committee members, Prof. Wolfgang Donner and Prof. Mario Kupnik, for their time and interest.

Furthermore, I am thankful for all the support, constructive feedback, and sharing of ideas and knowledge from Prof. Jurij Koruza, who even continued to support me after moving to Austria. I will always remember the visit to Graz as a special time during my PhD.

I greatly appreciate the discussions, open ear, and guidance of Dr. Lalitha Kodumudi Venkataraman and Dr. Till Frömling, without whom I would not have started the PhD.

I would like to thank Gila Völzke, Patrick Breckner, Daniel Isaia, and Siegfried Teuber for all the administrative and technical support. They not only made a lot of things easier, but without them, some parts would not have been possible to achieve. This point is especially true for Siegfried Teuber, who patiently worked with me over three years on this project.

Additionally, I am grateful to all former and present members of the NAW group. They were always committed to having a pleasant working atmosphere, especially the barbeques and after-work meetings, which were great experiences. I want to thank Dr. Lovro Fulanović and Dr. Mao-Hua Zhang for reviewing my thesis, as well as Annisa Amanda Rahmi Harahap for being a motivated student and contributing to this work with her own bachelor's thesis. Furthermore, thank you to Max Gehringer and Andreas Wohninsland for being part of this journey from the beginning in so many ways I cannot name them all here.

I am very grateful for the close collaboration, exchange of knowledge, and highly detailed and helpful feedback from all the industry partners. Thank you for all the great project meetings and guidance throughout the entire project.

I am thankful for all the great and supportive friends who have always brought joy to my life outside this project by going climbing, having trips to Heidelberg, having lunch together, going for runs, founding a company, meeting in virtual games, and so much more.

Finally, I would like to thank my family, my parents and siblings, for their everlasting love and support, which go far beyond this thesis.

Curriculum Vitae

Work Experience

02/2019 – 04/2019	Research assistant, research group: Nonmetallic-Inorganic Materials, Technical University of Darmstadt
05/2019 – 12/2022	Research associate, research group: Nonmetallic-Inorganic Materials, Technical University of Darmstadt

Publications

Texture-based ferroelectric hardening in Na1/2Bi1/2TiO3-based piezoceramics. Physical Review Materials (accepted, not published yet), **D. Bremecker,** A. Wohninsland, S. Teuber, K.V. Lalitha, M. Hinterstein, J. Rödel

Characterization of crystal structure, electrical and electromechanical properties of Mg-doped $0.94Na_{1/2}Bi_{1/2}TiO_3$-$0.06BaTiO_3$. Journal of European Ceramic Society, **D. Bremecker**, M. Slabki, J. Koruza, J. Rödel

Influence of Zn^{2+} doping on the morphotropic phase boundary in lead-free piezoelectric $(1–x)Na_{1/2}Bi_{1/2}TiO_3$-$xBaTiO_3$. Journal of American Ceramic Society, **D. Bremecker**, L. K. Venkataraman, S. Teuber, J. Koruza, J. Rödel

Mechanically tuned conductivity at individual grain boundaries in polycrystalline ZnO varistor ceramics. Journal of Applied Physics, **D. Bremecker**, M. Gehringer, D. Isaia, J. Rödel, T. Frömling

Designing properties of $(Na_{1/2}Bi_x)TiO_3$-based material through A-site non-stoichiometry. Journal of Materials Chemistry C, T. Frömling, S. Steiner, A. Ayrikyan, **D. Bremecker**, M. Dürrschnabel, L. Molina-Luna, H.-J. Kleebe, K. G. Webber, M. Acosta

Conference Contributions

Processing and properties of $Na_{1/2}Bi_{1/2}TiO_3$-$BaTiO_3$:Al_2O_3 piezoceramic composites, Electroceramics XVII Conference, Darmstadt, Germany. **Daniel Bremecker**, Lalitha Kodumudi Venkataraman, Mihail Slabki, Jurij Koruza, Jürgen Rödel

Morphotropic phase boundary in pure and Zn^{2+}-doped lead-free (1-x)$Na_{1/2}Bi_{1/2}TiO_3$-x$BaTiO_3$ piezoceramics. Piezoelectrics for End Users XI, University of Sassari, Italy. **Daniel Bremecker**, Lalitha Kodumudi Venkataraman, Siegfried Teuber, Jurij Koruza, Jürgen Rödel

Tailoring of electrical and electromechanical properties in Mg-doped 0.94$Na_{1/2}Bi_{1/2}TiO_3$-0.06$BaTiO_3$. Ceramics in Europe, Krakow, Poland. **Daniel Bremecker**, Mihail Slabki, Jurij Koruza, Jürgen Rödel